



THE UNIVERSITY
of ADELAIDE

FACULTY OF SCIENCES
SCHOOL OF PHYSICAL SCIENCES

High-Energy Cosmic-Ray Propagation in the
Milky Way and the Associated Diffuse
Gamma-Ray Emission

PETER MARINOS

Principal Supervisor:
Prof. Gavin ROWELL

Co-Supervisor:
Dr. Sabrina EINECKE

Submitted: November, 2023
Accepted: January, 2024
Revised: March, 2025

Contents

Abstract	v
Declaration of Originality	vi
Acknowledgements	vii
1 Introduction	1
2 Modelling Cosmic-Ray Transport with GALPROP	5
2.1 Cosmic-Ray Transport	6
2.2 Cosmic-Ray Energy Losses and Gamma-Ray Production	10
2.2.1 Hadronic Processes	10
2.2.2 Leptonic Processes	12
2.2.3 Gamma-Ray Flux	18
2.2.4 Cooling Distances	21
2.3 CR Source Distributions	24
2.3.1 Galactic Disk	24
2.3.2 Spiral Arms	25
2.3.3 Disk and Spiral Arm Combinations	25
2.4 Interstellar Gas	27
2.5 Interstellar Radiation Fields	28
2.5.1 Freudenreich Spatial Model	29
2.5.2 Robitaille Spatial Model	33
2.6 Galactic Magnetic Fields	38
2.6.1 GALPROP Axisymmetric Exponential Model	39
2.6.2 Pshirkov Bi/Axisymmetric Spiral Models	39
2.7 GALPROP Setup	41

2.7.1	Diffusion and Injection Parameter Optimisation	42
2.7.2	Timestep	45
2.7.3	Propagation Grid	45
3	TeV Gamma-Ray Observations with H.E.S.S.	51
3.1	Gamma-Ray Observations	51
3.1.1	Extensive Air Showers (EASs)	52
3.1.2	Imaging Atmospheric Cherenkov Telescopes	55
3.2	The H.E.S.S. Galactic Plane Survey (HGPS)	56
3.2.1	Gamma-Ray Flux	58
3.2.2	Integration Beam	59
3.2.3	CR Background Estimation	59
3.2.4	Flux Sensitivity	63
3.2.5	H.E.S.S. Gamma-Ray Source Horizon in the MW	64
3.3	HGPS Source Characterisation and Classification	66
3.3.1	HGPS Source Characterisation	66
3.3.2	HGPS Galactic TeV Source Classifications	67
3.4	The HGPS Large-Scale Gamma-Ray Emission	71
3.4.1	The HGPS Diffuse Gamma-Ray Emission	72
4	Comparing GALPROP to the HGPS	75
4.1	Analysing the Large-Scale Emission	75
4.1.1	Sliding Window Parameters	76
4.2	Adapting the GALPROP Results for Comparison to the HGPS	79
4.2.1	GALPROP Flux Integration	80
4.2.2	Applying a Telescope Beam to GALPROP	80
4.3	Adapting the HGPS Results for Comparisons to GALPROP	83
4.3.1	Masking the Catalogued HGPS Sources	83
4.3.2	Unresolved Sources in the HGPS	87

5	First Paper: Diffuse TeV Gamma-Ray Predictions with GALPROP	89
6	Time-Dependent CR Injection	105
6.1	Motivation for a Time-Dependent Solution	105
6.2	Description of the Time-Dependent Solution	107
6.2.1	Time-Dependent Source Distribution	107
6.2.2	Time-Dependent Source Parameters	108
6.2.3	Time-Dependent Timesteps	109
6.3	Time-Dependent GALPROP Simulations: Trials and Optimisations	109
6.3.1	Length of Simulation	109
6.3.2	Sampling Interval	111
6.3.3	Simulation Timestep	112
6.3.4	Spatial Grid	114
6.3.5	CR Source Placement in Space and Time	116
7	Second Paper: Time Variability of Galactic CRs and Gamma Rays	117
8	CTA, the Galactic Plane Survey, and the Diffuse Emission	133
8.1	The ‘gammapy’ Python Package	134
8.1.1	Instrument Response Functions	134
8.1.2	Reconstructing the GALPROP Diffuse Flux	135
8.2	Detectability of the Diffuse Gamma-Ray Emission with CTA	136
8.2.1	Diffuse Gamma-Ray Emission Near HESS J1614–518	137
8.2.2	Diffuse Gamma-Ray Emission Near RX J1713.7–3946	138
9	Summary and Future Work	141
9.1	Future Work	142
9.1.1	Applications to TeV Gamma-Ray Observations	143
A	Running GALPROP	145
A.1	Grid Coordinate Setup	145

A.2	Time Coordinate Setup	147
A.3	GALPROP Output Examples	148
A.3.1	Time-Independent Output Examples	149
A.3.2	Time-Dependent Output Examples	152
B	HGPS Source Parameters	157
	Bibliography	160

Abstract

Cosmic rays (CRs) are electrons, protons, and other nuclei that have been accelerated to energies ranging from 1 MeV to 100 EeV (10^6 to 10^{20} eV). As CRs travel through the interstellar medium (ISM) they are deflected by the magnetic fields that permeate interstellar space, propagating for up to millions of years and across distances as large as thousands of parsecs.

While propagating, CRs collide with gas particles and interact with the infrared radiation from stars and the cosmic microwave background (CMB). These interactions create gamma-ray photons that can be observed at Earth. Observations of gamma rays show a large-scale background component of emission along the plane of the Milky Way. Even after a century since CRs were discovered there is no widespread consensus on the locations where Galactic CRs are accelerated, their composition, or which processes create most observed gamma rays.

Simulations of Galactic CR transport were performed with the software GALPROP, with the resulting gamma-ray flux calculated up to the PeV regime. The impact of altering parameters such as the number and distribution of CR sources, the distribution of infrared radiation between stars, and the distribution and strength of the Galactic magnetic field (GMF), were investigated. For the first time the modelling variation in the TeV predictions due to uncertainties in the Galactic distributions was quantified. Additionally, the modelling variation from considering a stochastic placement of the CR sources was quantified up to 1 PeV.

The simulation results were compared to the most detailed Galactic TeV gamma-ray survey: the H.E.S.S. Galactic plane survey (HGPS). The GALPROP predictions were broadly compatible with the large-scale emission from the HGPS after accounting for both the catalogued sources and estimates of the unresolved source fraction. At 1 TeV the gamma-ray emission from CR electrons was found to contribute $\sim 50\%$ to the large-scale emission, with this leptonic component increasing further as energy increased. The GMF was found to be an important modelling consideration above 1 TeV as it impacted the large-scale emission by approximately a factor of two. Additionally, the CR electron flux at Earth above 1 TeV was found to vary by over a factor of ten over a period of a few million years due to the short cooling times and diffusion distances of the TeV CR electrons. The GALPROP models were found to agree with observations of the diffuse gamma rays in the TeV regime by H.E.S.S., and the PeV regime by LHAASO, extending the demonstrated accuracy of GALPROP into the TeV–PeV regime.

The results in this thesis will aid in discovering the origin of the diffuse gamma-ray emission and allows constraints to be placed on how the CR sources are distributed in the MW. The results will also inform the next generation of experiments, such as the Cherenkov telescope array (CTA), on possible observation strategies and background considerations. It was also found that the proposed CTA Galactic plane survey will be sensitive enough to observe the large-scale diffuse gamma-ray emission in the TeV regime.

Declaration of Originality

I certify that this work contains no material which has been accepted for the award of any other degree or diploma in my name in any university or other tertiary institution and, to the best of my knowledge and belief, contains no material previously published or written by another person, except where due reference has been made in the text. In addition, I certify that no part of this work will, in the future, be used in a submission in my name for any other degree or diploma in any university or other tertiary institution without the prior approval of the University of Adelaide and where applicable, any partner institution responsible for the joint award of this degree.

The author acknowledges that the copyright of published works contained within this thesis resides with the copyright holder(s) of those works.

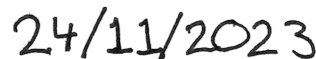
I give permission for the digital version of my thesis to be made available on the web, via the University's digital research repository, the Library Search, and through web search engines, unless permission has been granted by the University to restrict access for a period of time.

I acknowledge the support I have received for my research through the provision of an Australian Government Research Training Program Scholarship.

This thesis was submitted and accepted with a draft version of the paper "On the Temporal Variability of the Galactic Multi-TeV Interstellar Emission". This revised edition has been updated to include the published version of the manuscript.



Signature



Date

LIST OF MY PUBLISHED PAPERS WITHIN THIS THESIS:

- Paper 1: The Steady-State Multi-TeV Diffuse Gamma-Ray Emission Predicted with GALPROP and Prospects for the Cherenkov Telescope Array. Published in MNRAS in February 2023.
- Paper 2: On the Temporal Variability of the Galactic Multi-TeV Interstellar Emissions. Published in ApJ in March 2025.

Acknowledgements

I acknowledge the support I have received for my research through the provision of an Australian Government Research Training Program Scholarship. Travel grants were provided by both the Astronomical Society of Australia and the Australian Institute of Physics.

This thesis makes use of the software GALPROP (Moskalenko and Strong, 1998; Strong and Moskalenko, 1998) which can be found at <https://galprop.stanford.edu/>. GALPROP development is partially funded via NASA grants 80NSSC22K0477, 80NSSC22K0718, and 80NSSC23K0169. The Python packages utilised extensively throughout this work are: Numpy (Harris et al., 2020), matplotlib (Hunter, 2007), SciPy (Virtanen et al., 2020), Astropy (Robitaille et al., 2013; Price-Whelan et al., 2018), and gammapy (Deil et al., 2017). The software HEALPix (Górski et al., 2005), and the related Python package, is used for some results in this thesis. The public data from the H.E.S.S. Galactic plane survey (Abdalla et al., 2018e) is used for some results presented in this thesis and can be found at <https://www.mpi-hd.mpg.de/hfm/HESS/hgps/>. This thesis also makes use of NASA's Astrophysics Data System (<https://ui.adsabs.harvard.edu/>). The services provided by the Phoenix HPC service at the University of Adelaide supported all computational requirements.

On a more personal note, I would like to thank Prof. Gavin Rowell and Dr. Troy Porter. I would have never been able to finish without their support and indelible teachings. And thank you to Dr. Fabien Voisin for his tireless work on UofA's HPC service. I would also like to thank Dr. Sabrina Einecke, A. Prof. Guðlaugur Jóhannesson, and Dr. Igor Moskalenko for their support and input on my manuscripts. For my PhD colleagues, I would like to thank Tiffany Collins, Simon Lee, Olaf König, and Rami Alsulami.

I would also like to thank my beautiful partner, Dr. Hannah Twidale, for I fear the repercussions of omitting her mention. Thank you to Brad Michelbach and Wayne Maloney for all the coffee and beer, respectively. I must also thank my Mum, who listened to my endless ramblings and provided unremitting support throughout my PhD, and my Father, who was always there to join me at the Clipsal.

Chapter 1

Introduction

In the early nineteen hundreds, ionising radiation was thought to be caused by the decay of radioactive materials in Earth’s crust. The radiation would then travel upwards, ionising the atmosphere. A famous balloon flight by Viktor Hess in 1912 found that the radiation increased with altitude, showing that this ionisation radiation was from the cosmos – hence the name: cosmic rays (CRs; as coined by [Millikan and Cameron, 1928](#)). After another balloon flight during a solar eclipse, it was shown that this radiation was not from the Sun and must therefore come from outside the Solar system ([Hess, 1912](#)). Viktor Hess was later awarded a Nobel prize for these discoveries. Later, George Lemaître and Manuel Vallarta measured an anisotropy in the CR arrival direction by utilising two arrays of Geiger counters separated by a cloud chamber. The anisotropy is caused by the magnetic field of the Earth, with positive charges coming from the West. Lemaître and Vallarta observed that the majority of CRs came from the West, implying that most CRs had positive charges ([Lemaître and Vallarta, 1933](#)).

CRs are highly energetic (relativistic) particles, such as protons, anti-protons, atomic nuclei, electrons, positrons, and even neutrinos and anti-neutrinos, though usually only the charged particles are considered. CRs travel through space with velocities close to that of the speed of light – so close that it becomes more useful to discuss CRs in terms of their energy. CR energies are typically measured in eV, or electron-Volts, and can be in the range of 1 MeV to 100 EeV (10^6 to 10^{20} eV), or one billion to one hundred quintillion electron-Volts – enough energy to power a 60-Watt incandescent lightbulb for just over two seconds contained within a particle a trillion times smaller than a grain of sand ([Clay and Dawson, 1997](#)).

The study of CRs led to the discovery of many particles, from the muon by [Anderson and Neddermeyer \(1936\)](#) and its confirmation as a new particle by [Street and Stevenson \(1937\)](#). Both the pion and kaon were discovered through CR observations by [Lattes et al. \(1947\)](#). CRs are an integral part of the Milky Way (MW) and the interstellar medium (ISM). As CRs apply pressure to the interstellar gas they are essential to the formation and evolution of Galaxies and their stars ([Semenov et al., 2021](#)). CRs also affect the chemistry in the ISM ([Bayet et al., 2011](#)) and Earth’s atmosphere ([Nicolet, 1975](#)) and are responsible for the creation of certain elements such as boron.

The CR energy density in the Galactic plane is approximately 1 eV cm^{-3} , which is similar to the energy density of the Galactic magnetic field (GMF), the turbulent motions of the interstellar gas, and even that of the interstellar radiation field (i.e. all light emitted by stars, the CMB, and thermal emission from dust combined; [Webber, 1998](#)). Therefore, CRs represent an important dynamical component of the MW. However, after more than a century since their discovery, many open questions remain. The mechanisms that accelerate CRs to these extreme energies, and even the mechanisms behind how they travel away from their sources, are not fully understood.

The locations where CRs are accelerated are referred to as CR sources. These sources are thought to be shell-type supernova remnants (SNRs), pulsar wind nebulae (PWNe), stellar clusters, gamma-ray (γ -ray) binaries, or even the supermassive black holes at the centres of galaxies. There are a multitude of processes that can theoretically accelerate the CRs to the energies we observe, with each source type possibly employing more than one mechanism. The energy spectrum of CRs provides valuable insight into these acceleration processes, as each possible mechanism results in a different spectrum of CRs being injected into the ISM. However, as CRs are charged particles, their paths are deflected by the large-scale (>100 pc) and small-scale (<100 pc) magnetic fields throughout the MW.

Both the large-scale and small-scale magnetic fields in the MW have some randomness due to the ionised gases in the ISM creating their own localised magnetic fields. The CRs will scatter off the magnetic fields, performing a random walk through the ISM as they spread away from their acceleration sites. This process is known as diffusion. CR diffusion in the MW is a complex physical process – while CRs propagate they interact with the ISM, losing energy and creating γ rays through collisions with the ISM gas, bremsstrahlung interactions with the ISM nuclei, and inverse Compton scattering on low-energy photons. As γ rays are not deflected by the ambient medium they can be used to probe the underlying CR physics surrounding the CR accelerators and provide critical information on particle interactions.

The OSO-3 (Kraushaar et al., 1972) mission was a satellite launched in 1967 that observed X-rays and γ rays. OSO-3 observed a large structure of γ rays along the Galactic plane of the MW in the MeV to GeV energy range. Later, COS-B (Bignami and Hermesen, 1983) was able to distinguish discrete γ -ray sources from the large-scale structure. Following these observatories, the EGRET (Kanbach et al., 1989) mission was able to resolve over 200 γ -ray sources and provided the first detailed view of the large-scale γ -ray emission for energies between 30 MeV and 30 GeV (Hunter et al., 1997). With the launch of *Fermi*-LAT (Atwood et al., 2009), which is still in operation, there are now over 5,000 identified MeV to GeV γ -ray sources in the MW, with the total Galactic MeV and GeV γ -ray emission being dominated by a large-scale structure (Abdollahi et al., 2020). Maps of the all-sky EGRET and *Fermi*-LAT γ -ray emission can be seen in Figure 1.1. Both the EGRET and *Fermi*-LAT skymaps show discrete sources and a large structure along the Galactic plane. Difference in large-scale γ -ray structure can also be seen between 100 MeV and 1 GeV skymaps. For the TeV energy regime the dominant emission changes – the H.E.S.S. collaboration, in the H.E.S.S. Galactic plane survey (HGPS), found that the individual γ -ray sources dominated over the diffuse, large-scale γ -ray emission (Abdalla et al., 2018e). Despite five decades of observations of the large-scale γ -ray emission, the origin of the diffuse emission has not yet reached a consensus.

The large-scale γ -ray emission is defined as the γ -ray structure along the Galactic plane. It covers all Galactic longitudes and spans up to 10° in Galactic latitude for MeV γ rays. The large-scale γ -ray emission includes both the emission from unresolved γ -ray sources and the γ -ray emission from diffuse CRs. The large-scale *diffuse* γ -ray emission is that from only diffuse CRs (i.e. CRs that have travelled >100 pc from their initial site of acceleration). Recently the large-scale emission has been observed in the TeV energy range by Argo-YBJ (Bartoli et al., 2015), the PeV energy range by Tibet AS γ (Amenomori et al., 2021) and LHAASO (Di Sciacio, 2016; Cao et al., 2023), and will likely soon be observed by HAWC (Albert et al., 2022a). The Cherenkov telescope array (CTA; Acharya et al., 2018) is currently under construction and will likely observe the diffuse emission at TeV energies within its first decade (Acero et al., 2013; Acharya et al., 2018).

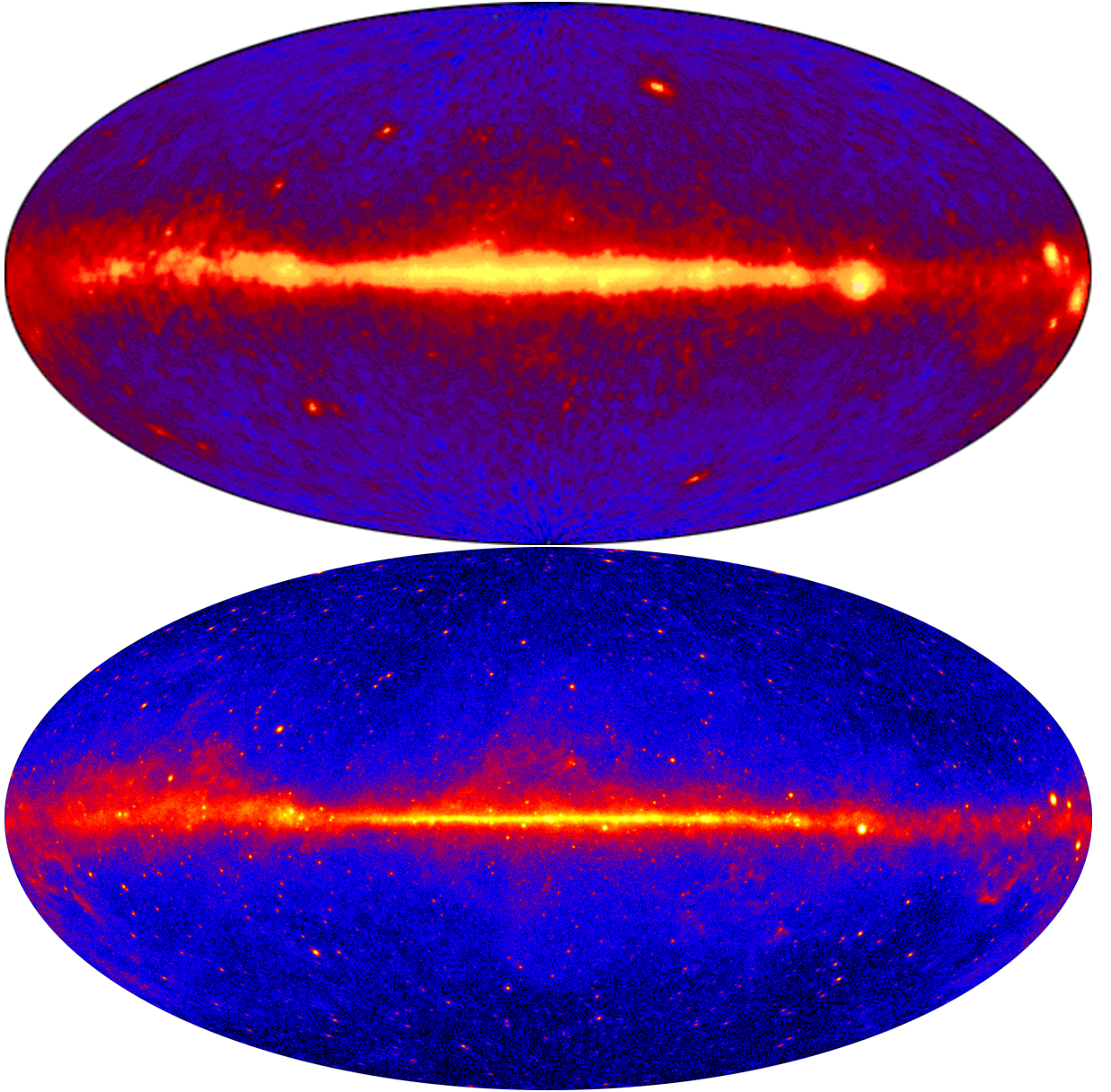


Figure 1.1: The EGRET γ -ray flux integrated above 100 MeV (top image; [Hartman et al., 1999](#)), and the *Fermi*-LAT γ -ray flux integrated above 1 GeV for the first five years of operation (bottom image; [Ackermann et al., 2012](#)).

The diffuse emission can overpower low surface-brightness γ -ray sources, especially in the GeV–TeV energy regime. Hence, it is critical that accurate and precise models of the background diffuse emission be constructed. For example, the *Fermi*-LAT collaboration employed some of the emissions predicted by the CR propagation software GALPROP as a background interstellar emissions model. Using GALPROP as a background model enabled the *Fermi*-LAT collaboration to extract γ -ray source characteristics and properties from the survey ([Ackermann et al., 2012](#)). With more sensitive TeV observatories, the dimmest γ -ray sources will only be observable if employing a well-motivated and accurate diffuse model as a background interstellar emissions model. Furthermore, diffuse emission estimates will improve the accuracy and precision of γ -ray source analyses at GeV–PeV energies. Improved diffuse emission estimates may even help confirm the existence of dark matter through the observations of CRs and γ rays from dark matter particle self-annihilations in the Galactic centre ([Conrad and Reimer, 2017](#)).

Creating accurate models of the MW’s γ -ray emission across the entire energy range requires modelling of multiple interacting systems and processes, such as: the gas density and its ionisation, atomic, and chemical composition, the distribution of CR sources across the Milky Way, the interstellar radiation field (ISRF), and the Galactic magnetic field (GMF). These processes and distributions must be modelled simultaneously. In this thesis the CR propagation and γ -ray production code GALPROP is used to perform this modelling.

Although the HGPS has been compared to various other TeV γ -ray facilities (e.g. [Neronov and Semikoz, 2020](#); [Abdalla et al., 2021](#)), there have been no comparisons with the simulated TeV γ -ray flux from CR propagation codes. The primary goal of this thesis is then to compare the large-scale TeV γ -ray emission (and estimates of the diffuse emission) from H.E.S.S. to the simulated diffuse TeV γ -ray emission from GALPROP. Characterising the precision of the models at TeV energies is integral to understanding the validity of using said models as backgrounds and will aid in constraining the origin of the diffuse γ -ray emission.

To achieve these goals, this thesis will begin by describing the GALPROP models in [Chapter 2](#) – from how CR diffusion is simulated, to how the γ -ray emission is calculated. A description of the Galactic distributions used throughout the modelling is also included. [Chapter 3](#) will then focus on γ -ray observations, particularly the HGPS, discussing limitations and important considerations for estimates of the TeV large-scale diffuse emission. [Chapter 4](#) will bring the simulations and observations together, detailing how a fair comparison between the predictions and observations was ensured. The first published work is included as [Chapter 5](#) and contains the results from the comparisons between GALPROP and the HGPS.

The GALPROP simulations are then extended to use a time-dependent solution to the diffusion equation. The motivations are discussed, and the results scrutinised, in [Chapter 6](#). The effects of using a time-dependent solution on the local CR results, the Galaxy-wide γ -ray results, and the implications for comparisons to the HGPS, are included in the second published work in [Chapter 7](#).

Future observations from CTA present a leap forward for TeV γ -ray measurements. Using the γ -ray predictions from GALPROP and the simulated performance of CTA, it will be determined whether future observations by CTA will be able to observe the diffuse γ -ray emission in [Chapter 8](#).

Finally, [Chapter 9](#) summarises the work and findings from this thesis and discusses future extensions.

Chapter 2

Modelling Cosmic-Ray Transport with GALPROP

Modelling the broad-band non-thermal γ -ray emissions within the Milky Way (MW) requires simultaneously accounting for the CR energy losses and non-thermal emissions, as all interactions are governed by the same physics. There are multiple software packages to perform these simulations, such as: GALPROP ([Moskalenko and Strong, 1998](#); [Strong and Moskalenko, 1998](#)), DRAGON ([Evoli et al., 2008](#)), and PICARD ([Kissmann, 2014](#)). This project uses the GALPROP framework for modelling CR transport throughout the MW.

GALPROP builds on the approach described by [Strong and Youssefi \(1993\)](#); [Strong and Youssefi \(1995\)](#); [Strong \(1996\)](#) and began with the goal of constraining CR production and propagation in the MW. GALPROP has an extensive history of successfully reproducing observations: from the local CR spectra (e.g. [Moskalenko et al., 2002](#); [Strong et al., 2004](#)), the Galactic synchrotron emission (e.g. [Strong et al., 2011](#)), and the Galactic diffuse γ -ray emission from MeV to PeV γ -ray energies (e.g. [Strong et al., 2004](#); [Porter et al., 2008](#); [Marinos et al., 2023](#); [Marinos et al., 2025](#)). The modelled interstellar non-thermal emission from GALPROP has been used extensively as a background model by the *Fermi*-LAT collaboration (e.g. [Abdo et al., 2010](#); [Acero et al., 2016a](#); [Acero et al., 2016b](#); [Ajello et al., 2016](#)), and systematic studies using CR propagation models such as GALPROP have been employed for extracting source properties for various supernova remnants (SNRs; [Acero et al., 2016b](#)). In the near future, GALPROP will aid CTA in determining source properties for faint sources such as PWNe. In this work GALPROP version 57 is utilised – for a full description of features before version 57 see [Strong et al. \(2013\)](#), and for the additions to version 57 see [Porter et al. \(2022\)](#).

GALPROP numerically solves the transport equation to calculate the propagation of charged CR particles moving between 3D pixels (also named voxels, and are referred to as the propagation cells in this thesis). GALPROP then uses these CR densities to calculate the all-sky γ -ray emission. GALPROP takes advantage of a wide variety of multi-messenger astronomical datasets, from CR flux measurements to radio observations, from both ground and space-based experiments. Data sources used by GALPROP include Ulysses, both of the *Voyager* probes, Bell Labs, *Fermi*-LAT, PAMELA, AMS, and many others.

This chapter begins with an overview of CR propagation and γ -ray production, with a focus on the distances and time scales involved in modelling diffusion throughout the MW. The GALPROP input distributions will also be discussed, including: the CR source distribution, the ISM gas distribution, the interstellar radiation field (ISRF), and the Galactic magnetic field (GMF). The diffusion parameters, such as the CR flux spectral shapes, CR normalisations, etc., will also be discussed. A brief explanation on applying the information in this chapter to set up a physically informative GALPROP simulation is given in [Appendix A](#).

2.1 Cosmic-Ray Transport

CRs are relativistic particles such as electrons (e^-), positrons (e^+), anti-protons (\bar{p}), protons/hydrogen nuclei (p), and heavier nuclei¹. CRs can have energies as low as a 1 MeV (10^6 eV) or as high as 100 EeV (10^{20} eV). This thesis focuses on CRs in the 0.1– 10^3 TeV (10^{11} – 10^{15} eV) energy regime. These CRs have rest masses significantly smaller than their kinetic energies; hence, this energy regime is known as ultra-relativistic. The kinetic energy of a relativistic particle is given by:

$$E_k = (\gamma_{\text{CR}} - 1)m_{\text{CR}}c^2 \quad (2.1)$$

$$\gamma_{\text{CR}} = \frac{1}{\sqrt{1 - \beta_{\text{CR}}^2}} \quad (2.2)$$

$$\beta_{\text{CR}} = v_{\text{CR}}/c \quad (2.3)$$

where the subscript ‘CR’ denotes that the variable can be applied to any CR particle, γ_{CR} is the Lorentz factor, m_{CR} is the rest mass, c is the speed of light in a vacuum, and v_{CR} is the total velocity of the CR. The CR species can be any charged particle – from a hydrogen nucleus/proton to an iron nucleus, to an electron or positron. For the ultra-relativistic regime, where the kinetic energy is much larger than the rest mass of the CR (i.e. $\gamma_{\text{CR}} \gg 1$), the above equations simplify to:

$$E_k \approx \gamma_{\text{CR}}m_{\text{CR}}c^2 \quad (2.4)$$

$$\therefore \gamma_{\text{CR}} \approx \frac{E_k}{m_{\text{CR}}c^2} \quad (2.5)$$

where all variables have been defined previously. For a 1 TeV proton, which has a rest-mass energy of 0.938×10^9 eV, the ultra-relativistic approximation is accurate to 0.1%.

As CRs have an electric charge they are deflected by the magnetic fields that permeate interstellar space. The CRs will travel in a curved path along the magnetic field lines, where the radius of the curved path is known as the gyro-radius. The gyro-radius of a charged particle in a magnetic field is given by:

$$r_g = \frac{m_{\text{CR}}v_{\perp}}{|q_{\text{CR}}|B} \quad (2.6)$$

where B is the strength of the magnetic field, v_{\perp} is the velocity of the CR perpendicular to the magnetic field, and q_{CR} is the charge of the CR species. As the rest mass of an ultra-relativistic particle makes a negligible contribution to the total energy, the gyro-radius can be simplified as:

¹Although neutrinos (ν) can also be classified as CRs, this thesis focuses on charged particles.

$$E^2 = (pc)^2 + (m_{\text{CR}}c^2)^2 \quad (2.7)$$

$$\therefore E_k^2 \approx (pc)^2 \quad (2.8)$$

$$\Rightarrow r_g = \frac{E_k}{c|q_{\text{CR}}|B} \quad (2.9)$$

where p is the momentum of the CR perpendicular to the direction of the magnetic field. As the gyro-radius of a CR is proportional to the kinetic energy, lower energy CRs will be deflected more than higher energy CRs. Additionally, as the gyro-radius is inversely proportional to the magnetic field strength, CRs travelling through a stronger magnetic field will be deflected more than CRs travelling through a weaker magnetic field. For the Milky Way (MW), the magnetic field strength varies between 3–10 μG (Robitaille et al., 2012). Therefore, CRs with energies below approximately 10^{15} eV (10^3 TeV) will have gyro-radii of approximately 110–360 pc. As the Galactic disk of the MW has a thickness of approximately 200–300 pc, CRs with energies lower than 1 PeV are unlikely to escape the MW, resulting in a diffuse ‘sea’ of very-high-energy (VHE) CRs dispersed throughout the Galaxy.

As the process through which the CRs propagate throughout the Galaxy depends on the magnetic field, it is useful to define a particle rigidity, ϱ_{CR} . The magnetic rigidity is the resistance of a charged particle against deflection in a magnetic field/Lorentz force. The rigidity of a CR (ϱ_{CR}) is typically measured in Volts and is given by:

$$\begin{aligned} \varrho_{\text{CR}} &= Br_g \\ &= \frac{E_k}{c|q_{\text{CR}}|} \end{aligned} \quad (2.10)$$

where all variables have been defined previously. Equations 2.9 and 2.10 show that higher energy CRs (or CRs with lower electric charges) are more resilient against deflection by a magnetic field. Within the MW there are two components to the magnetic field; the regular field created by the global structure of the MW (e.g. the spiral arms), and the irregular field caused by local (i.e. <100 pc) variations caused by the ionised gas, stars, or other processes and objects. The regular field leads to a slow-moving bulk flow of CRs, while the irregular component introduces stochastic diffusion² as the CRs interact with (and are deflected by) random magnetohydrodynamic waves. Given the strength of the Galactic magnetic field (GMF; $\sim 3 \mu\text{G}$; Robitaille et al., 2012) and the $\sim\text{kpc}$ distances travelled by VHE CRs, the trajectories of the VHE CRs within the MW are dominated by diffusive processes.

As CRs diffuse they undergo a variety of interactions with the ISM – from proton–proton collisions (p – p collisions) with the ISM gas, bremsstrahlung interactions with the ISM gas nuclei, inverse Compton (IC) scattering on the ISRF, and synchrotron interactions with magnetic fields. These processes transfer the CR’s energy to γ rays or other lower-energy photons and particles, and will be discussed in more depth in Section 2.2.1 and Section 2.2.2. The time it takes for a CR to lose all of its kinetic energy via a particular process is known as the cooling time, and is given by:

²For a recent review of CR diffusion, see Becker Tjus and Merten (2020).

$$t_{\text{cool}}(E_k) = \int_0^{E_k} \frac{dE}{\dot{E}_k} \quad (2.11)$$

where \dot{E}_k is the rate that the CR loses kinetic energy. If \dot{E}_k , then the cooling time can be simplified to $t_{\text{cool}} = E_k / \dot{E}_k$.

CRs in the TeV regime travel in approximately straight lines between scattering events. During the scattering, the kinetic energy of the CR is transferred into photons. After the scattering event the CR will begin travelling in a different, random direction. This process is repeated until all kinetic energy is lost, and is referred to as a random-walk process. The diffusion distance is found by averaging over many scattering events. For a given diffusion time, $t(E_k)$, and by relating the random-walk theory to CR diffusion in three dimensions ([Chandrasekhar, 1943](#)), the root-mean-square distance that a CR will diffuse is described by the well-known equation:

$$d(E_k) = \sqrt{6D(E_k)t(E_k)} \quad (2.12)$$

where $D(E_k)$ represents the diffusion coefficient. It is worth noting that the average distance a CR will diffuse before losing all of its kinetic energy (i.e. the cooling distance) can be found by substituting the cooling time from [Equation 2.11](#) into [Equation 2.12](#).

Throughout the literature it is common to see the diffusion coefficient defined as a power law in energy, and sometimes as a function of both energy and magnetic field strength. The diffusion coefficient³ is given as a function of CR rigidity ([Seo and Ptuskin, 1994](#)) with the form:

$$D_{xx}(\varrho_{\text{CR}}) = \beta_{\text{CR}} D_{xx,0} \left(\frac{\varrho_{\text{CR}}}{\varrho_0} \right)^\delta \quad (2.13)$$

where δ is the spectral index of the diffusion coefficient (often called the diffusion index), and $\varrho_0 = 4 \text{ GV}$ is the rigidity at which the diffusion coefficient is normalised. The normalisation diffusion coefficient, $D_{xx,0}$ varies with the chosen CR source model (see [Section 2.7.1](#)). The diffusion index is typically given by $\delta = 1/3$ for a Kolmogorov spectrum of the ISM turbulence ([Kolmogorov, 1941](#)) and $\delta = 1/2$ for Iroshnikov-Kraichnan turbulence ([Iroshnikov, 1964](#); [Kraichnan, 1965](#)). In [Section 2.7.1](#) the diffusion index is treated as a parameter that is fit to observational CR data.

For a more complete picture of CR diffusion, the partial differential equation known as the transport equation must be used. GALPROP uses the differential transport equation in three spatial dimensions over time to propagate CRs through different volume elements, hereafter referred to as the ‘propagation cells’, or simply as cells. The calculation is performed for each nuclear species, where the partial differential transport equation ([Ginzburg and Syrovatskii, 1964](#); [Berezinskiĭ et al., 1990](#)) is given by:

³In general, D_{xx} and D_{pp} are diffusion tensors, allowing the diffusion speed to vary with direction. However, as GALPROP has not yet implemented anisotropic diffusion, they are referred to as diffusion coefficients throughout this work.

$$\begin{aligned}
\frac{\partial \psi}{\partial t} = & Q(\vec{r}, p) \\
& + \vec{\nabla} \cdot (D_{xx} \vec{\nabla} \psi - \vec{v}_{\text{conv}} \psi) \\
& + \frac{\partial}{\partial p} p^2 D_{pp} \frac{\partial}{\partial p} \frac{1}{p^2} \psi \\
& - \frac{\partial}{\partial p} \left(\dot{p} \psi - \frac{p}{3} (\vec{\nabla} \cdot \vec{v}_{\text{conv}}) \psi \right) \\
& - \frac{\psi}{T_f} - \frac{\psi}{T_r}
\end{aligned} \tag{2.14}$$

where $\psi = \psi(\vec{r}, p, t)$ is the CR density per unit of particle momentum at the coordinate \vec{r} and time t , \dot{p} is the change in the CR momentum over time, D_{xx} and D_{pp} are the spatial and momentum-space diffusion coefficients, respectively, and are assumed to be independent of the CR species, \vec{v}_{conv} is the convection velocity of the Galactic wind, and T_f and T_r are the time scales for nuclear fragmentation and radioactive decay, respectively. The source term, $Q(\vec{r}, p)$, captures all CRs being injected into the MW. The CRs being created as secondary particles will be discussed in [Section 2.2.1](#), and the CRs being injected into the MW by CR accelerators will be discussed in [Section 2.3](#).

For the individual terms in the transport equation: $\vec{\nabla} D_{xx} \vec{\nabla} \psi$ accounts for the spatial diffusion of the CRs, $\vec{\nabla} \cdot \vec{v}_{\text{conv}} \psi$ accounts for advection of the CRs due to the motion of the ISM gas, $\frac{\partial}{\partial p} p^2 D_{pp} \frac{\partial}{\partial p} \frac{1}{p^2} \psi$ accounts for the reacceleration of the CRs due to interactions with magnetic fields, $\frac{\partial}{\partial p} \dot{p} \psi$ accounts for radiative losses of the CRs, and $\frac{\partial}{\partial p} \frac{p}{3} (\vec{\nabla} \cdot \vec{v}_{\text{conv}}) \psi$ accounts for adiabatic expansion (and compression) of the ISM gas which decreases (or increases) the CR density within the volume of gas. The transport equation must be solved numerically as the combination of spatially and temporally varying differential terms make it impossible to find a closed analytical expression.

To numerically solve [Equation 2.14](#) GALPROP has a variety of solution methods that can be chosen by the user. The Crank-Nicolson finite differencing technique ([Press et al., 1992](#)) is used in this thesis, which is second-order accurate in time and unconditionally stable independent of the timestep size ([Press et al., 1992](#)). The Crank-Nicolson technique calculates the CR energy density moving from one spatial cell to another, where adjacent cells in all three spatial dimensions influence one another. The time-updating step for the Crank-Nicolson solution method is given by:

$$\psi_{j+1} = \psi_j + \frac{1}{2} \left[\left(\frac{\partial \psi}{\partial t} \right)_j + \left(\frac{\partial \psi}{\partial t} \right)_{j+1} \right] \Delta t \tag{2.15}$$

where j denotes the current timestep and Δt is the size of the timestep. A description of the full finite differencing technique in 3D, including descriptions of the boundary conditions for the various spatial axes, can be found in [Strong et al. \(2013\)](#). For accurate, meaningful results, the minimum timestep must be shorter than the fastest cooling time of any particle included in the simulation ([Equation 2.11](#)). Similarly, the size of the cells must be smaller than the shortest cooling distance of any particle in the simulation (found by substituting [Equation 2.11](#) into [Equation 2.12](#)).

2.2 Cosmic-Ray Energy Losses and Gamma-Ray Production

As CRs travel through the Galaxy they can interact with the ISM gas, the ISRF, and the GMF. These interactions will transfer the kinetic energy of the CRs into photons (including γ rays). The process of CRs converting their kinetic energy into other forms is often referred to as cooling. The rate of cooling depends on the process and the CR species, limiting the length of time and distance that the CRs can diffuse.

This section provides broad explanations of how γ -ray photons are produced through the various processes in the MW. References to the full formalism used by GALPROP will be included; however, the equations provided here will be approximations. The included approximations allow the cooling times and cooling distances (i.e. maximum diffusion distances) for various processes to be calculated to first order. The main assumptions made in this section will be for large-scale (>100 pc), Galaxy-wide diffusion, and for ultra-relativistic ($E_k > 0.01$ TeV) CRs.

2.2.1 Hadronic Processes

CRs can collide with the atoms in the ambient gas in the ISM, with these collisions being energetic enough to produce subatomic particles and γ rays. This interaction applies to CR protons and other heavier CR nuclei. In general, the hadronic emission is due to nuclei–nuclei (N – N) collisions.

The formalism used by GALPROP to calculate the hadronic emission can be found in [Moskalenko and Strong \(1998\)](#), which uses equations from [Dermer \(1986a\)](#) and [Dermer \(1986b\)](#). GALPROP calculates the full N – N collision interaction cross section for any CR nuclei from ^1H to ^{64}Ni onto a variety of gas species ([Strong and Moskalenko, 1998](#); [Strong et al., 2007](#); [Strong et al., 2009](#)). The total inelastic cross sections for p , d (deuteron), ^3He , and ^4He are parameterised for any arbitrary target, with GALPROP using the formalism from [Ferrando et al. \(1988\)](#); [Barashenkov and Polanski \(1994\)](#); [Wellisch and Axen \(1996\)](#). GALPROP also includes the formalism from [Tripathi et al. \(1996\)](#), with corrections given in [Porter et al. \(2022\)](#). As 90% of the ISM gas is hydrogen (see [Section 2.4](#)), and 90% of hadronic CRs are protons ([Mewaldt, 1994](#)), only proton–proton collisions (p – p collisions) will be discussed in depth here.

Proton–Proton Collisions

Neutral, positive, and negative pions (π) can be produced when a CR proton collides with another proton. To create a pion, the CR proton must have a total energy (rest mass plus kinetic energy) greater than approximately 1.22 GeV ([Kelner et al., 2006](#)). The pions decay quickly – charged pions have lifetimes of 2.6×10^{-8} s and neutral pions have lifetimes of 8.5×10^{-17} s ([Zyla et al., 2020](#)). Depending on the charge of pion, the decay produces γ rays, muons (μ), or neutrinos (ν). Diagrams of p – p collisions and the various pion pathways, along with the interaction equations, are shown in [Figure 2.1](#).

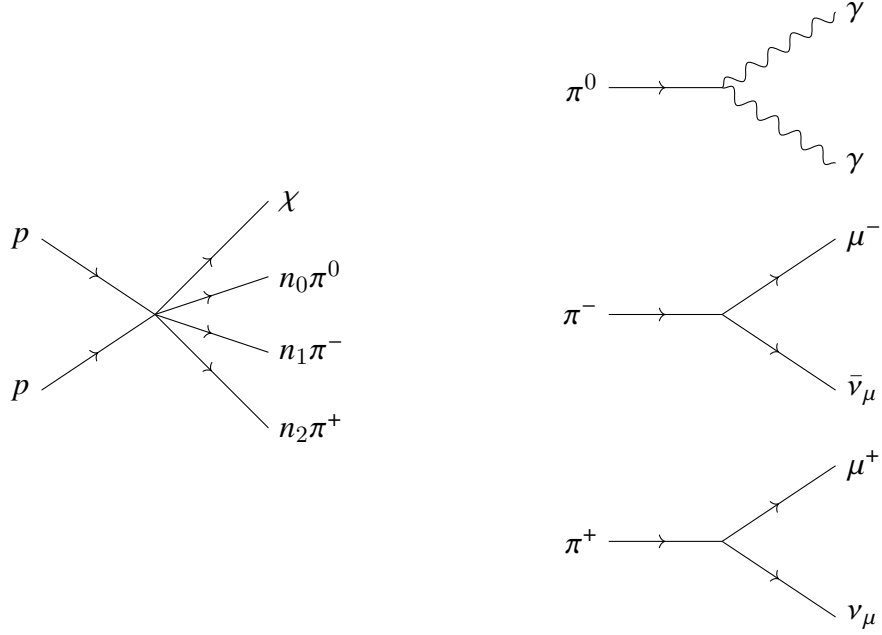


Figure 2.1: A p - p collision creating neutral pions (π^0) and charged pions (π^\pm) is shown on the left, with χ representing any additional particles created within the interaction to conserve baryon number and electric charge. The interaction has the equation $p + p \rightarrow \chi + n_0\pi^0 + n_1\pi^- + n_2\pi^+$, where the number of neutral, negative, and positive pions produced in the collision are given by n_0 , n_1 , and n_2 , respectively. The three pion decay pathways are shown on the right. The top pathway shows a neutral pion decaying into two γ rays (γ) via the equation $\pi^0 \rightarrow 2\gamma$. The central pathway shows a negatively charged pion decaying into a negatively charged muon (μ^-) and a muon antineutrino ($\bar{\nu}_\mu$) via the equation $\pi^- \rightarrow \mu^- + \bar{\nu}_\mu$. The bottom pathway shows a positively charged pion decaying into a positively charged muon (μ^+) and a muon neutrino (ν_μ) via the equation $\pi^+ \rightarrow \mu^+ + \nu_\mu$. Although it is not shown, the charged muons will decay further into electrons, positrons, muon antineutrinos, and electron antineutrinos ($\bar{\nu}_e$) via the equations $\mu^- \rightarrow e^- + \nu_\mu + \bar{\nu}_e$ and $\mu^+ \rightarrow e^+ + \bar{\nu}_\mu + \nu_e$.

The energy loss rate of CR protons due to collisions with the ISM hydrogen gas (Aharonian and Atoyan, 1996) is given by:

$$\left[\frac{dE_p}{dt} \right]_{pp} = \sigma_{pp} n_H f c E_p \quad (2.16)$$

where c is the speed of light in a vacuum, n_H is the number density of the ambient hydrogen gas (see Section 2.4), E_p is the kinetic energy of the CR proton. The elasticity of the collision is given by f and is a function of both the target gas species and the kinetic energy of the CR (Gaisser, 1990). For CR protons in the ultra-relativistic regime colliding with the ambient hydrogen gas, the elasticity is often approximated by $f = 0.5$. σ_{pp} is the cross section for a p - p collision and is calculated explicitly by GALPROP by using a function fit to cross-section data from (Dermer, 1986a). For a first-order approximation, the p - p collision cross section from 10 GeV to 1 PeV can be given by $\sigma_{pp} \approx 40 \times 10^{-31} \text{ m}^2$ following Aharonian and Atoyan (1996). The approximate cooling time for CR protons in the ISM is then given by:

$$t_{pp} = 5.3 \times 10^7 \left(\frac{n_H}{\text{cm}^{-3}} \right)^{-1} \text{ yr} \quad (2.17)$$

where all variables have been defined previously. With the above assumptions, the cooling time for the CR protons undergoing p - p collision interactions is proportional only to the density of the medium that the CR proton is travelling through.

Secondary Particle Creation

As shown in [Figure 2.1](#), p - p collisions may create secondary particles. In a similar fashion, N - N collisions are likely to create many secondary particles including other atoms with atomic numbers lower than the initial CR or ISM gas particle. GALPROP considers the following reactions for the calculation of secondaries: p - p , p - N , N - p , and N - N . The cross sections for these interactions can be found in [Tan and Ng \(1983\)](#). Calculations for \bar{p} production and propagation are given by [Moskalenko et al. \(2002\)](#); [Moskalenko et al. \(2003\)](#); [Kachelrieß et al. \(2015\)](#); [Kachelrieß et al. \(2019\)](#), and the production of the neutral mesons, secondary electrons, and positrons is calculated using the formalism from [Dermer \(1986a\)](#); [Dermer \(1986a\)](#). GALPROP can also use the more recent formalism from [Kamae et al. \(2006\)](#); [Kachelrieß and Ostapchenko \(2012\)](#); [Kachelrieß et al. \(2014\)](#); [Kachelrieß et al. \(2019\)](#).

The secondary particles can be considered as an additional source of CRs. The source term ($Q(\vec{r}, p)$) from [Equation 2.14](#) has a component due to secondary particle creation given by:

$$Q(\vec{r}, p) = \beta_{\text{CR}} c n_H(\vec{r}) \int \left(\psi_{\text{CR}}(\vec{r}, p) \frac{d\sigma(p, p')}{dp'} \right) dp \quad (2.18)$$

where ψ is the CR density (from [Equation 2.14](#)), \vec{r} is the Galactic position of the secondary production, and β_{CR} is given by [Equation 2.2](#). p' is the momentum of the secondary particle and $d\sigma(p, p')/dp'$ is the differential cross section of the secondary particle interaction, which is different for each process that can create secondaries. The full description of how the secondary source term is implemented in GALPROP can be found in [Moskalenko and Strong \(1998\)](#). The secondary source function implemented in v57 of GALPROP is defined for primary particles up to and including ^{64}Ni and includes secondary particle creation from nuclear fragmentation and radioactive decay of all isotopes ([Porter et al., 2022](#)).

2.2.2 Leptonic Processes

When a charged particle is decelerated it radiates its energy in the form of a photon. This emission mechanism disproportionately impacts low-mass particles, such as electrons, as they are decelerated more easily than higher-mass particles such as protons. In extreme environments such as active galactic nuclei (AGN), protons and heavier nuclei can be decelerated significantly and emit γ rays via the processes detailed in this section. However,

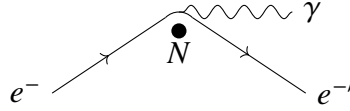


Figure 2.2: A Bremsstrahlung interaction, where an electron (e^-) is deflected by the strong electric fields around an atomic nucleus (shown by the black circle), giving the final states e^-' and γ . The equation for a Bremsstrahlung interaction is given by:

$$e^- + N \rightarrow e^-' + \gamma + N.$$

γ rays are unlikely to be emitted by hadronic CRs via these processes for the cases discussed in this thesis. Hence this section will only discuss the CR electrons⁴.

There are three main processes that cause CRs to be decelerated: bremsstrahlung, synchrotron radiation, and IC scattering. Bremsstrahlung and IC interactions in the $E > 1$ TeV energy regime are catastrophic processes, converting all kinetic energy of the electron into a single γ -ray photon. Synchrotron interactions do not often create γ rays and are more likely to produce radiation from radio to X-ray photons. However, a discussion of the synchrotron energy losses is included below as they are an important energy-loss mechanism for the CR electrons.

Bremsstrahlung

Bremsstrahlung radiation is emitted when a charged particle with some velocity is rapidly slowed down by the charged nucleus of another atom. As the charged particle is decelerated, the kinetic energy is transferred into a photon. Hence, CRs diffusing through the ISM gas can undergo bremsstrahlung interactions with the nuclei of the ambient ISM gas particles. In the relativistic regime a large fraction of the kinetic energy of the CR is converted into a high-energy γ ray. For an ultra-relativistic CR almost all of the kinetic energy is converted into a γ ray. A diagram of a bremsstrahlung interaction, along with the interaction equation, is shown in [Figure 2.2](#).

GALPROP calculates the full bremsstrahlung energy loss rate and bremsstrahlung interaction cross sections for a range of ambient ISM gas species for any CR energy. GALPROP calculates bremsstrahlung radiation from both leptonic and hadronic CR interactions with the ISM gas. The full formalism used by GALPROP for the bremsstrahlung calculations can be found in [Strong et al. \(2000\)](#).

For CR electrons, which produce the majority of bremsstrahlung radiation, the energy loss rate due to bremsstrahlung interactions is given by:

$$\left[\frac{dE_e}{dt} \right]_{\text{brem}} = c\beta_e \sum_s \left[n_s(\vec{r}) \int \left(E_\gamma \frac{d\sigma_{\text{brem}}(E_e, E_\gamma, s)}{dE_\gamma} \right) dE_\gamma \right] \quad (2.19)$$

where E_e is the kinetic energy of the electron, E_γ is the energy of the resulting γ ray, and $n_s(\vec{r})$ is the density of the ISM gas at the location \vec{r} , where the subscript s denotes the

⁴The leptonic emission processes also impact the CR positrons, and all equations are identical. Only the CR electrons are discussed here for simplicity.

atomic species of the gas (e.g. n_{H} is the density of the hydrogen gas, see [Section 2.4](#)). $d\sigma_{\text{brem}}(E_e, E_\gamma, s)/dE_\gamma$ is the differential cross section of a bremsstrahlung interaction on said ISM gas species, and is given by:

$$\frac{d\sigma_{\text{brem}}(E_e, E_\gamma, s)}{dE_\gamma} = \frac{\alpha r_e^2}{E_\gamma} \left(\left[1 + \left(\frac{\gamma_f}{\gamma_e} \right)^2 \right] \Phi_{s,1}(E_e, E_\gamma, s) - \frac{2\gamma_f}{3\gamma_e} \Phi_{s,2}(E_e, E_\gamma, s) \right) \quad (2.20)$$

$$\gamma_f = \frac{E_e - E_\gamma}{m_e c^2} \quad (2.21)$$

where α is the fine structure constant, γ_e is the Lorentz factor for the electron, γ_f is the final Lorentz factor for the electron (i.e. the Lorentz factor of the electron after the interaction) and $r_e \approx 2.817 \times 10^{-15}$ m is the classical radius of the electron. The functions $\Phi_{s,1}$ and $\Phi_{s,2}$ are calculated individually for every species of gas in the ISM via the Schiff formula ([Koch and Motz, 1959](#)) and represent the electron scattering.

The bremsstrahlung in the ISM can be approximated using similar assumptions as for the p - p collisions (see [Section 2.2.1](#)). The ISM gas consists of 90% hydrogen ([Ferrière, 2001](#), see [Section 2.4](#)). The most simplistic case is that for ionised hydrogen (H II) as it is an unshielded charge (i.e. it has no bound electron). Hence, the charge distribution of H II is due simply to the single proton in the nucleus. Using the Schiff formula for ionised hydrogen, it can be found that $\Phi_{\text{H II},1} = \Phi_{\text{H II},2} = \Phi_{\text{H II}}$, which is given by:

$$\Phi_{\text{H II}} = 4 \left[\ln \left(\frac{2E_e}{m_e c^2} \frac{E_e - E_\gamma}{E_\gamma} \right) - \frac{1}{2} \right] \quad (2.22)$$

where all variables have been defined previously. Following [Aharonian \(2004\)](#), further assumptions can be made. For CR electrons with energies $E_e > 2$ MeV the CR electron is unlikely to be captured by the nucleus. For this energy range the electron losses are a significant fraction of the total kinetic energy of the electron. Additionally, as the average ISM gas density is low (varying between 10^1 and 10^3 atoms cm^{-3}) a bremsstrahlung interaction is unlikely to produce a cascade of many collisions through the ISM gas. Hence, bremsstrahlung interactions can be viewed as individual collisions. These three assumptions allow the rate of energy lost via bremsstrahlung interactions at large scales (i.e. > 100 pc) to be simplified down to the form:

$$\left[\frac{dE_e}{dt} \right]_{\text{brem}} = \frac{9n_{\text{H}}\sigma_{\text{brem}}c}{7} E_e \quad (2.23)$$

where $\sigma_{\text{brem}} \approx 1.88 \times 10^{-30}$ m^2 is the integrated cross section for the bremsstrahlung interaction on H II for ultra-relativistic CR electrons. With these assumptions and simplifications, the final form for the cooling time [Aharonian \(2004\)](#) is given by:

$$t_{\text{brem}} = 4.0 \times 10^7 \left(\frac{n_{\text{H}}}{\text{cm}^{-3}} \right)^{-1} \text{ yr} \quad (2.24)$$

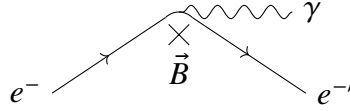


Figure 2.3: A synchrotron event, where an electron (e^-) is deflected by a magnetic field (\vec{B} , directed into the page) giving the final states e^-' and a lower-energy photon γ .

The equation for synchrotron interactions is given by: $e^- + \vec{B} \rightarrow e^-' + \gamma$.

where all variables have been defined previously. The cooling time for bremsstrahlung interactions at scales >100 pc depends only on the density of the medium through which the CR electron travels. Similarly to p - p collisions, gas clouds are expected to emit bremsstrahlung γ rays, and the kinetic energy of the CR electrons is transferred into γ rays faster as the ISM gas density increases.

Synchrotron Radiation

CR electrons travelling through a magnetic field are decelerated, emitting synchrotron photons in the process. Synchrotron radiation is typically made up of non-thermal, low-energy photons such as radio waves; however, it can also account for X-rays in extreme environments (e.g. around pulsars). Although the synchrotron photon flux is not calculated in this thesis, the synchrotron energy losses can become significant for Galactic regions with intense magnetic fields. The synchrotron losses impact the CR electron density throughout the MW. The GMF models considered in this work will be discussed later in [Section 2.6](#). A diagram of a synchrotron interaction, along with the interaction equation, is shown in [Figure 2.3](#).

The amount of energy an electron loses via synchrotron depends on the angle between the electron and the magnetic field lines ([Rybicki and Lightman, 1985](#)). For the regular component of the GMF GALPROP uses the formalism for the synchrotron energy losses (and the synchrotron photon flux) from [Rybicki and Lightman \(1985\)](#). For the irregular/random component, GALPROP uses the formalism from [Ghisellini et al. \(1988\)](#); [Waelkens et al. \(2009\)](#). For calculating the cooling times to first order, the interaction can be averaged over all possible angles. This assumption is fair if the velocities of the electrons are randomly oriented, which is valid if the electrons are truly diffuse. Hence, the energy loss rate ([Rybicki and Lightman, 1985](#)) can be approximated by:

$$\left[\frac{dE_e}{dt} \right]_{\text{syn}} = \frac{32\pi r_e^2}{9} c \beta_e^2 \gamma_e^2 U_B \quad (2.25)$$

$$U_B = \frac{|\vec{B}|^2}{8\pi} \quad (2.26)$$

where β_e is perpendicular to the magnetic field, $r_e \approx 2.817 \times 10^{-15}$ m is the classical radius of the electron, $|\vec{B}|^2$ is the magnitude of magnetic field vector, and U_B is the energy density of the magnetic field. For diffusion across large distances (>100 pc) it is important to consider the Galactic magnetic field, which will be discussed in more depth in [Section 2.6](#). Assuming the CRs are in the relativistic regime, and focusing on large distances, the cooling time can be simplified ([Aharonian, 2004](#)) giving:

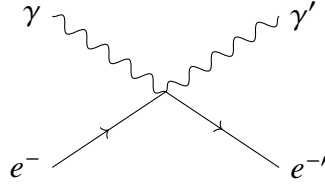


Figure 2.4: An IC scattering event, where a photon (γ) collides with an electron (e^-). The electron will impart some energy to the photon, giving the final states $e^{-'}$ and γ' . The equation for the IC scattering interaction is given by: $e^- + \gamma \rightarrow e^{-'} + \gamma'$.

$$t_{\text{syn}}(E_e) = 12 \times 10^6 \left(\frac{B}{\mu\text{G}} \right)^{-2} \left(\frac{E_e}{\text{TeV}} \right)^{-1} \text{ yr} \quad (2.27)$$

where all variables have been defined previously. The synchrotron cooling time is inversely proportional to the square of the magnetic field strength. The dependence of the γ -ray emission on the GMF, and the results on the impact of altering the GMF, will be discussed later in [Chapter 5](#).

Inverse Compton Scattering

Inverse Compton (IC) scattering is the process in which a CR electron interacts with a photon with lower energy, such as a CMB photon, infrared (IR), optical, ultra-violet, or X-ray photon. For some γ -ray sources, such as blazars, IC scattering can also occur on the radio photons emitted via synchrotron (synchrotron self-Compton; e.g. [Jones et al., 1974](#); [Bloom and Marscher, 1996](#)). The electron transfers some fraction of its kinetic energy to the photon, upscattering the photon to higher energies. In the relativistic regime the electron transfers a significant fraction of its kinetic energy to the photon, with the process being catastrophic in the ultra-relativistic regime. If the electron-photon system has enough total energy, then the photons can potentially be upscattered into the γ -ray regime, with this process significantly contributing to the γ -ray flux observed at Earth ([Aharonian et al., 1997](#)). A diagram of an IC scattering interaction, along with the interaction equation, is shown in [Figure 2.4](#).

The amount of energy transferred, and even the likelihood of the interaction, depends on the initial energies of both the electron and low-energy photon, as well as the relative angles between the electron and the photon. GALPROP calculates the anisotropic IC scattering, which considers the effects of the electron and photon angles relative to one another, with the full formalism for the anisotropic IC scattering cross sections found in [Moskalenko and Strong \(2000\)](#), with details on the full directionality of the ISRF is given in [Moskalenko et al. \(2006\)](#). The two most recent models for the background photon field used by GALPROP are given by [Porter et al. \(2017\)](#) and are detailed in [Section 2.5](#). For calculating the cooling time, the amount of energy transferred can be approximated to first order by averaging over all possible electron and background photon relative angles. Hence, the energy lost to IC scattering events ([Aharonian, 2004](#)) is given by:

$$\left[\frac{dE_e}{dt} \right]_{\text{IC}} = \frac{4\sigma}{3} c \gamma_e^2 U_{\text{rad}} \quad (2.28)$$

where U_{rad} is the energy density of the radiation field, which includes contributions from the cosmic microwave background (CMB; 0.26 eV cm^{-3} ; [Aharonian, 2004](#); [Fixsen, 2009](#)) and the interstellar radiation field (discussed later in [Section 2.5](#)). The IC scattering interaction cross section between the electron and photon is given by σ . The energy ranges of the electron-photon system where the recoil force on the electron is negligible is named the Thomson regime. For the Thomson regime the interaction cross section is constant, where the Thomson cross section ([Thomson and Thomson, 1933](#)) is given by:

$$\begin{aligned} \sigma_T &= \frac{8\pi}{3} r_e^2 \\ &\approx 6.652 \times 10^{-29} \text{ m}^2 \end{aligned} \quad (2.29)$$

where $r_e \approx 2.817 \times 10^{-15} \text{ m}$ is the classical radius of the electron. As the recoil force on the electron becomes significant, the IC scattering interaction enters the Klein-Nishina (KN) regime. The interaction cross section in the KN regime is smaller than in the non-relativistic limit, with the IC scattering interaction becoming less likely. Furthermore, in the KN regime the fraction of kinetic energy transfer approaches unity (i.e. the electron transfers all of its kinetic energy to the photon; [Blementhal and Gould, 1970](#)). The recoil force is significant when $\Gamma \gg 1$, where Γ is a unitless quantity given by:

$$\Gamma = \frac{4E_e E_b}{(m_e c^2)^2} \quad (2.30)$$

where E_b is the energy of the ‘background’ (low energy) photon. Rearranging for the electron energy and substituting various photon energies, the KN regime begins at $E_e \approx 100 \text{ TeV}$ for CMB photons and $E_e \approx 5 \text{ TeV}$ for IR photons, with both the CMB and IR fields accounted for in GALPROP (as described in [Section 2.5](#)). The KN cross section depends on the relative angle between the CR electron and background photon. When discussing diffuse electrons, the average over all angles can be taken. It is common throughout the literature to write the KN cross section in terms of the scattered photon energy (E_γ), or as a ratio of the scattered photon energy to the initial kinetic energy of the electron. Using the former convention, and recalling that the electron gives almost all its kinetic energy to the photon in the KN regime, the differential KN cross section is given by:

$$\frac{d\sigma_{\text{KN}}(E_e, E_b, E_\gamma)}{dE_\gamma} = 2\pi r_e^2 \frac{(m_e c^2)^2}{E_e^2 E_b} G(\Gamma, \xi) \quad (2.31)$$

$$G(\Gamma, \xi) = 2\xi \ln(\xi) + (1 + 2\xi)(1 - \xi) + \frac{(\xi\Gamma)^2(1 - \xi)}{2(1 + \xi\Gamma)} \quad (2.32)$$

$$\xi = \frac{E_\gamma}{\Gamma E_e (1 - E_\gamma/E_e)} \quad (2.33)$$

$$E_\gamma \approx (\gamma_e - 1)m_e c^2 + E_b \quad (2.34)$$

where E_γ is the energy of the resulting γ ray, $G(\Gamma, \xi)$ and ξ are unitless functions, and $E_b \ll m_e c^2 \ll E_e$. The assumption that $E_b \ll m_e c^2$ is true for both the CMB and IR photon fields. For electron energies $E_e \approx 10$ TeV and for incident IR photons, it is found that $E_e E_b \approx (m_e c^2)^2$. Taking this assumption, and further assuming that $E_e \approx E_\gamma$, the integral KN cross section simplifies to $\sigma_{\text{KN}} = 2\pi r_e^2 G(\Gamma, \xi)$. The latter form is common throughout the literature as IR photons account for the majority of the IC scattering. However, it should be noted that this approximation lies on the edge of the KN regime, and the condition $\Gamma \gg 1$ is only marginally satisfied.

In the KN regime the IC cross section decreases and the synchrotron losses begin to dominate over the IC losses. For $\Gamma < 10^4$, which is valid for $E_e \leq 100$ TeV and $E_b \leq 10^{-1}$ eV, the ratio of the energy radiated into synchrotron versus IC is given by:

$$\frac{[dE_e/dt]_{\text{IC}}}{[dE_e/dt]_{\text{syn}}} = \frac{U_{\text{rad}}}{U_B} \frac{1}{(1 + \Gamma)^{1.5}} \quad (2.35)$$

where all variables have been defined previously. For the Galactic ISRF (CMB, IR, optical, and ultra-violet photons), and a weaker Galactic magnetic field strength (inter-spiral-arm regions; $3 \mu\text{G}$; see [Section 2.6](#)) where the IC only just dominates over the synchrotron, the ratio of IC to synchrotron remains approximately constant for electron energies $E_e < 100$ TeV despite the KN cross section decreasing ([Moderski et al., 2005](#)). For stronger Galactic magnetic fields (intra-spiral-arm regions; $10 \mu\text{G}$; see [Section 2.6](#)), the synchrotron losses can dominate across all electron energies. Assuming electron energies $E_e < 100$ TeV the cooling time for the IC losses ([Aharonian, 2004](#); [Moderski et al., 2005](#)) is given by:

$$t_{\text{IC}}(E_e) = 3.1 \times 10^8 \left(\frac{U_{\text{rad}}}{\text{eV cm}^{-3}} \right)^{-1} \left(\frac{E_e}{\text{GeV}} \right)^{-1} \text{ yr} \quad (2.36)$$

where all variables have been defined previously. Although this equation is accurate for electron kinetic energies $E_e < 100$ TeV, it over-estimates the electron IC scattering losses on the IR component of the ISRF for $E_e > 100$ TeV. For the CMB component, the equation is valid up to $E_e > 1$ PeV. Above these energies the electrons become more likely to lose energy via synchrotron interactions, and [Equation 2.36](#) becomes an overestimate of the IC scattering cooling time.

The IC scattering cooling time is inversely proportional to U_{rad} , which is isotropic for the CMB photon field and follows the distribution of stars in the MW for IR, optical, and UV photons. The dependence of IC scattering on the ISRF, as well as the impacts on the γ -ray emission caused by altering the ISRF, will be discussed later in [Chapter 5](#).

2.2.3 Gamma-Ray Flux

The γ -ray emissivity represents the magnitude of γ -ray radiation emitted by some volume. The emissivity is a function of the γ -ray energy and is described in GALPROP as a function of position. The γ -ray emissivity is given by:

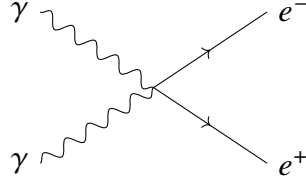


Figure 2.5: A pair production event, where two photons (γ) collide, creating an electron-positron pair (e^- and e^+ , respectively). The equation for the pair production interaction is given by: $\gamma + \gamma \rightarrow e^- + e^+$.

$$\varepsilon(\vec{r}, E_\gamma) = \frac{1}{V} \int \left(\frac{d\sigma(E_k, E_\gamma)}{dE_\gamma} \psi(\vec{r}, E_k) \right) dE_k \quad (2.37)$$

where V is the volume of the propagation cell and $d\sigma(E_k, E_\gamma)/dE_\gamma$ is the differential cross section of an interaction with a CR with kinetic energy E_k creating a γ ray with energy E_γ . As the synchrotron emission is not calculated in this thesis, the equations for the synchrotron emissivity (Strong et al., 2013, Equations 51–57) are not included here. The γ -ray flux (J , provided by GALPROP in units of $\text{MeV}^{-1} \text{cm}^{-2} \text{s}^{-1} \text{sr}^{-1}$) is the integral over the line of sight (x) of the emissivity. The IC, bremsstrahlung, and pion-decay γ -ray fluxes, respectively, are given by:

$$J_{\text{IC}}(\ell, \ell, E_\gamma) = \frac{1}{4\pi} \int \varepsilon_{\text{ic}}(\vec{r}, E_\gamma) dx \quad (2.38)$$

$$J_{\text{brem}}(\ell, \ell, E_\gamma) = \frac{1}{4\pi} \sum_s n_s(\vec{r}) \int \varepsilon_{\text{brem}}(\vec{r}, E_\gamma) dx \quad (2.39)$$

$$J_{\pi^0}(\ell, \ell, E_\gamma) = \frac{1}{4\pi} \sum_s n_s(\vec{r}) \int \varepsilon_{\pi^0}(\vec{r}, E_\gamma) dx \quad (2.40)$$

where (ℓ, ℓ) are the Galactic sky coordinates and $n_s(\vec{r})$ is the density of the ISM gas at the location \vec{r} . For bremsstrahlung emission and pion-decay emission the γ -ray emissivity is defined per gas species (s). Therefore, a sum must be performed over the ISM gas species when calculating the pion-decay and bremsstrahlung γ -ray flux integrals.

Pair Absorption

As γ rays travel through the ISM they may collide with a background photon from the CMB or ISRF (see Section 2.5). This interaction creates an electron-positron pair, as shown in Figure 2.5, with each particle obtaining half of the energy of the initial γ ray in the centre-of-momentum reference frame. The electron-positron pair may instantly annihilate with one another or diffuse away and become lower-energy secondary CRs. As pair absorption reduces the γ -ray flux that reaches Earth it is common to define the effect of pair absorption as an optical depth ($\tau_{\gamma\gamma}$) along the line of sight. The optical depth calculation used in GALPROP accounts for the full directionality of the ISRF (Moskalenko et al., 2006; Porter et al., 2018) and is given by:

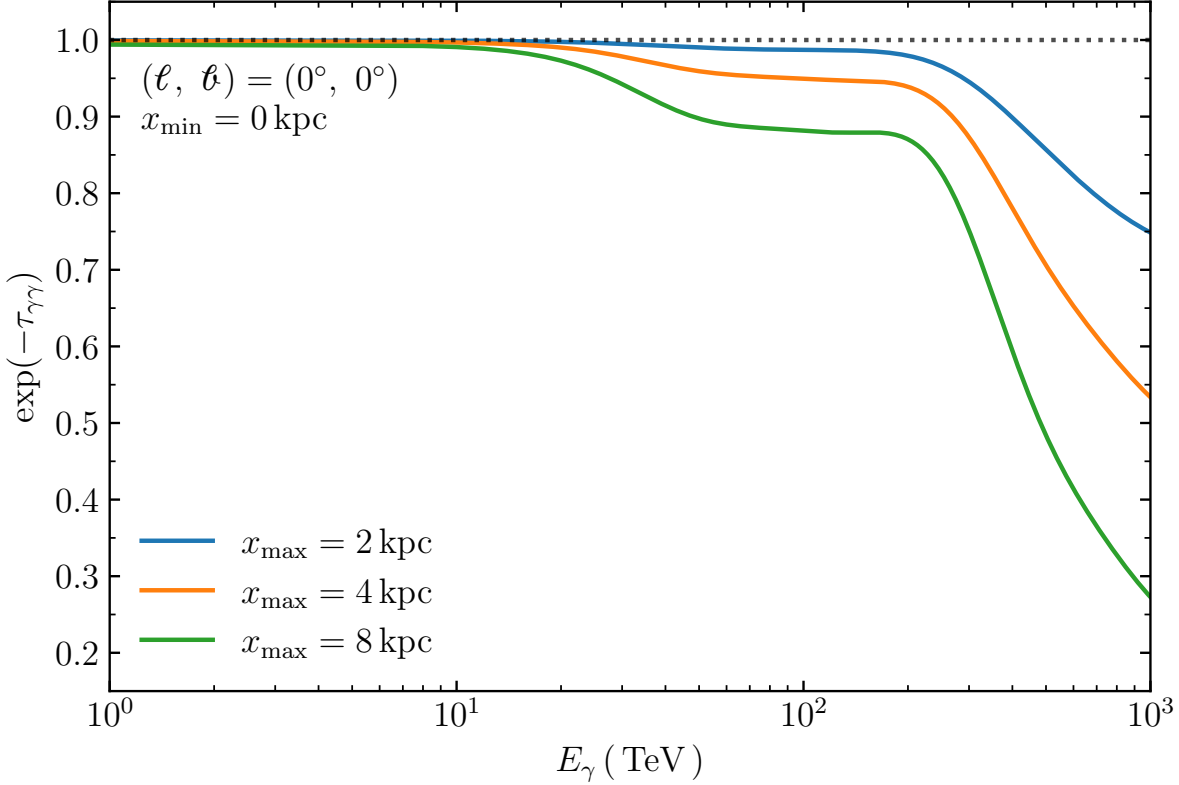


Figure 2.6: The transmittance along the line-of-sight due to pair-production as a function of the γ -ray energy. The line-of-sight integral is in the direction of the Galactic centre (GC) and goes from 0 kpc to 2 kpc (blue), 4 kpc (orange), and 8 kpc (green). The absorption was calculated for the R12 ISRF model (see [Section 2.5.2](#)).

$$\tau_{\gamma\gamma}(\ell, \ell, E_\gamma) = \iiint \left(\frac{d\mathcal{F}(\vec{r}, E_b, \Omega)}{dE_b d\Omega} \sigma_{\gamma\gamma}(E_c) (1 - \cos \Theta) \right) dx dE_b d\Omega \quad (2.41)$$

$$E_c = \sqrt{\frac{E_b E_\gamma (1 - \cos \Theta)}{2}} \quad (2.42)$$

where E_c is the centre-of-momentum system energy of the two photons, Θ is the angle between the momenta of the two photons from the observer's perspective, Ω is the solid angle, $d\mathcal{F}(\vec{r}, E_b, \Omega)/dE_b d\Omega$ is the differential background photon flux at the point \vec{r} , and $\sigma_{\gamma\gamma}$ is the KN cross section for the two photons interacting. The pair-absorption cross section in the relativistic regime from [Jauch and Rohrlich \(1976\)](#) is given by:

$$\sigma_{\gamma\gamma}(E_c) = r_e^2 \pi \left(\frac{m_e c^2}{E_c} \right)^2 \left(\ln \left(\frac{2E_c}{m_e c^2} \right) - 1 \right) \quad (2.43)$$

where all variables have been defined previously. Similarly as for IC scattering, there are two regimes for the pair absorption that depends on the KN suppression factor. For $E_e < 100$ TeV the γ rays will interact with the IR component of the ISRF, while for $E_e > 100$ TeV the γ rays will create electron-positron pairs on the CMB radiation.

The pair-production transmittance (i.e. the fraction of γ -ray flux not absorbed by the production of electron-positron pairs) along the line-of-sight is shown in [Figure 2.6](#). The observed absorption in the 10–200 TeV energy range is due to γ -ray pair-production on the IR photons. For energies >200 TeV the observed absorption is due to γ -ray pair-production on CMB photons.

For a γ -ray source located 4 kpc towards the Galactic centre (GC), which is approximately halfway between Earth and the GC, $\sim 5\%$ of γ rays in the 10–200 TeV energy range are absorbed due to pair-production. The fraction of absorbed γ rays increases to $\sim 45\%$ for 1 PeV γ rays. For a source located at the GC, approximately 15% of γ rays are absorbed due to pair-production in the 10–200 TeV energy range, with the absorbed fraction increasing to almost 75% for 1 PeV γ rays.

As the absorption for γ -ray energies in the 10–200 TeV range depends on the ISRF density, the absorption is maximised towards the GC and minimised for the Galactic poles. For γ -ray energies >200 TeV the absorption depends only on the isotropic CMB field. Therefore, the γ -ray pair-absorption on the CMB depends only on the distance that the γ rays travel. On Galactic scales there is an effective horizon for ~ 1 PeV γ rays beyond which the γ rays are unable to reach Earth.

2.2.4 Cooling Distances

As CRs interact with the ISM and create γ rays their kinetic energy is converted into photons. Due to their energy losses there will be maximum diffusion distance that a CR of a given energy will be able to diffuse. For CR protons above 1 GeV p – p collisions (as discussed in [Section 2.2.1](#)) are the dominant energy-loss (i.e. ‘cooling’) process. For CR electrons the dominant cooling process varies between bremsstrahlung, synchrotron, and IC, depending on the ISM conditions (e.g. the ISM gas density and magnetic field strength) and kinetic energy.

The maximum distance that a CR can travel before losing its kinetic energy via a given process is known as its cooling distance, and the time it takes for the CR to lose that energy is known as the cooling time. Both the cooling distance and cooling time must be known to a first-order approximation to define a reasonable simulation with GALPROP. To simulate CR diffusion, GALPROP creates a spatial grid and calculates the CRs travelling between the propagation cells (discussed later in [Section 2.7.3](#)). For accurate results the propagation cells in a GALPROP simulation must be smaller than the shortest cooling distance of any particle being propagated such that the CRs can travel between the propagation cells.

The cooling distance for each process can be calculated to first order by substituting the relevant cooling times into the equation for the diffusion distance ([Equation 2.12](#)). The cooling times for the four main interactions were derived in [Sections 2.2.1](#) and [2.2.2](#) after taking a range of assumptions for the ISM conditions and CR energies. The cooling times are given by: [Equation 2.17](#) (p – p collisions), [Equation 2.24](#) (bremsstrahlung), [Equation 2.27](#) (synchrotron), [Equation 2.36](#) (IC). The cooling distances for all four processes are then given by:

$$d_{\text{pp}}(E_p) = 3.25 \times 10^{-11} \sqrt{\left(\frac{D_0}{\text{cm}^2 \text{s}^{-1}}\right) \left(\frac{E_p}{10 \text{ GeV}}\right)^\delta \left(\frac{n_{\text{H}}}{\text{cm}^{-3}}\right)^{-1}} \text{ pc} \quad (2.44)$$

$$d_{\text{brem}}(E_e) = 2.82 \times 10^{-11} \sqrt{\left(\frac{D_0}{\text{cm}^2 \text{s}^{-1}}\right) \left(\frac{E_e}{10 \text{ GeV}}\right)^\delta \left(\frac{n_{\text{H}}}{\text{cm}^{-3}}\right)^{-1}} \text{ pc} \quad (2.45)$$

$$d_{\text{syn}}(E_e) = 1.54 \times 10^{-11} \sqrt{\left(\frac{D_0}{\text{cm}^2 \text{s}^{-1}}\right) \left(\frac{E_e}{10 \text{ GeV}}\right)^\delta \left(\frac{B}{\mu\text{G}}\right)^{-2} \left(\frac{E_e}{\text{TeV}}\right)^{-1}} \text{ pc} \quad (2.46)$$

$$d_{\text{IC}}(E_e) = 7.95 \times 10^{-11} \sqrt{\left(\frac{D_0}{\text{cm}^2 \text{s}^{-1}}\right) \left(\frac{E_e}{10 \text{ GeV}}\right)^\delta \left(\frac{U_{\text{rad}}}{\text{eV cm}^{-3}}\right)^{-1} \left(\frac{E_e}{\text{GeV}}\right)^{-1}} \text{ pc} \quad (2.47)$$

where D_0 is the normalisation of the diffusion coefficient, δ is the diffusion index, E_p and E_e are the kinetic energies of the proton and electron, respectively, n_{H} is the density of the ionised hydrogen gas in the ISM, B is the magnetic field strength, and U_{rad} is the radiation energy density of the ISRF. Note that the IC cooling distance (Equation 2.47) is an upper-bound that assumes the CR electron is not in the KN regime (see Section 2.2.2). This assumption is valid for $E_e < 100 \text{ TeV}$, with Equation 2.47 being an overestimate for higher CR electron energies⁵.

Taking $\delta = 0.5$, Equation 2.44 shows that the maximum distance CR protons can diffuse is proportional to $E_p^{0.25}$. As the diffusion distance has an increasing slope in kinetic energy, the CR protons travel further as energy increases.

There are many processes via which CR electrons convert their kinetic energy into other forms, and those processes compete depending on the energy of the electron. Hence, the cooling distances for CR electrons varies significantly with energy. From Equation 2.45, the cooling distance for bremsstrahlung interactions is proportional to $E_e^{0.25}$. From Equations 2.46 and 2.47 the cooling distance for synchrotron and IC, respectively, is proportional to $E_e^{-0.25}$ and depends on either the magnetic field strength or the background IR radiation energy density. The dominant energy loss process changes with both kinetic energy and the ISM conditions in a given position. If either synchrotron or IC losses dominate, then the CR electrons diffuse shorter distances as their energy increases.

How the dominant cooling process changes with energy and the ISM conditions is shown in Figure 2.7. For a strong magnetic field ($10 \mu\text{G}$) and low gas density (10^1 cm^{-3}), bremsstrahlung losses dominate for CR electrons up to energies $\sim 20 \text{ GeV}$. For a weak magnetic field ($3 \mu\text{G}$) and a high gas density (10^3 cm^{-3}), bremsstrahlung losses dominate up to energies $\sim 5 \text{ TeV}$.

For a weak Galactic magnetic field ($3 \mu\text{G}$) the IC losses and synchrotron losses compete for electron kinetic energies $E_e < 100 \text{ TeV}$. For this regime the ratio of the IC losses to the synchrotron losses is approximately equal (Moderski et al., 2005). For $E_e > 100 \text{ TeV}$ the IC scattering cross section with the CMB field becomes KN suppressed, and the IC cooling times and cooling distances in Figure 2.7 become an overestimate. However, as the synchrotron energy losses begin to dominate for $E_e > 100 \text{ TeV}$, Figure 2.7 is valid for finding the timestep size and spatial grid size for all shown kinetic energies to first order.

⁵As the purpose of these equations is to find the maximum energy losses of the CRs, and as the synchrotron losses dominate above $E_e < 100 \text{ TeV}$, the KN suppression of the IC scattering cross section at higher energies is not accounted for here.

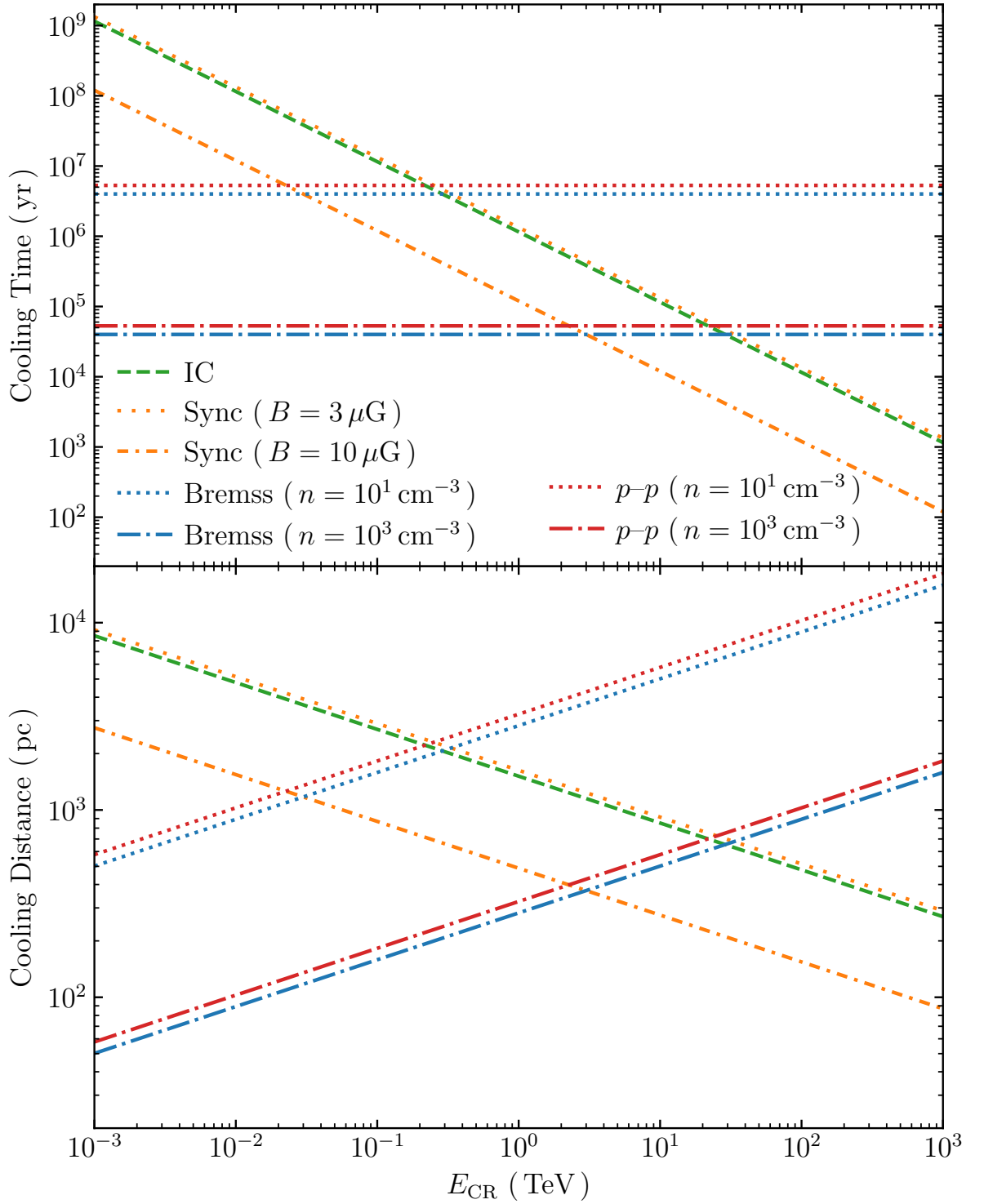


Figure 2.7: The cooling times (top) and cooling distances (bottom) as functions of the CR proton or electron kinetic energy. The cooling times for p - p collisions, bremsstrahlung, synchrotron, and IC are given by Equations 2.17, 2.24, 2.27, and 2.36, respectively. The cooling distances are taken from Equations 2.44–2.47. The values for n and B were taken as Galactic averages, the IC cooling times/distances are calculated for the IR component of the ISRF, and the value $D_0 = 10^{28} \text{ cm}^2 \text{ s}^{-1}$ was used.

2.3 CR Source Distributions

The transport equation (Equation 2.14), includes a source term, $Q(\vec{r}, p)$ that captures all new CRs of momentum p at location \vec{r} being added into the MW through various processes. The source term due to secondary particle creation was discussed in Section 2.2.1. The source term for CRs injected into the MW by sources is defined as the source distribution ($\rho(\vec{r})$) multiplied by the injection spectra, where the injection spectra can be a function of time. The source distribution defines where the CRs are being injected into the MW, and the source term represents the CR flux being injected at any given location. The time-independent source term⁶ for injected CRs is given by:

$$Q(\vec{r}, p) = \rho(\vec{r}) \frac{d\mathcal{N}_{\text{CR}}}{dp} \quad (2.48)$$

where \mathcal{N}_{CR} is the injected CR density. Due to the short cooling times of the electrons, a 3D spatial distribution for the CR injection must be used to reproduce the local electron and positron spectra (Shen, 1970; Shen and Mao, 1971). Additionally, a 3D source distribution must be utilised to accurately model the large-scale structure in the γ -ray sky (Porter et al., 2017).

GALPROP originally used a source distribution that was Gaussian in both the R and Z coordinates (Strong and Moskalenko, 1998) and was able to reproduce the EGRET γ -ray observations from Strong and Mattox (1996). Currently GALPROP uses a superposition of two source distributions, referred to as the spiral arm component and the Galactic disk component (Werner et al., 2015)⁷. The source distributions are parameterised in cylindrical coordinates (R, ϕ, Z) with the origin at the GC.

When operating in a time-independent mode GALPROP does not simulate individual CR acceleration sites such as SNRs and PWNe, with each cell injecting a constant flux of CRs. For the time-dependent mode the source distribution represents a probability density function and will be discussed in more depth in Section 6.2.1. In both cases, the CR source distribution is unitless. The Galactic CR density is normalised at the end of the simulation such that the CR flux at the Solar location is equal to the observed CR flux at Earth (discussed in more depth in Section 2.7.1).

2.3.1 Galactic Disk

The Galactic disk component of the CR source distribution is modelled following Yusifov and Küçük (2004) and consists of a shifted radial exponential function, where the exponential is shifted such that the density at the GC is non-zero. The flat disk is then convolved with an exponential scale height above the plane (Porter et al., 2017). The source density within the disk is given by:

⁶The time-dependent source term will be discussed later in Section 6.2.1.

⁷The CR propagation code DRAGON models the CR source distribution as a two-dimensional disk (Evoli et al., 2017), while PICARD (Kissmann et al., 2015) uses the same CR source distribution as GALPROP.

$$\rho_{\text{disk}}(R, Z) = \left(\frac{R + R_{\text{off}}}{R_{\odot} + R_{\text{off}}} \right)^{\mathfrak{N}_1} \exp \left[-\mathfrak{N}_2 \left(\frac{R - R_{\odot}}{R_{\odot} + R_{\text{off}}} \right) \right] \exp \left(-\frac{|Z|}{H_{Z,\rho}} \right) \quad (2.49)$$

where $\mathfrak{N}_1 = 1.64$ and $\mathfrak{N}_2 = 4.01$ are parameters found by fitting the function to the distribution of observed pulsars via a least-mean-squares method. $R_{\text{off}} = 0.55$ kpc is the radial distance the exponential is shifted by, and $H_{Z,\rho} = 0.2$ kpc is the scale height of the disk. The distance to the GC is given by $R_{\odot} = 8.5$ kpc, which was the IAU recommended distance from the GC to Earth at the time of the model's creation (Kerr and Lynden-Bell, 1986). The Galactic disk component is symmetric in the angle around the GC (ϕ).

2.3.2 Spiral Arms

The spiral arm component of the CR source density follows the model of the major arms from Robitaille et al. (2012) (R12; which is discussed in more depth in Section 2.5.2). As the R12 model was constructed to follow the distribution of infrared photons in the MW, the CR spiral arms were altered to better follow the distribution of SNRs in the MW (Porter et al., 2017). The scale height ($H_{Z,\rho}$) was set to be equal to that from the disk source distribution, and the four spiral arms are normalised such that all four arms inject an equal amount of total CR luminosity into the Galaxy. The four arms are denoted by $j = 1, 1', 2, \text{ and } 2'$, with the total spiral arm distribution being the sum over all four. The spiral arm source density is given by the equations:

$$\rho_{\text{arms}}(R, \phi, Z) = \sum_j \exp \left(-\frac{R - R_{\odot}}{H_R} \right) \exp \left(-\frac{[\phi - \phi_j(R)]^2}{W_{\rho}^2} \right) \exp \left(-\frac{|Z|}{H_{Z,\rho}} \right) \quad (2.50)$$

$$\phi_j(R) = \alpha_j \ln \left(\frac{R}{R_{j,\min}} \right) + \phi_{j,\min} \quad (2.51)$$

where the scale radius $H_R = 3.5$ kpc, the width of the spiral arms has been set to a constant value of $W_{\rho} = 0.75$ kpc, and the function ϕ_j is the spiral arm winding equation. The arm parameter α_j is the winding constant, $R_{j,\min}$ is the minimum radius for the arm, and $\phi_{j,\min}$ is the starting angle of the arm. The maximum angular extent of the arms is given by $\Delta = 6$ rad (i.e. the arms extend from $\phi_{j,\min}$ to $\phi_{j,\min} + \Delta$). The parameters for each of the four spiral arms can be found in Table 2.1.

2.3.3 Disk and Spiral Arm Combinations

The combined source distributions use the disk and spiral arm components (Equation 2.49 and Equation 2.50, respectively). The combined distribution is defined such that some fraction of the CR flux at the Solar position is due to the spiral arm component, with the remaining CR flux from the disk component. This normalisation condition ensures that all of the combined distributions return the same CR flux at the Solar position (Porter et al., 2017).

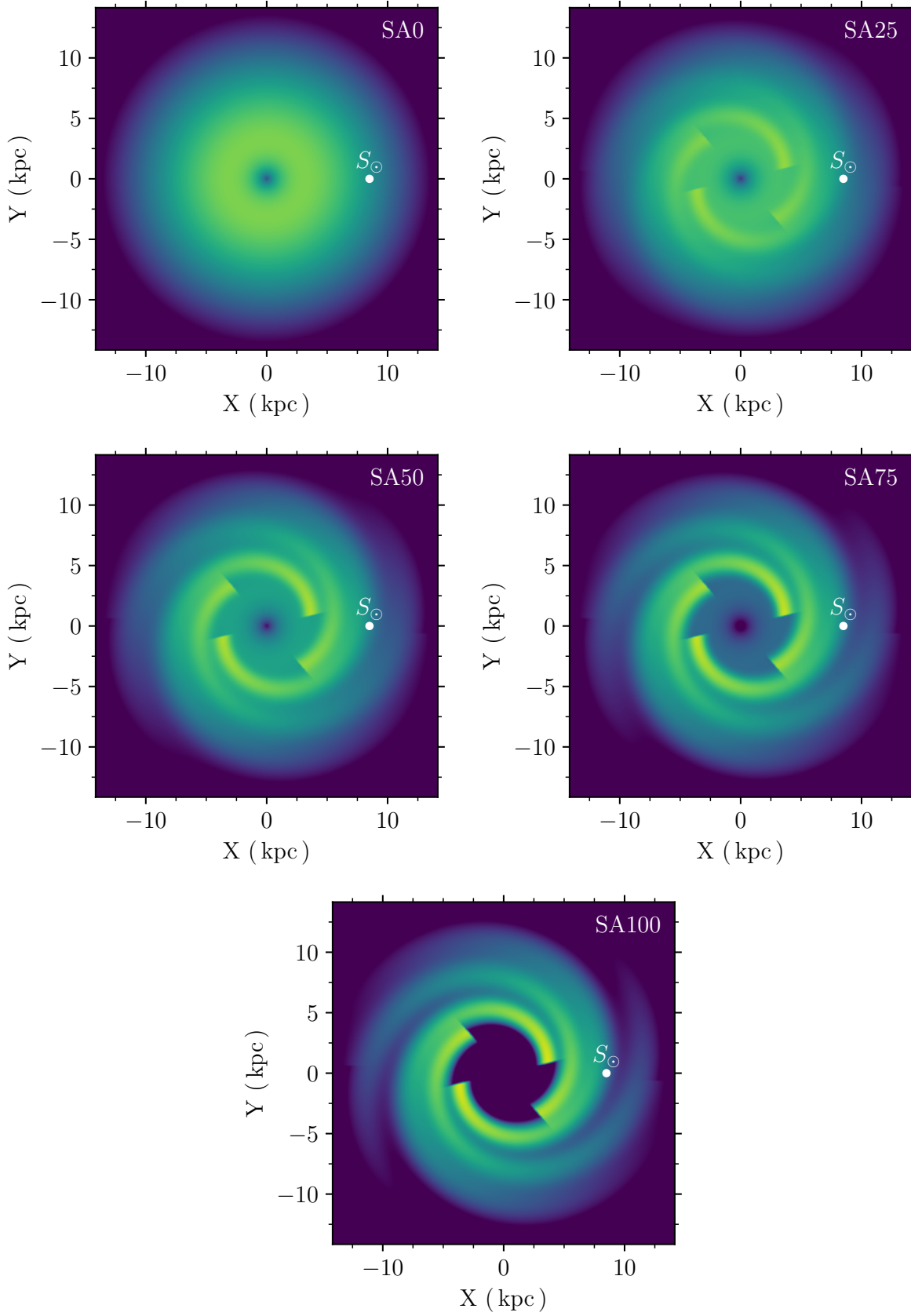


Figure 2.8: The CR energy density in arbitrary units for the SA0 (top left), SA25 (top right), SA50 (centre left), SA75 (centre right), and SA100 (bottom) integrated over the Z-axis. All panels have an identical colour scaling, and the Solar location is shown by S_{\odot} .

Arm	α_j	$R_{j,\min}$ (kpc)	$\phi_{j,\min}$ (rad)
1	4.18	3.8	0.234
1'	4.18	3.8	3.376
2	4.19	4.5	5.425
2'	4.19	4.5	2.283

Table 2.1: Parameters used for constructing the spiral arm source distribution (Robitaille et al., 2012, shown in Figure 2.8), where α_j is the spiral arm winding constant, $R_{j,\min}$ is the minimum radius of the spiral arm, and $\phi_{j,\min}$ is the starting angle of the arm.

In this thesis, five different injection ratios between the Galactic disk and the spiral arms were chosen. The source distributions are denoted by the percentage of CR luminosity at the Solar position from the spiral arm component, with the remaining luminosity at the Solar position being injected from the Galactic disk. For example, SA25 denotes that 25% of the CR source luminosity at the Solar position is injected by the spiral arms, with the remaining 75% being injected by the Galactic disk. The chosen CR source distributions were as follows: SA0, SA25, SA50, SA75, and SA100 – giving a wide range of possible combinations to enable an analysis of how the simulated diffuse emission changes with the different SA models. The five chosen CR source distributions can be seen in Figure 2.8.

2.4 Interstellar Gas

The ISM gas is mostly comprised of hydrogen and helium with ratios of approximately 90% and 10%, respectively (Ferrière, 2001). The hydrogen can be found in the atomic (H I), molecular (H₂), or ionised (H II) states, while the helium is mostly neutral. For the hydrogen, H I constitutes ~60% of the mass averaged over the MW, while H₂ and H II contain 25% and 15%, respectively (Ferrière, 2001). The H II gas has a low number density and scale height ~few 100 pc, while the H₂ gas forms high density molecular clouds.

Both the pion-decay emission (from p - p collisions, see Section 2.2.1) and the flux from bremsstrahlung interactions (see Section 2.2.2) are proportional to the interstellar gas density. Therefore, structures observed in the hadronic γ rays and the leptonic bremsstrahlung γ rays are tied to the structure in the ISM gas density. The spatial density distribution of the interstellar gas also impacts the CR energy losses and the fragmentation of the CR nuclei. As the ISM gas density is responsible for both the propagation of CRs and the related γ -ray emissions, Galactic CR propagation models must utilise 3D ISM observations.

GALPROP uses the gas column-density maps based on the HI4PI survey (Ben Bekhti et al., 2016) and the composite CO survey (Dame et al., 2001), with a correction for the contribution of ‘dark gas’⁸ (Grenier et al., 2005) using a map of optical depth at 353 GHz

⁸Dark gas refers to cold, dense gas. The dark gas is optically thick to its own emissions, and so cannot

based on *Planck* data (Aghanim et al., 2016). Both of these gas surveys have angular resolutions of approximately 0.1° .

Quantifying the ISM gas spatial density relies on measuring doppler shifts in spectral lines to find the velocity towards or away from Earth. The gas column density maps for the atomic and molecular hydrogen are split into Galactocentric radial bins using a rotation curve (Ackermann et al., 2012). The spatial resolution of the gas surveys along the line of sight is limited by the broadening of the spectral lines. The spectral lines are broadened by the random kinematics of the gas caused by, for example, the gas temperature and turbulence within the gas. To improve the resolution along the line of sight GALPROP smooths the gas column density between the velocity bins by performing a weighted average over the velocity axis, where the weighting factors are derived from gas density models. The smoothing procedure ensures that the gas density is spread over the propagation cells, preventing discontinuities in the gas density that can arise due to the cells being much smaller than the line-of-sight resolution of the gas surveys.

For the H II gas, GALPROP employs the NE2001 model (Cordes and Lazio, 2002; Cordes and Lazio, 2003; Cordes, 2004) with updates from Gaensler et al. (2008). The NE2001 model is comprised of a thin disk, a thick disk, and spiral arms. Cavities and clumps in the known ISM gas distribution are also included in the NE2001 model. For the H I gas, GALPROP employs the gas density model from Jóhannesson et al. (2018), which is obtained using a maximum-likelihood fit between an idealised distribution and the LAB H I-survey (Kalberla et al., 2005) and the composite CO survey (Dame et al., 2001). The Jóhannesson et al. (2018) model is comprised of a warped and flaring disc, four spiral arms, and a central bar. Due to the complexity of the ISM gas model, which includes cavities and clumps, there is no simplistic functional form. The models are calculated with the GALGAS code (Jóhannesson et al., 2018), with the resulting files from Jóhannesson et al. (2018) used as inputs for GALPROP in this thesis.

2.5 Interstellar Radiation Fields

Both the IC emission (see Section 2.2.2) and Galactic absorption of γ rays via pair production of electrons and positrons (see Section 2.2.3) depend on the background radiation in the MW. The background interstellar radiation field, or ISRF, has an average energy density close to 1 eV cm^{-3} , which is similar to the energy density of CRs, the GMF, and the turbulence in the interstellar gas (Strong et al., 2013).

The ISRF encompasses all low-energy electromagnetic radiation within the Galaxy generated by both internal and external sources. The ISRF includes infrared, optical, and UV emission from stars, infrared light from interstellar dust radiating heat, and the CMB. Early models of the ISRF include, e.g. Cowsik and Voges (1974); Bignami and Piccinotti (1977); Mathis et al. (1983). However, these models were not self-consistent – i.e. they did not couple the absorption of light by dust with the re-emission of infrared light. Later models of the ISRF that are fully self-consistent include, e.g. Porter and Strong (2005);

be observed via emission line spectroscopy. The mass of the dark gas in the MW is similar to the mass of the molecular gas. For a detailed description, see Grenier et al. (2005).

Normalisation	Wavelength Band			
	J	K	L	M
$U_{\text{F98,disk},0}$	8.144	6.648	3.511	1.782
$U_{\text{F98,dust},0}$	4.642	1.152	2.180	3.236
$U_{\text{F98,bar},0}$	10.52	8.817	4.538	2.255

Table 2.2: The normalisation parameters for each of the wavelengths present in the DIBRE survey (Freudenreich, 1996). All units are in $\text{MJy sr}^{-1} \text{kpc}^{-1}$ and can be converted using $1 \text{ MJy sr}^{-1} \text{kpc}^{-1} = 9.522 \times 10^9 \text{ W pc}^{-3} \text{ Hz}^{-1} \text{ sr}^{-1}$.

Popescu et al. (2017).

Within GALPROP there are two 3D ISRF models in use. These are referred to as F98 (from Freudenreich, 1998) and R12 (from Robitaille et al., 2012). The F98 model includes a Galactic bar and does not include any spiral arms, while the R12 model includes the spiral arms but does not include a Galactic bar. Although the R12 more accurately predicts the infrared emission for the Galactic longitudes $|\ell| \leq 60^\circ$, both the F98 and R12 models are equivalent solutions and are considered as upper and lower limits on the Galactic infrared emissions. Both of the ISRF models are self-consistent and are parameterised in cylindrical coordinates (R, ϕ, Z) with the origin at the GC. For the remainder of this section the radiation energy density, U_{rad} , is denoted by U_{F98} and U_{R12} for the F98 and R12 distributions, respectively, with additional subscripts defining the components of the respective radiation energy densities.

2.5.1 Freudenreich Spatial Model

The F98 ISRF model (Freudenreich, 1998) combines both the stellar emission and infrared emission from dust. It has 47 free parameters and is constructed to have good agreement with the diffuse infrared background experiment (DIBRE; Freudenreich, 1996) survey taken with the *cosmic background explorer (COBE)* satellite. The F98 model combines a stellar disk, a Galactic bar, and a dust layer. The F98 model is parameterised in cylindrical coordinates (R, ϕ, Z) ; however, the F98 model also uses the transformed coordinates (X', Y') for creating the hole in the Galactic disk, and the transformed coordinates (X'', Y'', Z'') for constructing the central Galactic bar.

The disk and bar distributions are sums over the four wavelengths present in the DIBRE survey; namely $\nu = 1.25 \mu\text{m}$, $2.2 \mu\text{m}$, $3.5 \mu\text{m}$, and $4.9 \mu\text{m}$ (labelled as J, K, L, and M, respectively), with each wavelength having a separate normalisation. The normalisation values for each wavelength band and model component are shown in Table 2.2. The total radiation energy density of the F98 ISRF is shown in Figure 2.9, and is given by the sum over all components:

$$U_{\text{F98}}(R, \phi, Z) = U_{\text{F98,disk}}(R, \phi, Z) + U_{\text{F98,dust}}(R, \phi, Z) + U_{\text{F98,bar}}(R, \phi, Z) \quad (2.52)$$

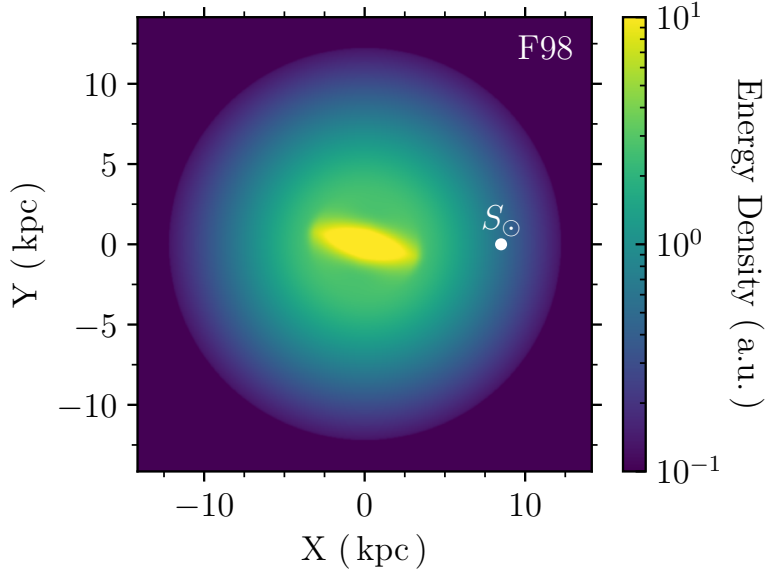


Figure 2.9: The F98 ISRF energy density in arbitrary units integrated over the Z -axis. The Solar location is shown by S_{\odot} .

where U_{F98} denotes the total radiation energy density and the additional subscripts denote the individual components.

F98 Stellar Disk Distribution

The F98 stellar disk is described by an inner and outer truncated (i.e. set to zero) exponential in R , follows a sech^2 in Z , and has a warped mid-point in the Z axis. The distribution is a sum over the wavelength-band counting index, ν , with each wavelength normalised by the parameter $U_{\text{F98,disk},\nu,0}$. The normalisation values for the different frequency bands in the DIBRE data are given in Table 2.2. The radiation energy density of the disk is given by the equation:

$$\begin{aligned}
 U_{\text{F98,disk}}(R, \phi, Z) = & h_{\text{disk}}(X', Y') \sum_{\nu} U_{\text{F98,disk},\nu,0} \\
 & \times \exp\left(-\frac{R}{H_{R,\text{disk}}}\right) \\
 & \times \text{sech}^2\left(\frac{Z - \bar{Z}(R, \phi)}{H_{Z,\text{disk}}}\right)
 \end{aligned} \tag{2.53}$$

where $H_{Z,\text{disk}} = 0.3457 \text{ kpc}$ is the disk scale height, and the disk scale radius is given by:

$$H_{R,\text{disk}} = \begin{cases} 2.6045 \text{ kpc}, & R \leq R_{\text{F98,max}} \\ 0.5 \text{ kpc}, & R > R_{\text{F98,max}} \end{cases} \tag{2.54}$$

where $R_{\text{F98,max}} = 12.18 \text{ kpc}$ is the radius of the disk. The function $h_{\text{disk}}(X', Y')$ creates a hole in the Galactic disk, where the (X, Y) coordinates are rotated clockwise by the

angle $\phi_0 = 13.79^\circ$ to give the transformed coordinates (X', Y') . The functional form of the stellar hole is given by:

$$h_{\text{disk}}(X', Y') = 1 - \exp \left[- \left(\frac{R_h(X', Y')}{H_{R,\text{disk-hole}}} \right)^{\omega_{H,\text{disk}}} \right] \quad (2.55)$$

$$[R_h(X', Y')]^2 = (X')^2 + (eY')^2 \quad (2.56)$$

where $\omega_{H,\text{disk}} = 1.711$ is the disk hole power, $H_{R,\text{disk-hole}} = 2.973 \text{ kpc}$ is the scale radius of the stellar disk hole, and $e = 0.8554$ is the eccentricity of the hole.

The mean height of the Galactic plane, $\bar{Z}(R, \phi)$, is equal to zero for Galactic radii less than $R_w = 4.34 \text{ kpc}$ from the GC. After R_w , the mean height is modelled as a cubic polynomial in R and is sinusoidal in ϕ . The sinusoidal polynomial has the effect of warping the Galactic plane, where the warping increases in amplitude as the Galacto-centric radius increases. The warping of the Galactic disk is given by:

$$\bar{Z}(R, \phi) = \begin{cases} 0, & u \leq 0 \\ (c_1 u + c_2 u^2 + c_3 u^3) \sin(\phi - \phi_w), & u > 0 \end{cases} \quad (2.57)$$

$$u = R - R_w \quad (2.58)$$

where $\phi_w = 0.44^\circ$ is the straight-line azimuthal node, and the polynomial coefficients are given by $c_1 = 0.01118$, $c_2 = -0.00192$, and $c_3 = 0.000795$.

F98 Dust Distribution

The F98 dust layer follows a similar distribution to the F98 stellar disk, including a similar hole around the GC. The hyperbolic-sine function in the Z -axis is raised to a different power compared to the disk distribution, and the mean height is warped by an extra factor $\Pi = 1.782$ to better reproduce the data from the DIBRE experiment. The radiation energy density of the dust distribution is given by the equation:

$$\begin{aligned} U_{\text{F98,dust}}(R, \phi, Z) = & h_{\text{disk}}(X', Y') h_{\text{dust}}(X', Y') \sum_{\nu} U_{\text{F98,dust},\nu,0} \\ & \times \exp \left(- \frac{R}{H_{R,\text{disk}}} \right) \\ & \times \exp \left(- \frac{2R}{3H_{R,\text{dust}}} \right) \\ & \times \text{sech}^{10/3} \left(\frac{|Z - \Pi \bar{Z}(R, \phi)|}{H_{Z,\text{dust}}} \right) \end{aligned} \quad (2.59)$$

where the $H_{R,\text{dust}} = 3.066 \text{ kpc}$ is the dust scale radius, $H_{Z,\text{dust}} = 0.1520 \text{ kpc}$ is the dust scale height, the disk scale radius $H_{R,\text{disk}}$ is given by Equation 2.54, and the disk hole function h_{disk} is given by Equation 2.55. The dust hole function, h_{dust} , is given by:

$$h_{\text{dust}}(X', Y') = 1 - \exp \left[- \left(\frac{R_h(X', Y')}{H_{R,\text{dust-hole}}} \right)^{\omega_{H,\text{dust}}} \right] \quad (2.60)$$

where $H_{R,\text{dust-hole}} = 2.615 \text{ kpc}$ is the dust scale radius, $\omega_{H,\text{dust}} = 2.150$ is the dust hole power, and the radius of the hole (R_h) is given by Equation 2.56. Although GALPROP uses the dust distribution from the F98 model, some of the dust distribution parameters used in the above equations are not completely identical (Porter et al., 2017). The scale lengths and scale heights, the central hole, and the elliptical warp are taken from the F98 model as above, while the dust properties and composition are changed such that they agree with Draine and Li (2007). The dust normalisation was then set to be identical to the R12 model. This was necessary as GALPROP requires a wider range of wavelengths down into the UV spectrum for its ISRF calculations, which are not present in the original F98 model. As the extinction and emissivity calculations for the F98 dust distribution in Freudenreich (1998) are unused by GALPROP, they are not included here. For completeness, the original F98 dust distribution normalisation values are included in Table 2.2.

F98 Bar Distribution

The F98 bar distribution⁹ is described by ellipsoid in the coordinates (X'', Y'', Z'') . These double-primed coordinates are found by rotating the primed coordinates (X', Y') clockwise into the Z -axis by the best-fit pitch angle $\phi_{\text{pitch}} = -0.023^\circ$. To represent the bar structures seen in other galaxies, the bar ellipsoid has ‘boxy’ edges (i.e. the ellipse ends abruptly) along the Z'' axis and rounded edges along the X'' and Y'' axes. The radiation energy density of the ellipsoid decreases following a sech^2 function with an exponential cut off at the Galacto-centric radius $R_{\text{end}} = 3.128 \text{ kpc}$. The radiation energy density of the bar is given by:

$$U_{\text{F98,bar}}(R_b) = \sum_{\nu} U_{\text{F98,bar},\nu,0} \text{sech}^2(R_b) \times \begin{cases} 1, & R \leq R_{\text{end}} \\ \exp \left[- \left(\frac{R - R_{\text{end}}}{H_{\text{end}}} \right)^2 \right], & R > R_{\text{end}} \end{cases} \quad (2.61)$$

where $H_{\text{end}} = 0.461 \text{ kpc}$ is the scale length of the bar cut off in the (X'', Y'', Z'') coordinate frame. The variable R_b follows the equation for an ellipsoid in the (X'', Y'', Z'') coordinate frame, with the ellipsoid defined by the shape parameters $(S_X, S_Y, S_Z) = (1.696, 0.6426, 0.4425)$. The bar is generated using “face-on” and “edge-on” parameters, denoted by \perp and \parallel respectively. The equation for the face-on radius (i.e. the radius perpendicular to the Z'' axis) is given by:

$$(R_{\perp})^{C_{\perp}} = \left(\frac{|X''|}{S_X} \right)^{C_{\perp}} + \left(\frac{|Y''|}{S_Y} \right)^{C_{\perp}} \quad (2.62)$$

$$\therefore R_{\perp} = \left[\left(\frac{|X''|}{S_X} \right)^{C_{\perp}} + \left(\frac{|Y''|}{S_Y} \right)^{C_{\perp}} \right]^{1/C_{\perp}} \quad (2.63)$$

⁹Shown here is the corrected form implemented in GALPROP, as per Macias (2017)

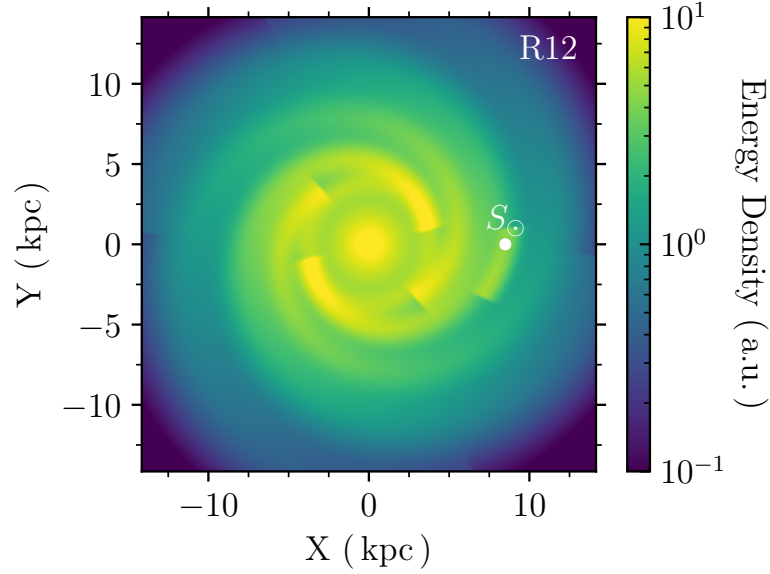


Figure 2.10: The R12 ISRF energy density in arbitrary units integrated over the Z -axis. The Solar location is shown by S_{\odot} .

where $C_{\perp} = 1.574$. The edge-on radius (i.e. the radius parallel to the Z'' axis) is then included to calculate the radius of the bar ellipsoid (R_b), which is given by:

$$(R_b)^{C_{\parallel}} = R_{\perp}^{C_{\parallel}} + \left(\frac{|Z''|}{S_Z} \right)^{C_{\parallel}} \quad (2.64)$$

$$\therefore (R_b)^{C_{\parallel}} = \left[\left(\frac{|X''|}{S_X} \right)^{C_{\perp}} + \left(\frac{|Y''|}{S_Y} \right)^{C_{\perp}} \right]^{C_{\parallel}/C_{\perp}} + \left(\frac{|Z''|}{S_Z} \right)^{C_{\parallel}} \quad (2.65)$$

where the edge-on parameter is given by $C_{\parallel} = 3.501$. The bar ellipsoid is a rounded diamond in the (X'', Y'') plane as the perpendicular shape parameter $C_{\perp} < 2$. Conversely, the bar ellipsoid has more pronounced vertices in the Z'' axis as the parallel shape parameter $C_{\parallel} > 2$.

2.5.2 Robitaille Spatial Model

The R12 ISRF model (Robitaille et al., 2012) has good agreement with latitudinal and longitudinal profiles for the emission in the near-infrared to far-infrared wavelengths from the Galactic legacy midplane survey extraordinaire (GLIMPSE; Churchwell et al., 2009) and multiband infrared photometer for *Spitzer* (MIPSGAL; Carey et al., 2009) surveys taken with the *Spitzer space telescope*. The R12 ISRF model also has good agreement with the improved reprocessing of the IRIS survey (Miville-Deschênes and Lagache, 2005) survey taken with the *infrared astronomical satellite (IRAS)* instrument. As the spiral arm source distribution (Section 2.3.2) is derived from the R12 spiral arm model, the two models share many parameters.

The R12 model components are constructed include an axisymmetric bulge, an exponential disk, a star forming ring, spiral arms, and a Galactic dust. The disk, bulge, and

ring distributions are sums over the counting index $i = 1, \dots, 87$ (hereafter referred to as the spectral type), which denote each of the different stellar types from the main sequence, pre-main sequence, giant stars, stars on the asymptotic giant branch, and planetary nebulae. These are named the SKY models, and are originally from [Wainscoat et al. \(1992\)](#), being developed further by [Cohen \(1993\)](#), [Cohen \(1994\)](#), and [Cohen \(1995\)](#). Each stellar class has its own normalisation values ([Wainscoat et al., 1992](#), see their Table 2). The total radiation energy density of the R12 model is shown in [Figure 2.10](#), and is given by the sum over all components:

$$U_{\text{R12}}(R, \phi, Z) = U_{\text{R12,disk}}(R, Z) + U_{\text{R12,bulge}}(R, Z) + U_{\text{R12,arms}}(R, \phi, Z) + U_{\text{R12,ring}}(R, Z) + U_{\text{R12,dust}}(R, Z) \quad (2.66)$$

where U_{R12} denotes the total radiation energy density and the additional subscripts denote the individual components.

R12 Disk Distribution

The radiation energy density within the Galactic disk is given by a decreasing exponential which is truncated beyond $R_{\text{R12,max}} = 15$ kpc. The radiation energy density of the disk component is given by:

$$U_{\text{R12,disk}}(R, Z) = \begin{cases} \sum_i U_{\text{R12,disk},i} \exp\left(-\frac{R - R_\odot}{H_R}\right) \exp\left(-\frac{|Z|}{H_{Z,i}}\right), & R < R_{\text{R12,max}} \\ 0, & R \geq R_{\text{R12,max}} \end{cases} \quad (2.67)$$

where $H_R = 3.5$ kpc is the radial scale length, $U_{\text{R12,disk},i}$ is the spatial radiation energy density of the i^{th} spectral type, and $H_{Z,i}$ is the scale height perpendicular to the Galactic plane of the i^{th} spectral type. The distance to the GC is given by $R_\odot = 8.5$ kpc, which was the IAU recommended distance from the GC to Earth at the time of the model's creation ([Kerr and Lynden-Bell, 1986](#)).

R12 Bulge Distribution

The central bulge of the MW represents a region where the distribution of stars extends further vertically out of the Galactic plane and is comprised mostly of stars that are older than those found within the Galactic plane ([Binney et al., 1997](#)). The radiation energy density within the Galactic bulge is given by:

$$U_{\text{R12,bulge}}(R, Z) = U_{\text{R12,bulge},0} [\kappa^{-1.8} \exp(-\kappa^3)] \sum_i U_{\text{R12,bulge},i} \quad (2.68)$$

$$\kappa = \frac{\sqrt{R^2 + K_{\text{bulge}}^2 Z^2}}{R_{\text{bulge}}} \quad (2.69)$$

Arm	α_j	$R_{j,\min}$ (kpc)	$\phi_{j,\min}$ (rad)	W_j (kpc)	Δ_j (rad)
1	4.18	3.8	0.234	0.55	6
1'	4.18	3.8	3.376	0.55	6
2	4.19	4.5	5.425	0.55	6
2'	4.19	4.5	2.283	0.55	6
L	4.57	8.100	5.847	0.30	0.55
L'	4.57	7.591	5.847	0.30	0.55

Table 2.3: The spiral arm parameters used for constructing the R12 spiral arms (Robitaille et al., 2012). The values for arms 1, 1', 2, and 2' are the same as for the spiral arm source distribution shown in Table 2.1.

where $U_{\text{R12,bulge},0} = 3.6$ is a unitless global normalisation factor, $U_{\text{R12,bulge},i}$ is the normalisation constant for the i^{th} spectral type, κ is a unitless function of radial distance from the GC and height above the Galactic plane, $K_{\text{bulge}} = 1.6$ is the bulge axis ratio (i.e. major axis length over the minor axis length), and $R_{\text{bulge}} = 2 \text{ kpc}$ is the central radius of the bulge.

R12 Spiral Arm Distributions

The radiation energy density within the spiral arms is split into two categories, with the counting variable $j = 1, 1', 2, 2'$ denoting the four major arms, and $j = L, L'$ denoting the two local spurs (also commonly referred to as the minor arms). All arms and spurs are given the same arm winding function as in the source spiral arms (see Equation 2.51), with the parameter values for all the R12 spiral arms given in Table 2.3. The shape parameters for the four major arms are equal to those for the spiral arm source distribution given earlier in Section 2.3. The radiation energy density within the arms is set to zero when the distance from the GC to the centre of the arms is less than R_{\min} .

For the two local spurs ($j = L, L'$) the radiation energy density within the arms is modelled as a step function. The local spur parameter values are given in Table 2.3. The distance from the centre of the local spur to some position is given by φ_j . The radiation energy density is given by the same functional form as for the disk (see Equation 2.67) when $\varphi_j \leq W_j$, and the radiation energy density is set to zero when $\varphi_j > W_j$. The local spurs are described by the equation:

$$U_{\text{R12},j=L,L'}(R, \phi, Z) = \begin{cases} U_{\text{R12,A}} \sum_i U_{\text{R12,arms},i} \exp\left(-\frac{R - R_{\odot}}{H_R}\right) \exp\left(-\frac{|Z|}{H_{Z,i}}\right), & \varphi_j \leq W_j \\ 0, & \varphi_j > W_j \end{cases} \quad (2.70)$$

where $U_{\text{R12,A}} = 5$ is a unitless global normalisation factor, and the other constants are the

same as for the disk component given in Equation 2.67. The distance from some position to the centre of an arm, φ_j , is given by:

$$\varphi_j = \exp\left(\frac{\phi_j(R) - \phi_{j,\min}}{\alpha_j}\right) R_{j,\min} \quad (2.71)$$

where the equation is derived by rearranging the arm winding function given by Equation 2.51. For the four major arms ($j = 1, 1', 2, 2'$) the radiation energy density is given by the same functional form as for the disk; however, unlike for the minor arms which use a step function, the major arms are modelled with a Gaussian profile perpendicular to the arms. The major arms are then given by:

$$\begin{aligned} U_{\text{R12},j=1,1',2,2'}(R, \phi, Z) = U_{\text{R12,A}} \sum_i U_{\text{R12,arms},i} \\ \times \exp\left(-\frac{R - R_\odot}{H_R}\right) \\ \times \exp\left(-\frac{|Z|}{H_{Z,i}}\right) \\ \times \exp\left(-\frac{[\phi - \phi_j(R)]^2}{W_j}\right) \end{aligned} \quad (2.72)$$

where the arm-specific values are given in Table 2.3 and $\phi_j(R)$ is given by Equation 2.51. The four major arms are described as Gaussian cylinders which are wound around the Galaxy as logarithmic spirals. In a similar fashion as for the source distribution arms, $U_{\text{R12},j=1,1',2,2'}(R, \phi, Z) = 0$ for $\phi_j \geq \Delta_j$ (i.e. the arms extend from $\phi_{j,\min}$ to $\phi_{j,\min} + \Delta_j$). The radiation energy density is also set to zero when the distance from the GC to the centre of the arm is less than $R_{j,\min}$ (i.e. $U_{\text{R12},j=1,1',2,2'}(R, \phi, Z) = 0$ for $R < R_{j,\min}$).

The total spiral arm radiation energy density is given by the sum of all the radiation energy densities across the arms and spurs, which are themselves sums over the spectral type i . The total component of the radiation energy density from the spiral arms for the R12 model is then given by:

$$U_{\text{R12,arms}}(R, \phi, Z) = \sum_j U_{\text{R12,j}} \quad (2.73)$$

R12 Ring Distribution

The Galactic ring represents a toroidal structure around the GC (Clemens et al., 1988), though its existence is debated (e.g. see Dobbs and Burkert, 2012). The Galactic ring is included in the R12 model, with the radiation energy density within the Galactic ring being given by a Gaussian distribution. The maximum of the Gaussian, i.e. the centre of the ring, is located at $R_{\text{ring}} = 6.75$ kpc from the GC. The ring distribution has a Gaussian width of $H_{R,\text{ring}} = 0.96$ kpc. The radiation energy density decreases as an exponential

from the Galactic plane, using the same scale height as Equation 2.67 and Equation 2.70. Hence, the ring component is given by the equation:

$$U_{\text{R12,ring}}(R, Z) = U_{\text{R12,ring},0} \sum_i U_{\text{R12,ring},i} \exp\left(-\frac{(R - R_{\text{ring}})^2}{2H_{R,\text{ring}}^2}\right) \exp\left(-\frac{|Z|}{H_{Z,i}}\right) \quad (2.74)$$

where $U_{\text{R12,ring},0} = 25$ is a unitless global normalisation constant, and $U_{\text{R12,ring},i}$ is the normalisation constant for the i^{th} spectral type.

R12 Dust Distribution

The radiation energy density of IR emitted by dust within the Galaxy is given by a radial Gaussian up to the transition radius R_{smooth} . The dust distribution is modelled as decreasing exponential for radii $R > R_{\text{smooth}}$. Similarly to the previously discussed R12 components, the radiation energy density from the dust is modelled as a decreasing exponential in Z . It is worth noting that unlike the previous R12 components, the dust distribution does not depend on the stellar type. The dust model is adopted from [Draine and Li \(2007\)](#), which uses a mixture of dust grains from neutral and ionised polycyclic aromatic hydrocarbons, amorphous silicates, and carbonaceous dust grains which follow a size distribution from [Weingartner and Draine \(2001\)](#). The radiation energy density from the dust component is then given by:

$$U_{\text{R12,dust}}(R, Z) = U_{\text{R12,dust},0} \exp\left(-\frac{|Z|}{H_{Z,\text{R12,dust}}}\right) \times \begin{cases} \kappa_0 \exp\left(-\frac{(R - R_{\text{dust}})^2}{2H_{R,\text{R12,dust}}^2}\right), & R < R_{\text{smooth}} \\ \exp\left(-\frac{R}{H_R}\right), & R \geq R_{\text{smooth}} \end{cases} \quad (2.75)$$

where the dust normalisation constant is given by $U_{\text{R12,dust},0} = 10^{-25} \text{ g cm}^{-3}$, the scale height of the dust is given by $H_{Z,\text{R12,dust}} = 0.1 \text{ kpc}$, the Gaussian peaks at a distance of $R_{\text{dust}} = 4.5 \text{ kpc}$, the Gaussian has a scale radius of $H_{R,\text{R12,dust}} = 1 \text{ kpc}$, and $H_R = 3.5 \text{ kpc}$ is the same as before.

The value R_{smooth} is defined as the transition radius, where the radial distribution goes from a Gaussian to a decreasing exponential. The Gaussian distribution is then normalised by the value κ_0 , which is defined such that the transition is smooth to the first order – i.e. both the function and its first derivative are equal at the transition point $R = R_{\text{smooth}}$. The equations for R_{smooth} and κ_0 , as well as their approximate values, are given by:

$$R_{\text{smooth}} = \frac{H_{R,R12,\text{dust}}^2}{H_R} + R_{\text{dust}} \approx 4.79 \text{ kpc} \quad (2.76)$$

$$\kappa_0 = \frac{\exp\left(-\frac{R_{\text{smooth}}}{H_R}\right)}{\exp\left(-\frac{(R_{\text{smooth}} - R_{\text{dust}})^2}{2H_{R,R12,\text{dust}}^2}\right)} \approx 0.27 \quad (2.77)$$

where all parameters have been defined previously.

2.6 Galactic Magnetic Fields

The synchrotron cooling (see [Section 2.2.2](#)), which is a major contributor to the electron energy losses at 1–10 TeV energies (as shown in [Figure 2.7](#)), depends on the magnetic fields that permeate the ISM. As VHE CRs travel through the MW their paths become twisted and bent around the magnetic field, where the degree of deflection depends on the CR energy and the magnetic field strength (as discussed in [Section 2.1](#)). The Galactic CR density distribution will in part be determined by the GMF, as CRs (especially electrons) will be slowed or even trapped in regions where the magnetic field is strong.

The GMF has two components that are approximately equal in strength. Charged particles flow along the field lines of the large-scale regular component ([Beuermann et al., 1985](#)). There is also the small-scale irregular component (sometimes referred to as the ‘random’ component, see [Sun et al., 2008](#)) which is randomly oriented by the ionised interstellar gas clouds and the turbulent motions within the ISM gas. The random component is produced by SNe and other powerful outflows in the Galaxy and are typically smaller than 100 pc in size ([Gaensler and Johnston, 1995](#); [Haverkorn et al., 2008](#)). There is a further random anisotropic field (also known as a ‘striated’ component) that is produced by a large-scale compression and stretching of the irregular component of the GMF ([Beck, 2001](#)). The striated field is aligned with the large-scale regular component, but with reversals in direction on smaller scales.

GALPROP has a variety of available GMF models from across the literature, two of which are utilised in this work. Although the GALPROP axisymmetric exponential (GASE) model is a simple exponential disk that is not fit to observations, it is used commonly throughout the literature (e.g. [Korsmeier and Cuoco, 2022](#); [Qiao et al., 2022](#)). The other GMF investigated here is the [Pshirkov et al. \(2011\)](#) bisymmetric spiral (PBSS) model, which includes the spiral arm structure and is fit to rotation measures (RMs) of extragalactic sources. Other notable GMF models within GALPROP that are not used in this thesis include, e.g. [Sun et al. \(2008\)](#); [Jaffe et al. \(2010\)](#); [Sun and Reich \(2010\)](#); [Jansson and Farrar \(2012\)](#). The GMF models are parameterised in cylindrical coordinates (R, ϕ, Z) with the origin at the GC.

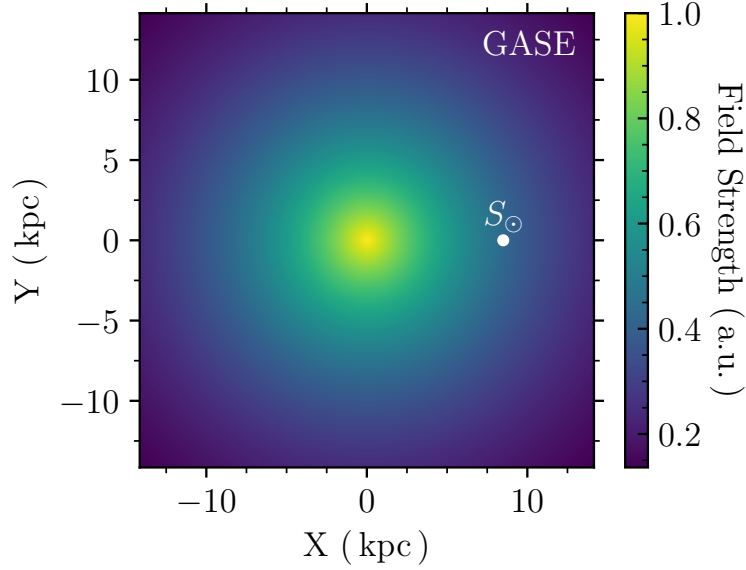


Figure 2.11: The GASE GMF field strength in arbitrary units integrated over the Z -axis. The Solar location is shown by S_{\odot} .

2.6.1 GALPROP Axisymmetric Exponential Model

The GALPROP axisymmetric exponential (GASE; [Strong et al., 2000](#)) model is a simple exponential disk in the radial direction and an absolute exponential in height. The GASE model does not include any spiral arms or other more complex Galactic structures. The magnetic field strength is given by:

$$B_{\text{GASE}}(R, Z) = B_{\text{GASE},0} \exp\left(\frac{R - R_{\odot}}{H_{R,\text{GASE}}}\right) \exp\left(-\frac{|Z|}{H_{Z,\text{GASE}}}\right) \quad (2.78)$$

where $B_{\text{GASE},0} = 5 \mu\text{G}$ is the field strength at Earth, $H_{R,\text{GASE}} = 10 \text{ kpc}$ is the radial scale-length, and $H_{Z,\text{GASE}} = 2 \text{ kpc}$ is the scale height of the disk. The distance to the GC is given by $R_{\odot} = 8.5 \text{ kpc}$, which was the IAU recommended distance from the GC to Earth at the time of the model's creation ([Kerr and Lynden-Bell, 1986](#)).

The GASE distribution is shown in [Figure 2.11](#). Due to the GASE GMF's incompatibility with rotation measures of extragalactic radio sources it is not considered an accurate representation of the magnetic field. However, it is still commonly used throughout the literature due to its simplicity (e.g. [Korsmeier and Cuoco, 2022](#); [Qiao et al., 2022](#)). The GASE model is considered as a baseline distribution to compare against in [Chapter 5](#).

2.6.2 Pshirkov Bi/Axisymmetric Spiral Models

There are two GMF models from [Pshirkov et al. \(2011\)](#), both of which are constructed to agree with the Faraday RMs of extragalactic radio sources in the national radio astronomy observatory very large array (NRAO VLA) sky survey (named the NVSS; [Condon et al., 1998](#)) RM catalogue, as well as a compilation of RMs of sources from [Kronberg and](#)

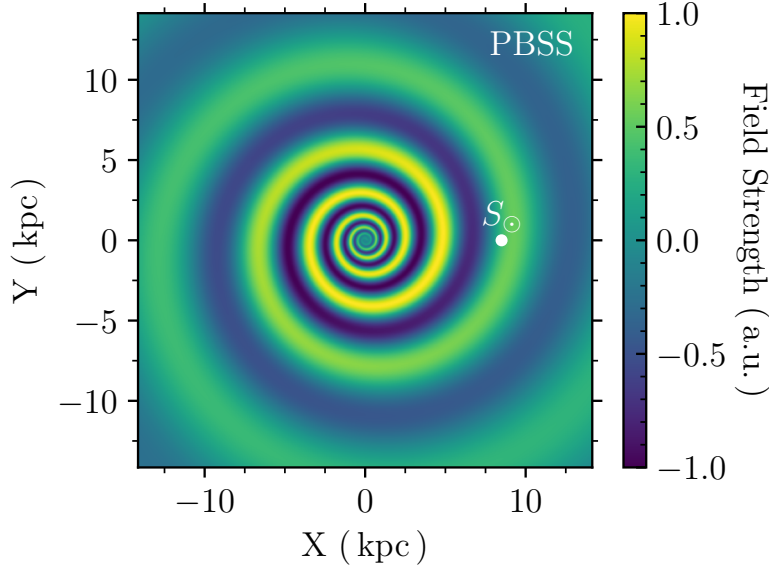


Figure 2.12: The PBSS GMF field strength in arbitrary units integrated over the Z -axis. The Solar location is shown by S_{\odot} . The halo component of the PBSS distribution has not been included to reproduce the distribution employed by GALPROP (Porter et al., 2017).

Newton-McGee (2011). The Pshirkov et al. (2011) GMFs consist of two components: a Galactic halo, and the spiral arms. The two Pshirkov et al. (2011) models differ only in the direction of the spiral arm magnetic field. The two models are referred to as the Pshirkov bisymmetric spiral (PBSS) distribution and the Pshirkov axisymmetric spiral (PASS) distribution. The PBSS GMF is shown in Figure 2.12.

Pshirkov Spiral Arm Distributions

The PBSS and PASS spiral arms are constructed from a decreasing exponential in height with logarithmic spiral arms. Each arm is identical in size and rotated π radians with respect to one another. The strength of the Pshirkov et al. (2011) spiral arm magnetic field is given by:

$$B_{\text{PBSS}}(R, \phi, Z) = B_{\text{P,disk}}(R) \cos \left[\phi - \phi_b \ln \left(\frac{R}{R_{\odot}} \right) + \phi_a \right] \exp \left(-\frac{|Z|}{H_{Z,\text{P}}} \right) \quad (2.79)$$

where $H_{Z,\text{P}} = 1$ kpc is the scale height of the magnetic field. The only functional difference between the PBSS and PASS GMF models is that the absolute value is taken on the cosine term for the PASS model to ensure that the spiral arms point in the same direction. The disk term, $B_{\text{P,disk}}$, is constant for the Galacto-centric radius $R < R_{\text{P,disk}}$ and inversely proportional to the Galacto-centric radius for $R > R_{\text{P,disk}}$. The central disk is given by:

$$B_{\text{P,disk}}(R, \phi) = B_{\text{P,disk},0} \frac{R_{\odot}}{\cos \phi} \times \begin{cases} 1/R_{\text{P,disk}}, & R < R_{\text{P,disk}} \\ 1/R, & R \geq R_{\text{P,disk}} \end{cases} \quad (2.80)$$

where $B_{\text{P,disk},0} = 2 \mu\text{G}$ is the magnetic field strength normalisation and $R_{\text{P,disk}} = 5 \text{ kpc}$ is the distance from the GC where the field strength is assumed to be independent of the Galacto-centric radius. The cosine term from Equation 2.79, which controls how the arms are wound around the Galaxy, depends on the angles ϕ_a and ϕ_b which are given by:

$$\phi_a = \phi_b \ln \left(1 + \frac{R_{\text{rev}}}{R_{\odot}} \right) - \frac{\pi}{2} \quad (2.81)$$

$$\phi_b = \frac{1}{\tan(\phi_p)} \quad (2.82)$$

where $\phi_p = -6^\circ$ is the pitch angle of the arms and $R_{\text{rev}} = -0.6 \text{ kpc}$ is the radial distance from the Solar position towards the first field reversal, with negative distances implying that the field reversal occurs in the direction towards the GC.

Pshirkov Halo Distribution

The halo component represents a large structure located above and below the Galactic plane. It is constructed from a decreasing radial exponential and a height function. The magnetic field strength of the Galactic halo is given by:

$$B_{\text{halo}}(R, Z) = B_{\text{halo},0} \left[1 + \left(\frac{|Z| - Z_{\text{halo}}}{H_{Z,\text{halo}}} \right)^2 \right]^{-1} \frac{R}{H_{R,\text{halo}}} \exp \left(1 - \frac{R}{H_{R,\text{halo}}} \right) \quad (2.83)$$

where $B_{\text{halo},0} = 4 \mu\text{G}$ is the halo magnetic field strength normalisation, $Z_{\text{halo}} = 1.3 \text{ kpc}$ is the vertical location of the halo, and $H_R = 8 \text{ kpc}$ is the scale radius of the halo. The parameter H_Z is the scale height of the halo and differs between the northern (positive Z) and southern (negative Z) hemispheres. For the northern hemisphere the scale height is given by $H_{Z,\text{halo,north}} = 0.25 \text{ kpc}$, and for the southern hemisphere the scale height is given by $H_{Z,\text{halo,south}} = 0.4 \text{ kpc}$.

As the halo component of the Pshirkov et al. (2011) GMF lies 1.3 kpc above/below the plane, it has a negligible impact on Galactic CR diffusion and γ -ray production in the MW (Porter et al., 2017). Hence, it is not used within GALPROP. The halo component is included here for completeness.

2.7 GALPROP Setup

Within GALPROP the CR densities are normalised by a single condition – that all CR spectra (protons, electrons, helium, etc) at the Solar position reproduce their respective locally observed spectra within measurement systematics and uncertainties. The local

spectra are post propagation, with the CR fluxes depending on the chosen source distribution, the ISM gas, the ISRF, and the GMF. Therefore, the CR normalisation procedure in GALPROP must be performed post-propagation. Additionally, the propagation grid must be appropriately defined – the cells must be smaller than the shortest cooling distance of any CR (see [Section 2.2.4](#)). This section details how the CR normalisation is performed and how the propagation grid is defined.

2.7.1 Diffusion and Injection Parameter Optimisation

The critical condition for any CR diffusion simulation is that all CR spectra, from electrons to protons to iron, reproduce the measured CR spectra at the Solar location. Reproduction is ensured by treating the diffusion and injection parameters for each CR species as free parameters. Optimising these parameters needs to be performed for each CR source distribution, as altering where the CRs are injected impacts the local CR spectra.

To normalise and optimise the propagation parameters and source spectra, the procedure in [Porter et al. \(2017\)](#) and [Jóhannesson et al. \(2018\)](#) are followed using the CR data from [Jóhannesson et al. \(2019\)](#) (see their Table 1) for each source distribution. An initial optimisation of the propagation models is made by fitting to the observed CR spectra using data from the alpha magnetic spectrometer (AMS-02) ([Aguilar et al., 2014](#); [Aguilar et al., 2015a](#); [Aguilar et al., 2015b](#); [Aguilar et al., 2017](#); [Aguilar et al., 2018](#)) and *Voyager* ([Cummings et al., 2016](#)) in the GeV energy range where the diffuse CR sea is the dominant source of CRs. The fitting procedure is performed individually for the following CR spectra: Be, B, C, O, Mg, Ne, and Si. These seven spectra are then kept fixed. The next step in the optimisation procedure is to fit the spectra for electrons, protons, and He. The proton normalisation directly impacts the propagation and injection of the heavier elements, so the proton spectrum is optimised iteratively until all spectra converge to the local observations. As the optimisation method extrapolates outside the energy range of the data (MeV to TeV), a best-fit model is then determined via a χ^2 test on each of the spectra.

The optimisation procedure can be performed for any arbitrary source distribution and gas distribution and is included as a separate program in GALPROP version 57. Although the program automatically calculates all relevant parameters, it must be manually initiated by the user prior to any GALPROP propagation for each new source and ISM gas distribution. The optimisation program ensures that all of the source distributions used in GALPROP give the same local CR spectra, which reduces any inconsistencies between the distributions that may arise due to the limited data statistics and coverage over the modelled energy range.

Currently, the normalisation procedure only accounts for the source distribution and the gas distribution. This assumption is valid for protons and heavier elements which are not heavily impacted by the ISRF or GMF. However, it may not be valid for electrons in the >10 TeV regime which are significantly impacted by the GMF ([Marinos et al., 2023](#)).

In GALPROP, and commonly elsewhere in the literature, the CR injection spectra are given by power laws. In GALPROP the injection spectra can be defined separately for each individual CR species. However, it is typical to define the spectra separately

for electrons, protons, helium, with all CR species heavier than helium sharing the same spectrum with different normalisations. For this thesis, the proton and electron spectra are normalised at the Solar position to the CR normalisation constants given by J_p and J_e at the energies $E_{k,p} = 100 \text{ GeV}$ and $E_{k,e^-} = 34.5 \text{ GeV}$ respectively, with heavier elements normalised relative to the proton spectrum at 100 GeV nuc^{-1} . The injection spectra are given by:

$$\frac{d\mathcal{N}_{\text{CR}}}{dp} = J_{\text{CR}} \varrho_{\text{CR}}^{-\eta_{\text{CR}}} \quad (2.84)$$

where p is the momentum of the CR, \mathcal{N}_{CR} is the injected CR density, J_{CR} is the normalisation of the CR spectrum, ϱ_{CR} is the rigidity of the CR, and η_{CR} is the injection spectral index for the CR species. The spectral index in GALPROP can be broken into different regions, where the slope of the CR injection spectrum can be altered. The breaks used in this thesis are given by the rigidities $\varrho_{\text{CR},1}$ and $\varrho_{\text{CR},2}$, and the spectral indices are given by $\eta_{\text{CR}} = \eta_{\text{CR},0}$ for rigidities $\varrho_{\text{CR}} < \varrho_{\text{CR},1}$, $\eta_{\text{CR}} = \eta_{\text{CR},1}$ for rigidities $\varrho_{\text{CR},1} < \varrho_{\text{CR}} < \varrho_{\text{CR},2}$, and $\eta_{\text{CR}} = \eta_{\text{CR},2}$ for rigidities $\varrho_{\text{CR}} > \varrho_{\text{CR},2}$.

In GALPROP the injection spectra can have an arbitrary number of spectral breaks, and the transitions between each of breaks can be smoothed via the parameter \mathfrak{s} . Although this functionality is not used in this thesis, the full form for the CR injection spectrum for each CR species is then given by:

$$\frac{d\mathcal{N}}{dp} = J \left(\frac{\varrho}{\varrho_0} \right)^{-\eta_0} \prod_i \left(1 + \left(\frac{\varrho}{\varrho_i} \right)^{\left[\frac{\eta_i - \eta_{i+1}}{\mathfrak{s}_i} \right]} \right)^{\mathfrak{s}_i} \quad (2.85)$$

where ϱ_0 is the normalisation rigidity for the given CR species, i is the counting parameter for the spectral breaks, and ϱ_i is the rigidity of the i^{th} spectral break. The parameter \mathfrak{s}_i is the smoothing parameter for the i^{th} spectral break, and is negative for $|\eta_i| < |\eta_{i+1}|$ and positive for $|\eta_i| > |\eta_{i+1}|$. The CR subscripts have been dropped for simplicity; however, each parameter in Equation 2.85 can be controlled separately for each individual CR species.

The diffusion coefficient from Equation 2.13, is normalised to $D_{xx,0}$ at the rigidity $\varrho_0 = 4 \text{ GV}$, and has a spectral index given by δ . The diffusion coefficient spectral index depends on the chosen source model. As of version 57, GALPROP assumes an isotropic and homogeneous spatial diffusion coefficient, with an anisotropic diffusion tensor planned for a future release. The diffusion coefficient is sometimes linked to the magnetic field strength due to the CRs diffusing more slowly through stronger magnetic fields (e.g. see Gabici et al., 2007). Linking the magnetic field to the diffusion coefficient is important for regions with magnetic fields on the order of $10 \mu\text{G}$. Although the diffusion coefficient in GALPROP can be linked to the GMF strength (e.g. Ackermann et al., 2015), this functionality is not used in this thesis as the average GMF strength is on the order of $3 \mu\text{G}$. The CR spectral parameters and the diffusion parameters for all five source distributions used throughout this thesis are shown in Table 2.4. The source distributions themselves, and the equations that define them, are detailed in Section 2.3.

Table 2.4: The optimised GALPROP propagation parameters for each of the five source distributions.

Parameter	SA0	SA25	SA50	SA75	SA100
$D_{xx,0}$ [10^{28}]	4.36	4.39	4.55	4.67	4.66
δ	0.354	0.349	0.344	0.340	0.339
v_{Alfven}	17.8	18.2	18.1	19.8	19.1
J_p [10^{-9}]	4.096	4.404	4.113	4.329	4.394
J_{e^-} [10^{-10}]	3.925	4.444	3.994	4.428	4.502
$\eta_{e^-,0}$	1.616	1.390	1.488	1.455	1.521
$\eta_{e^-,1}$	2.843	2.756	2.766	2.763	2.753
$\eta_{e^-,2}$	2.493	2.460	2.470	2.447	2.422
$\varrho_{e^-,1}$	6.72	5.27	5.14	5.54	5.29
$\varrho_{e^-,2}$	52.4	81.6	67.7	70.7	79.7
$\eta_{p,0}$	1.958	1.928	1.990	1.965	2.009
$\eta_{p,1}$	2.450	2.464	2.466	2.494	2.481
$\eta_{p,2}$	2.391	2.411	2.355	2.374	2.414
$\varrho_{p,1}$	12.0	12.3	12.2	14.5	13.5
$\varrho_{p,2}$	202	157	266	108	125
$\eta_{\text{He},0}$	1.925	1.886	1.956	1.937	1.971
$\eta_{\text{He},1}$	2.417	2.421	2.432	2.467	2.443
$\eta_{\text{He},2}$	2.358	2.369	2.320	2.347	2.376
$\varrho_{\text{He},1}$	12.0	12.3	12.2	14.5	13.5
$\varrho_{\text{He},2}$	202	157	266	108	125
$\eta_{Z,0}$	1.328	1.519	1.426	1.630	1.624
$\eta_{Z,1}$	2.377	2.390	2.399	2.399	2.418
$\eta_{Z,2}$	2.377	2.390	2.399	2.399	2.418
$\varrho_{Z,1}$	3.16	4.21	3.44	4.61	4.50
$\varrho_{Z,2}$ [10^3]	5.00	5.00	5.00	5.00	5.00

- $\eta_{\text{CR},0}$ is the power-law index before the first break
- $\eta_{\text{CR},1}$ is the power-law index between the first and second breaks
- $\eta_{\text{CR},2}$ is the power-law index after the second break
- $\varrho_{\text{CR},1}$ [GV] is the rigidity of the first break
- $\varrho_{\text{CR},2}$ [GV] is the rigidity of the second break
- The subscript Z is used for all CR nuclei with atomic numbers $Z \geq 3$
- The diffusion coefficient ($D_{xx,0}$) is measured in $\text{cm}^2 \text{s}^{-1}$
- The Alfven velocity (v_{Alfven}) is measured in km s^{-1}
- The CR normalisation constants (J_p and J_{e^-}) are measured in $\text{MeV}^{-1} \text{cm}^{-2} \text{s}^{-1} \text{sr}^{-1}$

2.7.2 Timestep

The transport equation, given in [Equation 2.14](#), is solved for some timestep, Δt . Numerically solving the transport equation only provides information on processes that occur on timescale of a similar size to the chosen timestep. However, the CRs diffusing in the MW lose energy at different rates depending on their energy (as seen in [Figure 2.7](#)). To capture the diffusion of all particles at all energies, the timestep used in the time-independent solution¹⁰ of the transport equation varies during the simulation. The initial timestep, Δt_0 , should be on the order of the longest cooling time of any particle being simulated. The timestep is then decreased iteratively, with the k^{th} timestep being given by:

$$\Delta t_k = \ell^k \Delta t_0 \quad (2.86)$$

where ℓ is the timestep factor and must be less than one. The timestep is reduced iteratively until the final timestep (Δt_{final}) is reached, which should be as short as the shortest cooling time of any particle being simulated (see [Figure 2.7](#)). Solving the transport equation via this method allows changes across many orders of magnitude of time to be simulated accurately and efficiently. The transport equation is solved iteratively for each timestep M times, or until the solution is stable.

2.7.3 Propagation Grid

GALPROP creates a virtual MW that consists of cells, where this grid of cells contains the ISM densities and is what the CRs diffuse through. The propagation grid is defined in the coordinates (X, Y, Z), with three different grid functions available in GALPROP – a linear function, a tan function, and a step function. A description of the linear and tan grid functions is provided below, and an explanation on setting up the propagation grid within GALPROP is provided in [Section A.1](#).

For the CR propagation results to be valid, the cell size at the observer’s position must be small enough to accurately capture the CR densities. In order to capture the CR diffusion across the cell, the cell size must be smaller than the shortest cooling distance of any CR particle included in the simulation¹¹. As the cooling distances for protons and electrons have different energy dependencies (see [Section 2.2.4](#)), it will be the lowest-energy proton or the highest-energy electron that dictates the cell size. See [Figure 2.7](#) for calculations on the diffusion and cooling distances.

For the descriptions of the grid functions provided below, the following definition is used: $Q(\zeta)$ is the transformed coordinate at the ζ^{th} point, and can refer to either the X , Y , or Z axes. The parameters Q_{min} and Q_{max} are the minimum and maximum extents of the axis, and the relationship $Q(\zeta = 0) = Q_{\text{min}}$ and $Q(\zeta = N_{\text{cells}} - 1) = Q_{\text{max}}$ are used to define the bounds of the transformed axes. The linear and tan gridding functions, their first derivative (i.e. the sizes of the cells as a function of distance from the GC), and their

¹⁰The time-dependent timestep will be discussed later in [Section 6.2.3](#).

¹¹Depending on the chosen differential equation solver, the cells may need to be an order of magnitude smaller than the shortest cooling distance ([Porter et al., 2022, Appendix D](#)).

subtended angles from Earth, are shown in [Figure 2.13](#). The impact of the tan gridding function on the 2D cell sizes can be observed in [Figure A.2](#).

Linear Grid Function

The linear grid function is the standard approach. It gives all cells the same size defined by the step size (ΔQ). The linear grid function is given by:

$$Q_{\text{lin}}(\zeta) = \Delta Q \zeta + Q_{\text{min}} \quad (2.87)$$

where the physical size of the cells along the Q axis is given by the derivative, and has the functional form:

$$\begin{aligned} \frac{dQ_{\text{lin}}(\zeta)}{d\zeta} &= \Delta Q \\ &= \frac{Q_{\text{max}} - Q_{\text{min}}}{N_{\text{cells}} - 1} \end{aligned} \quad (2.88)$$

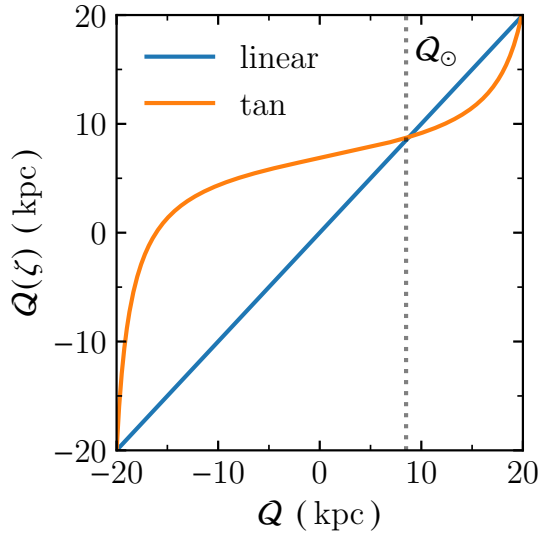
where the parameters Q_{min} , Q_{max} , and ΔQ are given by the user for each coordinate axis (i.e. X , Y , and Z), and N_{cells} is the number of cells along the axis. The distance from the Solar position to a cell can be defined as $Q_R = Q(\zeta) - Q_{\odot}$. Typically, the coordinate system used by GALPROP sets $X_{\odot} = 8.5$ kpc, $Y_{\odot} = 0$ kpc, and $Z_{\odot} = 0$ kpc.

The angle subtended by the cells as a function of their distance from the Solar position is given by:

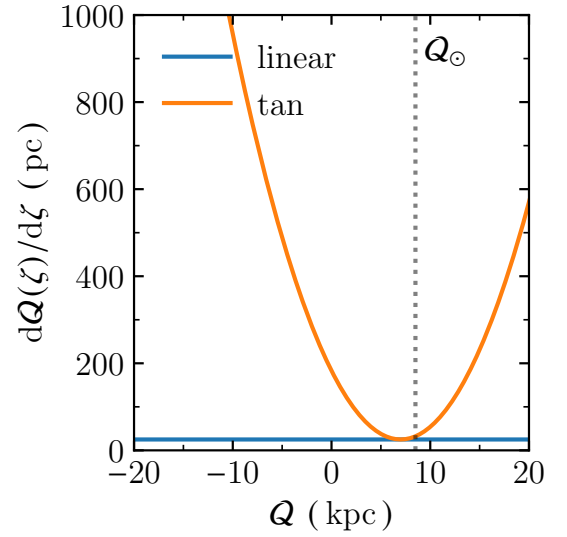
$$\begin{aligned} \theta_{\text{lin}} &= 2 \left| \arctan \left(\frac{dQ_{\text{lin}}(\zeta)/d\zeta}{2Q_R} \right) \right| \\ &= 2 \left| \arctan \left(\frac{\Delta Q}{2Q_R} \right) \right| \end{aligned} \quad (2.89)$$

where all variables have been defined previously. As the cell size is a constant, the angle subtended by the cell asymptotes to zero as the distance to said cell increases (as seen in [Figure 2.13](#)). Cells far from the observer's location have a minimal impact on the line-of-sight integral for the γ -ray intensities due to their small angular size. Additionally, as the emission follows the r -squared law, distant cells do not contribute significantly to the emission integrated over the line of sight. Hence, the linear grid does not efficiently utilise computational resources for regions far from the Solar location.

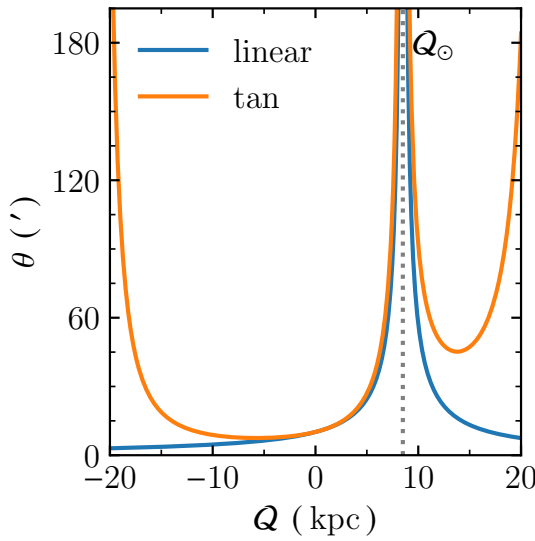
As the CR protons diffuse large (>200 pc) distances, the cells can be large ($\Delta Q \sim 100$ pc), saving on computation time while still giving reasonable results. However, for CR electrons the grid size needs to be on the order of the cooling distances, which can be less than 100 pc for >10 TeV electrons (see [Figure 2.7](#)).



(a) The gridding function for the linear and tan functions.



(b) The derivative of the gridding function, which is equivalent to the cell size.



(c) The subtended angle of the cell size in arcminutes.

Parameter	Linear	Tan
ΔQ [kpc]	0.025	0.025
Q_{\min} [kpc]	-20	-20
Q_{\max} [kpc]	20	20
Q_0 [kpc]	—	7
Q_{ref} [kpc]	—	26.5
λ	—	50
N_{cells}	1601	316

(d) The parameter values used for Figures 2.13a through 2.13c, with the resulting number of cells given by N_{cells} .

Figure 2.13: An example of the linear and tan grid functions that can be used in GALPROP. In all subfigures the Solar location is given by $Q_{\odot} = 8.5$ kpc and shown by the vertical dashed line. The parameter values used (d) are representative of a typical X axis in GALPROP. For an example where the variable cell size of the tan gridding function is visible on the two-dimensional grid see Figure A.2.

Tan Grid Function

An optimisation to the gridding functions can be made to save on computational resources without impacting the propagation of the CRs by increasing the size of the cells for larger distances from the observer. The increasing cell size is achieved by using a ‘tan’ grid function, which maintains an approximately constant subtended angle for large distances from the observer. The tan grid function is defined such that the solution to the partial differential equations remains stable, and is given by:

$$Q_{\text{tan}}(\zeta) = \frac{\Delta Q}{a} \tan [a(\zeta - \zeta_0)] + Q_0 \quad (2.90)$$

$$\begin{aligned} a &= \frac{\Delta Q}{Q_{\text{ref}} - Q_0} \tan \left[\arccos \left(\frac{1}{\sqrt{\lambda}} \right) \right] \\ &= \frac{\Delta Q}{Q_{\text{ref}} - Q_0} \sqrt{\lambda - 1} \end{aligned} \quad (2.91)$$

$$\zeta_0 = \frac{-1}{a} \arctan \left(\frac{a(Q_{\text{min}} - Q_0)}{\Delta Q} \right) \quad (2.92)$$

$$N_{\text{cells}} - 1 = \frac{1}{a} \left[\arctan \left(\frac{a(Q_{\text{max}} - Q_0)}{\Delta Q} \right) - \arctan \left(\frac{a(Q_{\text{min}} - Q_0)}{\Delta Q} \right) \right] \quad (2.93)$$

where the parameters Q_{min} , Q_{max} , Q_0 , Q_{ref} , and λ are set by the user. Q_0 is the ‘centre’ of the axis (where the grid has the highest resolution), Q_{ref} is the location where the size of the grid is equal to $\lambda\Delta Q$, λ is a parameter defining the rate of growth of the grid and must be greater than one, and N is the number of cells along the axis. Equation 2.91 arises from the condition that the size of the grid (i.e. first derivative) at the position Q_{ref} must equal $\lambda\Delta Q$. Equation 2.92 arises from the condition that $Q(\zeta = 0) = Q_{\text{min}}$, and Equation 2.93 gives the number of grid cells along the axis and arises from the condition that $Q(\zeta = N_{\text{cells}} - 1) = Q_{\text{max}}$. The size of the cells is given by the first derivative:

$$\frac{dQ_{\text{tan}}}{d\zeta} = \frac{\Delta Q}{\cos^2 [a(\zeta - \zeta_0)]} \quad (2.94)$$

where all variables have been defined previously. When $Q(\zeta) = Q_{\text{ref}}$, then the size of the grid is $dQ/d\zeta = \lambda\Delta Q$. In the transformed coordinates, this occurs at:

$$\zeta_{\text{ref}} = \frac{1}{a} \left[\arctan \left(\frac{a(Q_{\text{ref}} - Q_0)}{\Delta Q} \right) - \arctan \left(\frac{a(Q_{\text{min}} - Q_0)}{\Delta Q} \right) \right] \quad (2.95)$$

where all variables have been defined previously. For the case that the grid cell size is largest at the edges of the Galaxy (i.e. $Q_{\text{ref}} = Q_{\text{max}}$), Equation 2.95 is equal to the number of cells minus one (i.e. $N_{\text{cells}} - 1$; Equation 2.93). Just as for the linear grid, it is useful to find the angle subtended by a cell, which is given by:

$$\theta_{\text{tan}} = 2 \left| \arctan \left(\frac{dQ_{\text{tan}}/d\zeta}{2Q_R} \right) \right| \quad (2.96)$$

where all variables have been defined previously. For the majority of the MW the cells have a near-constant subtended angle. The tan grid function, the cell size, and the subtended angle are shown in [Figure 2.13](#). The impacts of using a tan grid on the size of the cells can be seen in [Figure A.2](#). There is a discontinuity at the Solar position as when Earth is located in a cell, that cell covers the entire 4π steradians of the sky. Towards the Galactic anticentre the cells are nearby and larger. Hence, the subtended angles of the cells towards the Galactic anticentre are large ($>1^\circ$). However, the impact on the calculations is minor as the CR density (and the γ -ray flux) is low in the outer Galaxy. Near Q_{\min} and Q_{\max} the angle subtended by the cells increases rapidly – as these locations are far from Q_\odot , the γ rays produced in these cells has little impact on the γ -ray flux measured by the observer due to the r -squared law. The tan grid function has only a negligible impact on the diffuse γ -ray calculations.

Chapter 3

TeV Gamma-Ray Observations with H.E.S.S.

CRs with energies below 10 PeV do not travel in straight lines. Hence, VHE CRs cannot be traced back to their original sites of acceleration. Insights into the underlying acceleration physics must then be found through observations of the γ rays emitted as the CRs interact with the ISM. In this thesis the TeV γ -ray data from the high energy stereoscopic system (H.E.S.S.) is utilised.

When a γ ray (or CR) strikes Earth's upper atmosphere a shower of high-energy particles is created [Auger et al. \(1939\)](#). The particles in the shower will be travelling faster than the local speed of light (i.e. the speed of light through air), creating a cone of Cherenkov light ([Cherenkov, 1937](#)) in the upper atmosphere. Imaging atmospheric Cherenkov telescopes (IACTs) observe γ rays indirectly by measuring this Cherenkov light.

H.E.S.S. is an IACT array consisting of five telescopes located in the Khomas Region of Namibia at an altitude of 1800 metres. Four of the telescopes have diameters of 12 m and are arranged in a 120×120 m square with the vertices aligned north/south and east/west. The fifth IACT has a diameter of 28 m and is located in the centre of the square. As the telescopes are separated by 85–170 m they can observe the same atmospheric showers from different perspectives (up to five, one for each telescope) allowing for a more accurate reconstruction of the original location of the γ ray on the sky. H.E.S.S. is well suited to observing γ rays in the 30 GeV to 10 TeV energy range and is able to achieve a sensitivity of one percent of the flux of the Crab nebula for an observation time of 50 hours ([Aharonian et al., 2006e](#)). H.E.S.S. has performed one of the most comprehensive surveys of the TeV γ -ray emission along the Galactic plane, named the H.E.S.S. Galactic plane survey (HGPS). This survey is the main observational dataset used throughout this thesis.

This chapter begins with a brief overview of how IACTs operate and the background physics behind their observations. The specifics of the H.E.S.S. telescope array will then be detailed – from its performance, to how it collects observational data. A discussion on the TeV diffuse γ -ray emission is also included, including the challenges faced in extracting the diffuse γ -ray emission from the HGPS.

3.1 Gamma-Ray Observations

Visible light photons are only mildly attenuated as they travel through the atmosphere. Conversely, the atmosphere completely blocks γ -ray photons from reaching the ground from space. As γ rays strike the atmosphere they create a shower of energetic, charged

particles that rain down to the ground called an extensive air shower (EAS). This effect can be exploited by IACTs to indirectly observe γ rays.

3.1.1 Extensive Air Showers (EASs)

Extensive air showers are created by both CRs and γ rays – when they strike the Earth’s atmosphere their energy is converted into one or more secondary particles. These secondary particles are energetic enough to create tertiary particles, and so on – repeating until no energy remains in the system. These particle cascades were first discovered by [Auger et al. \(1939\)](#) and can be comprised of tens of thousands of energetic sub-atomic particles. EASs typically cover approximately 1 km^2 by the time they reach the ground.

There are two types of EASs. Hadronic showers are initiated by CR nuclei, and electromagnetic showers are initiated by electrons and γ rays. Hadronic showers also contain electromagnetic sub-showers ([Grieder, 2010](#)). For γ -ray observations, the interest is in selecting only the showers initiated by γ rays; however, both types are explained below as the hadronic component is an important background that must be accounted for in observations.

EASs are computed in generations (g), with the zeroth generation ($g = 0$) being the initial particle, the first generation ($g = 1$) being populated with the particles created from the initial interaction, the second generation ($g = 2$) being all particles created by the first generation, and so on. A diagram of both leptonic and hadronic showers and how they evolve at each generation is shown in [Figure 3.1](#).

Electromagnetic Showers

Electromagnetic showers are initiated by either a γ ray or an electron striking the upper atmosphere. A cascade of γ rays, electrons, and positrons travel towards the ground, creating additional particles and photons in the process. The Heitler shower model ([Heitler, 1954](#)) assumes that the shower consists entirely of γ rays and e^\pm created via pair production and bremsstrahlung interactions. The equations describing the EM shower interactions are given by:

$$\gamma + N \rightarrow e^+ + e^- + N \quad (3.1)$$

$$e^\pm + N \rightarrow e^\pm + N + \gamma \quad (3.2)$$

where γ represents a γ ray, N represents a nucleus in Earth’s atmosphere, and e^\pm represent electrons/positrons. [Equation 3.1](#) describes the γ -ray interactions (pair production) and [Equation 3.2](#) describes the electron or positron interactions (bremsstrahlung) as they travel through the atmosphere. Although the ratio between the bremsstrahlung and pair-production interaction lengths is approximately 7/9, the Heitler model assumes that the interaction lengths are equal. The Heitler assumption simplifies the situation, with the energy of the shower halving at each generation and each interaction process growing at the same rate. Therefore, the energy deposited by the shower as a function of the generation is given by:

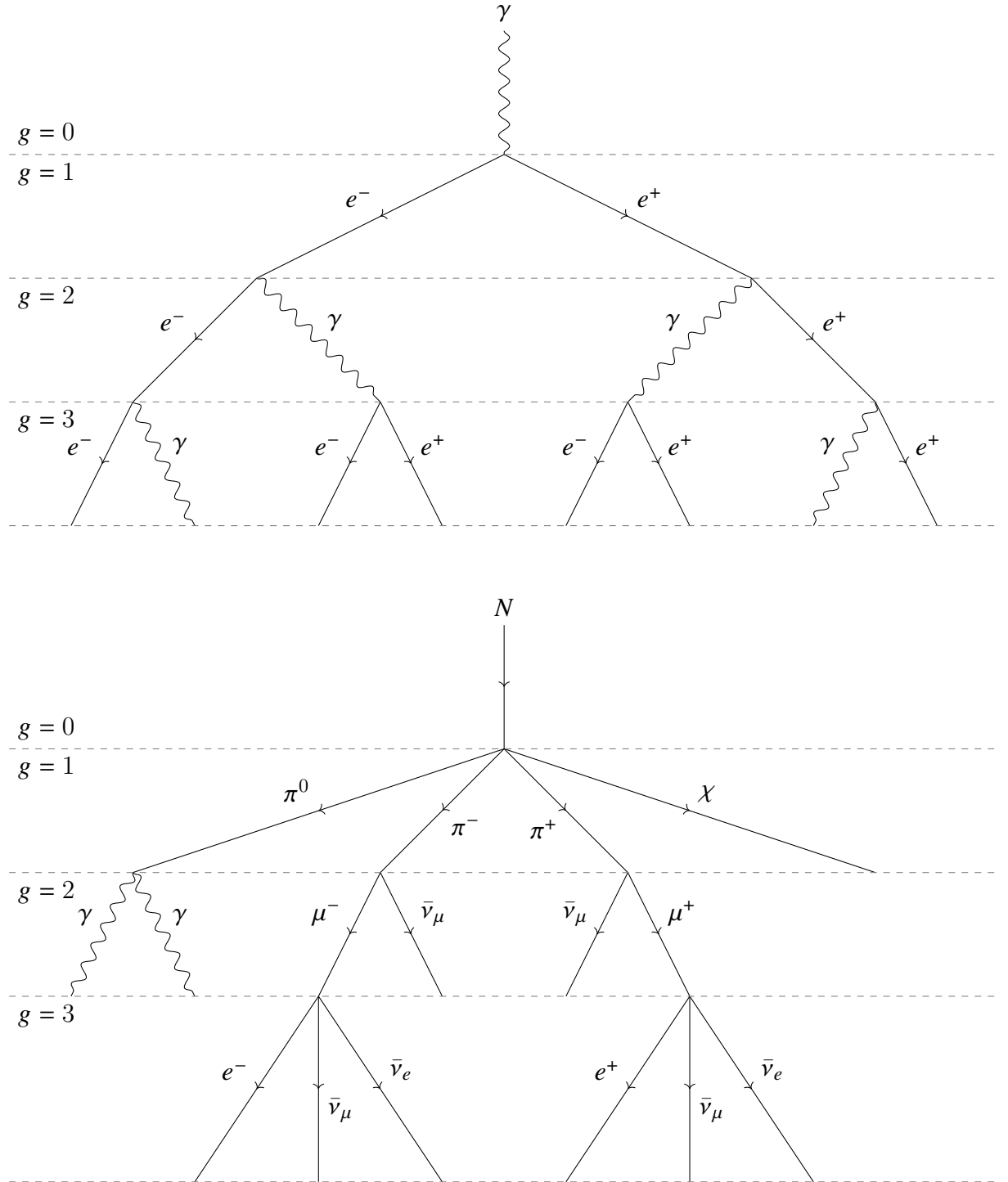


Figure 3.1: Diagram of the Heitler model (Heitler, 1954) of a lepton-initiated shower (top) and a hadron-initiated shower (bottom). The interaction/radiation lengths are not to scale, and multiple products may be created at each intersection on the diagram. The particles represented by χ may be protons, neutrons, and other atomic nuclei. See text for descriptions.

$$E_{\text{lep}}(g) = \left(\frac{1}{2}\right)^g E_0 \quad (3.3)$$

where $E_{\text{lep}}(g)$ is the energy of the leptonic shower at the g^{th} shower generation and E_0 is the initial energy of the lepton. The shower continues propagating downwards until ionisation losses with the atmosphere begin to dominate over the bremsstrahlung energy losses (~ 86 MeV; [Engel et al., 2011](#)).

Hadronic Showers

Hadronic showers are initiated by CR hadrons, i.e. protons or other heavier nuclei, striking the upper atmosphere. Hadronic showers in the TeV regime are considered a background component for γ -ray observations (as will be discussed later in [Section 3.2.3](#)). A CR collision may create charged pions, neutral pions, or split the nuclei into smaller atoms. The charged pions continue to undergo further interactions with the atmospheric particles, while the neutral pions decay too quickly (8.5×10^{-17} s; [Zyla et al., 2020](#)) to interact with other nuclei. The charged pions may decay into charged muons and muon antineutrinos, and the charged muons decay into electrons, positrons, muon antineutrinos, and electron antineutrinos. The decays of the neutral pions and charged muons create additional electromagnetic sub-showers within the hadronic shower. Additionally, charged pions with energies $E_{\pi^\pm} \gtrsim 30$ GeV are more likely to interact with the atoms and molecules in the atmosphere before decaying into charged muons ([Engel et al., 2011](#)). The equations describing the hadronic shower interactions are given by:

$$N + N \rightarrow \chi + n_0\pi^0 + n_1\pi^- + n_2\pi^+ \quad (3.4)$$

$$\pi^0 \rightarrow \gamma + \gamma \quad (3.5)$$

$$\pi^\pm \rightarrow \mu^\pm + \bar{\nu}_\mu \quad (3.6)$$

$$\mu^\pm \rightarrow e^\pm + \bar{\nu}_\mu + \bar{\nu}_e \quad (3.7)$$

where π^\pm represents charged pions, π^0 represents a neutral pion, μ^\pm represents charged muons, $\bar{\nu}_\mu$ represents a muon antineutrino, $\bar{\nu}_e$ represents an electron antineutrino, and χ represents any additional particles created to conserve baryon number and electric charge (e.g. protons, neutrons, smaller nucleons, etc.) and create additional reaction chains within the shower. The values n_0 , n_1 , and n_2 are the numbers of neutral, negative, and positive pions, respectively.

Hadronic air showers quickly become a complex web of hadronic interactions, namely nucleon-nucleon (N - N), pion-nucleon (π - N), nucleon-nucleus (N - A), nucleus-nucleus (A - A), and pion-nucleus (π^\pm - A) interactions ([Grieder, 2010](#)). These interactions occur concurrently with the electromagnetic sub-showers from the decay of the neutral pions. At each generation, two thirds of the energy goes into the hadronic component of the shower and one third of the energy goes into the electromagnetic sub-showers. For the progenitor with initial energy E_0 , the energy deposited into the hadronic and electromagnetic components is given by:

$$E_{\text{had}}(g) = \left(\frac{2}{3}\right)^g E_0 \quad (3.8)$$

$$E_{\text{EM}}(g) = \left[1 - \left(\frac{2}{3}\right)^g\right] E_0 \quad (3.9)$$

where $E_{\text{had}}(g)$ is the energy of the hadronic shower component at the g^{th} shower generation, and $E_{\text{EM}}(g)$ is the energy of the electromagnetic shower component at the g^{th} shower generation.

Due to the variety of interactions, some of which create particles with masses greater than that of an electron/positron, the hadronic showers appear more irregular than leptonic showers. Furthermore, the hadronic showers often have larger lateral extents due to the higher-mass particles being able to travel further from their interaction sites. Hadronic showers are often discriminated apart from leptonic showers through the use of Monte Carlo simulations of showers (e.g. CORSIKA; Heck et al., 1998).

3.1.2 Imaging Atmospheric Cherenkov Telescopes

Unlike traditional telescopes that contend against atmospheric effects, IACTs focus on the light generated within the atmosphere. IACTs observe the Cherenkov light (Cherenkov, 1937) emitted by charged particles travelling through the atmosphere. This Cherenkov light is coherent and is emitted along the axis of the shower in a cone shape, where the shower axis is aligned with the progenitor's direction of travel. When observing the shower directly along its axis, the Cherenkov cone appears as a near-perfect circle. In the much more likely case that the shower is observed off axis, the Cherenkov cone appears as an ellipse. The shower ellipse is parameterised with the ‘Hillas parameters’ (Hillas, 1985), with the major axis of the ellipse pointing towards the shower axis. Two or more IACTs are then used to geometrically reconstruct the starting location of the shower in the sky. Viewing the shower with a larger number of IACTs provides a more accurate reconstruction of the arrival direction¹. A simplified diagram showing an EAS viewed from two telescopes, along with the geometric reconstruction of the γ ray arrival direction, is provided in Figure 3.2.

IACTs observe EASs from both CRs and γ -ray photons. Unlike photons, which travel in straight lines and can be traced back to their origin, CRs are deflected by magnetic fields such as the Solar magnetic field and the Galactic magnetic field (as discussed in Section 2.1). As the CRs below 100 PeV do not point to their origin, IACTs carefully select events to exclude as many CR showers as possible, with one of these methods discussed later in Section 3.2.3.

As IACTs observe EASs within the atmosphere, their ‘effective’ area is equal to the area of the Cherenkov light pool on the ground². The effective area of an IACT varies with the energy of the particle or photon that initiated the shower and various other observational parameters (such as the zenith angle, etc.). For H.E.S.S. the effective area

¹See Bernlöhner et al. (2013) for a summary of IACT observational techniques.

²In contrast, the area of a traditional optical telescope is equal to the area of the lens or primary mirror.

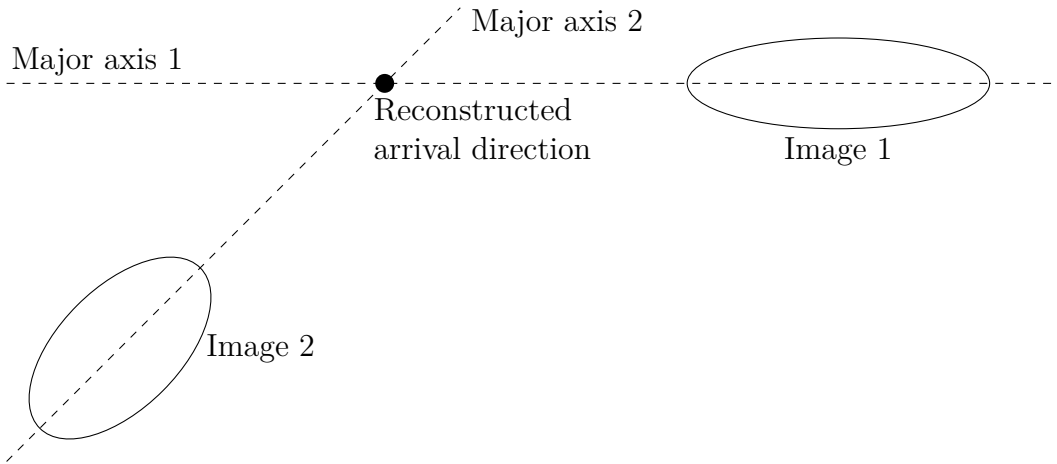


Figure 3.2: A simplified diagram of a single EAS event observed by two telescopes. Each ellipse represents the image seen by an IACT, and the dashed lines represent the major axes of the ellipses. The intersection of the major axes of all the ellipses is the arrival direction of the initial γ ray.

can be on the order of 0.2 km^2 ($2 \times 10^5 \text{ m}^2$; Aharonian et al., 2006e), and the future next-generation γ -ray observatory, the Cherenkov telescope array (CTA), will reach an effective area on the order of 1 km^2 (Bernlöhner et al., 2013)³. These massive effective areas are integral for γ -ray astronomy, as for even the brightest sources the γ -ray flux is approximately $10 \text{ photons km}^{-2} \text{ s}^{-1}$ in the TeV regime (Crab flux; Abdalla et al., 2018e).

Examples of IACTs include H.E.S.S. in the Khomas Region (Namibia), the major atmospheric gamma imaging Cherenkov telescopes (MAGIC; Baixeras, 2003) on the Spanish island La Palma, and the very energetic radiation imaging telescope array system (VERITAS; Weekes et al., 2002) in Arizona (United States of America). CTA sites are currently being constructed in both La Palma (Spain) and Paranal (Chile).

3.2 The H.E.S.S. Galactic Plane Survey (HGPS)

The H.E.S.S. Galactic plane survey (HGPS; Aharonian et al., 2005a; Aharonian et al., 2006f; Abdalla et al., 2018e) was a decade-long observation program, with data being collected from 2004 to 2013. The HGPS is constructed from many 28-minute-long observations, hereafter known as runs, with a total observation time of 2673 hours. The observations span the Galactic latitudes $|\ell| \leq 3^\circ$ and Galactic longitudes $65^\circ \leq \ell \leq 250^\circ$, and has a resolution of $4.8'$. The HGPS is the highest resolution and the most sensitive TeV γ -ray survey of the Galactic plane to date. The HGPS has a variable sensitivity as low as 0.4% of the Crab nebula (4 mCrab)⁴ for the Galactic centre (GC), worsening to 20 mCrab at the edges of the survey where there was a lower exposure time.

³For further comparison, the detection areas of optical telescopes are generally on the order of 500 cm^2 . The largest optical telescopes currently in operation have detection areas on the order of 100 m^2 (e.g. the large binocular telescope; Hill, 2010).

⁴Units of %Crab are commonly used throughout VHE γ -ray astronomy, with the value used in this thesis given by $J_{\text{Crab}}(E \geq 1 \text{ TeV}) = 2.26 \times 10^{-11} \text{ cm}^{-2} \text{ s}^{-1}$ (Aharonian et al., 2006e) unless otherwise stated.

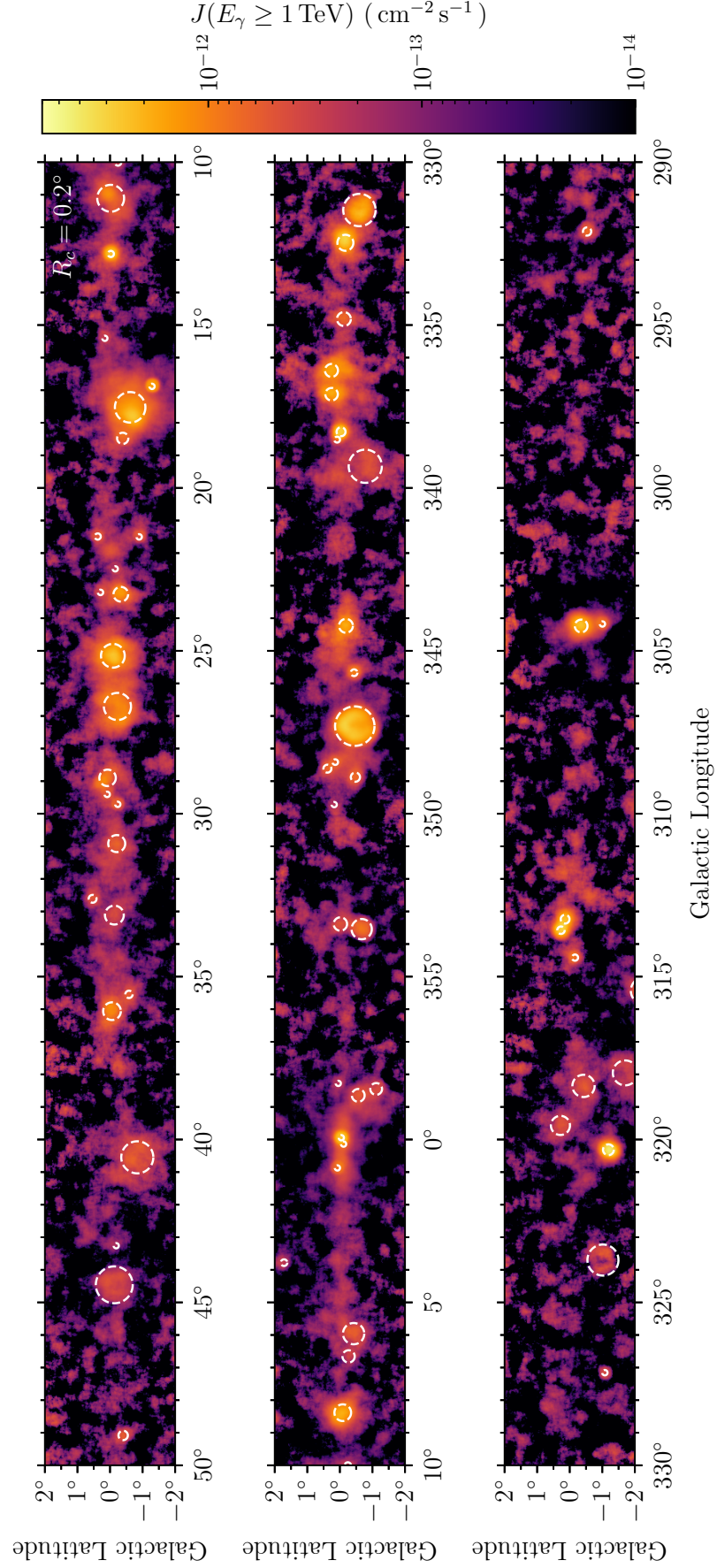


Figure 3.3: HGPS flux map integrated for energies $E_\gamma \geq 1$ TeV for Galactic longitudes $\ell = 290^\circ$ to $\ell = 50^\circ$ and Galactic latitudes $|\ell| \leq 2^\circ$ for the $R_c = 0.2^\circ$ map (described in [Section 3.2.2](#)). The catalogued γ -ray sources are shown by the white dashed circles.

The HGPS γ -ray flux map⁵ for Galactic longitudes $\ell = 290^\circ$ to $\ell = 50^\circ$ and Galactic latitudes $|\ell| \leq 2^\circ$ is shown in Figure 3.3, with catalogued γ -ray sources shown by the white circles.

3.2.1 Gamma-Ray Flux

IACTs, and other types of VHE instruments, record EASs from both CRs and γ rays as ‘events’. The event list contains all properties of the observed air showers, such as the reconstructed arrival position, the reconstructed energy of the initial particle or photon, etc.. The number of observed EASs are then converted to a γ -ray flux. For the HGPS two regions are defined, known as the *on* and *off* regions. These two regions will be discussed later in Sections 3.2.2 and 3.2.3, respectively. The signal (or ‘excess’) number of γ -ray events, N_γ , is given by:

$$N_\gamma = N_{\text{on}} - \alpha N_{\text{off}} \quad (3.10)$$

where N_{on} and N_{off} are the number of events in the *on* region and *off* region, respectively, and α is the ratio of the exposure in each region. From the number of excess counts, the γ -ray flux in the HGPS was calculated via the equation:

$$F = \frac{N_\gamma}{N_{\text{exp}}} \int_{E_1}^{E_2} J_{\text{ref}}(E_\gamma) dE_\gamma \quad (3.11)$$

where F is the integral flux between the γ -ray energies E_1 and E_2 , E_γ is the γ -ray energy, $J_{\text{ref}}(E_\gamma)$ is the reference/assumed functional form of the γ -ray flux (see below), and N_{exp} is the expected/predicted number of γ -ray counts. The expected number of γ -ray counts is given by:

$$N_{\text{exp}} = \sum_R t_R \int_{E_{\text{min}}}^{\infty} J_{\text{ref}}(E_r) A_{\text{eff}}(E_r, \mathbf{q}_R) dE_r \quad (3.12)$$

where E_r is the reconstructed energy of the γ ray, the sum is performed over all observation runs (R) for a given source, t_R is the live time of the given run, and E_{min} is the minimum threshold energy for an observation (i.e. the lowest γ -ray energy that could be observed in the run). \mathbf{q}_R represents all observational parameters for the given run, including values such the zenith angle, which telescopes were included, and which cuts were applied to the data. $A_{\text{eff}}(E_r, \mathbf{q}_R)$ is the effective area of H.E.S.S. for a given observation run as a function of the reconstructed energy and the observational parameters and is obtained through Monte Carlo simulations.

⁵The HGPS (Abdalla et al., 2018e) γ -ray source catalogue, γ -ray flux, sensitivity, significance, γ -ray flux uncertainty, and γ -ray flux upper-limit data maps are available at <https://www.mpi-hd.mpg.de/hfm/HESS/hgps/>.

The reference differential γ -ray source flux (J_{ref}) is the assumed functional form of the γ -ray flux, and is used in calculating both the expected number of γ -ray counts (N_{exp}) and the integrated γ -ray flux. The reference flux is taken as a power law and is given by:

$$J_{\text{ref}}(E_\gamma) = J_\gamma \left(\frac{E_\gamma}{E_0} \right)^{-\eta} \quad (3.13)$$

where J_γ is a reference normalisation differential flux, E_0 is the γ -ray energy at which the reference flux is normalised, and η is a spectral index. The integrated γ -ray flux given in Equation 3.11 does not depend on J_γ (which can be found by substituting in Equations 3.12 and 3.13); therefore, the normalisation constant can be chosen arbitrarily. The HGPS integrated γ -ray flux maps use a normalisation energy given by $E_0 = 1$ TeV, and the γ -ray spectral index $\eta = 2.3$ is taken as the average for the γ -ray sources in the Galactic plane. The systematic uncertainty of η is ± 0.2 – Abdalla et al. (2018e) found that when varying η in this range the integrated flux varied by less than 5%.

3.2.2 Integration Beam

The number of excess counts (Equation 3.10) requires integrating the observed EAS events within an *on* region. For the HGPS the *on* region is defined a circle with a constant radius, R_c , which is referred to as either the containment radius or the integration radius. The *on* region radius must be larger than the point spread function (PSF) of the telescope (i.e. larger than 0.08° for H.E.S.S.). The number of counts in a given region is the integration of all counts within said region, divided by the solid angle of the region. Hence, the number of EAS counts in the *on* region, N_{on} , is given by:

$$N_{\text{on}} = \frac{1}{2\pi(1 - \cos(R_c))} \int_{R_c} N_{\text{events}} d\Omega \quad (3.14)$$

where Ω is the solid angle of the *on* region with radius R_c and N_{events} is the total number of events. Utilising an *on* region that is larger than the PSF increases the significance of the observation, especially on scales of the same size as the integration radius. However, it reduces the ability to distinguish structure on scales smaller than R_c . The HGPS flux maps uses integration radii of either $R_c = 0.1^\circ$ or $R_c = 0.2^\circ$, and so is well suited to resolve γ -ray structures that are approximately 0.1° or 0.2° in radius. A comparison between the $R_c = 0.1^\circ$ and the $R_c = 0.2^\circ$ γ -ray flux maps can be seen in Figure 3.4.

3.2.3 CR Background Estimation

CR air showers, which typically outnumber γ -ray air showers by a factor of a thousand, are considered as background events for γ -ray observatories. The CR EASs are suppressed by applying machine-learning algorithms to remove CR-like events (see Ohm et al., 2009, with the HGPS specifically using the analysis cuts in their Table 2a).

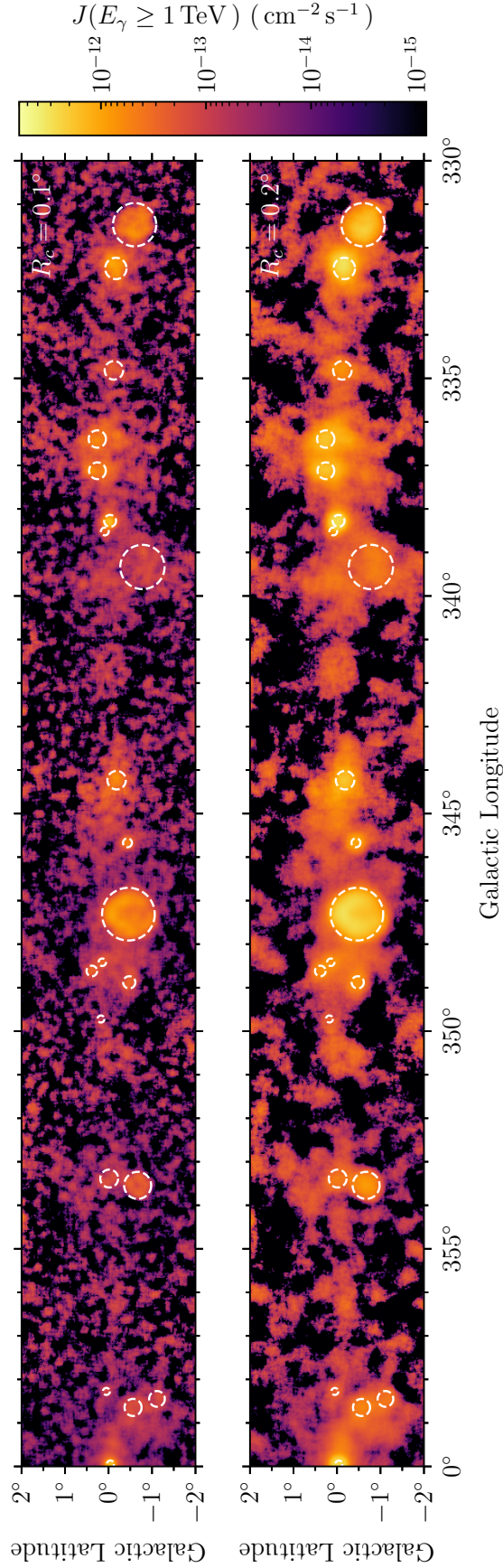


Figure 3.4: HGPS flux map for Galactic longitudes $\ell = 330^\circ$ to $\ell = 0^\circ$ and Galactic latitudes $|\ell| \leq 2^\circ$ for the $R_c = 0.1^\circ$ map (top) and the $R_c = 0.2^\circ$ map (bottom). The catalogued γ -ray sources are shown by the white dashed circles, and both maps are shown with an identical colour scale.

Some contamination due to the CR EASs will remain after the initial cuts are applied. An estimate of the contamination due to CR air showers in the *on* region is calculated by defining an *off* region. Ideally, the *off* region includes only CR EASs and not γ -ray showers. If this condition is satisfied, then the number of counts given in Equation 3.10 is due purely to γ -ray EASs. If γ -ray emission is included in the *off* region, then the CR background in the *off* region will be over-estimated.

H.E.S.S. employs multiple background estimation techniques, such as the ‘standard’ ring method or the ‘reflected’ ring method (Berge et al., 2007). These background methods can introduce their own systematic uncertainties (Aharonian et al., 2006; Berge et al., 2007), and are chosen based on the situation to reduce the systematics. However, neither of these two methods are suitable for the HGPS due to the large amount of statistically significant γ -ray emission in the Galactic plane.

To prevent statistically-significant γ -ray emission from being included in any background estimates, Abdalla et al. (2018e) defined ‘exclusion regions’ where no background estimate would be taken. The exclusion regions are defined from the statistical significance of an observation, S , where the HGPS uses the Li and Ma equation for the statistical significance (Li and Ma, 1983) given by:

$$S = \sqrt{2N_{\text{on}} \ln \left[\left(\frac{1 + \epsilon}{\epsilon} \right) \left(\frac{N_{\text{on}}}{N_{\text{on}} + N_{\text{off}}} \right) \right] + 2N_{\text{off}} \ln \left[(1 + \epsilon) \left(\frac{N_{\text{off}}}{N_{\text{on}} + N_{\text{off}}} \right) \right]} \quad (3.15)$$

where ϵ is the ratio of time spent taking *on*-region observations (t_{on}) to the time spent taking *off*-region observations (t_{off}), i.e. $\epsilon = t_{\text{on}}/t_{\text{off}}$ (Li and Ma, 1983). Equation 3.15 is utilised in the HGPS to create a significance map, where the *off* regions were defined as a ring with an inner radius of 0.7° and a thickness of 0.44° . To avoid large systematic effects near the edges of the FoV, the only events included in the *on* and *off* regions are those reconstructed within a 2° radius of the centre of the field of view (FoV, which has a full radius of 5°). The 2° -radius FoV is referred to as the reduced FoV. This process identifies regions with a significance of 5σ , which are then expanded by an additional 0.3° beyond the 5σ contour.

When using the above ring-background method to define the exclusion regions, it was found that statistically significant emission was still included in the *off* regions (Abdalla et al., 2018e). Hence, the significance map is recreated iteratively. In each iteration the *off* regions cannot include emission in the previously calculated exclusion regions. Each iteration defines a new set of exclusion regions and is repeated until all of the exclusion regions are stable.

For the final flux map the HGPS uses an ‘adaptive’ ring background. Much like for the construction of the exclusion regions, only events reconstructed within the central 2° of the FoV are included. For a given pixel position, a ring is drawn with a constant thickness of 0.44° and a minimum inner radius of 0.7° . If a large portion of the ring overlaps with an exclusion region then the inner radius is increased such that the acceptance integrated within the ring is greater than four times the acceptance at the given pixel position⁶. The

⁶The acceptance map is the expected number of observed CR events across all observations. The acceptance map is normalised such that outside the exclusion regions the expected number of counts is equal to the observed counts.

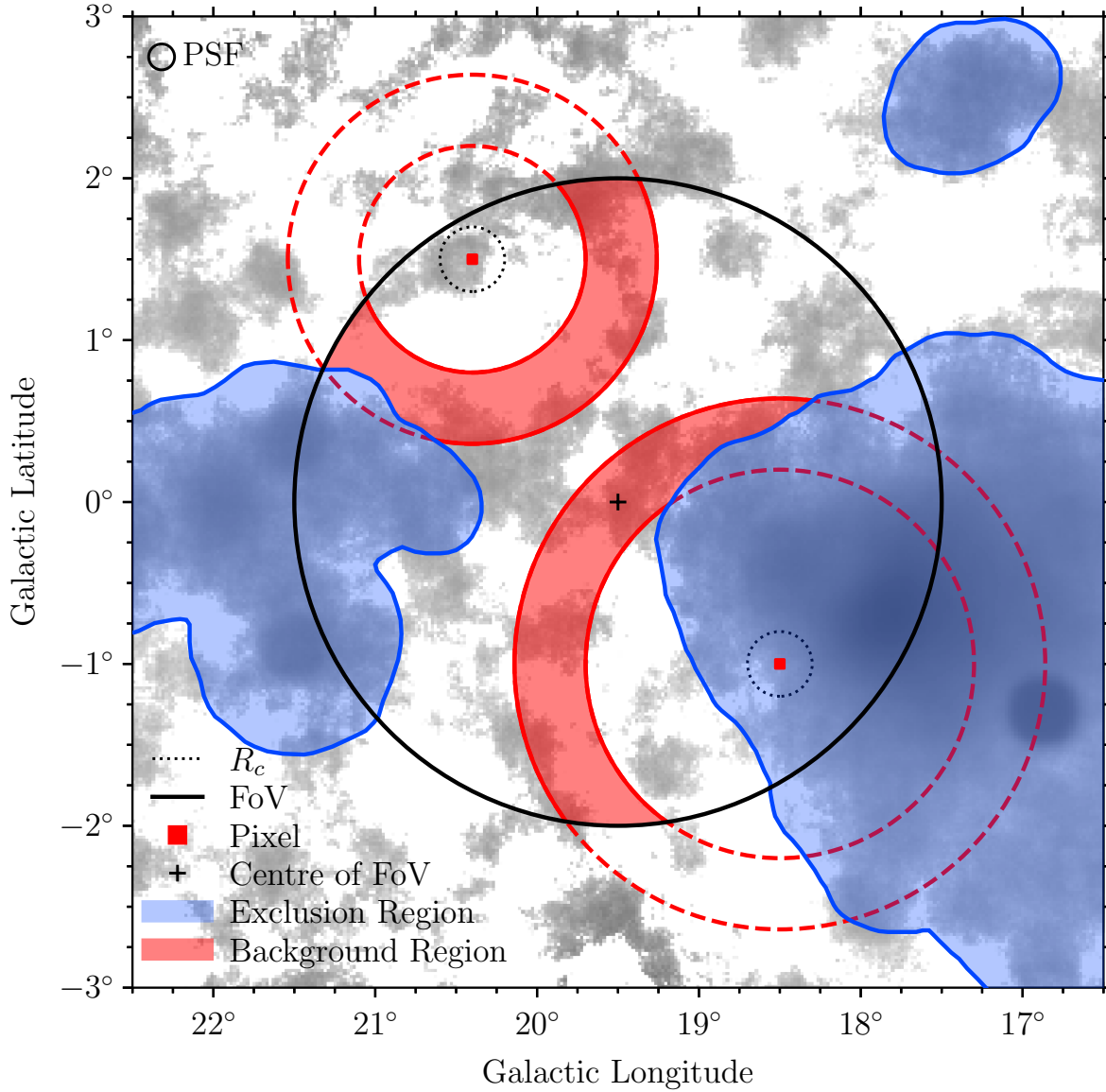


Figure 3.5: A demonstration of the adaptive ring background subtraction method, shown for an arbitrary location in the HGPS ([Abdalla et al., 2018e](#)). The HGPS γ -ray flux is shown in reverse greyscale, with the PSF of H.E.S.S. in the top-left corner. The reduced FoV has a radius of 2° and is shown by the black circle, with the black cross representing the centre of the FoV. Two pixels were chosen arbitrarily and are shown by the red squares. The γ -ray flux for each pixel is integrated from the *on* regions shown by the dotted black circles. The background γ -ray flux is integrated from the *off* regions shown by the red rings. The background estimate is not taken from the exclusion regions (shown in blue). The *off*-region ring can be adaptively enlarged from an inner radius of 0.44° to a maximum inner radius of 1.7° to limit the statistical uncertainties, as demonstrated by the pixel highlighted in the lower-right. The process for calculating the exclusion regions and the radii of the rings is detailed in the text in [Section 3.2.3](#).

outer ring radius is limited to a maximum of 1.7° to limit systematics associated with the outer region of the FoV. The number of EAS counts in the *off* region is given by:

$$N_{\text{off}} = \frac{1}{\Omega_{\text{off}}} \int_{\text{off}} N_{\text{events}} d\Omega \quad (3.16)$$

where Ω_{off} is the solid angle of the *off* region (i.e. background region). From Equation 3.10, the number of counts for a given pixel is then given by:

$$\begin{aligned} N_\gamma &= N_{\text{on}} - a N_{\text{off}} \\ &= \left(\frac{1}{2\pi(1 - \cos(R_c))} \int_{R_c} N_{\text{events}} d\Omega \right) - \left(\frac{a}{\Omega_{\text{off}}} \int_{\text{off}} N_{\text{events}} d\Omega \right) \end{aligned} \quad (3.17)$$

where all parameters have been defined previously, and the number of counts measured in the *on* region is given by Equation 3.14. A demonstration of this method being applied to two arbitrarily-chosen pixels can be seen in Figure 3.5.

3.2.4 Flux Sensitivity

The flux sensitivity is defined as the minimum flux (F_{min}) needed for a source fully contained within the *on* region to be detected above the CR background at the 5σ level. The flux sensitivity of the HGPS is calculated by taking Equation 3.11 and substituting N_γ with \hat{N}_γ , where \hat{N}_γ is defined as the number of γ -ray events required for a 5σ detection above the background. The value of \hat{N}_γ is determined by numerically solving Equation 3.15 for N_{on} , i.e. \hat{N}_γ is found such that the condition $S(N_{\text{on}} = \hat{N}_\gamma) = 5$ is satisfied for the number of observed background counts (N_{off}).

The sensitivity curves for H.E.S.S., and many other γ -ray facilities, are shown in Figure 3.6, where any flux above the sensitivity curves is considered to be a confident detection. The sensitivity curves are shown for point sources that are completely contained within the PSF of the observatory. The sensitivity of H.E.S.S. and other IACTs can be simplified to a relation that depends on the radius of the source, σ_{source} , and is given by:

$$F_{\text{min}}(\sigma_{\text{source}}) \propto \sqrt{\frac{\sigma_{\text{source}}^2 + \sigma_{\text{PSF}}^2}{\sigma_{\text{PSF}}^2}} \quad (3.18)$$

where $\sigma_{\text{PSF}} = 0.08^\circ$ is the PSF of H.E.S.S.. For sources much smaller than the PSF (i.e. for point sources) the flux sensitivity is constant. For extended sources (i.e. for sources larger than the PSF) the flux sensitivity worsens linearly with source size (Hinton and Hofmann, 2009). Additionally, the flux sensitivity scales with the square-root of the livetime of an observation via the relationship given by:

$$F_{\text{min}}(t_{\text{on}}) \propto \frac{1}{\sqrt{t_{\text{on}}}} \quad (3.19)$$

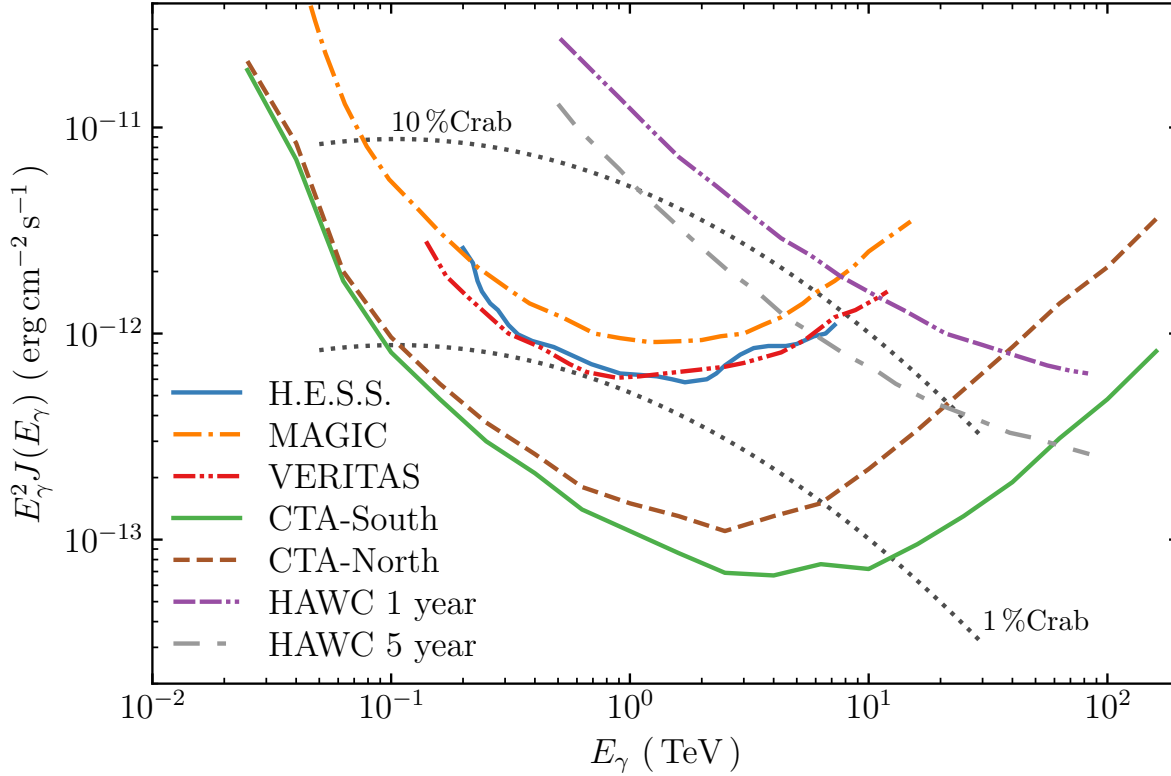


Figure 3.6: The 5σ sensitivity for various γ -ray facilities. Sensitivities are shown for a 50-hour observation, unless stated otherwise. The sensitivity curves are from the following: H.E.S.S. (Holler et al., 2015), MAGIC (Aleksić et al., 2016), VERITAS (Horan et al., 2007), CTA-South/CTA-North (Acharya et al., 2018), and HAWC (Abeysekara et al., 2017b). The Crab flux (dotted black line) has been calculated as a log-parabola following Aleksić et al. (2015).

3.2.5 H.E.S.S. Gamma-Ray Source Horizon in the MW

The sensitivity can be utilised to calculate the astronomical horizon for a survey (r_{\max}). From the flux-luminosity relationship, the maximum distance is given by:

$$F_{\min} = \frac{L}{4\pi r_{\max}^2} \quad (3.20)$$

$$\therefore r_{\max} = \sqrt{\frac{L}{4\pi F_{\min}}} \quad (3.21)$$

where L is some γ -ray source luminosity. Taking the Crab nebula and using the flux defined earlier ($J_{\text{Crab}}(E \geq 1 \text{ TeV}) = 2.26 \times 10^{-11} \text{ cm}^{-2} \text{ s}^{-1}$; Aharonian et al., 2006e) at a distance of 2 kpc (Kaplan et al., 2008), the luminosity of the Crab nebula is approximately $10^{34} \text{ erg s}^{-1}$. Figure 3.7 shows the γ -ray point-source source horizon for γ -ray sources with $L \approx 100\%$ Crab, which varies between 5–14 kpc depending on the exposure along a given direction. For γ -ray sources with $L \approx 10\%$ Crab, the γ -ray point-source horizon decreases to between 1–4 kpc. As the γ -ray source horizon does not extend to the far side of the MW, estimates of the number of undetected γ -ray sources in the HGPS range from hundreds to thousands (e.g. see Actis et al., 2011; Acharya et al., 2018).

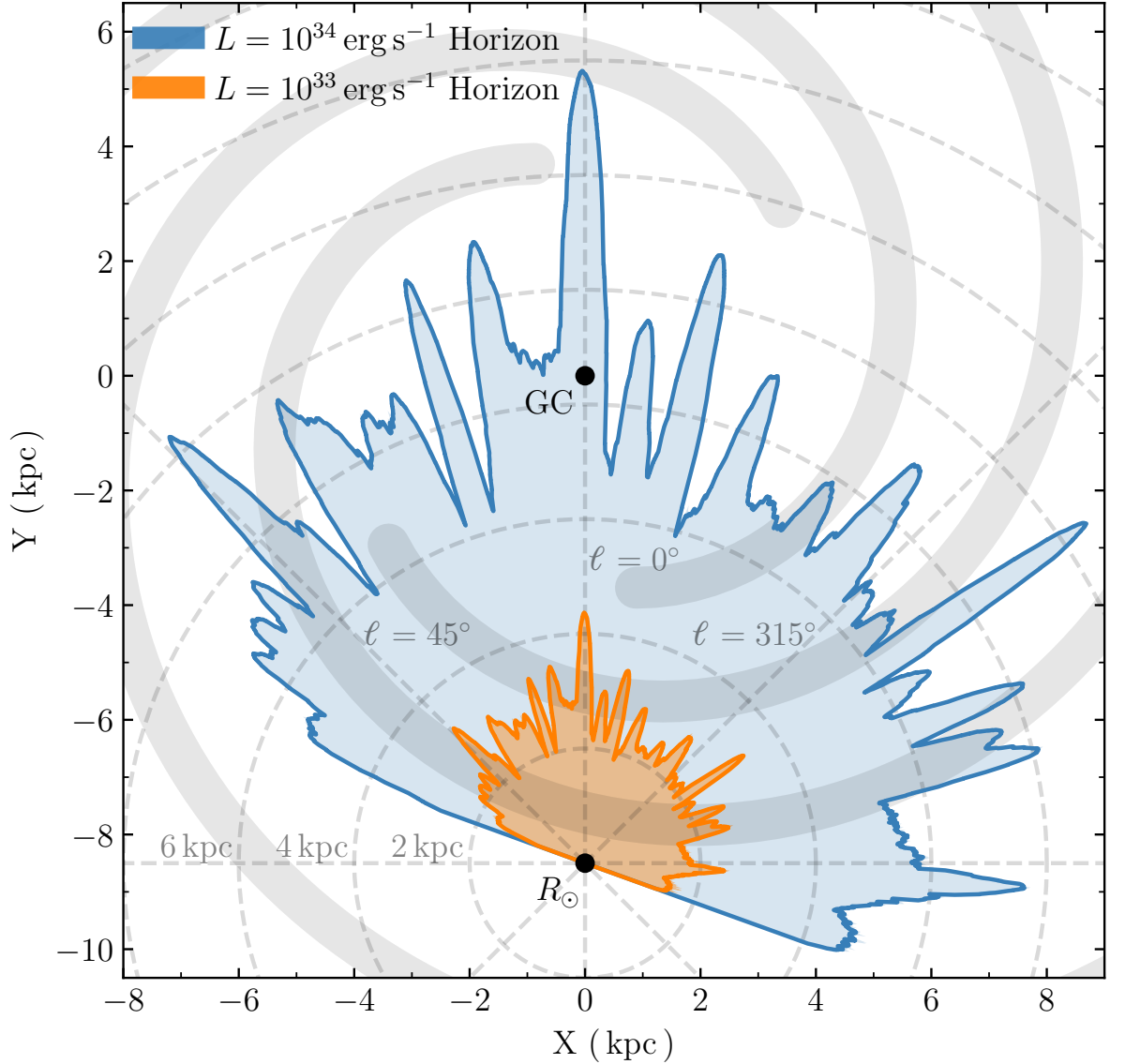


Figure 3.7: A top-down view of the MW showing the 5σ point-source detection horizon for the HGPS for γ -ray luminosities $10^{34} \text{ erg s}^{-1}$ ($\sim 100\%$ Crab; blue) and $10^{33} \text{ erg s}^{-1}$ ($\sim 10\%$ Crab; orange). The GC is located at the origin, with the Solar location shown by $R_{\odot} = 8.5 \text{ kpc}$ from the GC (Kerr and Lynden-Bell, 1986). Galactic longitude and the radial distance from Earth are shown by the dashed grey lines. The solid grey lines represent the Robitaille et al. (2012) spiral arms, which are discussed in more depth in Section 2.5.2.

The horizon calculation above does not account for the angular size of the source. As shown in Equation 3.18, the sensitivity of H.E.S.S. worsens linearly with source size for extended γ -ray sources. As 61 of the 78 catalogued γ -ray sources are extended, the depth of the HGPS is over-estimated in Figure 3.7 for most known γ -ray sources.

3.3 HGPS Source Characterisation and Classification

CRs interact with the ISM to create γ rays, with the various processes detailed in Section 2.2. The CR flux is highest nearby to their sites of acceleration. Hence, the regions in close proximity to the CR accelerators will emit additional γ rays. The regions of enhanced γ -ray emission are known as γ -ray sources.

The HGPS catalogued a total of 78 γ -ray sources along the Galactic plane. However, many of the catalogued γ -ray sources are not located nearby to any known CR accelerator. This section will detail how the catalogued γ -ray sources in the HGPS are characterised and classified.

3.3.1 HGPS Source Characterisation

The spatial profiles of most γ -ray sources in the HGPS can be modelled as one or more Gaussians. For a source at some Galactic coordinates (ℓ_0, b_0) , the surface brightness of the source is modelled as:

$$S_{\text{source}}(r, F_{\text{source}}, \sigma_{\text{ang}}) = F_{\text{source}} \frac{1}{2\pi\sigma_{\text{ang}}^2} \exp\left(-\frac{r^2}{2\sigma_{\text{ang}}^2}\right) \quad (3.22)$$

$$r = \sqrt{(\ell - \ell_0)^2 + (b - b_0)^2} \quad (3.23)$$

where S_{source} represents the surface brightness of the source, F_{source} is the totally spatially integrated flux of the source, and r is the distance from the centre of the source. The angular size of the source region, σ_{ang} , is calculated from the source radius (σ_{source}) and the PSF of H.E.S.S. ($\sigma_{\text{PSF}} = 0.08^\circ$) and is given by:

$$\sigma_{\text{ang}} = \sqrt{\sigma_{\text{source}}^2 + \sigma_{\text{PSF}}^2} \quad (3.24)$$

where all parameters have been defined previously. For all point-like sources the radius is given by $\sigma_{\text{source}} = 0^\circ$; hence, the angular size of the source region is given by $\sigma_{\text{ang}} = \sigma_{\text{PSF}}$. The modelling parameters for all 78 sources in the HGPS, as calculated by Abdalla et al. (2018e), can be found in Table B.1.

Ten sources found in the HGPS are morphologically complex. Despite being characterised with a position, radius, and surface brightness, these ten sources cannot easily be

Classification	Number of Sources
Binary	3
Stellar Cluster	4
SNR	8
Composite	8
Not Associated	11
PWN	12
Not Firmly Identified	32
Total	78

Table 3.1: A summary of the source classifications of the catalogued γ -ray sources observed in the HGPS (Abdalla et al., 2018e). For details on the different source classifications, see text.

modelled as a collection of Gaussians. The ten morphologically-complex γ -ray sources are listed as a ‘shell’ spatial model in Table B.1, or are a component of the GC region, and will be discussed in more depth in Section 4.3.1.

3.3.2 HGPS Galactic TeV Source Classifications

The 78 TeV γ -ray sources observed in the HGPS were originally classified into six categories, which are defined by the class of object responsible for the acceleration of the CRs. The original categories were titled: ‘supernova remnant (SNR)’, ‘pulsar wind nebula (PWN)’, ‘composite’, ‘binary’, ‘not firmly identified’, and ‘not associated’. Four of the TeV γ -ray sources in the HGPS were later reclassified into a seventh category titled ‘stellar cluster’. While H.E.S.S. has recently observed the recurrent nova RS Ophiuchi (Aharonian et al., 2022a), no TeV recurrent nova sources are present in the HGPS data. Additionally, while H.E.S.S. is able to observe extra-Galactic γ -ray sources, no such sources are found in the HGPS data. The seven γ -ray source categories represented in the HGPS are briefly discussed below, with the number of sources in each classification summarised in Table 3.1.

Supernova Remnants

When a star undergoes a supernova explosion, a large amount of energy ($\sim 10^{53}$ erg) is released into the surrounding medium. Of the total energy, 99% is transferred into the creation of neutrinos. The remaining 10^{51} erg goes into the kinetic energy of the expanding shock front (Hillas, 2005). The large shock is called a supernova remnant. CRs are accelerated within the SNR shock via a process known as diffusive shock acceleration (sometimes called first-order Fermi acceleration; Fermi, 1949; Aharonian et al., 2004). Due to the large amount of γ rays being produced within the SNR shock, and due the CRs escaping and creating γ rays in the nearby surrounding ISM, SNRs can have complex morphologies that are difficult to model. The eight SNR γ -ray sources identified in the HGPS are given in Table 3.2.

Source Name	Accelerator	Classification Reference
HESS J0852–463	Vela Junior	Aharonian et al. (2005e)
HESS J1442–624	RCW 86	Abramowski et al. (2018)
HESS J1534–571	G323.7001.0	Abdalla et al. (2018a)
HESS J1713–397	RX J1713.7–3946	Aharonian et al. (2004)
HESS J1718–374	G349.7+0.2	Abramowski et al. (2015c)
HESS J1731–347	G353.6–0.7	Abramowski et al. (2011a)
HESS J1801–233	W 28	Aharonian et al. (2008b)
HESS J1911+090	W 49B	Abdalla et al. (2018f)

Table 3.2: The eight SNR γ -ray sources in the HGPS, along with the name of the SNR that is accelerating the CRs and the reference that classified the source.

Source Name	Accelerator	Classification Reference
HESS J0835–455	Vela X	Aharonian et al. (2006d)
HESS J1303–631	G304.10–0.24	Abramowski et al. (2012)
HESS J1356–645	G309.92–2.51	Abramowski et al. (2011b)
HESS J1418–609	G313.32+0.13	Aharonian et al. (2006b)
HESS J1420–607	G313.54+0.23	Aharonian et al. (2006b)
HESS J1514–591	MSH 15–52	Aharonian et al. (2005b)
HESS J1554–550	G327.15–1.04	Abdalla et al. (2018e)
HESS J1747–281	G0.87+0.08	Aharonian et al. (2005d)
HESS J1818–154	G15.4+0.1	Abramowski et al. (2014b)
HESS J1825–137	G18.00–0.69	Aharonian et al. (2006c)
HESS J1837–069	G25.24–0.19	Marandon et al. (2008)
HESS J1849–000	G32.64+0.53	Abdalla et al. (2018e)

Table 3.3: The twelve PWN γ -ray sources in the HGPS, along with the name of the pulsar that is accelerating the CRs and the reference that classified the source.

Pulsar Wind Nebulae

Pulsars are created when a large star undergoes a supernova explosion. The most likely outcome from the creation of the pulsar is that the rotational axis and magnetic axis will be misaligned. The misaligned, rotating magnetic field creates an electric field via Faraday’s law ([Faraday, 1832](#)), which in turn creates a drag force that slows the rotation of the pulsar. Therefore, the pulsar’s rotational energy is transferred into the electromagnetic fields, which then accelerate CRs. This process creates an energetic wind of CRs ([Gaensler and Slane, 2006](#)), especially electrons, which interact with the ISM to create a nebula that emits γ rays (see [Section 2.2](#)). The 12 PWN γ -ray sources identified in the HGPS are given in [Table 3.3](#).

Source Name	Accelerator	Classification Reference(s)
HESS J1119–614	G292.2–0.5	Abdalla et al. (2018e)
HESS J1640–465	G338.3–0.0	Abramowski et al. (2014c) , Gotthelf et al. (2014)
HESS J1714–385	CTB 37A	Aharonian et al. (2008a)
HESS J1813–178	G12.8–0.0	Funk et al. (2007) , Gotthelf and Halpern (2009)
HESS J1833–105	G21.5–0.9	Abdalla et al. (2018e)
HESS J1834–087	W 41	Abramowski et al. (2015d)
HESS J1846–029	G29.7–0.3	Abdalla et al. (2018e)
HESS J1930+188	G54.1+0.3	Acciari et al. (2010) , Abdalla et al. (2018e)

Table 3.4: The eight composite γ -ray sources in the HGPS, along with the name of the composite object that is accelerating the CRs and the reference(s) that classified the source.

Source Name	Accelerator	Classification Reference
HESS J1018–589 A	1FGL J1018.6–5856	Abramowski et al. (2015a)
HESS J1302–638	PSR B1259–63	Aharonian et al. (2005c)
HESS J1826–148	LS 5039	Aharonian et al. (2006a)

Table 3.5: The three binary γ -ray sources in the HGPS, along with the name of the object accelerating the CRs and the reference that classified the source.

Composite Sources

When a pulsar is created during a supernova it will be given some ‘kick’ velocity. Depending on the magnitude of the kick velocity, the pulsar and surrounding PWN will remain inside the SNR shell for approximately 40 kyr ([Gaensler and Slane, 2006](#)). After the pulsar escapes the SNR the two accelerators can be easily differentiated. However, while the pulsar is within the SNR it can be difficult to distinguish which object is the dominant CR accelerator. Sources where the pulsar are within the SNR shell are classified as composite γ -ray sources. The eight composite γ -ray sources identified in the HGPS are given in [Table 3.4](#).

Binaries

There are two types of binary γ -ray sources: accretion powered and rotation powered ([Mirabel, 2006](#)). For an accretion-powered binary γ -ray source a stellar-mass black hole or neutron star orbits close enough to accrete matter from the companion star, forming a relativistic jet. Photons are boosted into the TeV energy range via IC upscattering with the CRs in the jet (e.g. LS 5039; [Paredes et al., 2000](#)). For a rotation-powered binary γ -ray source the wind from a rapidly spinning pulsar interacts with the wind of the companion star. The two opposing winds create a shock that can accelerate CRs into the TeV regime. Additionally, the VHE CRs upscatter photons via IC interactions (e.g. PSR B1259–63; [Dubus, 2006](#)). The three compact binary γ -ray sources identified in the HGPS are given in [Table 3.5](#).

Source Name	Accelerator	Classification Reference
HESS J1023–575	Westerlund 2	Mestre et al. (2021)
HESS J1646–458	Westerlund 1	Aharonian et al. (2022b)
HESS J1747–248	Terzan 5	Abramowski et al. (2011c)
HESS J1848–018	W 43	Abdalla et al. (2018e)

Table 3.6: The four γ -ray sources in the HGPS that were later reclassified as stellar clusters, along with the name of the cluster accelerating the CRs and the reference that classified the source.

Stellar Clusters

There are two types of stellar clusters: open clusters and globular clusters. Both types of stellar clusters are groupings of tens to hundreds of massive stars. The colliding stellar winds between the massive stars within the cluster creates many shock fronts which can accelerate CRs into the TeV regime via Fermi acceleration. Stellar clusters have only become a confirmed accelerator of TeV CRs in recent years, after the original HGPS data was released. The four γ -ray sources in the HGPS that were later reclassified as stellar clusters are given in [Table 3.6](#).

Not Firmly Identified

The H.E.S.S. sources that are not firmly identified have one or more nearby CR accelerators from the categories discussed above. However, it is not known which accelerator is responsible for the observed γ -ray emission. The sources that are not firmly identified can be placed into three sub-categories:

- There is a CR source observed nearby; however, the γ -ray emission can be explained by any of the categories discussed above, i.e. the class of the CR counterpart is not known. Examples include: HESS J1018.6–589 B ([Abramowski et al., 2015b](#)), HESS J1427–608 ([Guo et al., 2017](#)), and both HESS J1843–033 and HESS J1844–030 ([Cao et al., 2021b](#)).
- The CR accelerator class responsible for the γ -ray emission is known; however, the CR counterpart is only detected with a low significance. An example includes HESS J1848–018 ([Abdalla et al., 2018e](#)).
- Multiple CR accelerators are observed in close proximity to the γ -ray source. However, the γ -ray emission can be explained by any of the possible counterparts. For example, regions around HESS J1825–137 ([Collins et al., 2021](#)) exhibit spectral characteristics indicative of both an SNR and a PWN contributing to the CR acceleration around the source. Other examples sources include HESS J1804–216 ([Feijen et al., 2020](#)) and HESS J1841–055 ([Acciari et al., 2020](#)).

There are a total of 32 sources that are not firmly identified in the HGPS, all of which are included in [Table B.1](#) along with the parameters to model their spatial profiles.

Source Name	Longitude (°)	Latitude (°)
HESS J1457–593	318.35	–0.42
HESS J1503–582	319.57	0.29
HESS J1626–490	334.82	–0.12
HESS J1702–420	344.23	–0.19
HESS J1708–410	345.67	–0.44
HESS J1729–345	353.39	–0.02
HESS J1741–302	358.28	0.05
HESS J1745–303	358.64	–0.56
HESS J1828–099	21.49	0.38
HESS J1832–085	23.21	0.29
HESS J1858+020	35.54	–0.58

Table 3.7: All eleven γ -ray sources in the HGPS where it is not known whether or not they are a component of the diffuse TeV γ -ray emission. These sources are referred to as γ -ray sources with no known possible association. Longitude and latitude are listed in Galactic coordinates.

Sources with No Association

The H.E.S.S. sources with no association do not have a known CR counterpart, i.e. the CR source responsible for the γ -ray emission is unknown. There are two possible types of unassociated γ -ray sources. First, the γ -ray emission may be due to a dense molecular cloud being impacted by diffuse CRs (e.g. HESS J1457–593; [Abdalla et al., 2018c](#)) and is therefore an enhanced region of the diffuse γ -ray emission. Second, the γ -ray emission may be due to an undiscovered CR counterpart. The undetected accelerator could be a faint SNR or PWN in the nearby area (e.g. HESS J1741–302; [Abdalla et al., 2018c](#)) or an ancient PWN (e.g. HESS J1708–410; [Kaufmann and Tibolla, 2018](#)). Hence, it is impossible to determine if the unassociated γ -ray sources are part of the diffuse TeV emission with current observations. The sources with no association, and their relationship to estimates of the diffuse emission, will be discussed in more depth in [Section 4.3.1](#). All 11 γ -ray sources with no association are given alongside their Galactic coordinates in [Table 3.7](#).

3.4 The HGPS Large-Scale Gamma-Ray Emission

The HGPS observations show two components to the γ -ray emission along the Galactic plane: the 78 discrete γ -ray sources discussed above and a large-scale component. However, the large-scale emission was not detected to the 5σ level due to the worsening sensitivity for larger source sizes (discussed in [Section 3.2.4](#)). Hence, no conclusion can be made on the origin of the large-scale TeV emission – be it from a diffuse ‘sea’ of CRs or a population of unresolved γ -ray sources ([Abramowski et al., 2014a](#)). As the large-scale emission was not detected to the 5σ level, no further analysis was conducted during the HGPS.



Figure 3.8: A diagram of the sliding window method used by [Abdalla et al. \(2018e\)](#). The window is defined to be 20° wide and uses the Galactic latitude bounds $|\ell| \leq 3^\circ$. After the analysis is performed within the window it slides 2.5° in Galactic longitude, and the process is repeated.

If the large-scale structure is not properly accounted for it will contaminate the all γ -ray source analyses (such as morphological and spectral analyses) along the Galactic plane. To prevent this γ -ray flux contamination [Abdalla et al. \(2018e\)](#) created an ad-hoc large-scale model. First, an analysis mask based on the exclusion regions (see [Section 3.2.3](#)) is defined to ensure that significant γ -ray emission is not included in the large-scale emission model. A sliding window is then defined to be 20° wide in Galactic longitude with Galactic latitude bounds of $-3^\circ \leq \ell \leq +3^\circ$. Within the window the emission is characterised as a Gaussian. The window then slides 2.5° in Galactic longitude and the process is repeated. A diagram of the sliding window is shown in [Figure 3.8](#). The sliding window procedure is repeated for the entire plane and is interpolated to the longitudinal resolution of the HGPS (0.02°). The Gaussian within the window is constructed with the form:

$$F_{\text{win}}(\ell) = F_{\text{win,peak}} \exp \left(-\frac{(\ell - \mu_{\text{win}})^2}{2\sigma_{\text{win}}^2} \right) \quad (3.25)$$

where F_{win} is the flux of the large-scale emission in the window as a function of the Galactic latitude (ℓ), $F_{\text{win,peak}}$ is the peak flux within the window (not including the flux within the masked regions), μ_{win} is the latitudinal location of the peak flux in the window, and σ_{win} is the width of the Gaussian in the window. All variables ($F_{\text{win,peak}}$, μ_{win} , and σ_{win}) are calculated for each window using a maximum-likelihood function. The sliding-window method results in a 2D Gaussian as a function of both Galactic longitude and Galactic latitude. The estimate of the large-scale γ -ray emission obtained via this model is subtracted from the HGPS flux maps before the γ -ray sources are characterised⁷.

3.4.1 The HGPS Diffuse Gamma-Ray Emission

Although the sliding-window Gaussian provides a model of the large-scale emission, it does not distinguish between the unresolved sources or the truly diffuse components. Separating the unresolved source and diffuse components is challenging with the HGPS for three reasons: the integration beam size ([Section 3.2.2](#)), the adaptive ring background method ([Section 3.2.3](#)), and the limited γ -ray source horizon ([Section 3.2.5](#)). As the diffuse emission is not detected to the 5σ level, the H.E.S.S. collaboration does not consider the

⁷Note that the model of the large-scale emission is not subtracted from the public maps and is only applied when characterising the γ -ray sources.

2D Gaussian found via the sliding-window method as a formal estimate of the diffuse emission.

As discussed in [Section 3.2.2](#), the HGPS analysis is well suited to observing γ -ray emissions on the scale of the integration radius, R_c , where the provided public flux maps use $R_c = 0.1^\circ$ and $R_c = 0.2^\circ$. However, the diffuse γ -ray emission is expected to vary on scales greater than the maximum integration radius provided. The analysis by [Abramowski et al. \(2014a\)](#) found that the large-scale γ -ray emission for Galactic longitudes $-75^\circ < \ell < 60^\circ$ is approximately a Gaussian profile across Galactic latitude. The large-scale Gaussian has a standard deviation of approximately 0.4° in latitude. The analysis by [Abdalla et al. \(2018e\)](#) further shows that the standard deviation of the latitudinal profile varies from 0.1° – 0.5° depending on the Galactic longitude, with an average Gaussian width of approximately 0.4° in the GC region. Utilising a larger integration radius would increase the significance of the observed large-scale structure. As the containment radius is used in the construction of the flux maps, it is not possible to increase R_c without the original HGPS event lists.

The adaptive ring background method is used in the HGPS to subtract the CR background from the γ -ray observations (see [Section 3.2.3](#)). This background method assumes that there is no γ -ray emission in the *off* region. Some γ -ray emission is prevented from being included in the CR background estimate due to the use of exclusion regions placed around areas of significant γ -ray emission. However, the chosen exclusion regions do not consider the large-scale Galactic γ -ray emission as significant emission, and do not take into account the low-significance unresolved source emission. Depending on the specific location of the pixel and the morphology of the nearby exclusion regions, the adaptive ring background can (and often does) include the large-scale γ -ray emission as part of the CR background. As the adaptive ring method over-estimates the CR background, the HGPS flux can only be considered as a lower limit on the true large-scale γ -ray emission. The chosen background subtraction method has been shown to significantly alter the HGPS large-scale γ -ray analyses. The HGPS was compared to the HAWC GPS by [Abdalla et al. \(2021\)](#), subjecting the raw HGPS data to the same integration radius (0.4°) and background method that HAWC uses (the FoV background technique; [Berge et al., 2007](#); [Abdalla et al., 2021](#)). It was found that the HGPS flux was systematically increased by a median value of $1.9 \times 10^{-13} \text{ cm}^{-2} \text{ s}^{-1}$, or approximately 15%, across the Galactic plane⁸.

Although the HGPS has an unprecedented sensitivity for TeV γ rays, it does not probe deep enough to reach the other side of the MW (discussed in [Section 3.2.5](#) and demonstrated in [Figure 3.7](#)). An estimate provided by [Actis et al. \(2011\)](#) shows that there are hundreds (if not thousands) of γ -ray sources in the MW that H.E.S.S. is not sensitive enough to detect. Although unresolved, these γ -ray sources potentially contribute between 13% and 60% of the large-scale γ -ray flux ([Steppa and Egberts 2020](#) and [Cataldo et al. 2020](#), respectively). Detecting the unresolved γ -ray sources requires more sensitive observations, which requires a larger, more sensitive γ -ray facility.

⁸The flux maps created by [Abdalla et al. \(2021\)](#) are not publicly available. The estimate of the systematic difference between the adaptive ring background and the FoV background methods cannot be directly compared to the large-scale γ -ray estimates elsewhere in this thesis.

Chapter 4

Comparing GALPROP to the HGPS

Comparing the γ -ray emission predicted by GALPROP to the γ -ray emission observed by H.E.S.S. will aid in determining the contributions of the leptonic and hadronic components to the diffuse emission. Comparisons will also assist in constraining the Galactic structures such as the CR source distribution and the GMF.

Constructing a comparison between the models and observations is not trivial as the results from GALPROP and the HGPS differ in their construction. The GALPROP emission is given as a differential flux in units of $\text{MeV}^{-1} \text{cm}^{-2} \text{s}^{-1} \text{sr}^{-1}$, while the HGPS emission is given as a flux integrated above 1 TeV in units of $\text{cm}^{-2} \text{s}^{-1}$. Furthermore, GALPROP calculates the γ -ray flux by performing a line-of-sight integral for each pixel and emission type ([Section 2.2.3](#)), while the HGPS is built from an event list across many observation runs. Additionally, GALPROP is constructed such that the predicted γ -ray emission is truly diffuse. Conversely, the HGPS emission has contributions from unresolved γ -ray sources and a further 78 discrete γ -ray sources. The source components in the HGPS must be accounted for as they do not represent the diffuse emission.

Comparing the GALPROP predictions to the HGPS observations requires an analysis procedure that accurately represents both datasets simultaneously. Following [Abdalla et al. \(2018e\)](#) the analysis was chosen to be constructed from a sliding window. However, the sliding window used in this thesis to compare GALPROP to the HGPS must be altered to ensure fair and consistent analyses across both the predictions and observations. This chapter will detail the sliding window analysis method, and the specific parameter choices, that were made to ensure a fair comparison. Additionally, the sensitivity of the sliding-window analysis to changes in the window parameters will be quantified. This chapter will also detail the transformations applied to ensure compatibility between the GALPROP and HGPS flux maps. Comparisons between the GALPROP predictions and the HGPS observations are presented in [Chapter 5](#).

4.1 Analysing the Large-Scale Emission

The sliding-window analysis utilised by [Abdalla et al. \(2018e\)](#) is discussed in [Section 3.4](#). A window is defined with some longitudinal and latitudinal extent, and the emission contained within is characterised as a 2D Gaussian. The window then slides some distance in longitude and the analysis is repeated. This iterative process enabled the construction of an ad-hoc background component that could be subtracted from each γ -ray source analysis. However, the results were not considered an estimate of the diffuse emission due to the low significance and the presence of unresolved sources.

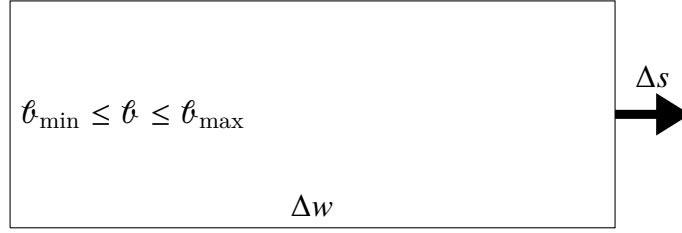


Figure 4.1: A diagram of the construction of the sliding window. The Galactic latitude bounds are given by $\ell_{\min} \leq \ell \leq \ell_{\max}$, the width is given by Δw , and the distance that the window slides in Galactic longitude is given by Δs .

To improve the data statistics the sliding-window analysis used to compare the GALPROP predictions to the HGPS observations instead takes an average of the flux within the window. The sliding window used here characterises the TeV large-scale emission as a longitudinal profile.

4.1.1 Sliding Window Parameters

The sliding window is defined by the height/latitudinal extent given by $\ell_{\min} \leq \ell \leq \ell_{\max}$, the width/longitudinal extent given by Δw , and the spacing between the windows given by Δs . A diagram of the sliding window and the parameter labels is shown in Figure 4.1.

As the sliding window analysis performed by (Abdalla et al., 2018e) was tuned for the creation of an ad-hoc background component, their analysis used the values $|\ell| \leq 3^\circ$, $\Delta w = 20^\circ$, and $\Delta s = 2.5^\circ$. As the analysis here is focused on characterising the large-scale emission the sliding window parameters are treated as free variables. The chosen parameters must be robust for both the GALPROP and HGPS analyses simultaneously, i.e. altering the sliding window parameters can have only a marginal impact on the analysis of either the GALPROP and the HGPS profiles. It should be noted that the HGPS results in this section use an integration radius of $R_c = 0.2^\circ$ (discussed in Section 3.2.2) and have masked the catalogued γ -ray sources. Details of the source masking procedure is provided later in Section 4.3.1.

Height of the Sliding Window

The HGPS is built from many exposures focused on bright γ -ray sources, most of which lie within the central 2° of the Galactic plane. Therefore, the sensitivity of the HGPS worsens towards regions above and below the Galactic plane. Figure 4.2 shows a latitudinal profile of the HGPS point-source sensitivity averaged across the longitudes $-75^\circ < \ell < 60^\circ$. The γ -ray flux averaged across these longitudes is also shown for comparison. The sensitivity is shown in units of %Crab, where the flux of the Crab nebula is defined as $J_{\text{Crab}}(E \geq 1 \text{ TeV}) = 2.26 \times 10^{-11} \text{ cm}^{-2} \text{ s}^{-1}$ (Aharonian et al., 2006e). For latitudes $|\ell| > 1^\circ$ the HGPS point-source sensitivity rapidly worsens with the minimum observable flux doubling by $|\ell| = 2^\circ$ and quadrupling by $|\ell| = 2.5^\circ$. There is an asymmetry in the HGPS exposure due to the focus on γ -ray sources at latitudes $|\ell| < 0^\circ$.

The maximum latitude bound of the sliding window is set to $\ell_{\max} = 1^\circ$, where the average sensitivity at is approximately equal to 2.25% of the Crab flux. Due to the

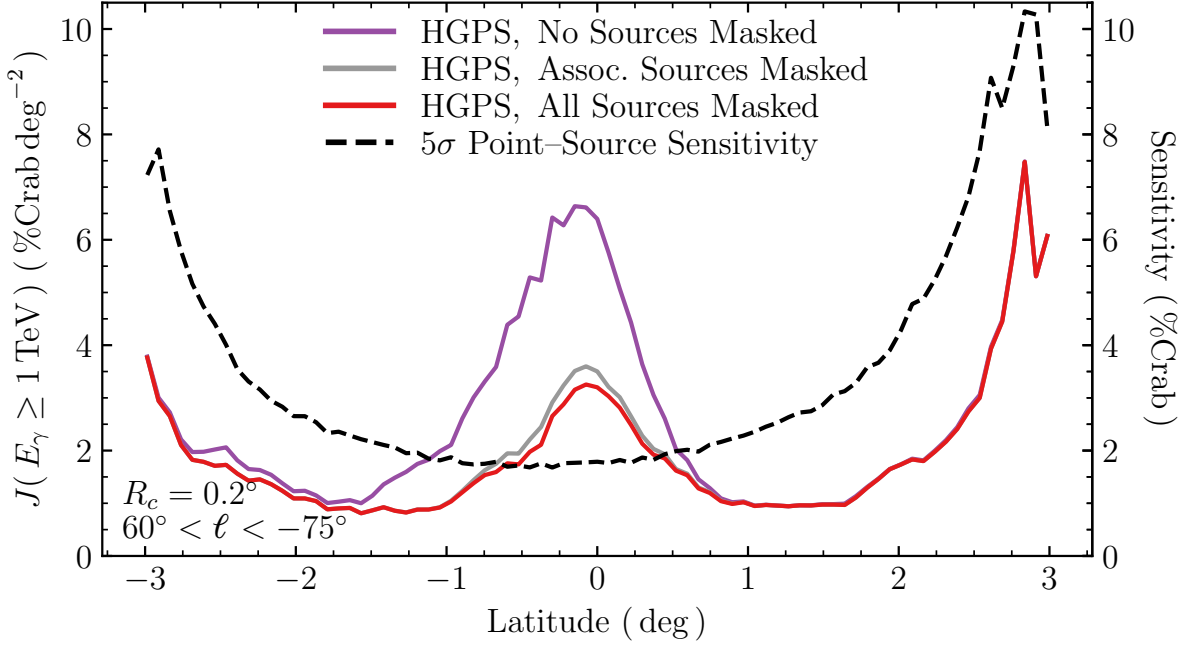


Figure 4.2: A latitudinal profile of the HGPS flux and sensitivity for the longitudes $-75^\circ < \ell < 60^\circ$, with a beam size of $R_c = 0.2^\circ$. The HGPS flux is shown in $\%Crab \text{ deg}^{-2}$ for no sources masked (purple), sources with an association masked (grey), and all sources masked (red). The sensitivity is shown by the black dashed line in units of $\%Crab$.

asymmetry in the HGPS exposure, the sensitivity worsens to the same level for the negative latitudes around $b_{\min} = -1.5^\circ$. The latitudinal bounds of the sliding window are then given by $-1.5^\circ < \ell < +1.0^\circ$, ensuring an approximately uniform exposure across the analysis region.

While the latitude bounds for the sliding window are an important consideration for the HGPS observations, the simulated GALPROP results have no effect analogous to the observational sensitivity worsening for higher latitudes. To ensure a consistent and equal comparison the latitude bounds for the HGPS analysis are also applied to the GALPROP sliding-window analysis.

Width of the Sliding Window

To improve the data statistics of the sliding-window analysis the window needs to be as wide as possible. However, if Δw is too large then the large-scale structure becomes averaged over Galactic longitude. For example, the Galactic centre (GC) and spiral arm tangents are approximately 20° in longitude apart. Therefore, emission from the GC and spiral arm tangents can contaminate measurements of one another if the sliding window has a width $\Delta w > 20^\circ$. Conversely, it was found that there were significant deviations in the HGPS longitudinal profile for sliding window widths $\Delta w < 10^\circ$ due to the lower data statistics for Galactic longitudes $-40^\circ \leq \ell \leq -80^\circ$. Figure 4.3 shows the results of the sliding window analysis on both the HGPS and GALPROP emission when varying the width of the sliding window from 10° to 20° .

As the GALPROP results are smoothly varying along the Galactic plane, there is little variation in the longitudinal profile between $\Delta w = 10^\circ$, $\Delta w = 15^\circ$, and $\Delta w = 20^\circ$.

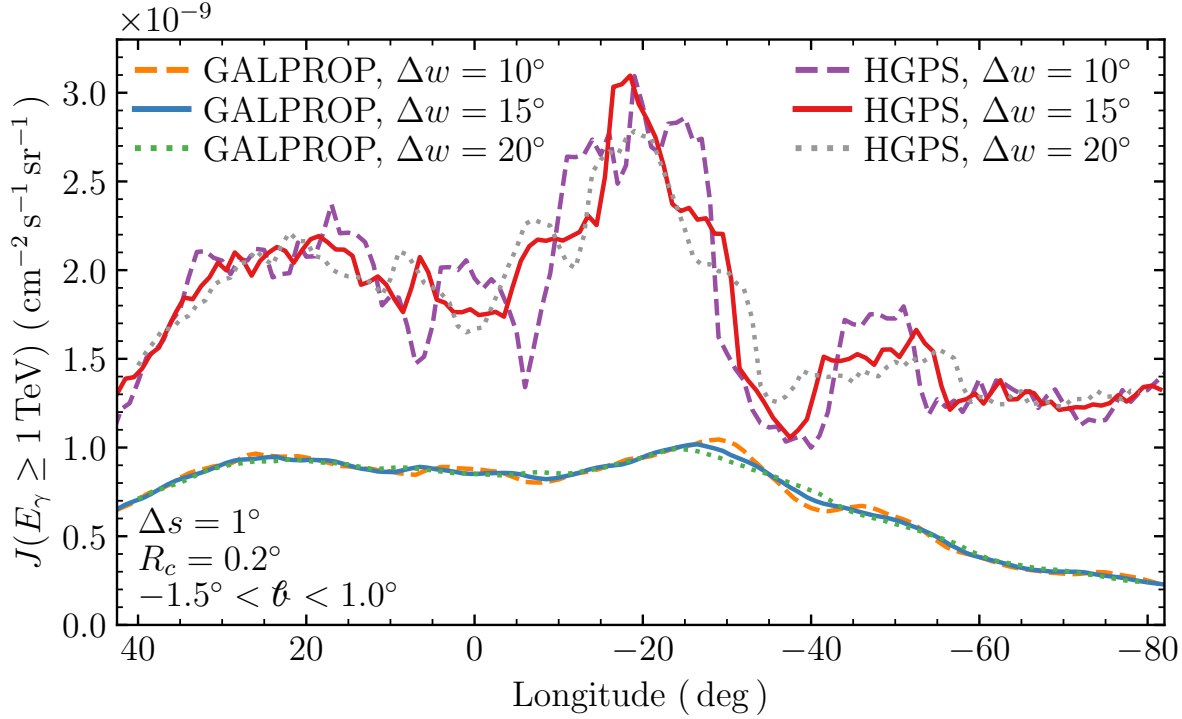


Figure 4.3: A longitudinal profile of both the HGPS and GALPROP flux, using a beam size of $R_c = 0.2^\circ$ and the latitude range $-1.5^\circ < \ell < +1.0^\circ$. The width of the sliding window, Δw , is varied from 10° (dashed), 15° (solid), and 20° (dotted).

However, some spatial information is lost in the $\Delta w = 20^\circ$ longitudinal profile in the GC region ($\ell = 0^\circ$). For the HGPS, there is little difference between the longitudinal profiles for $\Delta w = 15^\circ$ and $\Delta w = 20^\circ$. Larger deviations in the longitudinal profile due to lower data statistics begin to appear in the $\Delta w = 10^\circ$ profile.

The sliding window width was set to $\Delta w = 15^\circ$ for both GALPROP and the HGPS. This value for the window width ensures that the analysis is robust to $\pm 30\%$ changes in Δw for both the GALPROP predictions and the HGPS observations.

Spacing Between Windows

The spacing between the sliding windows, i.e. the longitude that the window is moved between each iteration, must be defined such that changes in the longitudinal profile can be extracted. The Nyquist condition states that to observe variation on a given scale the sampling rate must be at least half of said scale.

It is possible for the large-scale emission to vary on the scale size of the γ -ray sources. The average diameter of a γ -ray source in the HGPS is 0.18° (Abdalla et al., 2018e). Hence, to satisfy the Nyquist theorem, capturing variation on this scale size of the discrete γ -ray sources would require a sliding window spacing of 0.09° . Sampling on this scale is impossible as gas surveys used in the construction of the ISM models used by GALPROP have angular resolutions of approximately 0.1° (see Section 2.4).

The longitudinal structure of the large-scale emission may vary on the scale size of the angular separation between the γ -ray sources. The average angular separation between

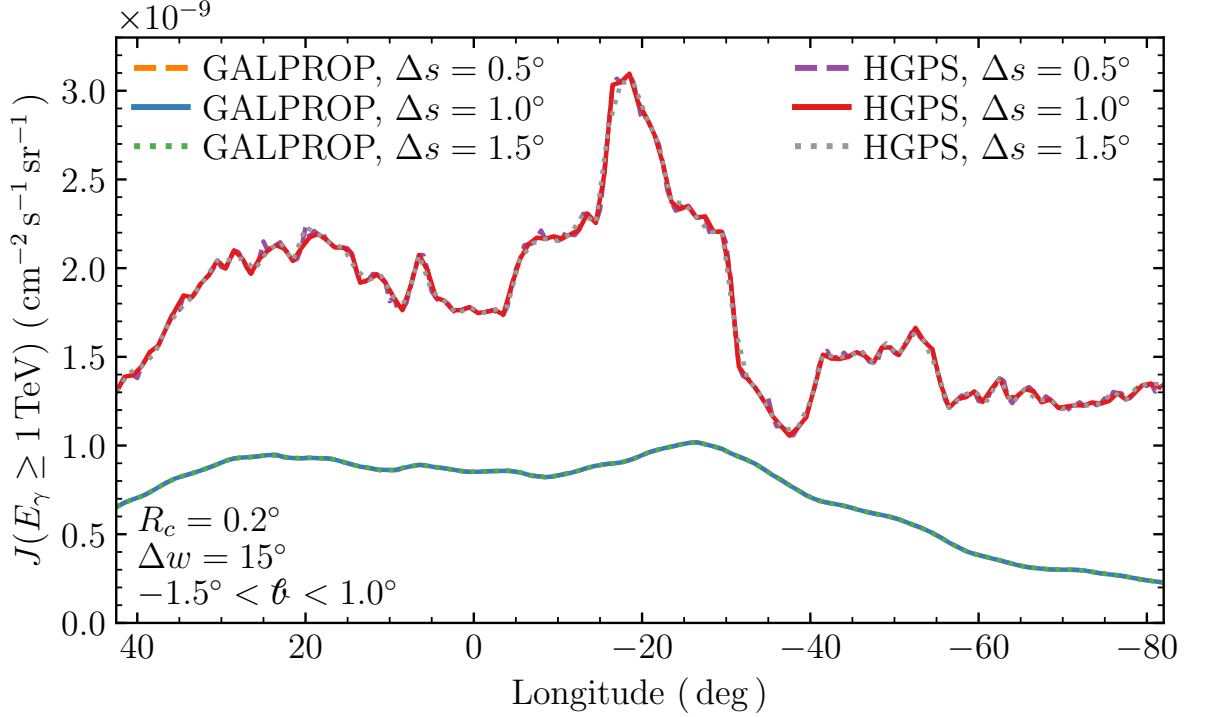


Figure 4.4: A longitudinal profile of both the HGPS and GALPROP flux, using a beam size of $R_c = 0.2^\circ$, a latitude range of $-1.5^\circ < \ell < +1.0^\circ$, and a window width of $\Delta w = 15^\circ$. The spacing between the sliding windows, Δs , is varied from 0.5° (dashed), 1.0° (solid), and 1.5° (dotted).

γ -ray sources is $\sim 2.5^\circ$ in longitude (Abdalla et al., 2018e). Approximately 20% of the γ -ray sources lie within 1.0° of another γ -ray source, with a particular pair being separated by only 0.03° in longitude. Although the structure between all sources cannot be captured due to the limit resolution of the GALPROP maps, the majority of the structure between γ -ray sources could be captured with a window spacing between 0.5° and 1.5° .

The sliding window analysis was performed on both the HGPS and GALPROP results, varying the sliding window spacing from 0.5° to 1.5° . The results are shown in Figure 4.4. As the sliding window analysis is not sensitive to changes in Δs for either the GALPROP predictions or HGPS observations for any of the chosen window spacings, the value $\Delta s = 1^\circ$ is chosen for simplicity. It should be noted that large deviations occur in the sliding-window analysis of the HGPS observations if the window spacing is larger than the average angular separation between γ -ray sources (i.e. for $\Delta s > 3^\circ$).

4.2 Adapting the GALPROP Results for Comparison to the HGPS

GALPROP calculates the γ -ray emission for each process discussed in Section 2.2 as a separate map. The maps are calculated for the entire sky using the HEALPix convention (Górski et al., 2005), which ensures an equal solid angle for each pixel. The

highest resolution achievable by GALPROP is limited by the resolution of the gas maps used in the propagation and γ -ray emission calculations (as discussed in [Section 2.4](#)). As of writing this thesis GALPROP is limited to ninth-order HEALPix files, i.e. the minimum pixel dimensions are $0.1145^\circ \times 0.1145^\circ$.

4.2.1 GALPROP Flux Integration

The public data from the HGPS is a γ -ray flux map with units of $\text{cm}^{-2} \text{s}^{-1}$ and has been integrated above 1 TeV. For the comparison between the HGPS and GALPROP to be compatible, the differential GALPROP flux needs to be integrated over the same range of energies, i.e. $E_\gamma \geq 1 \text{ TeV}$. However, the maximum simulated energy must be finite. For $\gtrsim 10 \text{ GeV}$ the differential γ -ray flux, $J(E_\gamma)$, can be described by a power law. The differential flux, and the integrated flux between energies E_1 and E_2 , are given by the equations:

$$J(E_\gamma) \propto E_\gamma^{-\eta} \quad (4.1)$$

$$\Rightarrow \int_{E_1}^{E_2} J(E_\gamma) dE_\gamma \propto \frac{1}{\eta - 1} \left(E_1^{1-\eta} - E_2^{1-\eta} \right) \quad (4.2)$$

where E_γ is the γ -ray energy and η is the spectral index. For discrete γ -ray sources, the spectral index typically takes values $2 < \eta < 3.5$, with the spectral index of the diffuse emission at TeV energies being in the range of $2.5 < \eta < 3$ ([Abdalla et al., 2018e](#)). From [Equation 4.2](#) it can be seen that setting $E_1 = 1 \text{ TeV}$ and varying E_2 from 50 TeV to 100 TeV impacts the integral flux by less than one part in ten thousand. The negligible impact was then confirmed numerically with the predicted emission from GALPROP. As the error is well within the modelling uncertainties of GALPROP, the integrated GALPROP emission uses the energy bounds of $E_1 = 1 \text{ TeV}$ and $E_2 = 50 \text{ TeV}$. The GALPROP skymaps integrated for energies $E_\gamma \geq 1 \text{ TeV}$ have units of $\text{cm}^{-2} \text{s}^{-1} \text{sr}^{-1}$.

4.2.2 Applying a Telescope Beam to GALPROP

GALPROP calculates the γ -ray skymaps by performing a line-of-sight integral over the emissivity (as discussed in [Section 2.2.3](#)). The line-of-sight integral effectively draws a line from the observer in the direction of a given pixel and ‘counts’ the photons along that line. The flux for a given GALPROP pixel is then divided by the solid angle of the pixel. In contrast, the γ -ray emission given in the HGPS ([Abdalla et al., 2018e](#)) is an integral over a circular ‘beam’ centred on each pixel (as discussed in [Section 3.2.2](#)).

To ensure compatibility between the GALPROP predictions and the HGPS observations, a telescope beam was applied to the HEALPix skymaps. To begin, the GALPROP predictions were converted to units of $\text{cm}^{-2} \text{s}^{-1}$ by multiplying the flux by the solid angle of the pixels. An integration beam with radius R_c was then drawn around each pixel in the skymap. However, integrating square pixels within a circular beam requires a correction factor, C , to be applied to the integral. The correction factor is equal to the solid angle of the beam divided by the total solid angle of all pixels within the beam, and is given by:

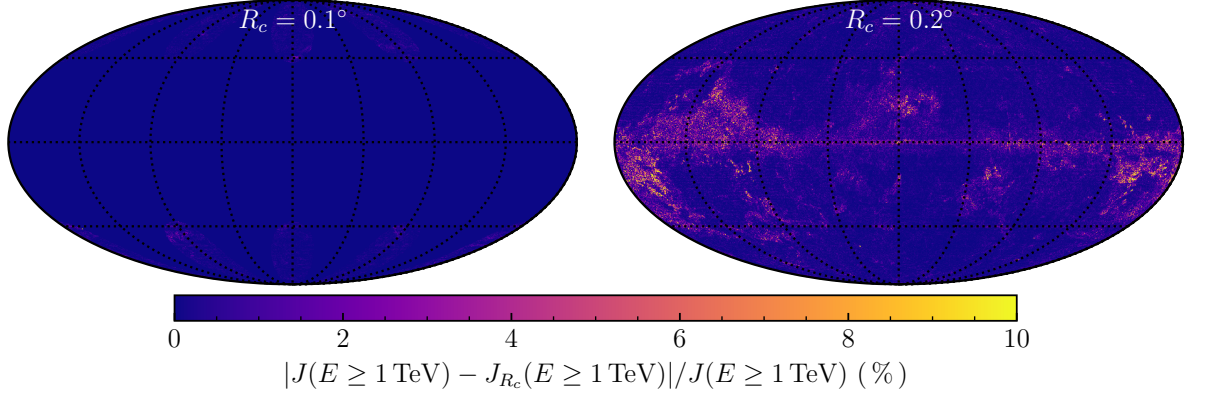


Figure 4.5: The absolute residuals, shown as a percentage, for the total GALPROP γ -ray flux integrated above 1 TeV after subtracting the emission integrated over a beam with radius $R_c = 0.1^\circ$ (left) and $R_c = 0.2^\circ$ (right). For the $R_c = 0.1^\circ$ beam the residuals are less than 1%. For $R_c = 0.2^\circ$, the residuals are less than 1% for most of the sky, approximately 4–5% for regions with γ -ray features with sizes $\sim 0.2^\circ$, and can reach up to 10% for the γ -ray features smaller than 0.2° .

$$C = \frac{A_{\text{beam}}}{N_{\text{beam}} A_{\text{pixel}}} \quad (4.3)$$

where $A_{\text{beam}} = 2\pi(1 - \cos(R_c))$ is the solid angle of the applied beam, A_{pixel} is the area of a pixel, and N_{beam} is the number of pixels contained within the beam. It should be noted that the correction term approaches unity for $A_{\text{beam}} \gg A_{\text{pixel}}$. The values of A_{pixel} and N_{beam} depend on the resolution of the HEALPix image. After the integration beam is applied, each pixel is divided by the solid angle of the beam (A_{beam}) such that the skymap has units of $\text{cm}^{-2} \text{s}^{-1} \text{sr}^{-1}$. This algorithm can be expressed as a function, where the predicted γ -ray flux from GALPROP integrated over a telescope beam (J_{beam}) is given by:

$$\begin{aligned} J_{\text{beam}}(\ell, \theta, E) &= \frac{1}{A_{\text{beam}}} C \int_{R_c} A_{\text{pixel}} J(\ell, \theta, E) d\Omega \\ &= \frac{1}{N_{\text{beam}}} \int_{R_c} J(\ell, \theta, E) d\Omega \end{aligned} \quad (4.4)$$

where (ℓ, θ) are the Galactic longitude and latitude, respectively, Ω is the solid angle, and the integral is performed over the beam with radius R_c . As can be seen from the simplified form of Equation 4.4, applying a telescope beam to the GALPROP output effectively averages the γ -ray flux over an angular scale size of R_c .

The γ -ray emission both before and after applying the telescope beam were compared to test if this procedure produces any systematic effects. This comparison was performed by calculating the residual emission between the original GALPROP predictions and the γ -ray flux after applying the telescope beam. The absolute residual emission, J_{residual} , is given by:

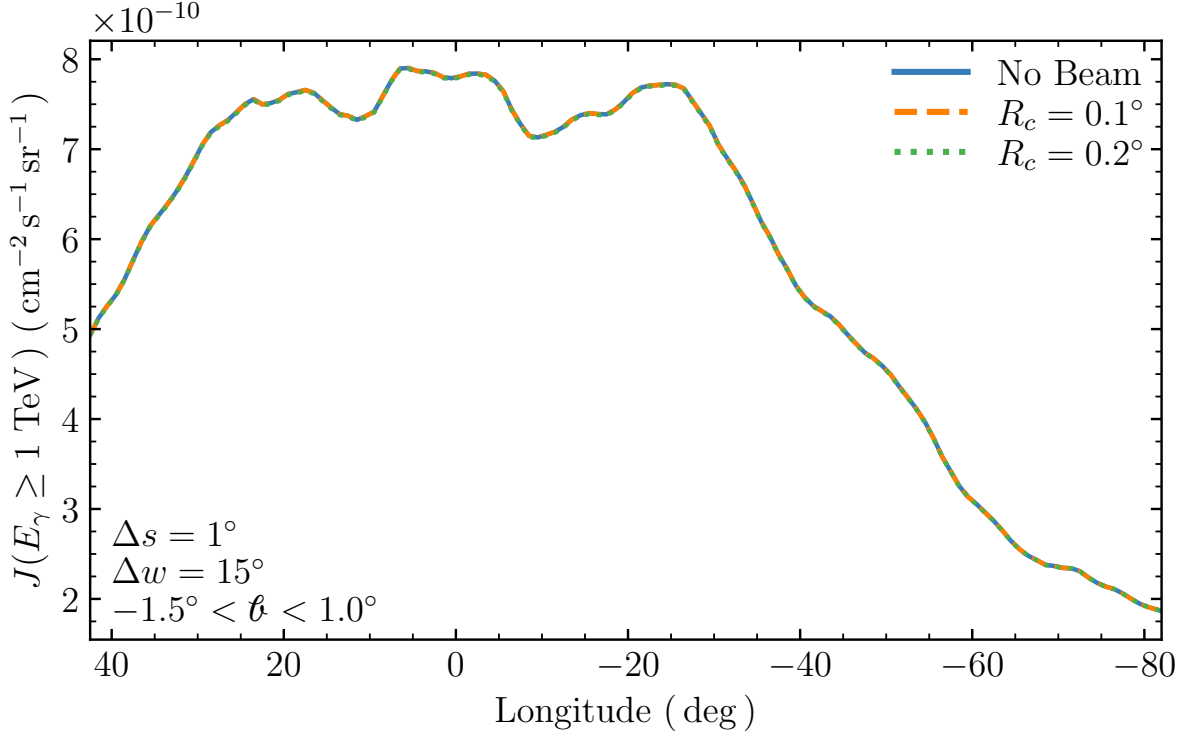


Figure 4.6: A longitudinal profile of the GALPROP emission with no telescope beam applied (blue), and telescope beams with radii $R_c = 0.1^\circ$ (orange dashed) and $R_c = 0.2^\circ$ (green dotted). The analysis follows the sliding window recipe discussed in [Section 4.1](#), with $\Delta s = 1^\circ$ and $\Delta w = 15^\circ$.

$$J_{\text{residual}}(\ell, \ell, E) = \frac{|J(\ell, \ell, E) - J_{\text{beam}}(\ell, \ell, E)|}{J(\ell, \ell, E)} \quad (4.5)$$

where all parameters have been defined previously. The residual emission between the original GALPROP predictions and after applying the telescope beams can be seen in [Figure 4.5](#) for both the $R_c = 0.1^\circ$ and $R_c = 0.2^\circ$ beams. The residual emission is calculated on the total γ -ray emission integrated above 1 TeV. The GALPROP outputs have pixels with a solid angle of 0.4×10^{-5} sr, which is similar in size to the solid angle of the $R_c = 0.1^\circ$ beam (10^{-5} sr). Hence, the absolute residual emission for the $R_c = 0.1^\circ$ beam is approximately zero across the entire 4π steradians of the sky. At the polar regions the absolute residuals are larger due to the HEALPix pixels being distorted¹. Also seen in [Figure 4.5](#) is that the absolute residuals for the $R_c = 0.2^\circ$ beam can be as large as 10%. As shown by [Equation 4.4](#), the γ -ray emission is averaged over the size of the beam. Hence, structures with radii smaller than the $R_c = 0.2^\circ$ beam are impacted. Such structures include the hadronic emission from nearby gas clouds.

The large-scale γ -ray structure has a Gaussian width across Galactic latitude, varying between 0.1° – 0.5° , with an average width of 0.4° around the GC region ([Abramowski et al., 2014a](#); [Abdalla et al., 2018e](#)). The large-scale emission then varies on scales larger than either the $R_c = 0.1^\circ$ or $R_c = 0.2^\circ$ beams. Therefore, while the absolute residual emission after applying the $R_c = 0.2^\circ$ can be as large as 10%, it is expected that the large-scale structure would be unaffected.

¹The HEALPix pixels are distorted at the polar regions to ensure a constant solid angle for each pixel.

To quantify any systematic effects that the telescope beam may have on the large-scale diffuse emission, a sliding-window analysis was performed (see [Section 4.1](#)). The results from the sliding-window analysis on the original GALPROP flux and after applying the $R_c = 0.1^\circ$ and $R_c = 0.2^\circ$ telescope beams are shown in [Figure 4.6](#). Applying either of the two telescope beams had a negligible impact on the large-scale emission predicted by GALPROP, with the differences between the longitudinal profiles being on the order of one part in ten thousand. Therefore, the GALPROP results are robust against the integration beam on the angular scales of interest (i.e. 0.1° and 0.2°).

4.3 Adapting the HGPS Results for Comparisons to GALPROP

The HGPS uses an equirectangular (i.e. cartesian) projection for the flux maps, with pixel dimensions of $0.02^\circ \times 0.02^\circ$ and units of $\text{cm}^{-2}\text{s}^{-1}$. For compatibility with the GALPROP skymaps, the HGPS flux is divided by the solid angle of the integration beam ($2\pi[1 - \cos(R_c)]$), where $R_c = 0.1^\circ$ or $R_c = 0.2^\circ$. Additionally, before the HGPS observations can be compared to the predicted diffuse TeV emission from GALPROP, all of the 78 catalogued γ -ray sources (discussed in [Section 3.3.2](#)) need to be accounted for.

4.3.1 Masking the Catalogued HGPS Sources

The largest contribution to the γ -ray emission observed in the HGPS is that from discrete, resolved sources. These sources are commonly referred to as catalogued γ -ray sources. To obtain an estimate of the large-scale γ -ray emission all of the catalogued γ -ray sources must be masked out. To account for the catalogued source emission, the recipe from [Abdalla et al. \(2018e\)](#) was followed. The morphological structure of the catalogued γ -ray sources is modelled and subtracted (i.e. masked) from the HGPS. A demonstration of the γ -ray source masking can be seen in [Figure 4.7](#).

The catalogued γ -ray sources can be classified by their morphological structure into one of the following four categories:

1. Shell: Sources in this category cannot be modelled in an easy, repeatable method. Shell-like sources show enhanced emission along their edges due to limb brightening and may have more complex structures within.
2. GC: A complex morphological region filled with many bright γ -ray sources that cannot be described by a simple spatial model.
3. Gaussian: Sources in this category can be modelled as one or more Gaussians. The majority of sources in the HGPS are in this category.
4. Point: Sources in this category can be modelled as a single Gaussian, as the sources are intrinsically smaller than the point spread function (PSF) of H.E.S.S..

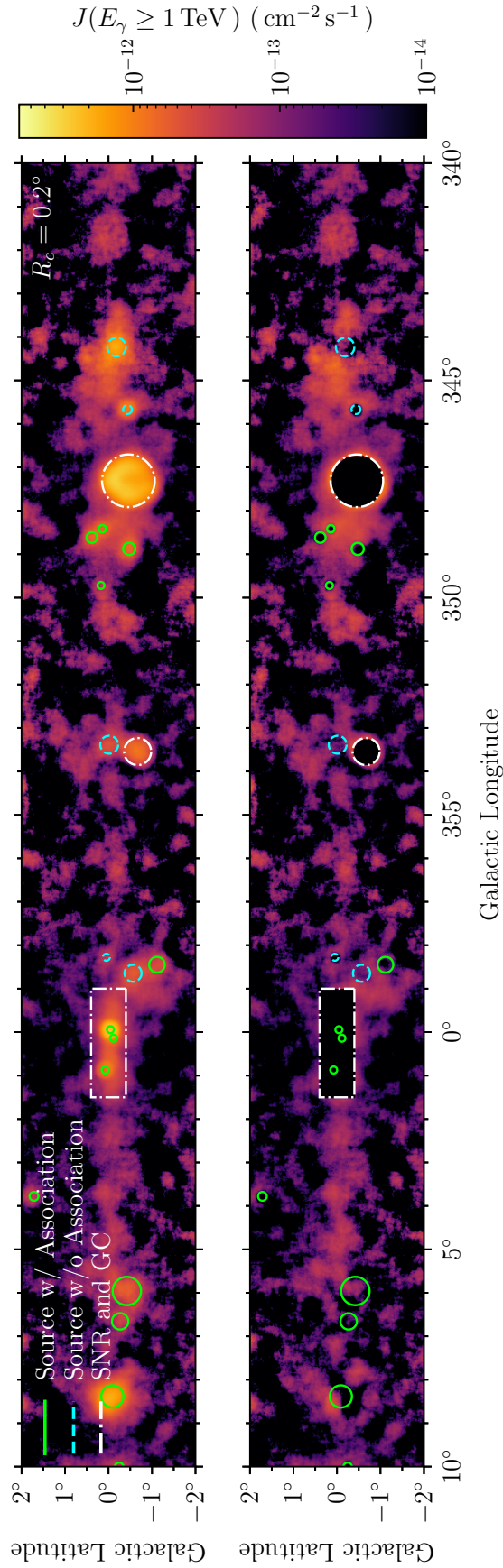


Figure 4.7: HGPS flux map for Galactic longitudes $10^\circ \leq \ell \leq 340^\circ$ and Galactic latitudes $-2^\circ < b < +2^\circ$ for the $R_c = 0.2$ map. The flux is shown before the mask is applied (top) and after the mask is applied (bottom). For a description of sources with and without an association, see text.

Shell-type Sources and the Galactic Centre

Shell-like sources are likely caused by SNRs accelerating CRs via diffusive shock acceleration as the SN shock expands into the surrounding ISM (Fermi, 1949). The collision between the SNR shock and ISM gas involves many complex interactions. The interactions between the two media results in a morphologically complex object. Shell-like sources are often asymmetric and contain detailed structures seen across many wavelengths. Due to the large number of poorly understood and unconstrained parameters, any systematic analysis applied to all shell-like sources performed by Abdalla et al. (2018e) lead to unconstrained or diverging analyses.

As shell-like γ -ray sources cannot be modelled in a systematic, repeatable fashion, their emission is instead cut from the map. All pixels within the shell radius are excluded from any further analyses. The outline of shell-like sources is taken as a circle, where the radius of the HGPS spectral analysis region (given in Table B.1) is used for the radius of the cut-out region. An example of the exclusion procedure on a shell-type SNR can be seen in Figure 4.7. The excluded γ -ray source is HESS J1713–397 at the coordinates $(\ell, b) = (347.31^\circ, -0.46^\circ)$ with a radius of 0.60° .

The GC is a complex multi-source region. Although Abdalla et al. (2018b) created a spatial model for the GC region, their model requires ISM gas data and multiple ad-hoc components. Similarly as for the shell-type sources, there exists no accurate, representative spatial model that can completely mask the GC without the inclusion of external data. Following Abdalla et al. (2018e) and the procedure for shell-like sources, the pixels within the GC region are excluded from any further analyses. The GC region is defined by the longitudinal bounds $-1.0^\circ \leq \ell \leq +1.5^\circ$ and latitudinal bounds $|b| \leq 0.4^\circ$ (Abdalla et al., 2018e), with the exclusion process shown in Figure 4.7.

Point Sources and Gaussian Sources

As discussed in Section 3.3.1, the point-like γ -ray sources are modelled as a single three-dimensional Gaussian with a standard deviation width equal to the PSF of H.E.S.S. (0.08°). The Gaussian sources are modelled as one or more three-dimensional Gaussian(s) that have a standard deviation width larger than the PSF of H.E.S.S..

The surface brightness of a γ -ray source ($S_{\text{source}}(\ell, b)$; Equation 3.22) is calculated individually for each point-like and Gaussian source as a function of the radial distance (r ; Equation 3.23) and the angular size (σ_{ang} ; Equation 3.24). Appendix B details how the parameters were calculated for each source, and the parameter values for all catalogued sources are provided in Table B.1. The modelled source surface brightness is subtracted from the HGPS image via the equation:

$$F_{\text{masked}}(\ell, b) = F_{\text{unmasked}}(\ell, b) - S_{\text{source}}(\ell, b) \quad (4.6)$$

where F_{unmasked} is the original HGPS flux and F_{masked} is the residual flux after subtracting the catalogued source components. For a given source, S_{source} is subtracted from the map for $r \leq 5\sigma_{\text{ang}}$ as $S_{\text{source}}(r \geq 5\sigma_{\text{ang}})$ is always below the uncertainty in the HGPS flux map. Examples of the source masking procedure can be seen in Figure 4.7.

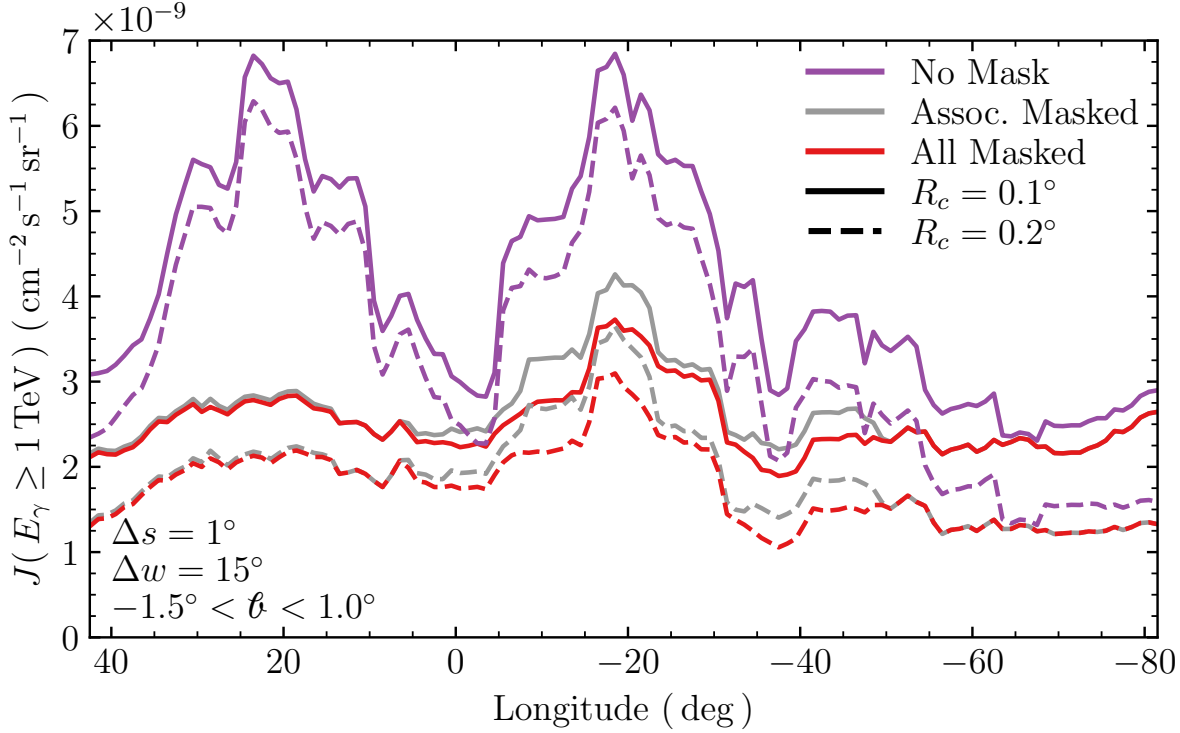


Figure 4.8: Longitudinal profile of the HGPS for $R_c = 0.1^\circ$ (solid lines) and $R_c = 0.2^\circ$ (dashed lines). The shown profiles are for no sources masked (purple), only sources with an association masked (grey), and all sources masked (red). The grey and red lines represent the range of the estimates of the HGPS large-scale γ -ray emission. The analysis follows the sliding window recipe discussed in [Section 4.1](#) with $\Delta s = 1^\circ$, $\Delta w = 15^\circ$, and $-1.5^\circ < \ell < 1.0^\circ$.

Choosing the Sources to Mask

The γ -ray sources catalogued in the HGPS can be split into two categories. The sources with a known nearby accelerator of CRs (or multiple possible accelerators) are labelled as an ‘associated source’, and the γ -ray sources without any observed nearby CR accelerator are labelled as ‘not associated’ (or as ‘no known association’). The classifications for the CR accelerators are discussed in more depth in [Section 3.3.2](#), with the binary, stellar cluster, SNR, composite, PWN, and ‘not firmly identified’ classifications being considered associated sources. The associated sources are not considered part of the large-scale γ -ray emission. Conversely, it is not known if the unassociated γ -ray sources can be considered as part of the large-scale emission. The eleven γ -ray sources catalogued in the HGPS that have no known association are shown in [Table 3.7](#), with their masking parameters shown in [Table B.1](#).

Two γ -ray flux maps were calculated from the HGPS – one where all 78 catalogued γ -ray sources were masked, and another where only the sources with a known association were masked from the analyses. The two γ -ray flux maps represent a lower and upper limit, respectively, on the large-scale emission after accounting for the discrete sources observed in the HGPS. A comparison between the longitudinal profiles for the two masks (as well as the un-masked HGPS) for both the $R_c = 0.1^\circ$ and $R_c = 0.2^\circ$ telescope beams is shown in [Figure 4.8](#).

The longitudinal profile of the HGPS with no sources masked (shown in Figure 4.8) represents the upper-bound on the TeV large-scale γ -ray emission along the Galactic plane. The difference between the ‘no sources masked’ and ‘all sources masked’ profiles represents the contribution of the catalogued γ -ray sources to the large-scale emission along the Galactic plane. Masking γ -ray sources decreases the large-scale emission by up to a factor of three; hence, the large-scale TeV γ -ray structure is dominated by γ -ray sources. Additionally, the difference between the two longitudinal profiles demonstrates that there is a concentration of γ -ray sources along the spiral arm tangents ($\ell \approx \pm 20^\circ$).

Comparing the large-scale emission between masking all sources and only masking sources with an association shows that most of the γ -ray sources with no known association lie between the longitudes $0^\circ < \ell < 310^\circ$, with the longitudinal profiles between the two masks differing by a maximum of 20% in this region. Masking all sources potentially overestimates the contribution of the γ -ray sources to the large-scale emission. Hence, the profile represents a lower limit on the large-scale emission after accounting for resolved sources. Conversely, masking only the sources with a known association represents an upper limit as the γ -ray source component is potentially underestimated. The difference between the two longitudinal profiles is a maximum of 20% for the Galactic longitudes $10^\circ < \ell < 310^\circ$. The two profiles are within 1% outside of this longitude range as only three of the eleven sources with no known association lie beyond the longitudes $10^\circ < \ell < 310^\circ$.

As discussed in Section 3.2.2 the HGPS emission is most sensitive to features with sizes similar to the integration radius, R_c . However, the large-scale γ -ray structure varies on scales larger than either of the telescope beams used in the HGPS, with an average Gaussian width in the GC region of 0.4° (Abramowski et al., 2014a; Abdalla et al., 2018e). Hence, the $R_c = 0.2^\circ$ profile has a higher significance for the large-scale emission. The difference between the longitudinal profiles taken on the $R_c = 0.1^\circ$ and $R_c = 0.2^\circ$ maps is independent of the applied source masks, varying between $0.5\text{--}1.0 \times 10^{-9} \text{cm}^{-2} \text{s}^{-1} \text{sr}^{-1}$. The $R_c = 0.2^\circ$ HGPS map is used for all further estimates of the large-scale γ -ray emission in this thesis.

4.3.2 Unresolved Sources in the HGPS

As discussed in Section 3.2.5, the HGPS has a limited source distance horizon beyond which H.E.S.S. cannot individually detect point sources. The source horizon depends on the luminosity of the source, the distance to the source, and the angular extent of the source. As the horizon did not extend to the other side of the Galaxy (Figure 3.7) there are many more γ -ray sources in the TeV energy range that remain undetected by H.E.S.S.. The number of unresolved sources is estimated to be in the range of hundreds to thousands (Actis et al., 2011). Although they are not individually detected, the unresolved sources contribute to the total observed large-scale γ -ray flux. While it is possible to mask the catalogued sources from the analysis, it is impossible to mask the unresolved sources. However, the flux that unresolved sources are likely to contribute to the large-scale emission can be estimated and subtracted from the observations.

An estimate from Steppa and Egberts (2020) suggests that unresolved sources contribute 13%–32% to the large-scale emission. This estimate was obtained by comparing the total flux observed in the HGPS to the total TeV luminosity produced by a modelled distribution of sources, with the total luminosity of TeV γ -ray sources based on PWN distributions.

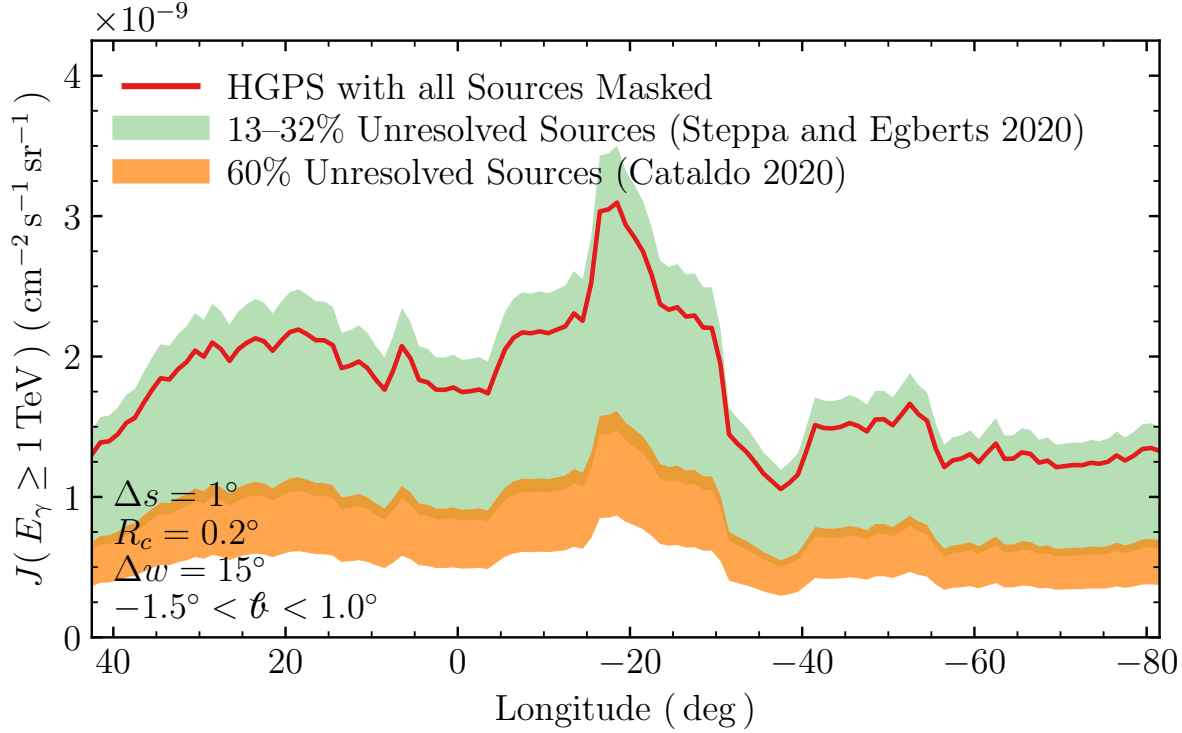


Figure 4.9: Longitudinal profile of the HGPS emission for a beam size of $R_c = 0.2^\circ$ and catalogued sources masked (red). Also shown is the HGPS after accounting for the systematic uncertainty ($\pm 30\%$), with unresolved source contributions of 13–32% (green; Steppa and Egberts, 2020) and 60% (orange; Cataldo et al., 2020). The analysis follows the sliding window recipe discussed in Section 4.1 with $\Delta s = 1^\circ$, $\Delta w = 15^\circ$, and $-1.5^\circ < \ell < 1.0^\circ$.

Another estimate from Cataldo et al. (2020) suggests that the fraction of unresolved sources could be as large as 60%. The Cataldo et al. (2020) estimate was obtained by using known SNR and PWN spatial distributions and luminosity distributions to calculate the number of detectable sources, as well as calculating the total γ -ray flux that all the sources would produce.

A combination of both the Steppa and Egberts (2020) and Cataldo et al. (2020) unresolved source estimates with the $\pm 30\%$ systematic uncertainty in the H.E.S.S. flux is shown in Figure 4.9. The HGPS profile is taken from the $R_c = 0.2^\circ$ flux map after subtracting all catalogued γ -ray sources. Subtracting the contribution from both the catalogued γ -ray sources and an estimate of the unresolved sources gives the residual emission of the HGPS on the scale-size of R_c . The only remaining component in the residual emission is expected to be the large-scale diffuse γ -ray emission. Hence, the estimates shown in Figure 4.9 can be considered estimates of the large-scale diffuse γ -ray emission. However, it should be noted that this estimate is below the 5σ detection threshold.

As the longitudinal profile shown in Figure 4.9 is taken after masking all 78 catalogued γ -ray sources, it is a lower bound on the residual large-scale emission. As the unresolved source component from Cataldo et al. (2020) is an upper limit, the residual emission found after subtracting the Cataldo et al. (2020) estimate is a lower bound of the TeV large-scale diffuse γ -ray emission.

Chapter 5

First Paper: Diffuse TeV Gamma-Ray Predictions with GALPROP

This chapter contains the manuscript titled: “The Steady-State Multi-TeV Diffuse Gamma-Ray Emission Predicted with GALPROP and Prospects for the Cherenkov Telescope Array”, which was published in the peer-reviewed journal MNRAS in February 2023.

As cosmic rays (CRs) diffuse throughout the interstellar medium (ISM) they interact with the ISM gas, the interstellar radiation field (ISRF), and the Galactic magnetic field (GMF). These interactions create broadband non-thermal emissions, from radio waves to ultra-high-energy gamma rays (γ rays). The *Fermi* large area telescope (*Fermi*-LAT) observed a large-scale diffuse γ -ray structure at GeV energies along the Galactic plane. More recently, the high-energy stereoscopic system (H.E.S.S.) in their Galactic plane survey (named the HGPS) observed a large-scale structure at TeV γ -ray energies. The emissions observed at GeV and TeV energies will be connected by a common origin of the CRs; however, the energy dependence of the emission, and the relative contribution from CRs that are diffuse or local to sources, is poorly understood.


In this manuscript it is shown that the model predictions from GALPROP broadly agree with the estimates of the diffuse TeV γ -ray emission from the HGPS after accounting for emission from catalogued γ -ray sources and the flux contribution from unresolved γ -ray sources. It is also found that the γ -ray emissions from inverse Compton (IC) scattering off CR electrons becomes an important component of the TeV γ -ray flux along the Galactic plane, and even dominates the total emissions above 10 TeV. Due to the importance of the CR electrons, future γ -ray observations in the 100 TeV energy range may be able to aid in constraining the GMF structure. Given the lower bounds on the diffuse emission that was found from both the HGPS and GALPROP, the upcoming Cherenkov telescope array (CTA) will likely be able to observe the large-scale diffuse structure at TeV γ -ray energies. The brightness of the GALPROP predictions indicate that more optimisation is necessary for applications to the more sensitive CTA GPS.

Due to the large number of variables in this thesis, the notation in this published work is not necessarily consistent with the other chapters.

Statement of Authorship

Title of Publication:	The Steady-State Multi-TeV Diffuse Gamma-Ray Emission Predicted with GALPROP and Prospects for the Cherenkov Telescope Array
Publication Status:	Published
Publication Details:	P. Marinos, G. Rowell, T. Porter, and G. Jóhannesson, MNRAS, Volume 518, Issue 4, February 2023, Pages 5036–5048

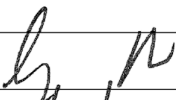
Principal Author


Name of Principal Author (Candidate):	Peter Marinos
Contribution to the Paper:	Simulation setup, ran simulations, data and simulation analysis, data and simulation interpretations, writing of paper.
Overall Percentage Contributed:	65%
Certification:	This paper reports on original research that I conducted during the period of my Higher Degree by Research candidature and is not subject to any obligations or contractual agreements with a third party that would constrain its inclusion in this thesis. I am the primary author of this paper.
Signature:	
Date:	23/01/2023

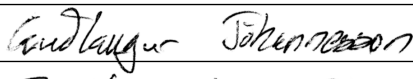
Co-Author Contributions

By signing the Statement of Authorship, each co-author certifies that:

- (i) the candidate's stated contribution to the publication is accurate (as detailed above);
- (ii) permission is granted for the candidate to include the publication in the thesis; and
- (iii) the sum of all co-author contributions is equal to 100% less the candidate's stated contribution.

Name of Co-Author:	Gavin Rowell
Contribution to the Paper:	Data and simulation interpretation, major paper review.
Overall Percentage Contributed:	15%
Signature:	
Date:	23/1/23

Name of Co-Author:	Troy Porter
Contribution to the Paper:	Simulation setup, simulation interpretation, major paper review.
Overall Percentage Contributed:	15%
Signature:	
Date:	22/11/2023

Name of Co-Author:	Guðlaugur Jóhannesson
Contribution to the Paper:	ISM gas model, diffusion parameter optimisation, paper review.
Overall Percentage Contributed:	5%
Signature:	
Date:	7 November 2022

The steady-state multi-TeV diffuse γ -ray emission predicted with GALPROP and prospects for the Cherenkov Telescope Array

P. D. Marinos¹,¹★ G. P. Rowell¹,¹ T. A. Porter²,² and G. Jóhannesson³,³

¹*School of Physical Sciences, University of Adelaide, Adelaide, South Australia 5000, Australia*

²*W. W. Hansen Experimental Physics Laboratory and Kavli Institute for Particle Astrophysics and Cosmology, Stanford University, Stanford, CA 94305, USA*

³*Science Institute, University of Iceland, IS-107 Reykjavik, Iceland*

Accepted 2022 November 3. Received 2022 November 3; in original form 2022 May 6

ABSTRACT

Cosmic rays (CRs) interact with the diffuse gas, radiation, and magnetic fields in the interstellar medium (ISM) to produce electromagnetic emissions that are a significant component of the all-sky flux across a broad wavelength range. The *Fermi*–Large Area Telescope (LAT) has measured these emissions at GeV γ -ray energies with high statistics. Meanwhile, the high-energy stereoscopic system (H.E.S.S.) telescope array has observed large-scale Galactic diffuse emission in the TeV γ -ray energy range. The emissions observed at GeV and TeV energies are connected by the common origin of the CR particles injected by the sources, but the energy dependence of the mixture from the general ISM (true ‘diffuse’), those emanating from the relatively nearby interstellar space about the sources, and the sources themselves, is not well understood. In this paper, we investigate predictions of the broad-band emissions using the GALPROP code over a grid of steady-state 3D models that include variations over CR sources, and other ISM target distributions. We compare, in particular, the model predictions in the very-high energy (VHE; $\gtrsim 100$ GeV) γ -ray range with the H.E.S.S. Galactic plane survey (HGPS) after carefully subtracting emission from catalogued γ -ray sources. Accounting for the unresolved source contribution, and the systematic uncertainty of the HGPS, we find that the GALPROP model predictions agree with lower estimates for the HGPS source-subtracted diffuse flux. We discuss the implications of the modelling results for interpretation of data from the next generation Cherenkov Telescope Array (CTA).

Key words: cosmic rays – ISM: magnetic fields – Galaxy: structure – gamma-rays: diffuse backgrounds.

1 INTRODUCTION

Cosmic ray (CR) particles are injected by sources, propagating over millions of years and eventually pervading the Galaxy. This process results in a ‘sea’ of CRs that produce broad-band all-sky emissions due to energy losses with the other components of the diffuse interstellar medium (ISM): the interstellar gas, the interstellar radiation field (ISRF), and the Galactic magnetic field (GMF). The leakage into the ISM from the individual CR sources also produces localized enhancements of the particle intensities on top of the background ‘sea’, which also contribute to the broad-band non-thermal sky brightness. The diffuse emissions by the CRs, therefore, encode critical information on their sources; how they are injected into the ISM and their propagation history, as well as the spatial distributions of the other ISM components. Observations of their non-thermal emissions can be used to provide essential insights for understanding how the CRs are accelerated up to the highest energies within the Galaxy.

At GeV γ -ray energies, the sky is dominated by the emissions produced by the CR sea throughout the Milky Way (MW), which have been measured and studied extensively with the *Fermi*–LAT (Ackermann et al. 2012). Recovering individual CR source characteristics at these energies relies on extracting them from the much brighter diffuse fore/background emissions that they are embedded within.

Determination of these fore/background emissions using a physically motivated methodology is desirable as it enables a more reliable estimate of the true source characteristics. Furthermore, residuals resulting from the subtraction of the fore/background emissions can be interpreted as true features of physical interest. Generally, analyses of the *Fermi*–LAT data employ physically motivated interstellar emissions models (IEMs) based on gas tracers and other templates modelled using the GALPROP code (e.g. Acero et al. 2016a, b; Ajello et al. 2016). Systematic studies using such IEMs have been employed for extracting source properties, in particular, for various supernova remnants (SNRs) that are the putative major CR source class (Acero et al. 2016b).

For the very-high energy (VHE) range, the emissions about source regions are brighter than the diffuse emission. The recent release of the H.E.S.S. Galactic plane survey (HGPS; Abdalla et al. 2018) shows localized, extended regions embedded in lower-intensity, broadly distributed emissions – similar to but not exactly the same as the *Fermi*–LAT data at lower energies. This is due to combined effects. The VHE CRs are more concentrated about the sources. Also, high-energy stereoscopic system (H.E.S.S.) uses ‘off source’ fields for background estimation, which likely removes some diffuse emissions and does not enable probing lower fluxes. Recovering source properties for dimmer sources requires proper assessment and accounting for the diffuse emissions.

The VHE diffuse emission is currently observed with low significance by H.E.S.S. (Abramowski et al. 2014), and the spectral extrapolation of a *Fermi*–LAT IEM indicates a general compatibility

* E-mail: peter.marinos@adelaide.edu.au

with the TeV flux observed by ARGO-YBJ (Bartoli et al. 2015). There is a connection between the GeV and TeV energy ranges, but the energy dependence of the mixture of emissions from the general ISM (true ‘diffuse’), those emanating from the relatively nearby interstellar space about the sources, and the sources themselves, is not well understood. Looking forward, accurately determining their relative contributions will be essential for the next generation of facilities that will have a significantly enhanced sensitivity. An example is the Cherenkov Telescope Array (CTA; CTA Consortium et al. 2019), which is currently under construction.

CTA will have a much larger field of view ($\sim 10^\circ$) than H.E.S.S., an improved angular resolution (by a factor $\gtrsim 5$), and will be at least an order of magnitude more sensitive (Actis et al. 2011). The lower flux levels that CTA will reach, and its much larger field of view, will make it extremely sensitive to the details of the diffuse emissions. CTA will also detect hundreds of new γ -ray sources. Consequently, source confusion, together with the other emissions, will likely be a significant issue that will need to be addressed. Distinguishing between the diffuse and general ISM related emissions, and extended emission coming from the $\gtrsim 10$ –100 pcs region, surrounding the sources will be critical for accurate recovery of the embedded source properties (Acero et al. 2013; Dubus et al. 2013; Ambroggi, De Oña Wilhelmi & Aharonian 2016).

In this paper, we use the GALPROP CR propagation package to model the diffuse emission into the VHE range for a grid of models that are categorized by CR source density and ISM target density distributions. The models are all spatially 3D and the CR intensity distributions through the ISM are solved for the steady-state case with the propagation parameters optimized to reproduce local CR data. We compare the model predictions with the HGPS observations, carefully accounting for the survey characteristics. We investigate the variation of the predictions for the diffuse emissions across this model grid and use it to estimate the modelling uncertainty. The GALPROP predictions are comparable to lower limits on the diffuse emission at TeV energies inferred from the HGPS observations, when accounting for current estimates of the unresolved source fraction in the data. We discuss also how the accurate modelling of the diffuse emissions and creation of TeV IEMs will be a critical element for maximizing the scientific return from the more sensitive observations by facilities such as CTA.

2 GALPROP MODELLING

The GALPROP framework (Moskalenko & Strong 1998; Strong & Moskalenko 1998) is a widely employed CR propagation package that now has over 25 years of development behind it. For this paper, we use the latest release (v57), where an extensive description of the current features is given by Porter, Jóhannesson & Moskalenko (2022).

2.1 Model set-up

For an assumed propagation phenomenology, the critical inputs for a GALPROP run are the CR source density distribution, together with the distributions of the other ISM components that result in the energy losses and corresponding secondary particle and emissions production. The CR source distribution is subject to considerable uncertainty, and we construct a representative set of 3D models varying the respective content of sources distributed in the Galactic disc and spiral arms. Meanwhile, GALPROP has well developed 3D models for the interstellar gas and radiation fields, and a collection of GMF models taken from the literature. We fix the interstellar

gas model and make predictions for combinations of the interstellar radiation and magnetic field distributions over the CR source density distributions. We describe in detail below these elements for our calculations.

2.1.1 The interstellar gas

The ISM gas consists mostly of H and He with a ratio of 10:1 by number (Ferrière 2001). It can be found in the different states, atomic (H I), molecular (H_2), or ionized (H II), while He is mostly neutral. H I is ~ 60 per cent of the mass, while H_2 and H II contain 25 and 15 per cent, respectively (Ferrière 2001). The H II gas has a low number density and scale height \sim few 100 pc. The H_2 gas is clumpy and forms high-density molecular clouds.

For this paper, we use the 3D gas density distributions for the neutral ISM developed by Jóhannesson, Porter & Moskalenko (2018). They were obtained using a maximum-likelihood forward model folding method to the LAB H I-survey (Kalberla et al. 2005), and the CFA composite CO survey (Dame, Hartmann & Thaddeus 2001). These neutral gas models include a warped and flaring disc, four spiral arms, and a central bulge. For the H II, we employ the NE2001 model (Cordes & Lazio 2002, 2003; Cordes 2004) with the updates by Gaensler et al. (2008). The CR energy losses and fragmentation (for nuclei) depend on the spatial density distribution for the interstellar gas.

For calculating gas-related γ -ray intensities, we use the gas column-density maps based on the HI4PI survey (HI4PI Collaboration et al. 2016) and the composite CO survey, with a correction for the contribution of missing so-called ‘dark gas’ (Grenier, Casandjian & Terrier 2005), using a map of optical depth at 353 GHz based on *Planck* data (Planck Collaboration et al. 2016). The gas column density maps for atomic and molecular hydrogen are split into Galactocentric radial bins using a rotation curve (Ackermann et al. 2012) due to the limited kinematic resolution of the data. The line-of-sight integration uses the gas density model to accurately weight the CR flux over the extent of the individual rings. This enables the use of the full resolution of the CR intensity solutions that determine the secondary emission emissivities. Helium and heavier elements are assumed to be identically distributed and are accounted for by correction factors.

2.1.2 The CR source distributions

While the SNRs are believed to be the principal CR source class, pulsar wind nebulae (PWNe) and other types likely contribute at some level, but the relative amount is poorly known. For the purpose of this paper, we do not specify the individual source classes that are typically given according to 2D Galactocentric averaged distributions (e.g. Ackermann et al. 2012). Instead we construct a set of synthetic distributions with systematic gradation of the proportion between disc and spiral arm components to investigate the effect of the 3D source distribution on the VHE γ -ray emissions.

We follow Porter, Jóhannesson & Moskalenko (2017) and Jóhannesson et al. (2018), using the disc-like distribution from Yusifov & Küçük (2004) and four spiral arms. The spiral arms have the geometry of those for the R12 ISRF model (see below), but with equal weighting for their normalizations. Our CR source distributions start with a purely disc-like distribution (that we term SA0), and increase with relative contribution by the spiral arms until the distribution is purely due to the spiral arms (termed SA100). Consequently, we have the SA0, SA25, SA50, SA75, and

5038 *P. D. Marinos et al.*

SA100 distributions corresponding to 0, 25, 50, 75, and 100 per cent, respectively, for the source luminosity contained in the spiral arms, with the remaining source luminosity in the disc-like component. The primary CR source spectra and other parameters are determined for each model by the optimization procedure described below.

2.1.3 The interstellar radiation and magnetic fields

The CR electrons and positrons lose energy via Compton and synchrotron interactions with the interstellar radiation and magnetic fields. Into the VHE range, these processes strongly influence the CR spectral intensities and correspondingly affect the intensity distribution for the γ rays. Because there is still uncertainty for the ISRF and GMF distributions, we employ representative models that are available within the GALPROP framework.

The ISRF encompasses the electromagnetic radiation within the Galaxy, including emission from stars, infrared light from interstellar dust radiating heat, and the cosmic microwave background (CMB). The state-of-the-art 3D ISRF models for the MW were developed by Porter et al. (2017) based on spatially smooth stellar and dust models. They have designations R12 and F98 that correspond to the respective references supplying the stellar/dust distributions (Freudenreich 1998; Robitaille et al. 2012). They similarly reproduce the data, but neither is an overall best match. The R12 model provides better correspondence toward the spiral arm tangents, but does not display the asymmetry associated with the bar (R12 has an axisymmetric stellar bulge), and the stellar disc scale length is incompatible with the near-IR profiles. Meanwhile, the F98 model has the disc scale length in better agreement with the near-IR data, incorporates the bulge/bar asymmetry, but has none of the structure associated with the spiral arms.

Both R12 and F98 models are providing equivalent solutions for the ISRF distribution. At least toward the inner Galaxy, where the ISRF intensity is most uncertain, they are providing lower and upper bounds as determined by pair-absorption effects on sources toward the Galactic centre (GC; Porter et al. 2018).

The GMF consists of the large-scale regular (Beuermann, Kanbach & Berkhuisen 1985) and small-scale random (e.g. Sun et al. 2008) components that are about equal in intensity. The random fields are mostly produced by the SNe and other outflows, which result in randomly oriented fields with a typical spatial scale of $\lesssim 100$ pc (Gaensler & Johnston 1995; Haverkorn et al. 2008). Also, there may be the anisotropic random (‘striated’) fields that are a large-scale ordering originating from stretching or compression of the random field (Beck 2001). This component is expected to be aligned to the large-scale regular field, with frequent reversal of its direction on small-scales. GALPROP includes multiple large-scale MW GMF models (Sun et al. 2008; Jaffe et al. 2010; Sun & Reich 2010; Pshirkov et al. 2011; Jansson & Farrar 2012).

In this paper, we use the bisymmetric spiral GMF model from Pshirkov et al. (2011), that we refer to as the Pshirkov bisymmetric spiral (PBSS), as a representative model with a spiral structure. We also employ the GALPROP axisymmetric exponential distribution (GASE; Strong, Moskalenko & Reimer 2000). It has the functional form for Galactocentric coordinates R, Z :

$$B(R, Z) = B_0 \exp\left(-\frac{R - R_0}{H_R}\right) \exp\left(-\frac{|Z|}{H_Z}\right), \quad (1)$$

where $B_0 = 5 \mu\text{G}$ is the magnetic field strength, $R_0 = 8.5$ kpc is the IAU recommended distance from the GC to the Earth (Kerr & Lynden-Bell 1986), and $H_R = 10$ kpc and $H_Z = 2$ kpc are the scale heights for the radial and height components, respectively.

This distribution is a simple, exponentially decreasing field in both Galactocentric radius and height above the plane, and does not include the spiral arms. Although, there are more modern GMF distributions that have better agreement with radio data, including those mentioned above, the GASE GMF is still commonly used throughout the literature (e.g. Korsmeier & Cuoco 2022; Qiao et al. 2022). The use of the GASE GMF in this work is, therefore, to allow us to better characterize the variation between commonly used GMF distributions.

2.1.4 Parameter optimization

For this paper, we assume a diffusive-reacceleration propagation model with isotropic and homogeneous spatial diffusion coefficient.¹ The consistency condition is that each combination of the inputs described above reproduces the local CR spectra. To ensure this, we optimize the propagation parameters and source spectra as described below.

The CR propagation calculations use a 3D right-handed spatial grid with the Solar system on the positive X -axis and $Z = 0$ kpc defining the Galactic plane with $R_S = 8.5$ kpc for the distance from the Sun to the GC. For runtime efficiency, we use the non-uniform grid functionality included with the v57 GALPROP release (Porter et al. 2022) for solving the propagation equations. We employ the tangent grid function where the parameters for the transformation function are chosen so that the X/Y resolution nearby the Solar system is ~ 30 pc, increasing to ~ 1.2 kpc at the boundary of the Galactic disc, which is at 20 kpc from the GC. In the Z -direction, the resolution is 15 pc in the plane, increasing to 0.6 kpc at the boundary of the grid at $|Z_{\text{halo}}| = 6$ kpc (Jóhannesson et al. 2016). The kinetic energy grid is logarithmic from 1 GeV to 1 PeV with 10 planes per decade.

We follow the procedure in Porter et al. (2017) and Jóhannesson et al. (2018) with the CR data from Jóhannesson, Porter & Moskalenko (2019) (see their table 1). For each of the source distributions, an initial optimization of the propagation models is made by fitting to the observed CR spectra from AMS-02 and *Voyager 1* in the GeV energy range, where the CR sea is the dominant source of CRs. This procedure is performed for the CR species: Be, B, C, O, Mg, Ne, and Si. These are kept fixed, and the injection spectra for electrons, protons, and He are tuned together. As the proton spectrum impacts the normalization of the heavier species, and therefore also impacts their propagation parameters, this process is performed iteratively until convergence. As we are extrapolating outside the energy range of the data, the best-fitting model for the source distributions is determined via a χ^2 test, and then its local CR spectra are used to re-optimize the CR data for the other source distributions. This is to ensure that all five source distributions give the same local CR spectra, reducing inconsistencies between the distributions due to limited data statistics and coverage over the modelled energy range. Examples between the model and data agreement are provided in Porter et al. (2017) up to 1 TeV/nucleon. For higher energies, the spread of the observations is larger, and a range of spectral indices can be consistent with the measurements. For example, for protons with energies around 10^6 GeV, the difference between experiments in the measured fluxes with uncertainties is approximately an order of magnitude (Choi et al. 2022). The parameters that vary with the source distributions are shown in Table 1.

¹Note that the spatial diffusion coefficient for the CR propagation can be linked to the GMF strength distribution in GALPROP (Ackermann et al. 2015), but we do not use this functionality for this paper.

Table 1. The optimized GALPROP propagation parameters for each of the five different source distributions.

Parameter	SA0	SA25	SA50	SA75	SA100
$D_{0,xx}$ [10^{28}]	4.36	4.39	4.55	4.67	4.66
δ_0	0.354	0.349	0.344	0.340	0.339
v_{Alfven}	17.8	18.2	18.1	19.8	19.1
J_p [10^{-9}]	4.096	4.404	4.113	4.329	4.394
J_{e^-} [10^{-10}]	3.925	4.444	3.994	4.428	4.502
γ_{0,e^-}	1.616	1.390	1.488	1.455	1.521
γ_{1,e^-}	2.843	2.756	2.766	2.763	2.753
γ_{2,e^-}	2.493	2.460	2.470	2.447	2.422
R_{1,e^-}	6.72	5.27	5.14	5.54	5.29
R_{2,e^-}	52.4	81.6	67.7	70.7	79.7
$\gamma_{0,p}$	1.958	1.928	1.990	1.965	2.009
$\gamma_{1,p}$	2.450	2.464	2.466	2.494	2.481
$\gamma_{2,p}$	2.391	2.411	2.355	2.374	2.414
$R_{1,p}$	12.0	12.3	12.2	14.5	13.5
$R_{2,p}$	202	157	266	108	125
$\gamma_{0,\text{He}}$	1.925	1.886	1.956	1.937	1.971
$\gamma_{1,\text{He}}$	2.417	2.421	2.432	2.467	2.443
$\gamma_{2,\text{He}}$	2.358	2.369	2.320	2.347	2.376
$R_{1,\text{He}}$	12.0	12.3	12.2	14.5	13.5
$R_{2,\text{He}}$	202	157	266	108	125
$\gamma_{0,z}$	1.328	1.519	1.426	1.630	1.624
$\gamma_{1,z}$	2.377	2.390	2.399	2.399	2.418
$\gamma_{2,z}$	2.377	2.390	2.399	2.399	2.418
$R_{1,z}$	3.16	4.21	3.44	4.61	4.50
$R_{2,z}$ [10^3]	5.00	5.00	5.00	5.00	5.00

Notes. $\gamma_{0,\text{CR}}$ is the power-law index before the first break, $\gamma_{1,\text{CR}}$ between the first and second, and $\gamma_{2,\text{CR}}$ after the second break.

$R_{1,\text{CR}}$ [GV] is the rigidity of the first break, and $R_{2,\text{CR}}$ [GV] is the rigidity of the second break.

The diffusion coefficient ($D_{0,xx}$) is measured in $\text{cm}^2 \text{s}^{-1}$, the Alfven velocity (v_{Alfven}) in km s^{-1} , and the CR normalization constants (J_p and J_{e^-}) are measured in $\text{MeV}^{-1} \text{cm}^{-2} \text{s}^{-1} \text{sr}^{-1}$.

The CR injection spectra are given by the power-law $dn/dp \propto R^{-\gamma}$ with two spectral breaks, and is defined separately for electrons, protons, Helium, and a single spectral form for all CR species heavier than Helium. The proton and electron spectra are normalized at the Solar position to J_p and J_{e^-} at the energies $E_{\text{kin},p} = 100 \text{ GeV}$ and $E_{\text{kin},e^-} = 34.5 \text{ GeV}$, respectively, with heavier elements normalized relative to the proton spectrum at 100 GeV/nuc. The CR spectral breaks are given by the rigidities $R_{1,\text{CR}}$ and $R_{2,\text{CR}}$, and the spectral indices are given by $\gamma = \gamma_{0,\text{CR}}$ for rigidities $R < R_{1,\text{CR}}$, $\gamma = \gamma_{1,\text{CR}}$ for rigidities $R_{1,\text{CR}} < R < R_{2,\text{CR}}$, and $\gamma = \gamma_{2,\text{CR}}$ for rigidities $R > R_{2,\text{CR}}$. The diffusion coefficient is given by the power-law $D(R) \propto \beta R^\delta$, and is normalized to $D_{0,xx}$ at the rigidity $R_{0,D} = 4 \text{ GV}$ with the spectral index given by $\delta = \delta_0$. The normalization rigidity, spectral breaks, and spectral index after the break are held constant across all models. Finally, as the γ -ray spectrum at a given energy always depends on more energetic CRs, we set the nuclei cut-off energy (E_{max}) to 1 PeV/nuclei across all models to ensure the correct treatment of the γ -ray spectrum up to 100 TeV.

Although, there are hints for a cut-off in the local (i.e. post propagation) electron spectrum above $\sim 10 \text{ TeV}$ (e.g. Aharonian et al. 2009; DAMPE Collaboration et al. 2017), local measurements are unable to constrain the CR electron spectrum across the entire MW due to the short ($< 1 \text{ kpc}$) travel distances of multi-TeV electrons. As electrons are known to be accelerated in the MW up to PeV energies by PWNe, no artificial cut-off is applied to the CR electron injection spectrum for our models.

2.2 Interstellar emissions modelling predictions

The propagation model parameters for each source distribution (Table 1) are used to calculate steady-state CR intensity solutions across the Galaxy using GALPROP. The spatial grid used for the CR propagation calculations is also employed for determining γ -ray emissivities. The γ -ray intensity maps at the Solar system location are obtained by line-of-sight (LOS) integration of the γ -ray emissivities for the standard processes (π^0 -decay, IC scattering), where the emissivities are determined for a logarithmic grid from 1 GeV to 100 TeV using five bins per decade spacing. We use a ninth-order HEALPix (Górski et al. 2005) isopixelization for the skymap generation.² All calculations of the IC component use the anisotropic scattering cross section (Moskalenko & Strong 2000), which accounts for the full directional intensity distribution for the R12/F98 ISRF models. The $\gamma\gamma \rightarrow e^\pm$ attenuation that affects the γ -ray intensities mainly $\gtrsim 10 \text{ TeV}$, is included in the LOS integration, where the optical depth calculation includes the directionality of the ISRF (Moskalenko, Porter & Strong 2006; Porter et al. 2018). For the R12/F98 ISRF models, the relevant precomputed optical depth maps included with the v57 GALPROP release are employed.

Fig. 1 shows the predicted fluxes from 1 GeV to 100 TeV averaged over different Galactic quadrants about the plane and within 30° of the north/south polar regions. For clarity, we show only the modelled fluxes for the SA0 and SA100 distributions for the R12/PBSS ISRF/GMF combination (other combinations display qualitatively similar trends). Along the plane, for the central longitudes ($l \leq |90^\circ|$) and central latitudes ($b \leq |10^\circ|$), the IC emission starts to account for a large fraction of the total γ -ray emission around 100 GeV, and dominates the TeV Galactic emission after 10 TeV, for all source distributions. For the outer-Galactic region, where there are fewer CR sources ($l \geq |90^\circ|$), the IC provides a strong relative contribution until $\sim 10 \text{ TeV}$ energies, when there is less variation overall between the SA distributions. Meanwhile, towards the polar regions ($b \geq |60^\circ|$), there is a much lower column density for the ISM gas, which results in a reduction of the π^0 -decay emissions intensity. Because the scale height of the ISRF is larger than that of the gas, the IC emission is reduced to a lesser degree over these parts of the sky. This results in it being the strongest component of the γ -ray sky brightness for all SA distributions across the entire spectrum, from 1 GeV to 100 TeV.

Fig. 2 shows the total flux for the various SA distributions averaged over the HGPS analysis region ($l \leq |40^\circ|$ and $-1.5^\circ < b < 1.0^\circ$). As the cooling time for VHE CR electrons is short, the impact of the source distribution is most easily seen for the IC emission contribution. Source density distributions with a higher weighting for CR sources in the arms generally boost the IC signal. This is due to the greater concentration of CR injection about the arms together with the higher ISRF/GMF densities that are also similar in distribution to the sources. This ‘density squared’ effect (Porter et al. 2017) enhances the emissions over the more smoothly distributed model combinations. The impact is such that for the SA100 distribution the IC flux at 100 TeV is a factor ~ 2 brighter than that from the SA0 distribution.

Enhancements due to the ISRF distribution mainly affect the IC emissions for energies $\lesssim 10 \text{ TeV}$. In Fig. 3, we show predicted fluxes over the HGPS region with variation for the ISRF model. Below $\sim 100 \text{ GeV}$, the stronger optical ISRF about the spiral arms in the R12 model enhances the IC emissions when compared to the

²This gives a pixel size of 6.9 arcmin, which is similar to the point-spread function of H.E.S.S. (4.8 arcmin).

5040 *P. D. Marinos et al.*

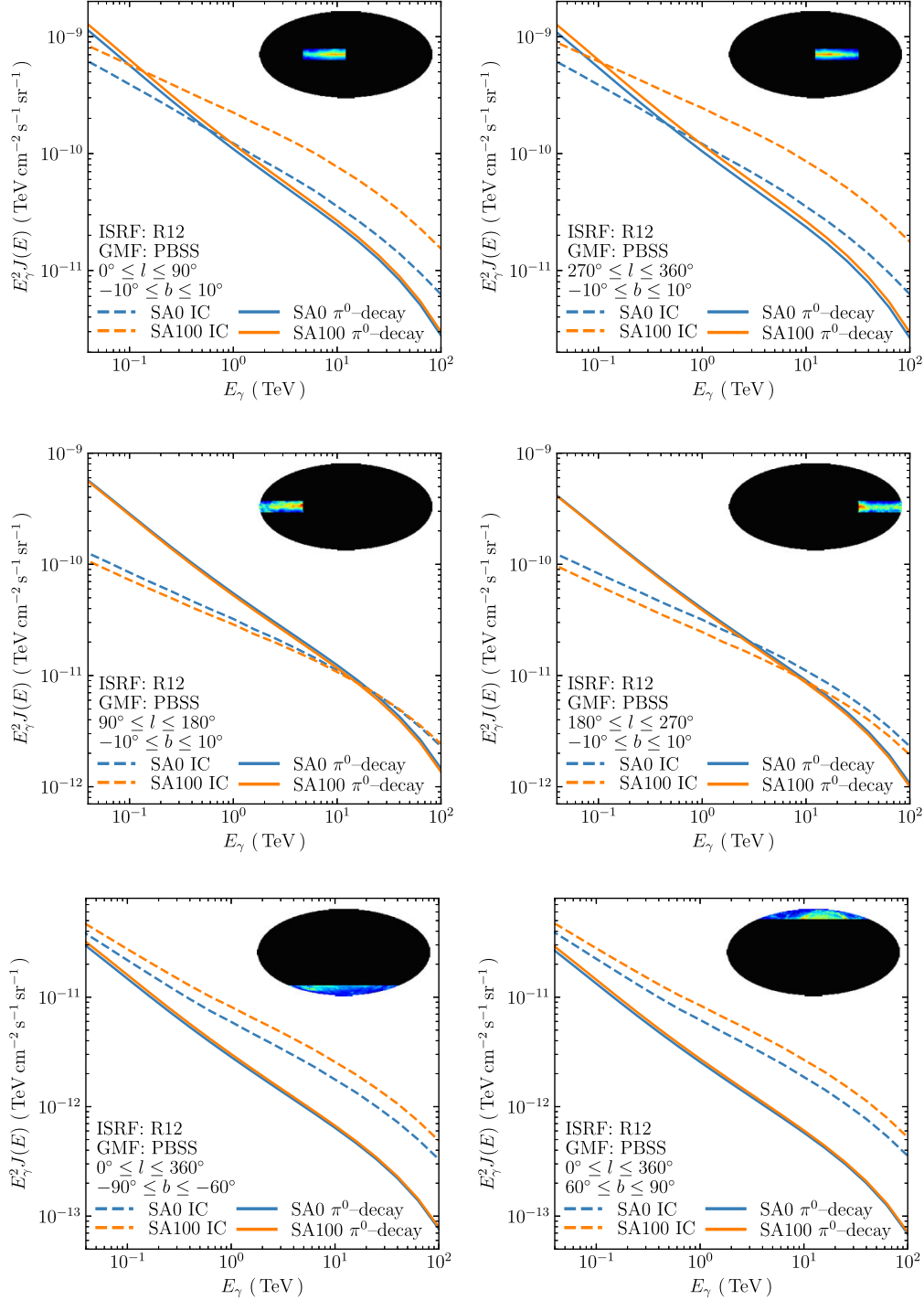


Figure 1. Model spectra for the γ -ray emission for four quadrants along the Galactic plane as well as the poles, with the inset showing the sky regions from which the flux was taken. The SA0 and SA100 models are shown as upper and lower bounds, with the solid lines corresponding to π^0 -decay and the dashed lines corresponding to IC emission. For all regions, the ISRF was chosen to be R12 and the GMF was chosen to be PBSS.

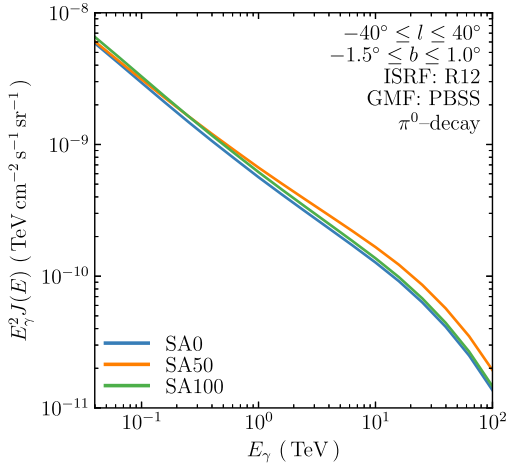
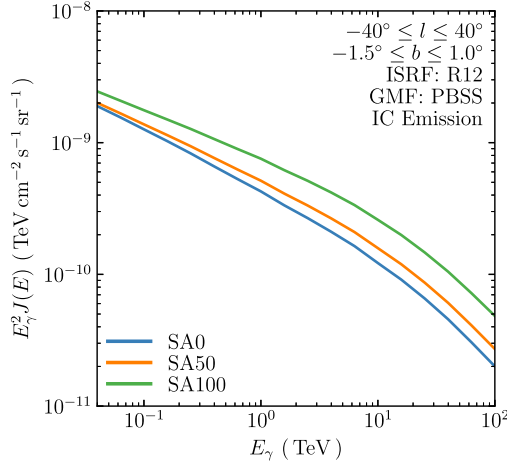


Figure 2. The model spectra averaged over the box ($l \leq |40^\circ|$) and ($-1.5^\circ < b < 1.0^\circ$) for the R12 ISRF and the PBSS GMF. SA0 is shown in blue, SA50 in orange, and SA100 in green. TOP: IC emission, BOTTOM: π^0 -decay.

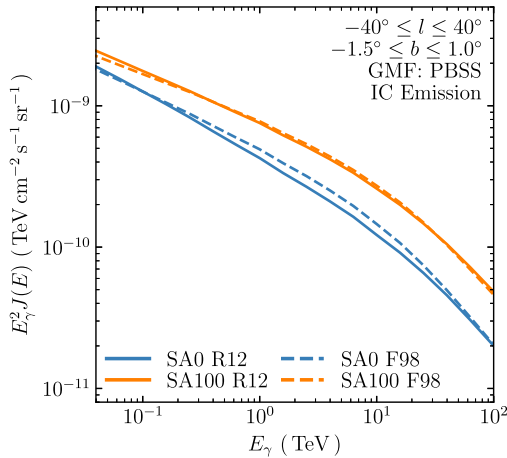


Figure 3. The model spectra of the IC emission averaged over the box ($l \leq |40^\circ|$) and ($-1.5^\circ < b < 1^\circ$) for the PBSS GMF. The source distributions shown are SA0 (blue) and SA100 (orange), and the ISRF distributions shown are R12 (solid line) and F98 (dashed line).

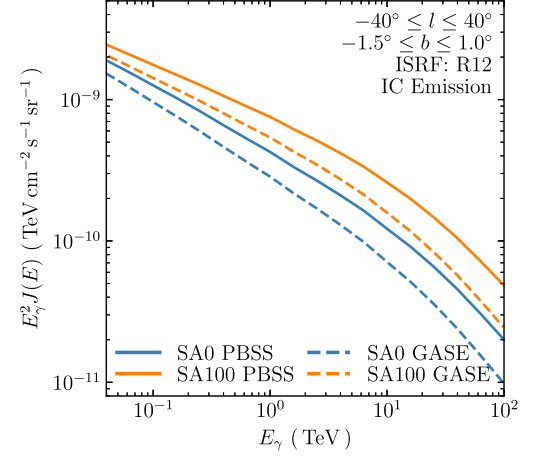


Figure 4. The model spectra of the IC emission averaged over the box ($l \leq |40^\circ|$) and ($-1.5^\circ < b < 1^\circ$) for the R12 ISRF. The source distributions shown are SA0 (blue) and SA100 (orange), and GMF distributions shown are PBSS (solid line) and GASE (dashed line).

F98 model. At higher energies, the Klein–Nishina (KN) suppression reduces this effect, and the predictions for both become closer due to how the IR component of the respective ISRF models is distributed relative to the CR electrons. For energies ~ 1 – 2 TeV the IC emission for the SA0 distribution varies ~ 10 per cent between the R12 and F98 ISRFs, while there is little variation switching between the ISRF models for the SA100 distribution. This variation for the SA0 distribution is due to the peaking of the source density about the GC. There is a correspondingly higher electron intensity across the inner Galaxy that can produce IC emissions. While for the SA100 distribution, there is little variation as the inner cut-off for the spiral arms effectively produces a central ‘hole’ in the electron intensity distribution. Therefore, there is much less IC emission coming from the inner Galaxy for this source density distribution. For energies $\gtrsim 10$ TeV even the IR component becomes KN suppressed as well, and only scattering of the CMB is contributing to the emission. The result is a negligible difference between the ISRF models at higher energies, where the different predictions is due solely to the varying source density distributions.

Fig. 4 shows the variation of the IC flux when the GMF model is varied for fixed ISRF distribution. Varying the GMF distribution has a significant effect on the IC emission as energy increases into the VHE range due to the synchrotron losses dominating the cooling time-scale for the electrons. At 1 TeV, the difference in the IC emission between the PBSS and GASE distributions is approximately 30 per cent, increasing to 100 per cent by 100 TeV. For synchrotron emission, the energy radiated by TeV electrons over time (\dot{E}/E) is proportional to the square of the magnetic field strength (B) of the medium that they diffuse through and the energy of the particle, i.e. $\dot{E}/E \propto E^2 B^2$. As the radiative losses of electrons depends strongly on the magnetic field strength, regions with higher GMF energy density will rapidly be depleted of high-energy electrons. The GASE distribution has the most intense region of the field at the GC, leading to the IC emission being greatly reduced in the GC when compared to the PBSS distribution.

Fig. 5 shows the longitudinal profile of the IC and π^0 -decay emission for the various source distributions for energy levels between 0.1 and 100 TeV. The π^0 -decay dominates the γ -ray emission

5042 *P. D. Marinos et al.*

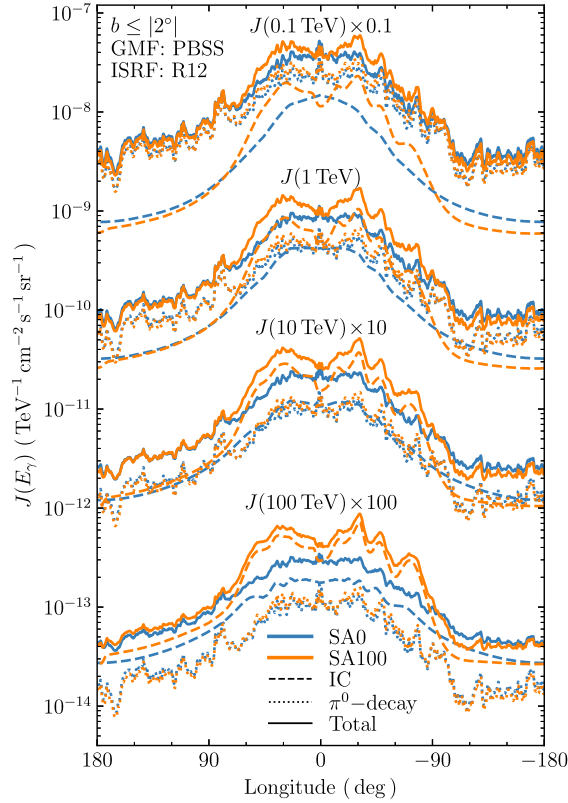


Figure 5. Longitude profile for $b \leq |2^\circ|$ along the Galactic plane for various energies using the R12 ISRF and the PBSS GMF distributions. The source distributions shown are SA0 (blue) and SA100 (orange), and the emission types shown are IC (dashed), π^0 -decay (dotted), and the total flux (solid). The profiles have been multiplied by the given factors to increase contrast.

for all longitudes for the energies $E < 1$ TeV. Because the energy losses for CR nuclei are slow and the diffusion is relatively fast, the propagated distributions for them are fairly smoothly distributed over all source distributions. There is, correspondingly, minimal impact on the π^0 -decay component in the longitudinal profiles. Meanwhile, the IC emission becomes dominant for $\gtrsim 10$ TeV energies. Because the energy losses are much faster for the electrons, its contribution to the profiles is much more sensitive to changes in the source distribution over most of the Galactic plane. As the majority of the spiral arms are located between the Earth and the GC, with one of the arms located in close proximity to the Earth, we see that for a larger fraction of CRs being injected into the spiral arms (e.g. SA100), the IC component becomes more intense for the central region (i.e. $l \leq |50^\circ|$). The IC emission is also boosted along the spiral arm tangents located at $l \approx |20^\circ|$. For the negative longitudes between the anticentre and perpendicular to the GC, i.e. for $-90^\circ < l < -180^\circ$, the IC emission decreases with an increasing fraction of CR injection in the spiral arms, and the difference between the source density distributions increases with increasing energy.

Across the entire plane for all source distributions, the IC emission dominates the γ -ray emission at 100 TeV. It is not a surprise that the spiral structure in the source density distributions including arms is evident in the profiles. However, at these energies there also appears to be structure for the SA0 density distribution IC profile similar to those models including arms that is not apparent at lower energies.

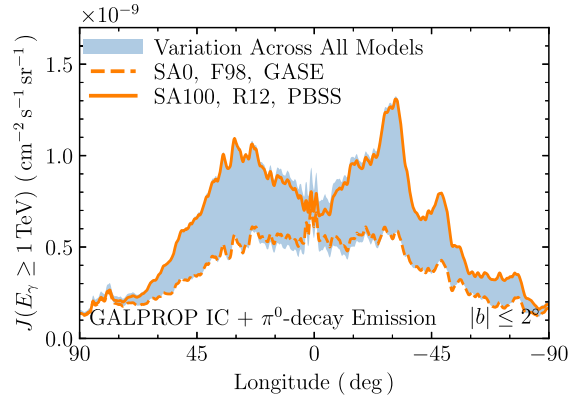


Figure 6. The envelope of the longitudinal profiles of the total average flux integrated above 1 TeV for Galactic latitudes $|b| \leq 2^\circ$. Two individual GALPROP runs are shown, using the SA100, R12, and PBSS distributions (solid), and SA0, F98, and GASE distributions (dashed).

Because of the KN suppression for the optical and IR components of the ISRF, the only photon field is the (uniform) CMB for IC processes. The energy density of the GMF varies, but is much higher than that for the CMB about the spiral arms, and hence determines the energy loss time-scale affecting the electron distribution. The observed structure in the 100 TeV IC profile for the SA0 distribution is, therefore, entirely due to that encoded in the PBSS GMF distribution, with its influence imprinted on the electron energy density.

For the spiral arms in the source distributions, the closest arm in the sky region $-90^\circ < l < -180^\circ$ is the Perseus arm located ~ 3 kpc away. For the source distributions with a high fraction of CR injection in the spiral arms (e.g. SA75 and SA100), there is a large void of electron sources between the Solar system and the Perseus arm, resulting in reduced TeV IC emission in that direction. However, as the Galactic disc component of the source distributions is smoothly varying, the source distributions with a low fraction of CR injection in the spiral arms (e.g. SA0 and SA25) have boosted TeV IC emission in these regions, as CRs are injected in the voids between the Solar system and the Perseus arm. This is not seen in the positive longitudes far from the GC ($90^\circ < l < 180^\circ$) as the Perseus arm is close enough to the Solar system such that there is no void in the electron densities in any of the source distributions. The proximity of the Perseus arm leads to a lower degree of variation in the IC emission in this region of the Galactic plane across the SA distributions. Figs 4 and 5, therefore, show that the source distributions with a larger fraction of sources in the spiral arms show increased IC emission along the arm tangents, with the IC emission dominating over the pion-decay at 1 TeV along the arms.

Fig. 6 shows the envelope of longitudinal profiles at 1 TeV of all the GALPROP runs across our model grid, i.e. any combination of the source distribution, ISRF, and GMF. Due to using a mix of distributions that include the spiral arms and those that do not (e.g. combining the SA0 with the PBSS distribution), no single GALPROP run describes the lower or upper bound of the envelope. However, from the upper/lower bounds, we infer that there is a ± 50 per cent variation over the entire grid of GALPROP predictions for models that are consistent with the local CR data. Changing the source distribution alone tends to alter the longitudinal profile most significantly toward the spiral arm tangents, where the variation can be up to ~ 40 per cent when comparing SA0 to SA100. Toward the inner Galaxy, there are smaller differences, due to both the lower number of sources about the GC for distributions with spiral arms, and to the smoothing from

the LOS integration over the long path lengths for these directions. For similar reasons, changing the ISRF model impacts the results only modestly (up to ~ 4 per cent) around the central plane $|l| \leq 30^\circ$. Meanwhile, changing the GMF model has the strongest effect around the central $|l| \leq 100^\circ$, where the impact can be up to ~ 20 per cent variation. We show overlaid in Fig. 6 two individual results – one with no spiral arms in the CR injection distribution, ISRF, or GMF (i.e. the SA0, F98, and GASE configuration), and the other having spiral arms in all three (i.e. the SA100, R12, and PBSS configuration). The variation between the predictions is generally driven by the increasingly complex 3D structures for the respective components of the models that we have considered.

3 COMPARING THE HGPS TO GALPROP

The HGPS represents the most comprehensive survey of the Galactic plane at TeV energies to date. Extraction of an estimate for the HGPS diffuse contribution requires accounting for the treatment of the CR background in the data. For this H.E.S.S. used the adaptive ring method, with a set of exclusion zones that cover approximately two thirds of the Galactic plane, such that no γ -ray sources are considered as part of the CR background estimate. However, this may subtract the diffuse γ rays that are captured in the background regions. The HGPS observations also include both discrete and unresolved sources, neither of which are part of the diffuse emission. We briefly describe how we address these issues below, with the full details given in Appendix A.

Our analysis of the HGPS uses the survey sky map with an integration/containment radius of $R_c = 0.2^\circ$, such that we are as sensitive as possible to the TeV diffuse γ -ray emission. We then use a sliding window method with parameters suitably optimized to reveal the longitudinal structure of the diffuse emission (see Appendix A). The sliding window is applied after the masking of known catalogued sources, which either subtracts the catalogued source component of the emission or excludes the catalogued source region from the analysis. It is also necessary to account for the unresolved sources, i.e. the ensemble of γ -ray sources below the detection threshold of H.E.S.S.. Although, they are not individually resolved, these unresolved sources still contribute to the total observed Galactic emission, providing an extended low surface brightness contribution to the observed flux. As they are not part of the truly diffuse emission, their contribution must be subtracted. We use estimates for the unresolved source component from Steppa & Egberts (2020) (herein SE20) and Cataldo et al. (2020) (herein C20) who give relative contributions to the HGPS of 13–32 and 60 per cent, respectively. We combine them with the systematic uncertainty in the H.E.S.S. fluxes to provide lower and upper limits for the diffuse γ -ray emission.

Fig. 7 shows the source-subtracted flux obtained with our method, together with the bounding estimates employing the different unresolved source contributions. This is shown together with the longitudinal profile of the HGPS sensitivity in units of per cent Crab.³ There is a large-scale γ -ray emission along the plane, similar to that found previously by Abramowski et al. (2014). Its brightness varies over the survey area, with the lowest level ~ 2 –3 times below the 5σ point source sensitivity of the HGPS.

We apply the same sliding window procedure to the GALPROP predictions over our model grid (Section 2) to enable a comparison

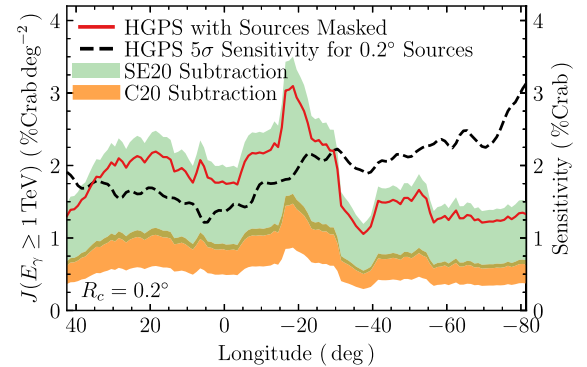


Figure 7. Longitudinal profile of the HGPS emission with catalogued sources subtracted (red), shown after the sliding window has been applied for a containment radius of $R_c = 0.2^\circ$ in units of per cent Crab deg^{-2} . Also shown are the effects of subtracting the unresolved source fractions as estimated by SE20 (green), and C20 (orange). The 5σ sensitivity of the HGPS for $R_c = 0.2^\circ$ is shown by the dashed black line in units of per cent Crab. The analysis uses an averaging windows with a width of $\Delta w = 15^\circ$ and height of $\Delta h = 2.5^\circ$, centred at a latitude of $b_0 = -0.25^\circ$ and spaced $\Delta s = 1^\circ$ apart.

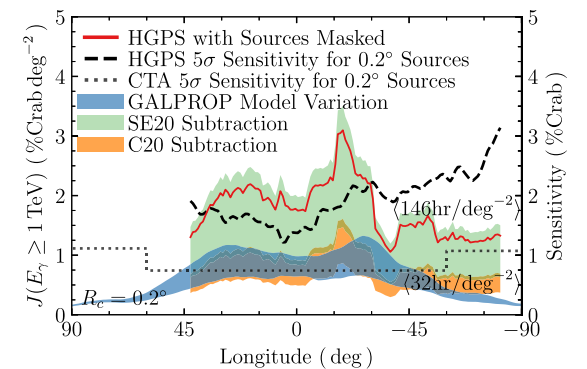


Figure 8. Longitudinal profiles integrated above 1 TeV for the GALPROP variation (blue) and the HGPS after catalogued sources are subtracted (solid red), shown after the sliding window has been applied for a containment radius of $R_c = 0.2^\circ$ in units of per cent Crab deg^{-2} . Also shown are the results after subtracting the unresolved sources, with the estimates of the unresolved sources calculated from the estimates given by SE20 (green), and C20 (orange). The 5σ sensitivity is shown for the HGPS (dashed black) and CTA GPS (dotted black) when using a containment radius of $R_c = 0.2^\circ$, both of which are shown in units of per cent Crab. Averaging windows were applied to both the HGPS and the GALPROP profiles, and have a width of $\Delta w = 15^\circ$ and height of $\Delta h = 2.5^\circ$, centred at a latitude of $b_0 = -0.25^\circ$ and spaced $\Delta s = 1^\circ$ apart.

with the HGPS diffuse flux estimates. Our GALPROP results were converted into units of per cent Crab deg^{-2} to allow comparisons to the HGPS sensitivity, which is given in units of per cent Crab. As GALPROP predicts only the diffuse interstellar emissions, the masking of catalogued and subtracting of the unresolved source component is not required. Fig. 8 shows the comparison between the HGPS longitudinal profile for the range of the GALPROP predictions (see Fig. 6) after the averaging window has been applied. Also shown are the HGPS estimates with subtraction of the SE20 and C20 unresolved source fractions and HGPS sensitivity profile.

³Units of per cent Crab are generally used in VHE γ -ray astronomy. We use the definition $J_{\text{Crab}}(E \geq 1 \text{ TeV}) = 2.26 \times 10^{-11} \text{ cm}^{-2} \text{ s}^{-1}$ (Aharonian et al. 2006)

5044 *P. D. Marinos et al.*

Our GALPROP-based models generally underpredict the large-scale TeV emission estimated from the HGPS. This is due to the HGPS data containing a large number of unresolved sources that artificially inflate the large-scale emission to levels above the TeV diffuse emission. Subtracting the unresolved sources from the large-scale emission via the estimates from SE20 or C20 provides a lower limit on the Galactic diffuse TeV emission. Accounting for this contribution, the GALPROP predictions broadly agree with the diffuse γ -ray emission estimate obtained by subtracting an unresolved source fraction from C20. However, this is not true across the whole longitude range where, e.g. around $l \sim -30^\circ$, we can find better agreement with estimated diffuse flux using the unresolved source fraction from SE20. It is, therefore, likely that the unresolved source contribution lies between those determined by SE20 and C20 across the region spanned by the survey, but it is not clear where either of the models is most applicable.

For Galactic longitudes $-80^\circ \leq l \leq -60^\circ$, the GALPROP predictions are below the lower-limit for the TeV diffuse emission. However, this region of the Galactic plane is well below the 5σ sensitivity of the HGPS, making it difficult to draw any conclusions on the diffuse emission. The disagreement could be due to poor statistics in the region, or that the GALPROP models are insufficiently optimized toward these directions.

4 DISCUSSION

4.1 Interstellar emission model predictions into the TeV energy range

Our work is the first systematic study using the GALPROP framework to predict the diffuse emissions into the TeV energy range for a grid of physical modelling configurations. For the steady-state models that we have considered, generally the π^0 -decay component produced by the CR nuclei interactions with the interstellar gas has only a small variation over the HGPS survey area (Fig. 2). Because the energy losses of these CRs are slow, they are distributed fairly smoothly across the MW with only mild imprints of the source density distribution. However, this is not the case for the IC emissions. Averaged over the HGPS survey area, there is a much stronger variation due to the choice of source distribution. The energy losses for the CR electrons are much more rapid than those for the nuclei. The concentration of the ISRF and GMF energy densities about the spiral arms combines to affect the γ -ray intensities toward those regions, because they approximately coincide toward, where, the source densities with arms tend to also be enhanced. Into the TeV energy range, the IC emissions have much higher sensitivity to the ISRF and GMF energy density distributions.

There are three composite source density distributions in our source density model grid (both Galactic disc and spiral arm components: SA25, SA50, and SA75). For a fixed target density distribution (i.e. holding the ISRF/GMF constant), comparing the 1 TeV γ -ray longitudinal profiles for these three composite source density distributions shows a variation of ~ 10 per cent. When comparing all five source density distributions, we find a much larger variation up to ~ 50 per cent. Altering the target densities as well as the source density distributions, as is done in Fig. 6, shows a variation up to ~ 100 per cent. The effect of progressively more complex 3D structures for the source density and ISRF/GMF components leads to more variation for the TeV emissions from the CR electrons for the propagation model phenomenology that we have used in this paper. However, the envelope of model predictions resulting from variations in the target densities is larger than that from solely changing the source density distribution. While our current understanding of the spatial

distributions of the ISM components that are the targets for producing the VHE emissions is incomplete, we have used models for them that are reasonably agreeing with data. The GALPROP predictions from our study are, therefore, representative of the likely uncertainty associated with current modelling for the VHE diffuse emissions.

We have used a grid of source density models, where the normalization is obtained by requiring consistency of the propagated CR intensity distributions with the data obtained at the Solar system. This is a well-motivated normalization condition, given the considerable uncertainties associated with correctly defining CR source population characteristics. However, there is an effective CR ‘horizon’ beyond which additional components may be added without any noticeable effect when normalizing to the local CR data. For example, CRs injected about the GC likely have a negligible impact on the intensities at the Solar system location. Correspondingly, a source density localized about the inner Galaxy, e.g. distributed similar to the stellar bulge/bar (Porter et al. 2017; Macias et al. 2019), will have its injected CR power as a free parameter. Such additions localized about the inner Galaxy require tuning at other frequencies, e.g. the GeV energy data, to correctly optimize parameters for use as a ‘background’ in the VHE regime. While the uncertainty band for the diffuse emissions that we estimated above is below the 5σ significance level of the HGPS (see Fig. 8), such additional components have the possibility to also contribute toward the inner Galaxy. At the moment, it is likely that a unique solution is not possible for precise estimation of the diffuse background for the HGPS data.

Our modelling has also shown that the IC emissions across the plane starts to become dominant over the π^0 -decay above 10 TeV (Fig. 5). The profiles for $\gtrsim 10$ TeV γ -ray energies display structure in the leptonic component that is due to the combination of the spatial distributions employed for our models. However, at the higher energies (~ 100 TeV), the situation becomes simpler, because the complications of the uncertainty in the ISRF distribution effectively disappear by the KN suppression of the optical and IR components. Only the GMF and source density distributions are determining the structure visible in the longitudinal profiles for these energies. Currently, the GMF models for the MW are poorly constrained, and are most commonly constructed by using rotation measures of extragalactic sources. Given that the GMF structure is observable at 100 TeV, the future VHE/UHE γ -ray observations provide an interesting possibility to constrain the GMF configurations. However, γ -ray emission is created by the convolution of the source density distribution and the target density distributions. The alignment of the GMF and source density distribution is not complete, which is not surprising given that the different tracers for the Galactic spiral structure show offsets (e.g. Vallée 2020). Therefore, using γ -ray observations to constrain the GMF will likely require γ -ray facilities many times more sensitive than what is currently available.

We note that for this paper, we have only considered steady-state models. Into the TeV energy range, the time-dependent solutions, particularly for the CR electrons, are likely necessary (Porter, Jóhannesson & Moskalenko 2019). For example, the Tibet AS γ data indicate that many of the γ rays detected within their $25^\circ < l < 100^\circ$, $|b| < 5^\circ$ window (Amenomori et al. 2021) are not close on the sky to known VHE γ -ray sources. The observational data from Tibet AS γ appears inconsistent with the simple models of Lipari & Vernetto (2018) and Cataldo et al. (2019),⁴ and a discrete

⁴These efforts do not use propagation codes, instead employing simple parametrizations for the CR spectra assuming steady-state conditions, and do not consider the 3D structure of the CR sources and ISM.

origin has been suggested (e.g. Dzhatdov [2021](#); Fang & Murase [2021](#)). Recent results from Vecchiotti et al. ([2022](#)) found that the discrepancy between models and the Tibet AS γ flux could be due to a population of unresolved PWNe, which would likely increase the leptonic component of the $\gtrsim 100$ TeV γ rays. PWN haloes have also been proposed as a large contributor to the unresolved sources for both H.E.S.S. and HAWC (Martin et al. [2022](#)), further suggesting that electrons contribute to the diffuse emission. The increasing contribution by the leptonic component with energy that we have shown in this paper, and its likely significant fluctuations, may help to explain the lack of correlation between the PeV γ rays observed by Tibet AS γ , and neutrinos seen along the Galactic plane. We also have results from HAWC (Abeysekara et al. [2017](#)) and LHAASO (Zhao et al. [2021](#)) that show for energies $\gtrsim 10$ TeV, the localization of emissions about individual sources is stronger. Incorporating time-evolution into the modelling seems to be necessary next step to accurately connect the GeV to 100s TeV energies emissions that are presumably coming from a common origin.

4.2 Application to CTA and other TeV facilities

CTA will perform a Galactic plane survey (GPS) over its first 10 years of operation, which will cover Galactic latitudes in the range $b \leq |5^\circ|$ and all Galactic longitudes, averaging 32 h of observation per square degree (CTA Consortium et al. [2019](#)). The CTA GPS will have an energy range from 100 GeV to 100 TeV, with a resolution of around 3 arcmin for energies above 1 TeV. The 5σ point source sensitivity of CTA's proposed 10 year survey will reach 1.8 mCrab for the inner $l \leq |60^\circ|$ and 3.8 mCrab for the outer Galactic longitudes. For comparison, the HGPS has a point source sensitivity of 4–20 mCrab between $40^\circ \leq l \leq 80^\circ$ with an average of 146 h of observation per square degree. The sensitivity of the proposed CTA GPS after adjusting for a containment radius of $R_c = 0.2^\circ$ is also shown in Fig. 8.

As CTA is expected to detect and resolve on the order of a thousand of new sources (Actis et al. [2011](#)), these exclusion regions will grow to encapsulate a significant fraction of the Galactic plane, if not the entire plane. Allowing nearby sources to contaminate the background, such as would be very likely along the Galactic plane without careful consideration, would significantly reduce the sensitivity of the observations (Ambrogi et al. [2016](#)).

CTA presents a leap forward in terms of the angular resolution it will achieve, with a PSF reaching approximately 1.8 arcmin for γ -ray measurements at 1 TeV. The all-sky HI and CO survey data, that is used for building the neutral ISM model used in this work have resolutions of 27.5 and 13.7 arcmin, respectively. This is adequate for comparisons to the HGPS, but not to CTA's expected GPS. New high-resolution ISM surveys, such as Mopra CO (Braiding et al. [2015](#); Braiding et al. [2018](#)) in the Southern hemisphere, and Nobeyama 45m CO (Minamidani et al. [2015](#); Umemoto et al. [2017](#)), and THOR HI/OH (Beuther et al. [2016](#); Wang et al. [2020](#)) in the Northern hemisphere have become available. High-resolution ISM surveys that can observe the small, dense clumps at comparable or better angular resolution to CTA will become a necessary modelling ingredient for future high-resolution comparisons to its GPS. Due to the high density of these clumps it will also become necessary to adapt the diffusion coefficient to the density of the ISM gas (e.g. Gabici, Aharonian & Blasi [2007](#); Gabici, Aharonian & Casanova [2009](#)).

From Fig. 8, we can see that CTA-South should be able to detect the TeV diffuse γ -ray emission to the 5σ level, given even our conservative estimates of the diffuse γ -ray emission predicted in this paper for the central 80° of longitude ($|l| \leq 40^\circ$). As has already been

seen with the sensitive *Fermi*–LAT data at lower energies, it will, therefore, be necessary to develop accurate models for the diffuse emission to separate individual source characteristics from it. This will be essential for resolving and detecting faint, extended TeV emissions, such as those such as those expected from PWN haloes, and for probing complex morphological structures of TeV sources. This will potentially allow the identification of currently unidentified sources in the HGPS and other current and future observations, such as those from CTA.

For the Galactic longitudes open to Northern-hemisphere observations, i.e. $l > |50^\circ|$, our estimates state that the diffuse emission flux at 1 TeV is below 5 mCrab deg^{-2} . This emission is below the extended source sensitivity for CTA-North, which is planned to perform the deepest GPS of any IACT in the Northern hemisphere at 1 TeV (CTA Consortium et al. [2019](#)). It is, therefore, unlikely that any IACT in the Northern hemisphere, such as VERITAS (Vassiliev [1999](#)) and MAGIC (Aleksic et al. [2012](#)), will observe the diffuse emission. Ground-level particle detectors in the Northern hemisphere, such as LHAASO (Sciasecio [2016](#)), HAWC (Abeysekara et al. [2013](#)), and Tibet AS γ (Sako et al. [2009](#)) are optimized for multi-TeV to PeV observations. This has allowed Tibet AS γ to successfully detect extended, presumably diffuse, emission at PeV energies (Amenomori et al. [2021](#)). However, as these particle detectors are optimized for multi-TeV to PeV observations, it is unlikely they will observe this diffuse emission around 1 TeV within their first 10 years of operation. The Northern hemisphere detector ARGO-YBJ was constructed to be more sensitive at TeV energies, and has measured the diffuse emission at 1 TeV after five years in the region $25^\circ < l < 100^\circ$. The emission predicted by our GALPROP models is within the uncertainty band estimated for these data (Bartoli et al. [2015](#)).

Observation of the Galactic diffuse emission below the PeV regime (e.g. around 1 TeV) will likely remain difficult with the current and the next generation of γ -ray observatories. For the Southern hemisphere, the planned ground-level particle detector SWGO (Albert et al. [2019](#)) has the possibility of observing the Galactic diffuse emission at 1 TeV around the GC within the first 10 years of operation, complementing the higher-resolution CTA-South observations.

5 SUMMARY

We have made a systematic comparison of the predicted diffuse TeV γ -ray emission over a grid of steady-state models generated using the GALPROP framework. For the models that we consider, the variations in source density, ISRF, and GMF distributions can have a significant effect on the predicted IC emissions at VHEs. The magnitude of the variation on the IC emissions around 1 TeV toward the GC can be ~ 50 – 60 per cent. This increases to ~ 100 per cent for ~ 100 TeV energies. The influence of differing ISRF distributions is most important for energies ≤ 1 TeV, modest for ~ 1 – 10 TeV, and vanishes $\gtrsim 40$ – 50 TeV due to the KN suppression that removes all but the CMB as a target photon field for Compton scattering processes at the highest energies. For energies $\gtrsim 20$ – 30 TeV, the CR source density and GMF distributions have the most significant impact on the predicted γ -ray emissions. Generally, the energy losses at VHEs for the CR electrons are most strongly influenced by the GMF distribution. The structure of the GMF is imprinted on the CR electron intensity distribution and, hence, the VHE diffuse emissions produced by them. This is seen in the IC emissions, with the GMF structure becoming more pronounced as energy increases into the ~ 100 TeV range.

Towards the inner Galaxy ($|l| < 40^\circ$, $|b| < 2^\circ$), we found that the leptonic component of the diffuse γ -ray emission begins to become an important consideration around 1 TeV, with the hadronic component dominating for most of the Galactic plane. At 10 TeV, the leptonic emission begins to dominate over the hadronic emission for the inner Galaxy, while the leptonic component is approximately equal in magnitude to the hadronic emission for the region ($|l| > 40^\circ$, $|b| < 2^\circ$). For the ~ 100 TeV energy range, our results show that the IC emission dominates the total diffuse γ -ray emission across the entire plane for all models that we considered. With the GMF structure imprinted on the IC emission in this energy regime, observations of the diffuse γ -ray emission are in a unique position to constrain the GMF structure. Furthermore, our GALPROP predictions and the importance of leptonic emissions for γ -ray energies $\gtrsim 100$ TeV may provide some insight on comparisons between the PeV diffuse γ -ray emission and neutrino fluxes. Due to how rapidly electrons in the 100 TeV to 1 PeV energy range lose their energy, our results motivate the need for a time-dependent solution for future work at these energies.

Our GALPROP predictions of the diffuse γ -ray emission match lower limits on the diffuse TeV emission inferred from the GPS carried out by the H.E.S.S. collaboration, after subtracting the unresolved source fraction estimates calculated from SE20 and C20. Because the GALPROP predictions overlap the lower limits of the TeV diffuse emission inferred from the HGPS after subtracting catalogued sources and estimates of the unresolved source contribution, further optimization of the models may not yield a meaningful impact on analysis for these data. However, the brightness of the GALPROP predictions indicates that it will be necessary to better optimize the models for the more sensitive proposed CTA GPS. The need for better, physically-motivated diffuse emission models at VHEs is further reinforced now that both LHAASO and Tibet AS γ (Amenomori et al. 2021; Zhao et al. 2021) have observed sources of PeV γ rays within the MW.

ACKNOWLEDGEMENTS

This research is supported by an Australian Government Research Training Program Scholarship. GALPROP development is partially funded via NASA grants NNX17AB48G, 80NSSC22K0718, and 80NSSC22K0477. Some of the results in this paper have been derived using the HEALPix (Górski et al. 2005) and Astropy (Astropy Collaboration et al. 2013, 2018) packages. This work was supported with supercomputing resources provided by the Phoenix HPC service at the University of Adelaide, and we want to thank F. Voisin in particular for his many hours spent configuring the HPC service to work efficiently with GALPROP.

DATA AVAILABILITY

The GALPROP configuration files can be found via the GALPROP website: <https://galprop.stanford.edu/>, and the HGPS results can be found via the HGPS (Abdalla et al. 2018) website: <https://www.mpg.de/hfm/HGPS/hgps/>.

REFERENCES

Abdalla H. et al., 2018, *A&A*, 612, A1
 Abeysekara A. U. et al., 2013, *Astropart. Phys.*, 50, 26
 Abeysekara A. U. et al., 2017, *Science*, 358, 911
 Abramowski A. et al., 2014, *Phys. Rev. D*, 90, 122007
 Acero F. et al., 2013, *Astropart. Phys.*, 43, 276

Acero F. et al., 2016a, *ApJS*, 223, 23
 Acero F. et al., 2016b, *ApJS*, 224, 8
 Ackermann M. et al., 2012, *ApJ*, 750, 3
 Ackermann M. et al., 2015, *ApJ*, 799, 86
 Actis M. et al., 2011, *Exp. Astron.*, 32, 193
 Aharonian F. et al., 2006, *A&A*, 457, 899
 Aharonian F. et al., 2009, *A&A*, 508, 561
 Ajello M. et al., 2016, *ApJ*, 819, 44
 Albert A. et al., 2019, preprint (arXiv:1902.08429)
 Aleksic J. et al., 2012, *Astropart. Phys.*, 35, 435
 Ambrogio L., De Oña Wilhelmi E., Aharonian F., 2016, *Astropart. Phys.*, 80, 22
 Amenomori M. et al., 2021, *Phys. Rev. Lett.*, 126, 141101
 Astropy Collaboration et al., 2013, *A&A*, 558, A33
 Astropy Collaboration et al., 2018, *AJ*, 156, 123
 Bartoli B. et al., 2015, *ApJ*, 806, 20
 Beck R., 2001, *Space Sci. Rev.*, 99, 243
 Beuermann K., Kanbach G., Berkhuijsen E. M., 1985, *A&A*, 153, 17
 Beuther H. et al., 2016, *A&A*, 595, A32
 Braiding C. et al., 2015, *PASA*, 32, e020
 Braiding C. et al., 2018, *PASA*, 35, e029
 Cataldo M., Pagliaroli G., Vecchiotti V., Villante F. L., 2019, *JCAP*, 12, 050
 Cataldo M., Pagliaroli G., Vecchiotti V., Villante F. L., 2020, *ApJ*, 904, 85
 Choi G. et al., 2022, in 37th International Cosmic Ray Conference. p. 94
 Cordes J. M., 2004, in Clemens D., Shah R., Brainerd T., eds, ASP Conf. Ser. Vol. 317, Milky Way Surveys: The Structure and Evolution of our Galaxy. Astron. Soc. Pac., San Francisco, p. 211
 Cordes J. M., Lazio T. J. W., 2002, preprint (astro-ph/0207156)
 Cordes J. M., Lazio T. J. W., 2003, preprint (astro-ph/0301598)
 CTA Consortium et al., 2019, Science with the Cherenkov Telescope Array. World Scientific Publishing Company, Singapore doi:10.1142/10986
 Dame T. M., Hartmann D., Thaddeus P., 2001, *ApJ*, 547, 792
 DAMPE Collaboration et al., 2017, *Nature*, 552, 63
 Dubus G. et al., 2013, *Astropart. Phys.*, 43, 317
 Dzhatdov T., 2021, preprint (arXiv:2104.02838)
 Fang K., Murase K., 2021, *ApJ*, 919, 93
 Ferrière K. M., 2001, *Rev. Mod. Phys.*, 73, 1031
 Freudenreich H. T., 1998, *ApJ*, 492, 495
 Gabici S., Aharonian F. A., Blasi P., 2007, *Ap&SS*, 309, 365
 Gabici S., Aharonian F. A., Casanova S., 2009, *MNRAS*, 396, 1629
 Gaensler B. M., Johnston S., 1995, *MNRAS*, 277, 1243
 Gaensler B. M., Madsen G. J., Chatterjee S., Mao S. A., 2008, *PASA*, 25, 184
 Górski K. M., Hivon E., Banday A. J., Wandelt B. D., Hansen F. K., Reinecke M., Bartelmann M., 2005, *ApJ*, 622, 759
 Grenier I. A., Casandjian J.-M., Terrier R., 2005, *Science*, 307, 1292
 Haverkorn M., Brown J. C., Gaensler B. M., McClure-Griffiths N. M., 2008, *ApJ*, 680, 362
 HI4PI Collaboration et al., 2016, *A&A*, 594, A116
 Jaffe T. R., Leahy J. P., Banday A. J., Leach S. M., Lowe S. R., Wilkinson A., 2010, *MNRAS*, 401, 1013
 Jansson R., Farrar G. R., 2012, *ApJ*, 757, 14
 Jóhannesson G. et al., 2016, *ApJ*, 824, 16
 Jóhannesson G., Porter T. A., Moskalenko I. V., 2018, *ApJ*, 856, 45
 Jóhannesson G., Porter T. A., Moskalenko I. V., 2019, *ApJ*, 879, 91
 Kalberla P., Burton W., Hartmann L., Arnal E., Bajaja E., Morras R., Pöppel W., 2005, *A&A*, 440, 775
 Kerr F. J., Lynden-Bell D., 1986, *MNRAS*, 221, 1023
 Korsmeier M., Cuoco A., 2022, *Phys. Rev. D*, 105, 103033
 Lipari P., Vernetto S., 2018, *Phys. Rev. D*, 98, 043003
 Macias O., Horiuchi S., Kaplinghat M., Gordon C., Crocker R. M., Nataf D. M., 2019, *JCAP*, 09, 042
 Martin P., Tibaldo L., Marcowith A., Abdollahi S., 2022, *A&A*, 666, A7
 Minamidani T. et al., 2015, in EAS Publ. Ser., 75-76, 193
 Moskalenko I. V., Strong A. W., 1998, *ApJ*, 493, 694
 Moskalenko I. V., Strong A. W., 2000, *ApJ*, 528, 357
 Moskalenko I. V., Porter T. A., Strong A. W., 2006, *ApJ*, 640, L155
 Planck Collaboration et al., 2016, *A&A*, 596, A109
 Porter T. A., Jóhannesson G., Moskalenko I. V., 2017, *ApJ*, 846, 67

- Porter T. A., Rowell G. P., Jóhannesson G., Moskalenko I. V., 2018, *Phys. Rev. D*, 98, 041302
- Porter T. A., Jóhannesson G., Moskalenko I. V., 2019, *ApJ*, 887, 250
- Porter T. A., Jóhannesson G., Moskalenko I. V., 2022, *ApJS*, 262, 30
- Pshirkov M. S., Tinyakov P. G., Kronberg P. P., Newton-McGee K. J., 2011, *ApJ*, 738, 192
- Qiao B.-Q., Liu W., Zhao M.-J., Bi X.-J., Guo Y.-Q., 2022, *Front. Phys.*, 17, 44501
- Robitaille T. P., Churchwell E., Benjamin R. A., Whitney B. A., Wood K., Babler B. L., Meade M. R., 2012, *A&A*, 545, A39
- Sako T., Kawata K., Ohnishi M., Shiomi A., Takita M., Tsuchiya H., 2009, *Astropart. Phys.*, 32, 177
- Sciascio G. D., 2016, *Nucl. Part. Phys. Proc.*, 279-281, 166
- Steppa C., Egberts K., 2020, *A&A*, 643, A137
- Strong A. W., Moskalenko I. V., 1998, *ApJ*, 509, 212
- Strong A. W., Moskalenko I. V., Reimer O., 2000, *ApJ*, 537, 763
- Sun X. H., Reich W., Waelkens A., Enßlin T. A., 2008, *A&A*, 477, 573
- Sun X.-H., Reich W., 2010, *RAA*, 10, 1287
- Umemoto T. et al., 2017, *PASJ*, 69, 78
- Vallée J. P., 2020, *ApJ*, 896, 19
- Vassiliev V., 1999, *Astropart. Phys.*, 11, 247
- Vecchiotti V., Zuccarini F., Villante F. L., Pagliaroli G., 2022, *ApJ*, 928, 19
- Wang Y. et al., 2020, *A&A*, 634, A83
- Yusifov I., Kılıçık I., 2004, *A&A*, 422, 545
- Zhao S., Zhang R., Zhang Y., Yuan Q., 2021, *PoS, ICRC2021*, 859

SUPPORTING INFORMATION

Supplementary data are available at [MNRAS](https://www.mnras.org/online) online.

GALDEFs.zip

Please note: Oxford University Press is not responsible for the content or functionality of any supporting materials supplied by the authors. Any queries (other than missing material) should be directed to the corresponding author for the article.

APPENDIX A: TRANSFORMING THE HGPS FOR COMPARISONS TO GALPROP

The HGPS comprises about 2700 h of observations spanning over 10 years. It covers almost 180 degrees of longitude, ranging from $l = 270^\circ$ – 65° , and spans over the latitudes $b \leq |5^\circ|$ with a resolution of 4.8 arcmin. The survey has a variable point-source sensitivity above 1 TeV being as low as just under ~ 0.5 per cent of the Crab flux (4 mCrab) for the GC, worsening to 20 mCrab as exposure time decreases at the edges of the survey. For this paper, we used the flux maps available at <https://www.mpi-hd.mpg.de/hfm/HESS/hgps/> from Abdalla et al. (2018).

The HGPS contains emission from discrete sources and unresolved sources on top of the diffuse γ -ray emission. The data also has the CR background influencing the measurements, and a variable exposure. To compare the HGPS to our GALPROP predictions, the HGPS needs to be transformed into a form more similar to the skymaps that GALPROP creates. In this appendix, we detail how the HGPS transformation is made and detail our analysis method.

A requirement of our analysis is that it should not be sensitive to the method used, and needs to be applied in a fair and representative way to both the HGPS observations and our GALPROP predictions. For this, we follow the analysis used by Abdalla et al. (2018) and perform a sliding window analysis. We selected the width of the window, $\Delta w = 15^\circ$, such that the integration area was as large as possible while not over-smoothing large-scale features such as the Galactic arms, and such that the results were robust to changes

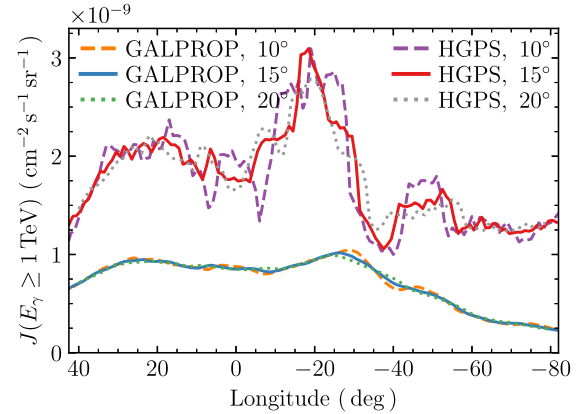


Figure A1. Longitudinal profiles of the $R_c = 0.2^\circ$ HGPS, and one of the GALPROP simulations integrated above 1 TeV. The width of the sliding window, Δw , is varied from 10° to 20° .

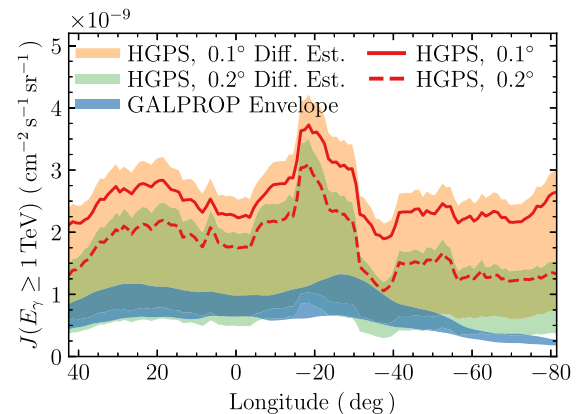


Figure A2. Longitudinal profiles of the HGPS and the envelope of the GALPROP results integrated above 1 TeV. The beam size used in creating the map, R_c , is equal to 0.1° or 0.2° . The unresolved source estimates from Steppa & Egberts (2020) and Cataldo et al. (2020) have been combined into a single shaded band for each integration radii.

of Δw on the order of 30 percent. The sensitivity of the HGPS and GALPROP results to changing the window width is shown in Fig. A1. Across most Galactic longitudes, the HGPS is most sensitive for $-1.5^\circ \leq b \leq 1.0^\circ$, as most of the observation time was spent in this region. These latitudes have a higher statistical significance, with latitudes outside this range having a significance below 5σ across wide areas of the Galactic plane. To ensure statistically significant data is used in our analyses, we chose the latitude bounds of the window to be defined by the height $\Delta h = 2.5^\circ$, and the central latitude $b_0 = -0.25^\circ$. Finally, we chose the spacing between the windows, $\Delta s = 1.0^\circ$, such that variation in the diffuse emission between γ -ray sources could be observed, as approximately 80 per cent of the γ -ray sources in the HGPS are separated by more than a degree in longitude.

The HGPS is well suited for resolving smaller sources that are approximately 0.1° or 0.2° in radius as H.E.S.S. uses an integration radius (R_c) of either 0.1° or 0.2° . However, as we expect the diffuse emission to vary on scales greater than 0.2° , it is likely suppressed by both integration radii. Because this effect can conceal the large-scale emission, any estimate of the diffuse emission obtained from the

5048 *P. D. Marinos et al.*

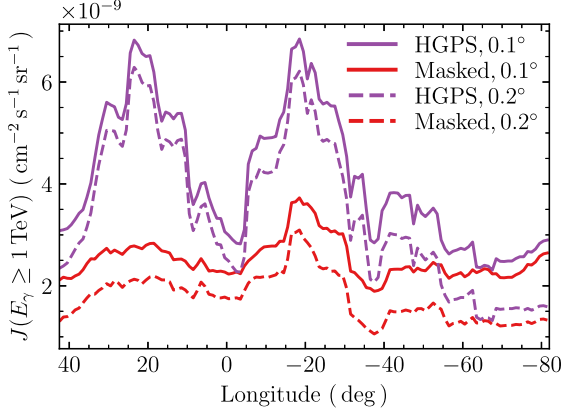


Figure A3. Longitudinal profiles of the average flux in the HGPS measurement. Shown are the HGPS results (purple), and the HGPS results with the catalogued sources masked from the image (red), with the two integration radii being $R_c = 0.1^\circ$ (solid) and $R_c = 0.2^\circ$ (dashed). Averaging windows have a width $\Delta w = 15^\circ$ and height $\Delta h = 2.5^\circ$, centred at a latitude of $b_0 = -0.25^\circ$ and spaced $\Delta s = 1.0^\circ$ apart.

HGPS data using $R_c = 0.2^\circ$ must be regarded as a lower limit. Fig. A2 shows the sensitivity of the analysis to changes in R_c . GALPROP doesn't have a beam, and there was no impact when applying an artificial beam to GALPROP as the results are smoothly varying.

The HGPS has catalogued a total of 78 sources in TeV γ rays. These sources represent localized regions in γ -ray flux from local particle accelerators, and are not modelled by GALPROP. As the local source emission is not a part of the Galactic diffuse emission, we must mask these sources from the HGPS. The methods outlined by Abdalla et al. (2018) are followed here, with complex morphological structures such as SNRs being cut out from the image and excluded from our analyses. Simple morphological structures are assumed to have Gaussian profiles, with their surface brightness (S_{Gauss} , equation (A1)) being subtracted from the image. This subtracts only the source component of the flux from the image:

$$S_{\text{Gauss}}(r|\phi, \sigma) = \phi \frac{1}{2\pi\sigma^2} \exp\left(-\frac{r^2}{2\sigma^2}\right), \quad (\text{A1})$$

where ϕ is the spatially integrated flux, and σ is the radius of the source. The offset $r = \sqrt{(l - l_0)^2 + (b - b_0)^2}$ is the radial distance from the source located at the Galactic coordinates (l_0, b_0) . A comparison between the HGPS with no source masking and the HGPS with all sources masked is shown in Fig. A3, where the results for all sources masked represents the residual emission along the Galactic plane on the scale of R_c , after the contribution from catalogued sources has been subtracted. Also seen in Fig. A3 is that the catalogued sources within the HGPS contribute a significant fraction of the measured γ -ray flux along the Galactic plane. A demonstration of the source masking can be seen for an arbitrary region in the Galactic plane in Fig. A4.

H.E.S.S. is unable to detect sources below a certain γ -ray luminosity, having a point-source horizon between 5–14 kpc for $10^{34} \text{ erg s}^{-1}$, decreasing to a horizon of 1–4 kpc for point-sources with a flux of $10^{33} \text{ erg s}^{-1}$. The HGPS horizon also decreases with an increasing source size. The sensitivity, given by the minimum flux (F_{min}) that can be observed, is shown in equation (A2):

$$F_{\text{min}}(\sigma_{\text{source}}) \propto \sqrt{\sigma_{\text{source}}^2 + \sigma_{\text{PSF}}^2} \quad (\text{A2})$$

where $\sigma_{\text{PSF}} = 0.08^\circ$ is the point spread function of H.E.S.S. and σ_{source} is the source size. Due to the sensitivity of H.E.S.S. worsening for extended sources, and as the HGPS source horizon does not cover the entire Galaxy, there are hundreds of TeV γ -ray sources within the MW that have not yet been resolved by H.E.S.S. (Actis et al. 2011; Abdalla et al. 2018). An estimation of the unresolved source contribution from Steppa & Egberts (2020) suggests that they contribute 13–32 per cent to the diffuse measurement by comparing the total flux observed in the HGPS to the total TeV luminosity produced by a distribution of sources with an estimate of the total luminosity of TeV sources based on PWNe distributions. Another estimate from Cataldo et al. (2020) states that the fraction of unresolved sources could be as large as 60 per cent by using known SNR and PWNe spatial distributions and a luminosity distribution to calculate the number of detectable sources as well as the total γ -ray flux that all the sources would produce. The result of this subtraction is shown in Fig. 7.

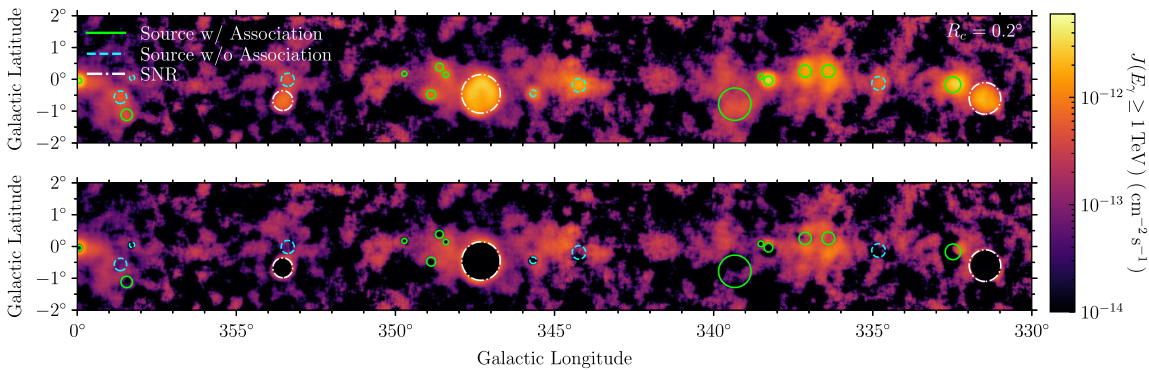


Figure A4. HGPS flux in $\text{cm}^{-2} \text{s}^{-1}$ between $l = 330^\circ$ and $l = 0^\circ$ for the $R_c = 0.2^\circ$ map, comparing before (top panel) and after (bottom panel) sources are masked from the image. Sources with a known association are shown with a solid green circle, sources without an association are shown with a dashed cyan circle, and SNRs are shown with a white dash-dotted circle.

This paper has been typeset from a \LaTeX file prepared by the author.

Chapter 6

Time-Dependent CR Injection

The results in the previous two chapters utilise a steady-state (time-independent) solution for the CR injection in the MW. The steady-state solution assumes that CRs are injected into the MW along a smoothly varying spatial distribution that does not evolve with time.

However, CRs are accelerated in localised, discrete region such as SNRs, PWNe, etc. (see [Section 3.3.2](#) for discussions on the various source classes). The steady-state assumption is valid for the >1 GeV CR protons (and heavier nuclei) as they are able to diffuse >1 kpc before losing their energy. Additionally, the cooling distances for the hadrons increases with their kinetic energy (see [Figure 2.7](#)). Conversely, CR electrons with energies greater than ~ 10 TeV have cooling times <1 kyr and cooling distances <200 pc, with the cooling times and distances decreasing with kinetic energy. Therefore, CR electrons in the TeV energy regime will not diffuse large distances away from their acceleration sites. It is not valid to assume that the CR electron density for kinetic energies $E_e > 10$ TeV is constant over time nor smoothly varying across the spatial axes.

This chapter will begin with a detailed discussion on the necessity of the time-dependent solution to CR injection. Also provided is a description of the methods GALPROP utilises to compute the time-dependent CR injection, and the computational resources required. Due to the additional complexity of the time-dependent models, tests are performed to ensure that GALPROP has been set up correctly and is providing accurate and reliable results.

6.1 Motivation for a Time-Dependent Solution

For the time-independent/steady-state solution in GALPROP, all CRs are injected into the MW by a smoothly varying source distribution (as discussed in [Section 2.3](#)). The source term for a given CR species, $Q(\vec{r}, p)$, is the product of the source distribution and the CR injection spectra (see [Equation 2.48](#)). The steady-state solution assumes that all CR species and energies are diffuse at all locations in the MW.

In reality, CRs are injected into the MW by a variety of objects (see [Section 3.3.2](#)) with finite sizes and lifetimes. Considering the placement of CR sources in both time and space requires using a time-dependent simulation. The injection and propagation of CRs in the ISM by individual, discrete sources with finite lifetimes has been investigated extensively (e.g. [Lingenfelter, 1969](#); [Ramaty et al., 1970](#); [Lingenfelter and Ramaty, 1971](#); [Lingenfelter and Higdon, 1973](#); [Lee, 1979](#)). Additionally, GALPROP has been capable of injecting CRs from discrete sources using the full time-dependent solution over two

decades (e.g. Strong and Moskalenko, 2001a; Strong and Moskalenko, 2001b; Swordy, 2003). However, the limited data statistics electron and positron observations into the TeV regime, coupled with the significant increase in the required computational resources for the time-dependent solution, has prevented widespread use until recently.

As improved observational results (e.g. Aharonian et al., 2009; Ambrosi et al., 2017; Kerszberg, 2017; Recchia et al., 2019) have been acquired it has become increasingly apparent that a smoothly varying source distribution is unable to reproduce some features in the local CR flux above 1 TeV. Recent studies that place individual CR accelerators within 1 kpc of Earth have successfully reproduced the higher-energy features in the local CR electron flux (e.g. Kobayashi et al., 2004; Ptuskin et al., 2006; Mertsch, 2011; Liu et al., 2015; Miyake et al., 2015; Mertsch, 2018; Evoli et al., 2021; Sudoh and Beacom, 2023). A time-dependent solution is also proving to be a requirement for accurate calculations of the γ -ray emission above 1 TeV due to the increasing contribution of the IC emission (e.g. Mertsch, 2018; Porter et al., 2019; Marinos et al., 2023).

A variety of recent observational γ -ray results in the >10 TeV energy range from HAWC, LHAASO, and Tibet AS γ further necessitate a time-dependent solution.

- Results from HAWC (Abeysekara et al., 2017a) and LHAASO (Zhao et al., 2022) show that the localisation of γ -ray emissions nearby individual CR sources is stronger for energies $\gtrsim 10$ TeV, suggesting that the γ -ray emission may be partly leptonic in origin.
- HAWC results show that the observed γ -ray emission around 50 TeV is not aligned with high-density gas clouds (Abeysekara et al., 2020), further suggesting that the γ -ray emission may not be purely hadronic in origin.
- LHAASO-KM2A observations of diffuse γ rays in the 10 TeV to 1 PeV energy range for Galactic longitudes $15^\circ < \ell < 235^\circ$ have fluxes 2–3 times larger than expected from hadronic CRs interacting with the ISM gas (Cao et al., 2023).
- Tibet AS γ results indicate that many of the γ rays detected within their $25^\circ < \ell < 100^\circ$, $|\ell| < 5^\circ$ window (Amenomori et al., 2021) do not coincide with known VHE γ -ray sources, suggesting that the majority of >100 TeV γ -ray emission is not from a diffuse collection of CRs (e.g. Dzhathoev, 2021; Fang and Murase, 2021).

Hence, the HAWC, LHAASO, and Tibet AS γ results all suggest that either the hadronic or leptonic component of the γ -ray flux is underpredicted. Recent results from IceCube (Abbasi et al., 2023) can be used to place limits on the hadronic component as neutrinos only arise from the hadronic interactions (see Section 2.2.1). Comparisons between the expected neutrino flux and current steady-state models shows agreement (e.g. Abbasi et al., 2023; Vecchiotti et al., 2023); however, the observational uncertainties are large and more modelling work is required. Given the HAWC, LHAASO, Tibet AS γ , and IceCube results, it is likely that the >10 TeV γ -ray emission is partly leptonic in origin. Therefore, a time-dependent solution to the CR transport equation is required to connect the γ -ray emissions from GeV to PeV energies.

Modelling the IC emission into the PeV regime requires sources of VHE electrons. Electrons are likely accelerated to PeV energies by PWNe and PWN halos. PWN halos are suggested to be a major contributor to the unresolved source contribution to the

H.E.S.S. and HAWC γ -ray emission (e.g. Cataldo et al., 2020; Martin et al., 2022), and a collection of PWNe could explain the discrepancy between models and the Tibet AS γ flux (Vecchiotti et al., 2022). As the sensitivity of HAWC, LHAASO, and Tibet AS γ improves, many sources that can accelerate electrons to energies above 100 TeV are being discovered (e.g. Cao et al., 2021a; Cao et al., 2021b; Burgess et al., 2022; Abe et al., 2023; Park et al., 2023a; Park et al., 2023b; Woo et al., 2023).

6.2 Description of the Time-Dependent Solution

The time-dependent solution in GALPROP has three major changes in its operation compared to the steady-state case: the source distribution, the source parameters, and the time-stepping method.

6.2.1 Time-Dependent Source Distribution

The time-independent source term, $Q(\vec{r}, p)$, was given in Equation 2.48, with the source distributions, $\rho(\vec{r})$, discussed in Section 2.3. For the steady-state mode, the CR source term is the product of the source distribution and the CR injection spectra. Hence, the source distribution effectively defines the amplitude of the injection spectra for each location in the MW. The result is a smoothly varying spatial distribution injected CRs.

In the time-dependent mode the CRs are injected by individual sources that are created throughout the MW. The source distribution is altered such that it describes the probability of a source being created at a given position in space and time – i.e. the amplitude of the source distribution represents the likelihood of a source being placed at a given position. The probability of a source being created at \vec{r} for a given timestep is described by:

$$P(\vec{r}, t) \propto \frac{N_{\text{sources}}}{t_{\text{final}}} \Delta t \rho(\vec{r}) \quad (6.1)$$

$$\int_V P(\vec{r}) dV = 1 \quad (6.2)$$

where the total probability is normalised such that the volume integral is equal to one, N_{sources} is the number of sources created throughout the simulation, and t_{final} is the length of time of the simulation. The factor $N_{\text{sources}}/t_{\text{final}}$ represents the average number of sources created per unit time. Once a source has been created, it will continue to inject CRs into the ISM throughout its lifetime given by t_{life} .

Let $C(\vec{r}, t)$ be defined such that if a source is placed at the location (\vec{r}, t) , then $C(\vec{r}, t) = 1$ for the lifetime of the source. If no source is located at (\vec{r}, t) , then $C(\vec{r}, t) = 0$. The time-dependent source term is then given by:

$$Q(\vec{r}, p, t) = \begin{cases} \frac{d\mathcal{N}_{\text{CR}}}{dp}, & \text{if } C(\vec{r}, t) = 1 \\ 0, & \text{if } C(\vec{r}, t) = 0 \end{cases} \quad (6.3)$$

where the subscript ‘CR’ denotes that the variable can describe any CR particle. The CR spectra ($d\mathcal{N}_{\text{CR}}/dp$; described in [Section 2.7.1](#)) are given by broken power laws as functions of the CR momentum, with the spectral parameters for protons, electrons, and helium given in [Table 2.4](#).

6.2.2 Time-Dependent Source Parameters

Parameters defining the lifetimes and number of sources must also be defined for a time-dependent model. The lifetime of the CR sources is given by t_{life} , and the average time between sources being created is given by $t_{\text{interval}} = t_{\text{final}}/N_{\text{sources}}$.

Estimates on the lifetime of CR accelerators vary significantly depending on the observational technique and the source type being considered. For SNRs, which make up the majority of the assumed CR accelerators, the estimated lifetimes vary between 30–300 kyr ([Blasi and Amato, 2012](#)). PWNe can accelerate CRs for longer than 100 kyr, though the older PWNe contribute much less to the Galactic CRs ([Giacinti et al., 2020](#)). Star clusters are also a candidate for the acceleration of CRs up to PeV energies ([Bykov, 2014](#)) and may have lifetimes up to 10 Myr ([Aharonian et al., 2019](#); [Bykov et al., 2019](#)).

Estimates on the rate of SNe vary depending on the observational technique. For example, estimates from the radioactive decay of ^{26}Al range between one SNe every 35–125 yr ([Diehl et al., 2006](#)). Averaging over many observational techniques provides a tighter constraint of one SNe every 45–85 yr ([Rozwadowska et al., 2021](#)). Statistical modelling from [Mertsch \(2018\)](#) suggests a lower rate of one SN every 500 yr to explain the CR electron spectrum above 1 TeV. As pulsars (and any associated PWNe) are formed by a subset of SNe, the creation rate of pulsars must be less than that for SNRs. However, the pulsar creation rate has no constraint tighter than that for SNe (e.g. [Keane and Kramer, 2008](#)).

The CR normalisation condition (see [Section 2.7.1](#)) is not impacted by either the source lifetime or the source creation rate. Hence, t_{life} and t_{interval} are free parameters. Currently, all time-dependent sources in GALPROP have the same lifetime, creation rate, and injection spectra – impulsive and continuous sources are not modelled separately, with no distinction between SNRs, PWNe, etc. being defined. Hence, GALPROP only considers a single ‘average’ source class. Previous time-dependent GALPROP results use the values $t_{\text{life}} = 100$ kyr and $t_{\text{interval}} = 100$ yr ([Porter et al., 2019](#)), which are representative of SNR-class CR accelerators. The effects of altering t_{life} and t_{interval} will be explored later in [Chapter 7](#).

6.2.3 Time-Dependent Timesteps

To capture diffusion across many differing timescales the steady-state solution used a variable timestep (see [Section 2.7.2](#)). However, the variable timestep method can only be applied if the CR injection is constant throughout time. Hence, the time-dependent mode of GALPROP utilises a constant timestep, Δt , where the timestep must be less than the shortest cooling time of any particle being simulated. Capturing diffusion on longer scales then requires repeatedly solving the transport equation for the given timestep while simultaneously evolving the source distribution.

GALPROP will propagate CRs from the initial time, t_{initial} , until the final time, t_{final} . The number of timesteps is then given by $(t_{\text{final}} - t_{\text{initial}})/\Delta t$. The CR density in the MW is set to zero, with CR accelerators being placed via the method described in [Section 6.2.1](#). The CR density at a given location will increase until the CR injection and energy-loss rates are balanced, after which the CR density will vary around some equilibrium value (i.e. steady-state value). For 1 GeV protons, reaching the steady-state values requires 500 Myr of simulation time ([Porter et al., 2019](#)). Accurately capturing the cooling of the electrons up to 1 PeV requires a timestep on the order of 100 yr. Therefore, the time-dependent solution requires a total of 5×10^6 timesteps. For comparison, a similar steady-state simulation requires only 500 timesteps.

To reduce computation time, GALPROP has implemented a “warm-start” functionality¹. GALPROP can be operated with a coarse timestep (e.g. $\Delta t > 1$ kyr) to allow all CRs to reach their steady-state values, after which the timestep can be reduced to the size required to accurately capture the cooling of the CR electrons (e.g. $\Delta t = 100$ yr).

6.3 Time-Dependent GALPROP Simulations: Trials and Optimisations

Optimisations and considerations can be made to improve the runtime and storage requirements of the time-dependent GALPROP simulations. This section details these optimisations, as well as any additional considerations required for the time-dependent solution. Tests are performed to ensure the validity of the results.

6.3.1 Length of Simulation

Before interpreting any results from the time-dependent simulations, it is important to ensure that all CRs within the MW have reached the steady-state values in all locations of interest and for all included CR species and kinetic energies. The time taken to reach the steady-state flux will depend on the energy of the CR, the source creation rate, the source lifetime, the ISM distributions (such as the ISM gas, the ISRF, and the GMF), and the source distribution.

¹The warm-start parameters, and how to use them to improve the computational efficiency, is explained in [Section A.2](#).

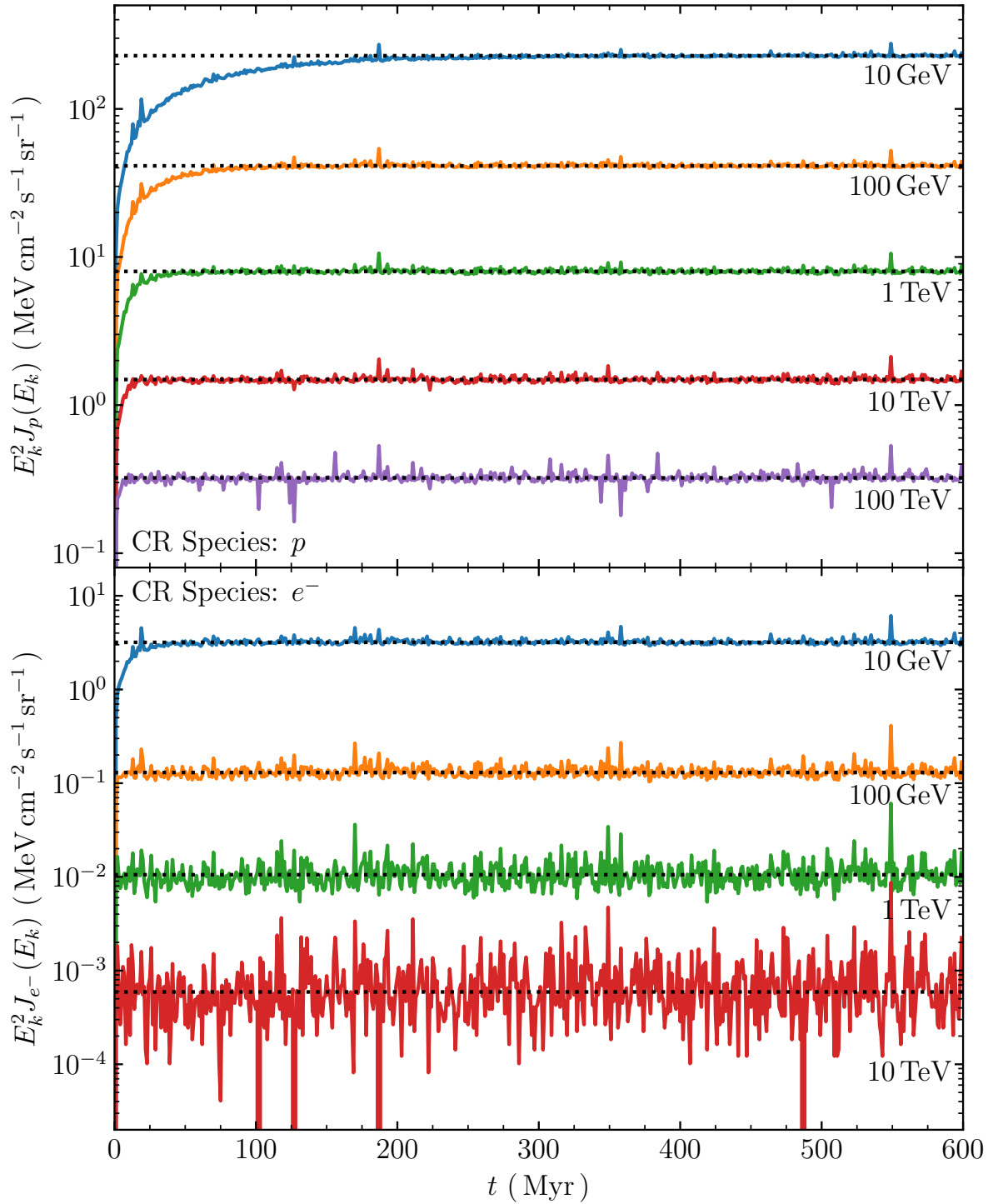


Figure 6.1: The CR proton (top) and electron (bottom) flux as a function of time at the Solar location for 10 GeV (blue), 100 GeV (orange), 1 TeV (green), 10 TeV (red), 100 TeV (purple). The time-independent (steady-state) fluxes are shown by the dotted black lines.

Figure 6.1 shows the CR flux at the Solar location as a function of time for protons and electrons at various energies between 10 GeV and 100 TeV. The steady-state/time-independent fluxes are included for comparison. As the CR protons cool significantly more slowly than the CR electrons (e.g. see Figure 2.7) they take longer to reach their steady-state values. Additionally, as the lower-energy protons propagate more slowly than the higher-energy protons, they require more time to reach their steady-state values.

A sliding window analysis can be utilised to calculate the time taken for the time-dependent values to be considered as varying around the steady-state values. For a given CR species and energy, the flux is considered to have reached equilibrium if the average over a 10 Myr period is greater than or equal to the steady-state value. For the given example, the 100 GeV CR protons require ~ 300 Myr to reach their steady-state values, while the 10 GeV protons require ~ 400 Myr. The 10 GeV CR electrons require only 50 Myr to reach their steady-state values.

Once the time-dependent results have reached steady state, the observed fluctuations are then due entirely to the assumed spatial and temporal variation of the CR sources. Figure 6.1 also shows that the relative variation in the CR density increases with the kinetic energy of the CRs, with the 10 TeV electrons varying by over a factor of ten at the Solar location. The relative variation in the CR flux, and the impacts on the Galactic diffuse γ -ray flux, will be explored further in Chapter 7.

6.3.2 Sampling Interval

GALPROP will output the CR flux for each CR particle found in each of the propagation cells, with these outputs being used to calculate the γ -ray skymaps. In the time-independent mode, a single output is created at the end of the simulation. For the time-dependent mode the output is created every t_{out} timesteps (referred to as the output interval or sampling interval). The sampling interval controls how much data is written during a time-dependent simulation and must be defined such that the variations on the scales of interest are captured.

The Nyquist condition states that to observe variation of a given frequency, f_N , the sampling frequency (f_S) must be at least double f_N , i.e. $f_S \geq 2f_N$. For the time-dependent solution there are two timescales of interest: how quickly the CR flux at the Solar location changes due to a CR accelerator being placed within a few hundred parsecs of Earth, and the variation on the timescale of the source lifetime.

From Figure 6.2, it can be seen that a single CR source being created near the Solar location increases the CR electron flux at 1 TeV by a factor of two over a timeframe of 10–100 kyr. Therefore, capturing the rise and fall of the CR flux caused by the individual sources requires a sampling interval ≤ 5 kyr. A sampling interval of 5 kyr more accurately captures the details (i.e. the peaks and troughs) in the time series compared to the 10 kyr sampling interval.

Figure 6.2 also shows that any single CR source increases the local CR flux for approximately 100–200 kyr. For the example shown in Figure 6.2, the source lifetime was defined as $t_{\text{life}} = 100$ kyr. Therefore, capturing individual sources contributing to the local CR flux requires a sampling interval approximately half of the source lifetime.

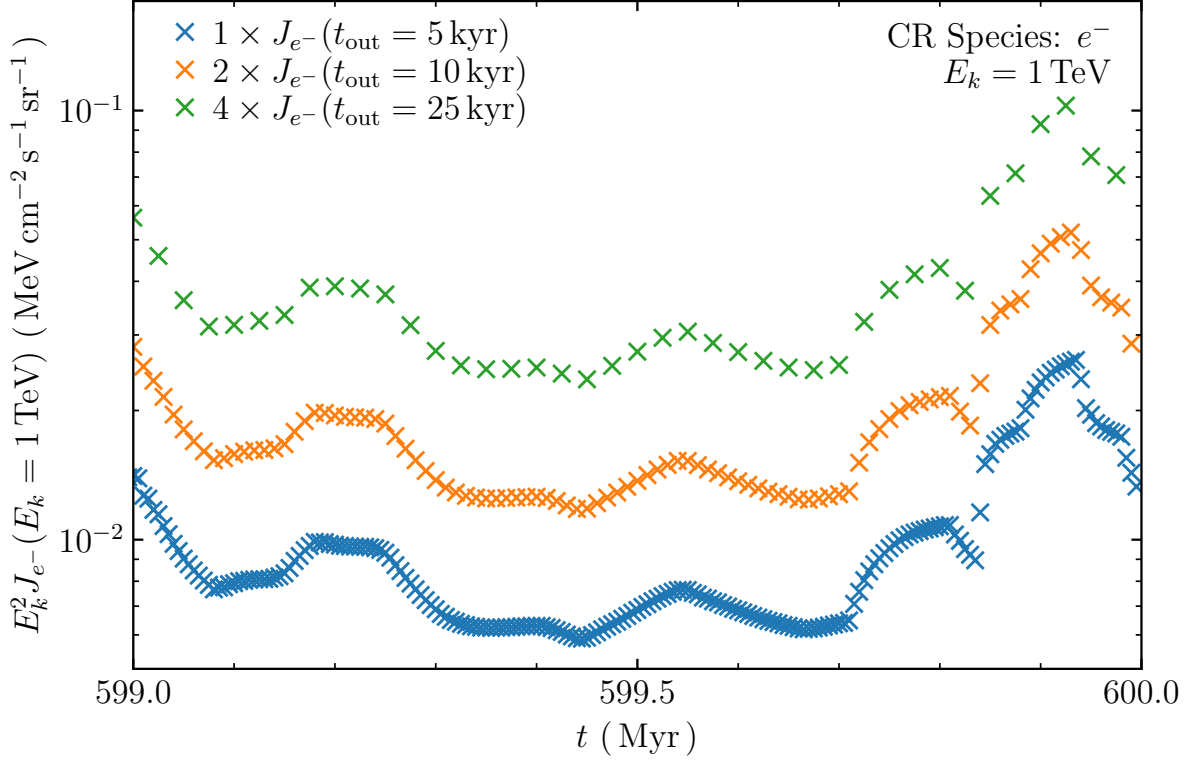


Figure 6.2: The local CR electron flux at 1 TeV as a function of time for the output intervals $t_{\text{out}} = 5$ kyr (blue crosses), $t_{\text{out}} = 10$ kyr (orange crosses), and $t_{\text{out}} = 25$ kyr (green crosses). The time-series values have been multiplied by the given factors to increase contrast.

6.3.3 Simulation Timestep

The computational resources required by GALPROP is proportional to the number of timesteps. However, as discussed in Section 6.2.3, the timestep (Δt) must be shorter than the shortest cooling time (see Figure 2.7) of any CR particle being propagated such that the cooling is accurately captured in the solution. The energy-loss calculations become approximated if the timestep is too large, with the impacts most significant nearby to the CR sources.

CR electron spectral envelopes are shown in Figure 6.3 for $\Delta t = 2500$ yr and $\Delta t = 100$ yr, which are the approximate cooling times for a ~ 1 TeV and ~ 1 PeV electron, respectively. Both envelopes use $t_{\text{out}} = 25$ kyr and are calculated over the entire range of results, i.e. from the minimum to the maximum values. CRs are injected up to 10 PeV and use the following ISM distributions: the SA100 source distribution, the R12 ISRF model, and the PBSS GMF model (see Sections 2.3, 2.5, and 2.6, respectively).

Above 1 TeV the CR flux envelopes begin to diverge. If $\Delta t > t_{\text{cool}}$ then the energy losses will be approximated. For ISM regions with low density, the cooling of the CR electrons will be under-estimated. Conversely, the energy losses will be over-estimated in regions with high ISM density. As the sources are placed in regions of high ISM density more often (see Sections 2.3 to 2.6), the energy losses are typically overestimated.

At 200 TeV the difference in the upper bound of the electron spectra can be as large as a factor of two. Above ~ 500 TeV no CR electrons reach the Solar location for $\Delta t = 2500$ kyr.

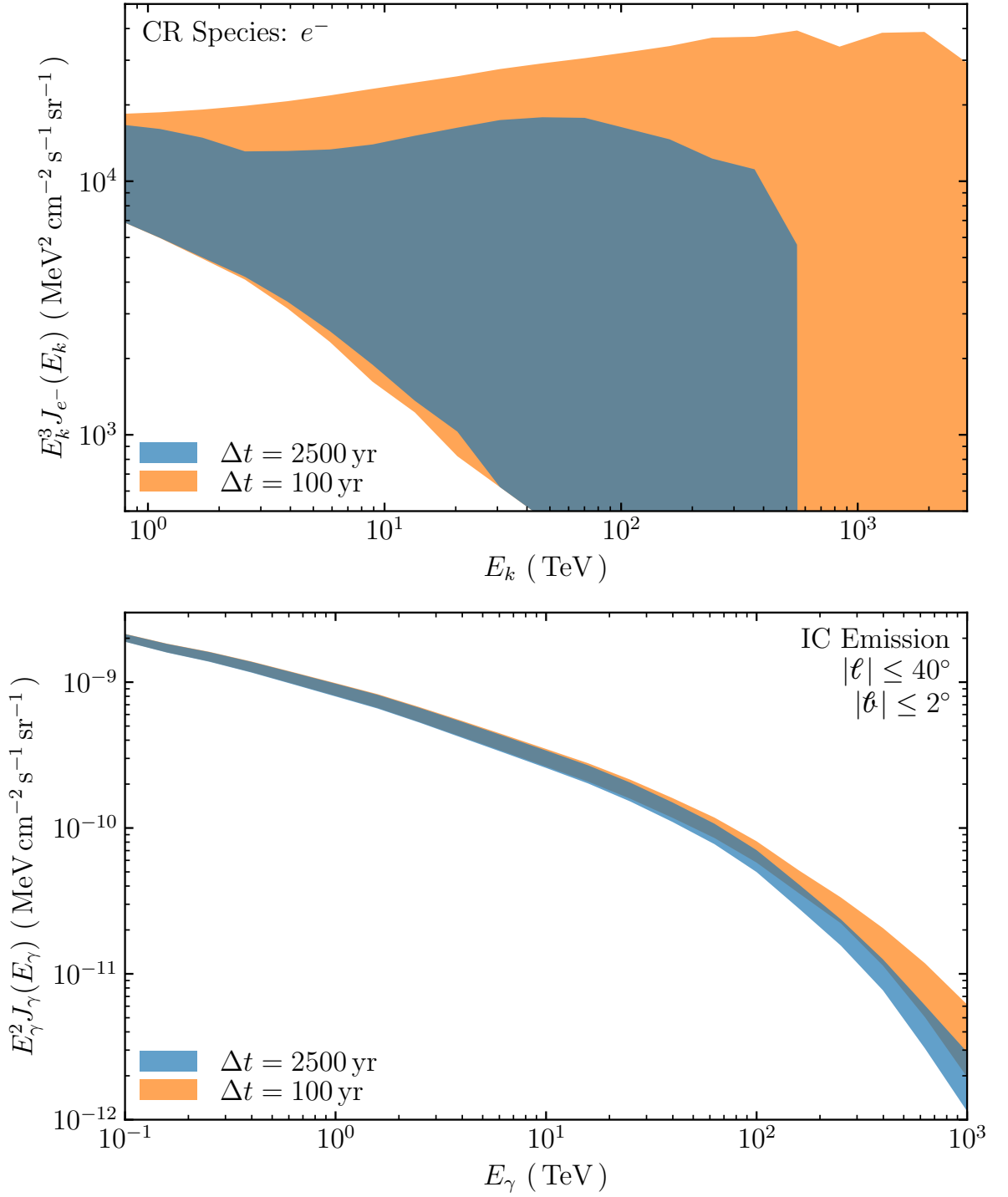


Figure 6.3: CR electron spectral envelopes at the Solar location (top) and the IC γ -ray emission spectral envelopes towards the GC region ($|\ell| \leq 40^\circ$, $|\ell| < 2^\circ$; bottom) for $\Delta t = 2500 \text{ yr}$ (blue) and $\Delta t = 100 \text{ yr}$ (orange). All envelopes use $t_{\text{out}} = 25 \text{ kyr}$ and are computed over a 5 Myr simulation period.

For $\Delta t = 100$ yr the local electron flux is computed accurately up to $E_{e^-} = 1$ PeV as the cooling time of a 1 PeV electron is on the order of 100–500 yr. Decreasing the timestep further to $\Delta t = 10$ yr was found to have no significant impact on the CR electron spectra below 1 PeV. For kinetic energies $E_{e^-} > 1$ PeV the uncertainty in the injection spectrum is larger than the variation between various timestep sizes.

Figure 6.3 also shows the spectral envelopes for the IC γ -ray emission for the Galactic centre (GC) region ($\ell < 40^\circ$, $|\ell| < 2^\circ$). While the local electron spectra begin to diverge at $E_{e^-} = 1$ TeV, the IC γ -ray emission towards the GC region for $\Delta t = 2500$ yr and $\Delta t = 100$ yr are approximately equal for γ -ray energies $E_\gamma < 100$ TeV. The IC γ -ray emission is less sensitive to changes in Δt compared to the local electron spectrum as the γ -ray flux is calculated via a line-of-sight integral (see Section 2.2.3). However, for the $\Delta t = 2500$ yr timestep and energies $E_{e^-} > 100$ TeV the over-estimated cooling often approximates the electron flux to zero. Hence, there are systematically fewer >100 TeV CR electrons in the MW, and the resulting IC γ -ray emission produced by the $E_{e^-} > 100$ TeV electrons is underestimated. For the 1 PeV IC γ -ray emission, the flux is underestimated by a factor of ~ 2 for $\Delta t = 2500$ yr.

The cooling time of the CR protons is $\gtrsim 100$ kyr and independent of their kinetic energies (see Figure 2.7). Hence, decreasing the timestep beyond 10 kyr does not impact the local CR proton spectrum. Furthermore, as heavier nuclei have longer cooling times than the CR protons, all hadronic spectra are simulated correctly for all timestep sizes $\Delta t \lesssim 100$ kyr.

6.3.4 Spatial Grid

Both the computation time and storage requirements for each individual timestep are proportional to the number of propagation cells along each axis. As discussed in Section 2.7.3, the propagation cells must be smaller than the shortest cooling distance of any included CR particle. Additionally, the size of the propagation cells may limit the resolution of the final γ -ray skymaps.

The CR hadrons have larger cooling distances than the CR electrons across most kinetic energies and Galactic conditions (see Figure 2.7). The minimum cooling distances of CR electrons is approximately 10–300 pc at 1 PeV depending on the ISM conditions. For CR protons and other hadrons, the minimum cooling distances are approximately 60– 10^3 pc at 10 GeV.

For time-dependent simulations the computation speed and the required storage can be improved by separating the CR hadrons and electrons into separate propagation grids, with the leptons having a finer spatial resolution. As the hadrons diffuse further, they can be simulated at half the resolution across each of the X , Y , and Z axes. Hence, the hadronic simulation will see a storage/speed improvement of a factor of 2^3 when compared to simulating all particles together. As the hadrons are no longer being simulated at a high spatial resolution, the simulation with a high spatial resolution will see a runtime and storage improvement by a factor equal to the number of unique species of CR hadrons being propagated. Figure 6.4 shows the hadrons and electrons being propagated on differing propagation grids.

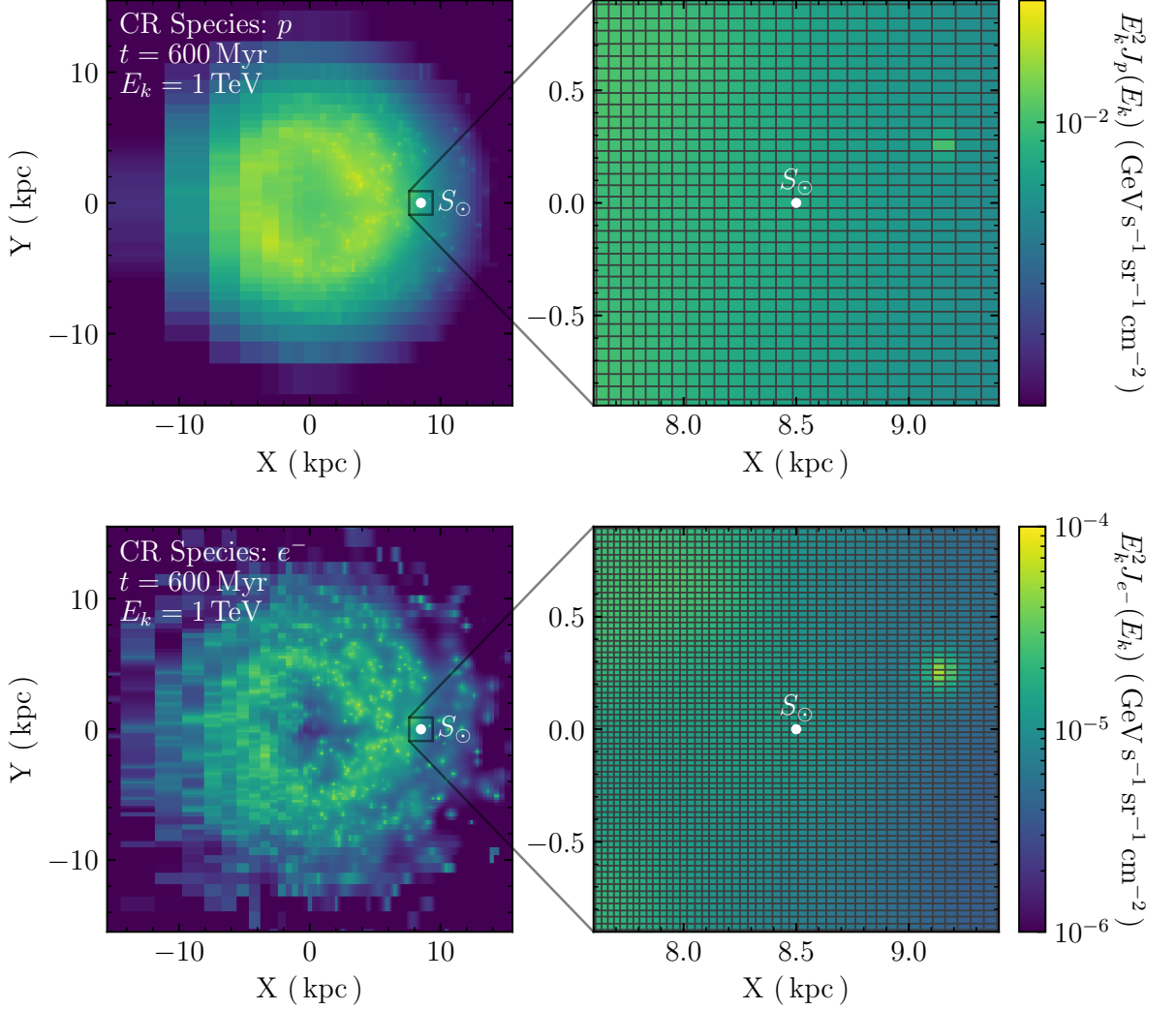


Figure 6.4: The CR energy density along the XY plane (i.e. $Z = 0$), at the simulation epoch $t = 600$ Myr, and kinetic energy $E_k = 1$ TeV. The CR protons (top) and electrons (bottom) are shown for the whole MW (left) and around the Solar location (right). The CR energy density is shown in units of $\text{GeV s}^{-1} \text{sr}^{-1} \text{cm}^{-2}$ with the proton and electron energy densities shown on a separate scale. The electrons were propagated at a finer spatial resolution to capture their short cooling distances at high energies (see text). The cell size increases with distance from the Solar location (see [Section 2.7.3](#)), with the cell size for the proton and electron simulations increasing at different rates. A CR source can be seen in the right-hand panels at $(X, Y) \approx (9.1, 0.3)$ kpc for both protons and electrons.

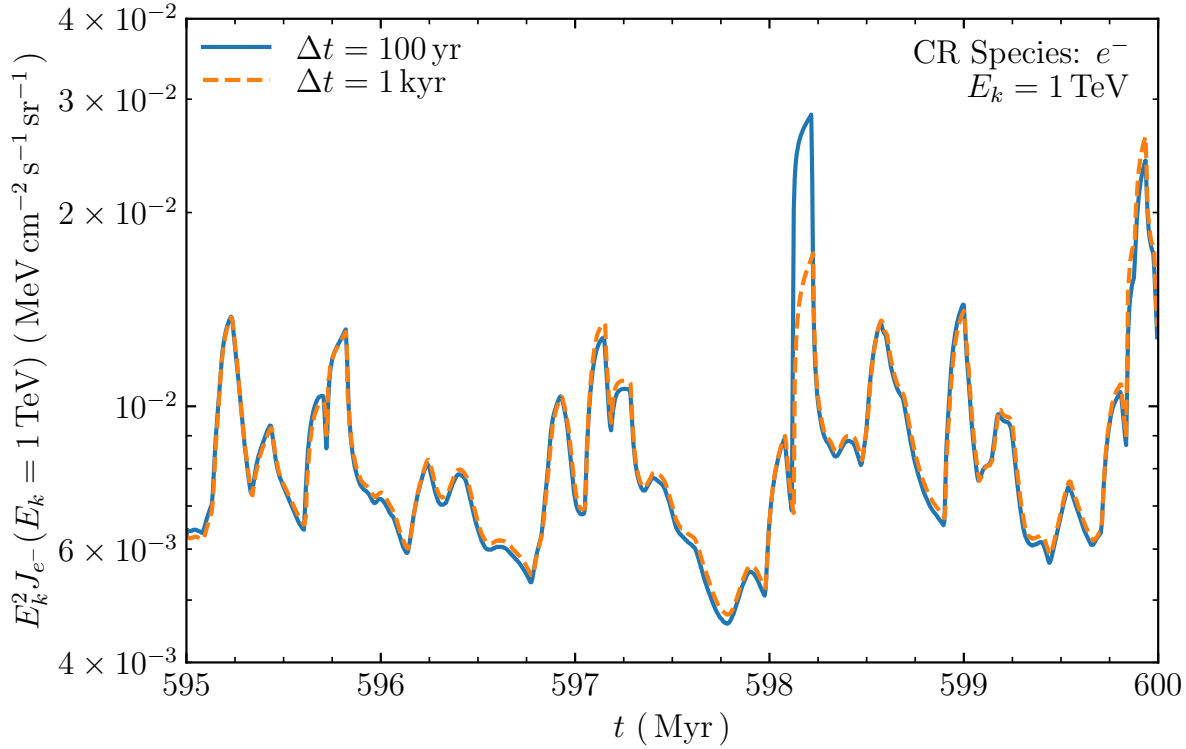


Figure 6.5: The CR electron flux at 1 TeV shown at the Solar location as a function of time for the timestep sizes $\Delta t = 100$ yr (solid blue) and $\Delta t = 1$ kyr (dashed orange).

6.3.5 CR Source Placement in Space and Time

To ensure consistency between GALPROP runs, propagating hadrons and leptons on separate spatial grids and altering the timestep cannot impact the placement of the CR sources. The placement of the CR sources must be identical in both the spatial and temporal axes such that comparisons can be made between the simulations.

In [Figure 6.4](#), a single CR source can be seen near the Solar location. The CR source is located at $(X, Y) \approx (9.1, 0.3)$ kpc for both the CR hadron and CR electron simulations, demonstrating that the sources are placed consistently independent of the spatial axes.

[Figure 6.5](#) shows the local CR electron flux at 1 TeV for both $\Delta t = 100$ yr and $\Delta t = 1$ kyr. The peaks in the time series are due to CR sources being placed < 400 pc from the Solar location. Importantly, the peaks and troughs are located at identical times between the two simulations, demonstrating that the sources are created at the same times independent of the timestep size. Together, [Figures 6.4](#) and [6.5](#) confirm that the placement of the CR sources is independent of the chosen spatial and temporal axes.

It should be noted that [Figure 6.5](#) shows a large increase in the CR electron flux at approximately 598.25 Myr due to a CR source being placed within 100 pc of the Solar location. There is a significant disagreement between the $\Delta t = 100$ yr and the $\Delta t = 1$ kyr time-series fluxes. The close proximity of the source highlights the impact of approximating the cooling calculations with too large a timestep, as discussed in [Section 6.3.3](#). The CR electron flux, and any temporal detail in the time-series flux, is more accurately calculated for $\Delta t = 100$ yr due to the cooling of the electrons being more accurately captured by the shorter timestep.

Chapter 7

Second Paper: Time Variability of Galactic CRs and Gamma Rays

This chapter contains the manuscript titled: “On the Temporal Variability of the Galactic Multi-TeV Interstellar Emissions”, which was published in the peer-reviewed journal ApJ in March 2025.

Cosmic rays (CRs) propagate throughout the Milky Way (MW) and interact with the various components of the interstellar medium (ISM) to produce broadband non-thermal emissions from radio waves to γ rays. As discussed in [Chapter 6](#), calculations of CR propagation and the resulting γ -ray emission throughout the MW typically assume that particle injection is steady across time and space. In reality, CRs are accelerated by discrete sources with finite lifetimes, such as: supernovae (SNe), pulsar wind nebulae (PWNe), and stellar clusters. As the locations and spectra of all CR sources in the MW are not precisely known, considering injection by individual and discrete regions introduces additional uncertainties to models of CR propagation and γ -ray production.

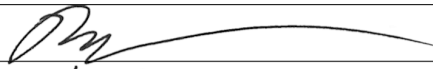
GALPROP is used in this manuscript to model CR propagation and γ -ray emission over a range of CR source lifetimes and creation rates. It was found that the variations in the CR and γ -ray fluxes that arise from uncertainties in the source parameters are similar in magnitude to the modelling uncertainty over an ensemble of steady-state simulations found in [Chapter 5](#). Despite the influence of the underlying source properties, it was found that the parameters cannot be recovered from observations of the local CR flux or the diffuse γ -ray emission. When comparing the GALPROP predictions to measurements of the diffuse γ -ray emission, it was found that the models and observations agree within their respective uncertainties up to 1 PeV. Additionally, the diffuse γ -ray predictions presented here can be used to estimate the unresolved source fraction in the LHAASO observations. For future observations by CTA the modelling variation presented here must be considered when using CR propagation codes to estimate the diffuse γ -ray emission.

Due to the large number of variables in this thesis, the notation in this published work is not necessarily consistent with the other chapters.

Statement of Authorship

Title of Publication:	On the Temporal Variability of the Galactic Multi-TeV Interstellar Emissions
Publication Status:	Published
Publication Details:	P. Marinos, T. Porter, G. Rowell, G. Jóhannesson, and I. Moskalenko, ApJ, Volume 981, Article 93, March 2025


Principal Author

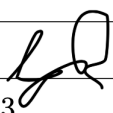
Name of Principal Author (Candidate):	Peter Marinos
Contribution to the Paper:	Simulation setup, ran simulations, data and simulation analysis, data and simulation interpretations, writing of paper.
Overall Percentage Contributed:	65%
Certification:	This paper reports on original research that I conducted during the period of my Higher Degree by Research candidature and is not subject to any obligations or contractual agreements with a third party that would constrain its inclusion in this thesis. I am the primary author of this paper.
Signature:	
Date:	15/11/2023

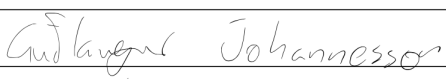
Co-Author Contributions

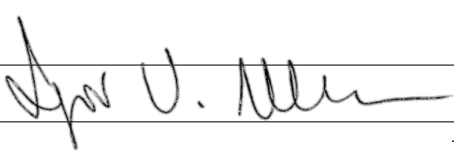
By signing the Statement of Authorship, each co-author certifies that:

- (i) the candidate's stated contribution to the publication is accurate (as detailed above);
- (ii) permission is granted for the candidate to include the publication in the thesis; and
- (iii) the sum of all co-author contributions is equal to 100% less the candidate's stated contribution.

Name of Co-Author:	Troy Porter
Contribution to the Paper:	Simulation setup, ran simulations, simulation interpretation, major paper review.
Overall Percentage Contributed:	15%
Signature:	
Date:	15/11/2023

Name of Co-Author:	Gavin Rowell
Contribution to the Paper:	Data and simulation interpretation, major paper review.
Overall Percentage Contributed:	10%
Signature:	
Date:	17/11/2023

Name of Co-Author:	Guðlaugur Jóhannesson
Contribution to the Paper:	ISM gas model, diffusion parameter optimisation, paper review.
Overall Percentage Contributed:	5%
Signature:	
Date:	23/11/2023

Name of Co-Author:	Igor Moskalenko
Contribution to the Paper:	Simulation setup and interpretation, paper review.
Overall Percentage Contributed:	5%
Signature:	
Date:	Nov 11, 2023



On the Temporal Variability of the Galactic Multi-TeV Interstellar Emissions

P. D. Marinos^{1,2}, T. A. Porter¹, G. P. Rowell², G. Jóhannesson³, and I. V. Moskalenko¹

¹ W. W. Hansen Experimental Physics Laboratory and Kavli Institute for Particle Astrophysics and Cosmology, Stanford University, Stanford, CA 94305, USA; pmarinos@stanford.edu

² School of Physical Sciences, University of Adelaide, Adelaide, South Australia 5000, Australia

³ Science Institute, University of Iceland, IS-107 Reykjavik, Iceland

Received 2024 November 5; revised 2025 January 13; accepted 2025 January 22; published 2025 February 28

Abstract

We use the GALPROP cosmic ray (CR) framework to model the Galactic CR distributions and associated nonthermal diffuse emissions up to PeV energies. We consider ensembles of discrete, finite lifetime CR sources, e.g., supernova remnants, for a range of creation rates and lifetimes. We find that the global properties of the CR sources are likely not directly recoverable from the current “snapshot” of the historic injection and propagation of CRs within the Galaxy that are provided by the data. We show that models for the diffuse γ rays based on the discrete/time-dependent scenarios we consider are able to explain the LHAASO very-/ultra-high-energy (VHE/UHE) γ -ray data with up to 50% contribution by unresolved leptonic sources at the highest energies. Over the models that we consider, variations in the diffuse VHE emissions can be $\sim 25\%$, which is comparable to those for the steady-state models that we investigated in an earlier work. Such variations due to the discrete/finite nature of the CR sources are an important factor that are necessary to construct accurate physical models of the diffuse emissions from the Galaxy at VHE/UHEs.

Unified Astronomy Thesaurus concepts: Particle astrophysics (96); Cosmic rays (329); Diffuse radiation (383); Gamma-rays (637); Interstellar emissions (840)

Materials only available in the online version of record: tar.gz files

1. Introduction

Cosmic ray (CR) particles are thought to be accelerated up to at least PeV energies by sources within the Milky Way (MW). The CRs propagate for millions of years through the interstellar medium (ISM), resulting in a diffuse “sea” of particles from GeV energies up to the so-called CR “knee”. As CRs diffuse they interact with various components of the ISM—i.e., the interstellar gas, the interstellar radiation field (ISRF), and the Galactic magnetic field (GMF)—, emitting nonthermal broadband emissions from X-rays to PeV γ rays in the process. Observations of the very-high-energy (VHE; > 100 GeV) γ -ray emission is essential in understanding how CRs are accelerated up to PeV energies and the mechanisms behind their propagation through the MW. Observations of VHE γ rays also provide insights into the spatial distributions of the ISM components.

The diffuse γ rays produced by the CR interactions in the ISM have been detected with high statistics in the 100 MeV to 100 s of GeV energy range by the Fermi Large Area Telescope (Fermi-LAT; e.g., M. Ackermann et al. 2012), and the High-Energy Stereoscopic System (H.E.S.S.) and Astrophysical Radiation with Ground-based Observatory at Ying Ba Jing (ARGO-YBJ) at TeV energies (A. Abramowski et al. 2014; B. Bartoli et al. 2015). While interstellar emissions models (IEMs) broadly agree with the sub-TeV observations (e.g., F. Acero et al. 2016a, 2016b; M. Ajello et al. 2016; P. D. Marinos et al. 2023), recent results from the Large High Altitude Air Shower Observatory (LHAASO) and Tibet airshower array (Tibet AS γ) in the >10 TeV regime indicate

that there is an excess of γ -ray emission from the Galactic plane compared to their model predictions (K. Fang & K. Murase 2021; Z. Cao et al. 2023). This excess emission could be due to some contribution from γ -ray sources that are not individually resolved or some other component of the ISM that is not well understood. Connecting the diffuse γ -ray emission across this broad energy range is crucial for developing physical models for the emissions themselves. These improved models will be required to extract properties from the faintest γ -ray sources, aiding in understanding how CRs are accelerated to PeV energies in the MW.

The often-used paradigm considered when modeling the diffuse emissions from the MW is the so-called “steady-state” approximation, where CR sources follow continuous spatial distributions with constant injection rate and the CR solution is obtained without any time-dependence (V. S. Berezhinskii et al. 1990). Our previous work quantified the steady-state diffuse γ -ray modeling uncertainty up to 100 TeV (P. D. Marinos et al. 2023) and demonstrated a non-negligible fraction of leptonic emission above 1 TeV. However, the short cooling distances ($\lesssim 1$ kpc) of the $\gtrsim 10$ TeV electrons necessitates the consideration of individual sites of CR injection. Since the CR injection spectra are not known for every accelerator and distance estimates for many CR sources are on the order of kiloparsecs, there is some intrinsic variance in the models. Such variance impacts all VHE emission predictions and has not yet been quantified.

In this paper, we take the next step and consider the effects by discrete/finite lifetime source ensembles, using the GALPROP⁴ framework to model the time-dependent CR solutions and associated nonthermal emissions from GeV to PeV energies. This extends the earlier work by



Original content from this work may be used under the terms of the Creative Commons Attribution 4.0 licence. Any further distribution of this work must maintain attribution to the author(s) and the title of the work, journal citation and DOI.

⁴ <http://galprop.stanford.edu>

T. A. Porter et al. (2019) to a broader range of model configurations, as well as a larger energy range. The configurations that we consider place CR accelerators stochastically in space and time according to likely viable encompassing models for the large-scale source distributions in the MW. We consider that the sources can have individual lifetimes from 10 kyr to 200 kyr. Creation rates over the range of one source every 50–500 yr are also tested. For the CR electrons, these variations allow us to fully explore the significant fluctuations in spectra due to these parameters (P. Mertsch 2018). We discuss the challenges in constraining the CR source parameters, namely the source lifetimes and creation rates, through observations of the diffuse γ -ray emission. We also apply our modeling results to observations of the diffuse emission from the H.E.S.S. Galactic Plane Survey (HGPS)⁵ and LHAASO in the energy range of 10 TeV to 1 PeV. We show that LHAASO’s observed γ -ray excess can be explained naturally by a component of unresolved pulsar wind nebulae (PWNe) and discuss the potential to constrain the source parameters from the diffuse emission.

2. Model Setup

The GALPROP framework (A. W. Strong & I. V. Moskalenko 1998; I. V. Moskalenko & A. W. Strong 1998) is a widely employed CR propagation package with an extensive history of reproducing the local CR results, Galactic synchrotron emission, and the Galactic diffuse γ -ray emission (e.g., A. W. Strong et al. 2000; I. V. Moskalenko et al. 2002; A. W. Strong et al. 2004; T. A. Porter et al. 2008; A. W. Strong et al. 2011; M. J. Boschini et al. 2020; P. D. Marinos et al. 2023). We use the latest release (version 57), where an extensive description of the current features is given by T. A. Porter et al. (2022). The full configuration files can be found in the `data.tar.gz` package.

We choose ISM distributions with spiral-arm structures that are consistent with the data. To place the CR sources we use a distribution with disk-like and spiral-arm components, with an equal relative contribution from each. This source distribution is hereafter referred to as SA50, where the number represents the percentage contribution from the spiral-arm component (see T. A. Porter et al. 2017, and references therein). For the inverse Compton (IC) emission and pair-absorption calculations, we use the ISRF developed by T. A. Porter et al. (2017) that includes spiral arms (designated R12; T. P. Robitaille et al. 2012). This ISRF accounts for the anisotropic scattering cross section for the IC emission. For the GMF, we use the bisymmetric spiral model developed by M. S. Pshirkov et al. (2011), hereafter referred to as PBSS. This GMF model includes the large-scale regular and small-scale random components of the magnetic field. For the 3D gas density, we use the model developed by G. Jóhannesson et al. (2018) and references therein. We take the CR injection and diffusion parameters from P. D. Marinos et al. (2023) with their values included within the configuration files supplied in the `data.tar.gz` package. The CR injection and diffusion parameters are obtained following the procedure in T. A. Porter et al. (2017) and G. Jóhannesson et al. (2018)—the postdiffusion spectra are fitted to data from the Alpha Magnetic Spectrometer (AMS02) and Voyager 1 using the source distribution and ISM gas model (see G. Jóhannesson et al. 2019, and references therein). Since

we normalize the CR spectra at energies above which the Solar modulation is critical, we use the force-field approximation instead of the more advanced GALPROP/HelMod framework (M. J. Boschini et al. 2020). For the CR diffusion calculations, we use a nonlinear spatial grid (tan spatial grid; T. A. Porter et al. 2022) with the spatial grid size around the solar location set to 7 pc. We use 10 kinetic energy bins per decade ranging from 1 GeV nuc^{-1} to 10 PeV nuc^{-1} for the CR propagation, and five bins per decade ranging from 1 GeV to 1 PeV for the γ -ray flux calculation. The γ -ray sky maps utilize a seventh-order HEALPix (K. M. Górski et al. 2005) isopixelization, giving a pixel size of $27/5 \times 27/5$. For the IC calculations, we use the anisotropic scattering cross section (I. V. Moskalenko & A. W. Strong 2000), and we account for the $\gamma\gamma \rightarrow e^\pm$ attenuation of the γ rays on the ISRF above ~ 10 TeV using the formalism from T. A. Porter et al. (2018). Descriptions for the optimization of the diffusion parameters can be found in P. D. Marinos et al. (2023), and references therein.

Comparisons between local hadronic CR observations and the steady-state GALPROP predictions are provided in T. A. Porter et al. (2017) up to 1 TeV nuc^{-1} . Comparisons between the local electron flux observations and the time-dependent GALPROP predictions will be discussed later in Section 3.

2.1. Time-dependent CR Source Parameter Optimization

For the time-dependent solution, we do not define the individual CR accelerator source types, e.g., supernova remnants (SNRs), PWNe, stellar clusters, and binary sources, because the relative CR contribution between the various source types in the MW is not adequately constrained. Instead, we approximate some “average” source class distribution based on Galactic SNR/PWN models (see SA50, discussed above). The source parameters are tuned under the steady-state assumption to reproduce the local CR spectra after propagation. The injection spectra therefore represent an average over all potential sources that contribute to the local flux. These spectra are then applied to each individual source in the time-dependent calculation. The parameters for the CR injection spectra, and their values for the SA50 source distribution, can be found in Table 1 of P. D. Marinos et al. (2023).

When operating with the time-dependent solution, we start by setting the CR density to zero across the entire MW. Sources are then placed stochastically in position and time, with the CR sea density increasing until the injection and energy losses are balanced. It is computationally expensive to perform these calculations for all CR species. However, since previous results have illustrated that the π^0 -decay emission is approximately constant over a 5 Myr period (T. A. Porter et al. 2019), we simplify the hadronic calculations to utilize the steady-state approximation (see Appendix). For the leptonic emission, we split the time-dependent propagation calculations into two periods: initial and final. The initial period runs for 100 Myr with a timestep of $\Delta t = 2.5$ kyr and allows the leptonic CR density to reach equilibrium. The final propagation period continues the calculations for another 5 Myr with the timestep decreased to $\Delta t = 100$ yr to ensure that the most rapid energy losses are accurately captured. All analyses are performed only on the final 5 Myr, with the CR electron densities and IC γ -ray flux being output once every 25 kyr.

For the time-dependent solution, the creation rate and lifetime of the CR sources are additional free parameters

⁵ <https://www.mpi-hd.mpg.de/hfm/HESS/hgps/>

Table 1

Names and Source Parameter Values for the Six Tested Combinations

Combination Name	Lifetime (kyr)	Creation Interval (yr)
L010R100	10	100
L050R100	50	100
L100R100	100	100
L200R100	200	100
L100R500	100	500
L100R050	100	50

Note. Source lifetimes are given in units of kyr, and the source creation intervals are given as the average number of years between sources being created in the MW.

which do not impact the CR normalization condition but will impact the energy-dependent magnitude of temporal variation.

Estimates on the rate of supernovae (SNe) vary depending on the observational technique. For example, estimates from the radioactive decay of ^{26}Al range between one SN every 35–125 yr (R. Diehl et al. 2006). Averaging over many observational techniques provides a tighter constraint of one SN every 45–85 yr (K. Rozwadowska et al. 2021). Statistical modeling from P. Mertsch (2018) suggests a lower rate of one SN every 500 yr to explain the CR electron spectrum above 1 TeV. Some unknown fraction of these SNRs will also have an associated PWNe.

Similarly, there is no tight constraint for the source lifetimes of the various source classes. Estimates for the lifetimes of SNRs vary between 30 and 300 kyr (P. Blasi & E. Amato 2012). PWNe can accelerate CRs for longer than 100 kyr, though the older PWNe contribute less to the Galactic CR electron flux density across all energies⁶ (G. Giacinti et al. 2020). Star clusters are another candidate for the acceleration of CRs up to PeV energies (A. M. Bykov 2014), and may accelerate CRs for up to 10 Myr (F. Aharonian et al. 2019; A. M. Bykov et al. 2019), but are expected to be hadronic accelerators. The presence of the Fermi bubbles suggests that the Galactic center (GC) region may experience phases of increased activity (M. Ackermann et al. 2014); however, we do not model the GC as an additional variable source due to the CR power injected within being a free modeling parameter (T. A. Porter et al. 2019).

To test the uncertainty in the time-dependent source parameters we test over the full range of values for the source parameters. The source lifetime is varied from 10 kyr up to 200 kyr, and the source creation interval is varied from one source every 50 yr to one source every 500 yr (i.e., a source creation rate of $0.02\text{--}0.002\text{ yr}^{-1}$). The source parameter combinations are denoted LxxxRyyy, where xxx represents the lifetime of the sources in kiloyears and yyy represents the creation interval in the average number of years between source creation. Due to the computational expense of the calculations, we chose only six combinations for the source lifetimes and source creation intervals for the leptonic injectors. Since the L100R100 parameter combination uses the most commonly found values, it is taken as our reference model. All six of our chosen parameter combinations can be found in Table 1. Given that we are sampling at intervals of 25 kyr and as the flux is expected to vary on timescales similar to the source lifetimes,

⁶ The injection spectrum for the sources can be set to decay over their lifetimes. However, we do not use this function in the present paper.

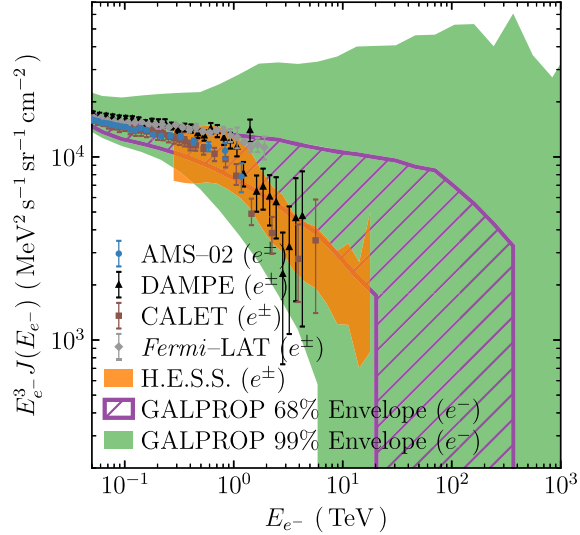


Figure 1. Kinetic energy spectrum for the primary CR electrons above 20 GeV at the Solar location for the final 5 Myr. The 68% and 99% envelopes of the electron spectrum over all six source parameter combinations (Table 1) are shown by the purple hatched area and green shaded band, respectively. The combined electron and positron spectrum is shown for AMS (blue circles; M. Aguilar et al. 2021), the Dark Matter Particle Explorer (black triangles; Q. Ambrosi et al. 2017), the Calorimetric Electron Telescope (brown squares; O. Adriani et al. 2023), Fermi-LAT (gray diamonds; S. Abdollahi et al. 2017), and H.E.S.S. (orange shaded band; F. Aharonian et al. 2009; D. Kerszberg 2017; S. Recchia et al. 2019).

the Nyquist condition is satisfied for all source parameter combinations except for L010R100.

3. Cosmic-Ray Variability

Figure 1 shows the primary CR electron flux predicted by GALPROP at the Solar location across all six source parameter combinations for the final 5 Myr. The GALPROP predictions are shown by two envelopes that contain the flux curves for the central 68% and 99% of timesteps. The 99% envelope removes significant outliers (e.g., timesteps with Earth being contained within the injector) while demonstrating the full variability over the 5 Myr simulation period.

For kinetic energies below 100 GeV, the primary electron spectrum is diffuse and steady across all epochs and source parameter combinations. At higher energies the time-dependent spectra diverge, with large fluctuations depending on the distance to the nearest electron injector. The full modeling variation is larger than a factor of two at 1 TeV and increases rapidly with energy. For epochs with an electron accelerator located with ~ 50 pc, the local primary electron flux approximately matches the injection spectrum. For epochs with no injectors within the electron cooling distance to the Sun, the local primary electron flux will be approximately equal to zero. Since the electron cooling distance via both IC and synchrotron energy losses depends on kinetic energy, we expect some energy-dependent cutoff in the primary electron flux above 100 GeV due to propagation losses (e.g., P. Mertsch 2011).

The cutoff in the primary electron flux occurs around 300 GeV for source parameter combinations with fewer injectors (e.g., shorter lifetimes, L010R100, or longer times between sources, L100R500). For source parameter combinations with

larger numbers of CR sources (e.g., L200R100 and L100R050), there are more accelerators in the Solar neighborhood at any time. The predicted flux is consistently high—fluctuations due to individual sources become negligible and the flux becomes more stable over time. The spectral cutoff in the primary electron spectrum was typically found at energies >10 TeV for the source parameter combinations with larger numbers of active sources. Across all source parameter combinations over a 5 Myr period, we found that the cut-off energy was typically around ~ 10 TeV.

For comparison, Figure 1 also includes the combined electron and positron spectra (with statistical and systematic uncertainties added in quadrature) for AMS02 (M. Aguilar et al. 2021), the Dark Matter Particle Explorer (Q. Ambrosi et al. 2017), the Calorimetric Electron Telescope (O. Adriani et al. 2023), Fermi-LAT (S. Abdollahi et al. 2017), and H.E.S.S. (<5 TeV; F. Aharonian et al. 2009, preliminary data for energies >5 TeV; D. Kerszberg 2017; S. Recchia et al. 2019)⁷. The softening in the all-electron spectrum above 1 TeV seen by the various instruments implies that there are currently no VHE lepton accelerators within the >1 TeV electron cooling distance to the Solar location. This cutoff is within our range of predictions, with the 68% envelope across all of our model configurations lying on the upper edge of the H.E.S.S. observations, but is generally consistent with the data. There are two possible explanations for the predictions lying on the upper edge of measurements. Either the Earth is currently experiencing a lower than average CR electron flux or the modeling setup needs some adjustment.

Geminga is a nearby leptonic accelerator that is located at a distance of 250 pc (J. Faherty et al. 2007). Observations of the extended TeV emission from the High Altitude Water Cherenkov Experiment (HAWC) show evidence for inhomogeneous diffusion around Geminga (A. U. Abeysekara et al. 2017a). Additionally, two-zone models have shown that these observations can be reproduced if CR diffusion in the nearest 30–50 pc to the sources is much slower than diffusion further away (e.g., Y. Fujita et al. 2010; K. Fang et al. 2018; G. Jóhannesson et al. 2019). From G. Jóhannesson et al. (2019), the cooling distance within the slow-diffusion zone (SDZ) for $\gtrsim 100$ TeV electrons was found to be $\lesssim 10$ pc. Using the standard relation that the cooling distance is proportional to $E^{-0.25}$, we find that $\gtrsim 1$ TeV electrons to be $\lesssim 30$ pc within the SDZ. Hence, we expect that the $\gtrsim 1$ TeV electrons from Geminga are unable to diffuse to Earth. Including SDZs around the sources will improve the agreement between the measurements and the 68% flux envelopes predicted by GALPROP.

As seen in T. A. Porter et al. (2019), the time-dependent CR flux varies around the steady-state values with large deviations (over 10 times for the 1 TeV CR electrons) due to the inclusion of discrete sources. Since the deviations typically increase the flux, quantifying the variability in the CRs and γ rays via a Gaussian fit does not accurately represent the underlying distribution. Instead, we define the containment, S_p , to quantify the factor difference from the steady-state flux to the level encompassing p -percent of time-dependent values—e.g., S_{68} contains 68% of the simulated timesteps.

We begin by calculating a list of the differences (denoted d_i) between the steady-state flux (J_{steady}) and the time-dependent

flux values at some time t (J_t) in the final 5 Myr of simulation time. These differences are calculated in logarithmic space and are given by:

$$d_i = |\log_{10}(J_{\text{steady}}) - \log_{10}(J_t)|. \quad (1)$$

The differences are then sorted in ascending order. The timestep, t , becomes an arbitrary counting index, i , such that $d_{i=0}$ is the smallest difference value and $d_{i=n}$ is the largest value. As the differences are sorted in ascending order, the containment factor is given by:

$$S_p = 10^{d_i} \big|_{i=\lfloor pn/100 \rfloor}, \quad (2)$$

where n is the number of time-dependent flux values. Because d_i is a sorted list, using the index $i = \lfloor pn/100 \rfloor$ ensures that p -percent of the n data points are within our containment factor. This definition of the containment factor allows us to quantify the magnitude of the asymmetric fluctuations over time at the p -percent level, while preventing large outliers from introducing a bias toward larger values. For example, $S_{68} = 2$ states that 68% of the time-dependent flux values across all timesteps are within a factor of two from the steady-state predictions and $i = \lfloor 68n/100 \rfloor$.

The containment factor can be calculated for any time-dependent flux predicted by GALPROP. For the containment factor calculations, we do not restrict the analysis to times that reproduce local CR electron flux measurements. We instead calculate deviations from the steady-state values to the 68 and 95% levels. These containment factors will filter timesteps contaminated by outliers/local sources. Additionally, it does not limit our analyses of the CR and γ -ray variability to local electron flux measurements taken at the current (i.e., an arbitrary) point in time.

Figure 2 shows the S_{68} and S_{95} containment factors for the CR electron flux at the Solar location for the six source parameter combinations for the final 5 Myr of the simulation. These results can be considered as an energy-dependent modeling uncertainty in the CR electron flux. At 1 TeV across all six source parameter combinations, the CR electron flux has containment factors of $S_{68} \gtrsim 1.3$ and $S_{95} \gtrsim 1.5$ (i.e., the flux varies around the steady-state values by factors of at least 1.3 and 1.5 at the 68% and 95% levels, respectively). Source parameter combinations with more sources have a consistently high local electron flux because an accelerator is always in the Solar neighborhood (within ~ 500 pc). Realizations with fewer sources fluctuate between high and low flux (nearby source and no nearby source, respectively), increasing the magnitude of the fluctuations. For example, the L100R050 electron flux at 1 TeV has a containment factor $S_{95} = 1.5$, while L100R500 is as large as $S_{95} = 2.5$. The fluctuations also grow rapidly with energy due to the electron synchrotron and IC cooling times decreasing—e.g., the L100R050 containment factor increases from $S_{95} = 1.5$ at 1 TeV to $S_{95} = 4.0$ at 50 TeV.

We also applied the containment factor analysis to the propagation cells in the local Galaxy, within 5 kpc of the Solar location. Figure 3 shows the S_{68} containment factor in the electron differential flux at 10 TeV in the XY plane for the L100R100 source parameter combination. The results shown here agree with the residual maps found by T. A. Porter et al. (2019). However, the analysis of the fluctuations in the CR flux shown here is not dominated by individual CR sources.

⁷ During the peer-review process, updated measurements from H.E.S.S. were reported (F. Aharonian et al. 2024). The new measurements do not impact our analyses or results.

THE ASTROPHYSICAL JOURNAL, 981:93 (13pp), 2025 March 1

Marinos et al.

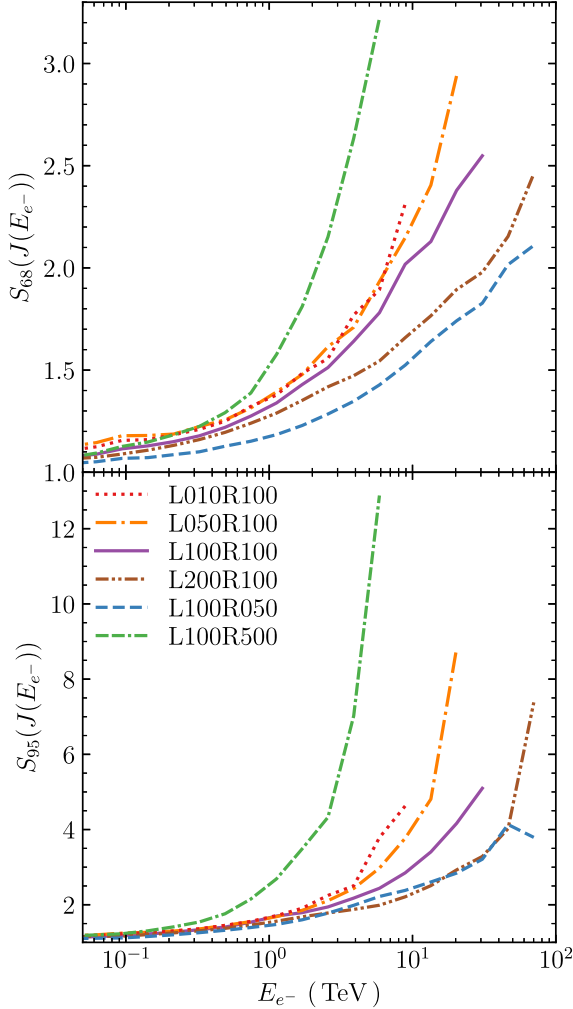


Figure 2. Containment factors for the CR electron spectra at the Solar location for the final 5 Myr. The six source parameter combinations are distinguished by the line colors and styles. The top panel shows the S_{68} containment factor and the bottom panel shows the S_{95} containment factor.

For energies below 1 TeV, the electrons are able to diffuse across the interarm regions, leading to relatively stable fluxes over interarm distances. The situation changes at higher energies—above 10 TeV the electron flux within the spiral arms is generally similar to the injected spectrum of CRs for most timesteps. The fluctuations within the arms are then relatively small. However, the ≥ 10 TeV electrons are unable to diffuse across the interarm regions due to strong synchrotron losses. Hence, the electron flux within the interarm regions varies from an order of magnitude smaller than those found in the arms up to the source injection spectra. Fluctuating between these extrema results in high magnitudes of variability in the interarm regions compared to those found within the spiral arms. From Figure 3, the 10 TeV CR electron flux in the interarm regions and Galactic voids can vary by up to a factor of $S_{68} \sim 4$. In contrast, the CR electron flux varies by factor of at most $S_{68} \sim 2$ within the spiral arms. The variation in the electron flux for the other five source parameter combinations

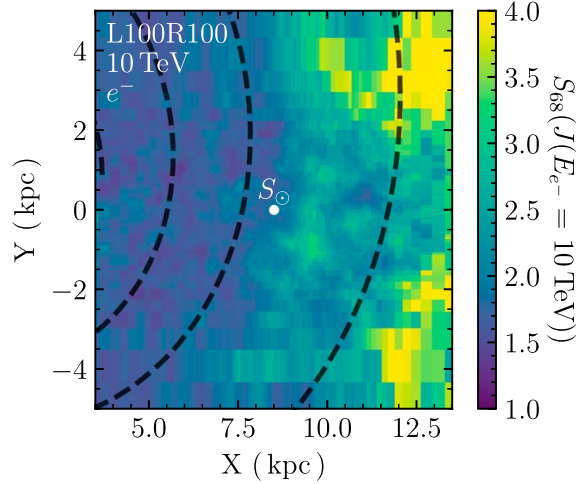


Figure 3. S_{68} containment factor in the differential electron flux for the L100R100 source parameter combination at 10 TeV across the final 5 Myr. The Solar location is shown by S_{\odot} , and the containment factor is taken along the XY plane (i.e., $Z = 0$ kpc). The spiral arms used in the source distribution are shown by the black dashed lines.

follows a similar morphology as the L100R100 combination in Figure 3.

The CR electron variation within the Galactic plane depends most strongly on the source distribution and is largely independent of the GMF strength. This behavior may be altered by using other GMF models or by linking the spatial diffusion coefficient to the GMF strength and is beyond the scope of this work.

4. Gamma-Ray Variability

In this paper we define the total γ -ray emission as the sum of the steady-state π^0 -decay emission and the time-dependent IC emission. For γ -ray energies > 100 GeV, the Bremsstrahlung emission contributes $< 1\%$ to the total emission at these energies and is not included. The γ -ray flux is calculated by performing a line-of-sight (LOS) integral over the emissivities for all pixels in the all-sky maps.

Since the IC component of the total γ -ray emission is of a similar magnitude to the π^0 -decay emission, the variability in the CR electrons throughout the MW (Figure 3) will lead to fluctuations in the total γ -ray emission. Figure 4 shows the S_{68} containment factors for the total γ -ray emission sky maps for all six source parameter combinations at 0.1 TeV, 1 TeV, and 10 TeV. The containment factor is calculated as the total variability of each pixel in the total γ -ray flux maps across the final 5 Myr of simulation time. The amplitude of the temporal variability of the total emission increases with energy due to both the variability in the CR electron flux growing rapidly (see Figure 2) and the IC emission becoming a more dominant component of the diffuse emission above 1 TeV (P. D. Marinos et al. 2023).

At 0.1 TeV, all but the L100R500 source parameter combinations have a similar degree of variability, with maximum containment factors ranging from $S_{68}(J_{L100R050}) = 1.15$ to $S_{68}(J_{L100R500}) = 1.35$. At 1 TeV the maximum containment factors range from $S_{68}(J_{L100R050}) = 1.4$ to $S_{68}(J_{L100R500}) = 2.5$, and at 10 TeV they range from

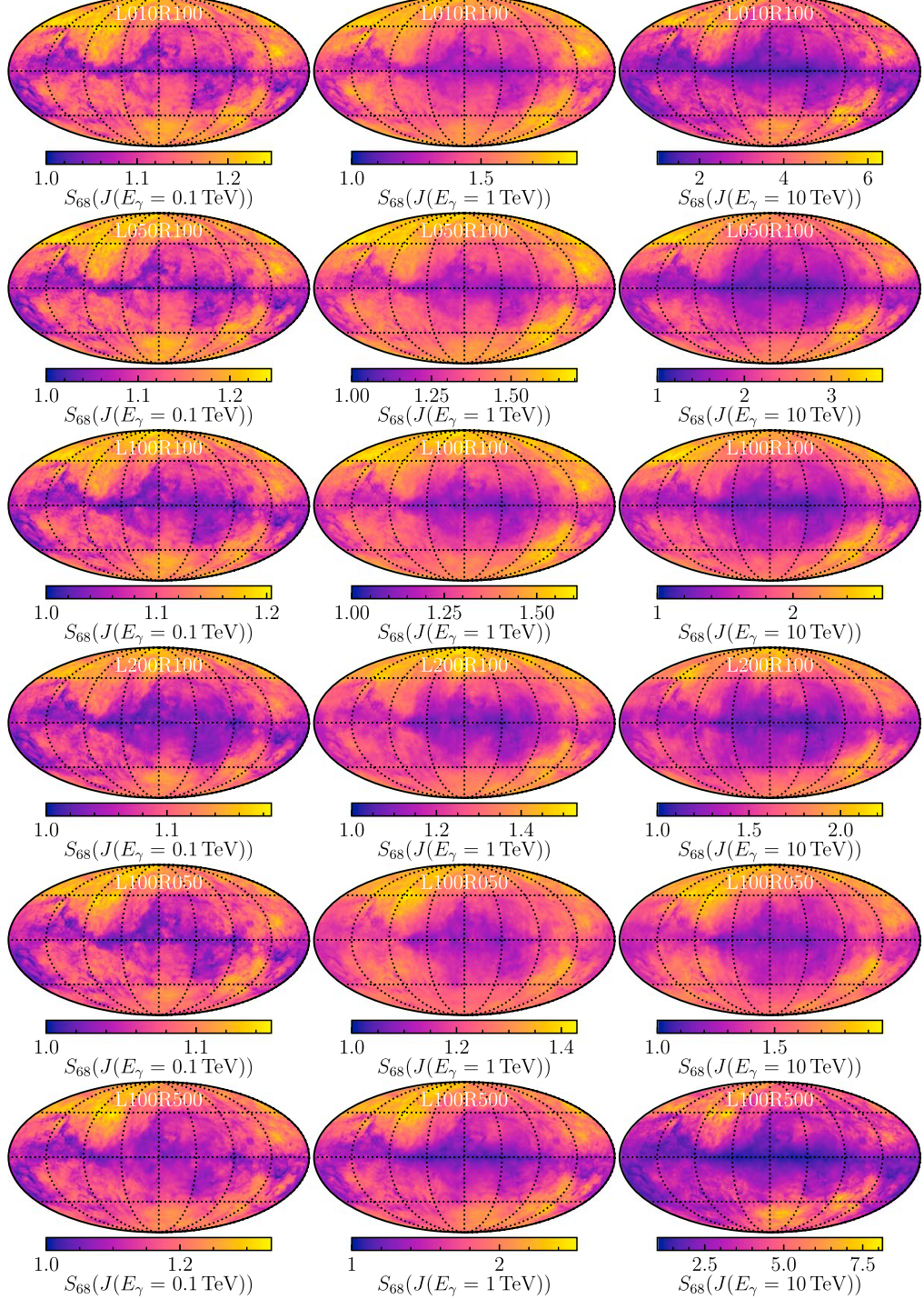


Figure 4. The total γ -ray emission S_{68} containment factor sky maps across the final 5 Myr. From left- to right-hand, the columns are: 0.1 TeV, 1 TeV, and 10 TeV. From top to bottom, the rows are: L010R100, L050R100, L100R100, L200R100, L100R050, and L100R500. The color scale changes for each sky map.

$S_{68}(J_{L100R050}) \sim 1.9$ to $S_{68}(J_{L100R500}) \sim 8$. Across the sky, the L100R050 and L100R500 parameter combinations are the least and most variable, respectively, for all energies. The

morphology of the containment factors is consistent between the six source parameter combinations and across all energies, with LOSs with higher ISM densities exhibiting lower

THE ASTROPHYSICAL JOURNAL, 981:93 (13pp), 2025 March 1

Marinos et al.

containment factors. The sky maps are more variable away from the Galactic plane and in the polar regions.

Across all energies and source parameter combinations, the region of the γ -ray sky with the smallest containment factors is the Galactic plane and toward the central region ($|l| < 90^\circ$, $|b| < 5^\circ$). The increased ISM densities included in the LOS integral toward the central Galaxy average out the contributions due to individual sources. Hence, there is a reduced degree of time-dependent modeling uncertainty along the Galactic plane. Conversely, the reduced ISM densities in the LOS integrals toward the Galactic poles and the outer Galactic regions off the plane ($|l| > 90^\circ$, $|b| > 20^\circ$) are the most variable locations in the sky across all six parameter combinations and energies.

The LHAASO Collaboration recently announced a detection of the diffuse γ -ray emission along the Galactic plane above 10 TeV (Z. Cao et al. 2023).⁸ The two Galactic regions analyzed by the LHAASO Collaboration were the “inner” and “outer” Galactic regions, defined by $15^\circ \leq l \leq 125^\circ$, $|b| \leq 5^\circ$ and $125^\circ \leq l \leq 235^\circ$, $|b| \leq 5^\circ$, respectively. In Figure 5, we show a comparison between the LHAASO observations and the GALPROP predictions for typical Galactic source parameters (L100R100). To ensure a fair comparison, the regions masked by the LHAASO Collaboration are also masked from the γ -ray sky maps generated by GALPROP before the flux is evaluated. For both LHAASO regions, we found that the hadronic and leptonic components compete.

To highlight as much of the modeling variation as possible while not being dominated by outlier results from 1 to 2 timesteps, we show the 99% envelopes for both the IC and total γ -ray emission. We see that the 99% envelope of the GALPROP total γ -ray predictions over the final 5 Myr for the L100R100 source parameter combination agrees with all LHAASO flux points within uncertainties.

We show the total emission in the LHAASO regions for the L010R100, L050R100, L200R100, and L100R500 source parameter combinations in Figure 6. Since the L200R100 and L100R500 parameter combinations have a similar power of CRs injected into the MW, their γ -ray flux envelopes are approximately equal. Hence, the L100R050 flux envelope is not shown. The L100R100 envelope is shown in Figure 5 and lies between the L050R100 and L200R100 flux envelopes. Generally, the parameter combinations with fewer sources have a slightly harder IC spectrum below ~ 100 TeV and a softer spectrum above ~ 100 TeV. However, there is significant degeneracy between the six parameter combinations within the two LHAASO regions. All combinations adequately describe the LHAASO observations. Hence, the diffuse emission observations from LHAASO along the Galactic plane do not currently offer further constraints for the source lifetimes or creation rates. The full range of predictions for the six chosen source parameter combinations represents the total time-dependent modeling uncertainty in the γ -ray emission across the current best-fit models.

We also compared the predicted local electron flux and the γ -ray flux from the two LHAASO analysis regions. No correlation was found for either LHAASO region. Hence, both LHAASO regions probe γ -ray flux from beyond the local electron horizon.

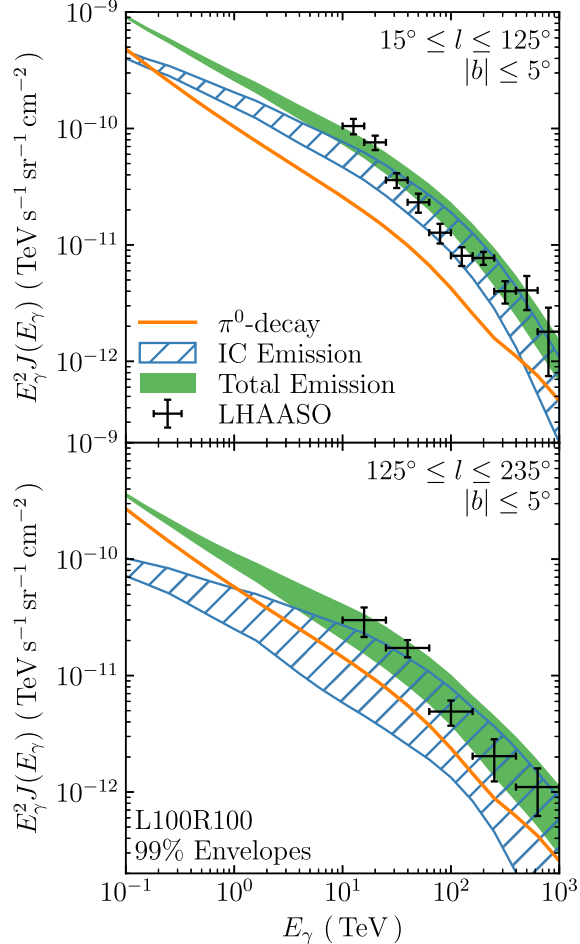


Figure 5. Differential γ -ray spectra for the LHAASO regions for the final 5 Myr of the L100R100 source parameter combination. The steady-state π^0 -decay emission is shown by the orange line and the 99% envelopes are shown for the time-dependent IC emission (blue hatched band) and the total γ -ray emission (green shaded band). The inner and outer LHAASO regions are shown in the top and bottom panels, respectively, with the data points from Z. Cao et al. (2023).

Figure 7 shows the γ -ray flux for the Galactic polar regions, defined by $b \geq 60^\circ$ and $b \leq -60^\circ$ for the north and south, respectively, over four of the six parameter combinations. Similarly as for Figure 6, we found that the L200R100 and L100R050 parameter combinations almost completely overlap due to injecting similar total powers of CRs. Additionally, the L100R100 combination lies between the L050R100 and L200R100 envelopes, and so was excluded for clarity. We found that the γ -ray flux in the two polar regions varies by over a factor of a hundred during the 5 Myr period. As with the LHAASO analysis regions (Figure 6), the envelopes from the six source parameter combinations completely overlap. As such, it is unlikely that the source parameters can be recovered from the polar diffuse emission for a single snapshot in time.

We expect the Galactic poles to be strongly influenced by the local CR electron flux. However, restricting the analysis to only

⁸ During the peer-review process, updated measurements from LHAASO were reported (LHAASO Collaboration 2024). The new measurements do not impact our analyses or results.

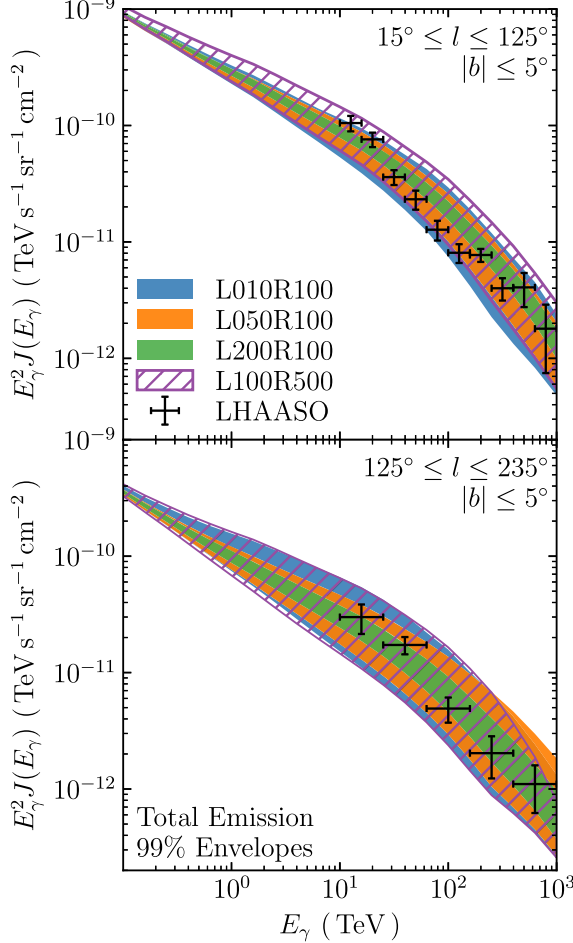


Figure 6. Differential γ -ray spectra for the LHAASO regions for the final 5 Myr across all source parameter combinations. The 99% envelopes are shown for the total γ -ray emission for the following source parameter combinations: L010R100 (blue shaded band), L050R100 (orange shaded band), L200R100 (green shaded band), and L100R500 (purple diagonally hatched band). The inner and outer LHAASO regions are shown in the top and bottom panels, respectively, with the data points from Z. Cao et al. (2023).

include timesteps that reproduce the local electron flux below 1 TeV does not significantly impact the prediction envelopes for the total polar γ -ray flux. The IC flux from the polar regions is therefore probing the electron flux beyond the local electron horizon.

Toward the polar region the isotropic diffuse γ -ray background will also contribute to the emission, and has an exponential cut off around 240 GeV (M. Ackermann et al. 2015). Above 1 TeV, the dominant component of the γ -ray flux toward the Galactic poles is then Galactic in origin. Toward this region, the IC component of the emission is dominant from 100 MeV to 1 PeV due to the ISRF scale height being larger than that for the ISM gas (e.g., T. A. Porter et al. 2019; P. D. Marinos et al. 2023). Additionally, the flux of secondary electrons/positrons predicted by GALPROP is typically an order of magnitude lower than that of the primaries. Therefore, the polar IC emission predicted by GALPROP is due largely to

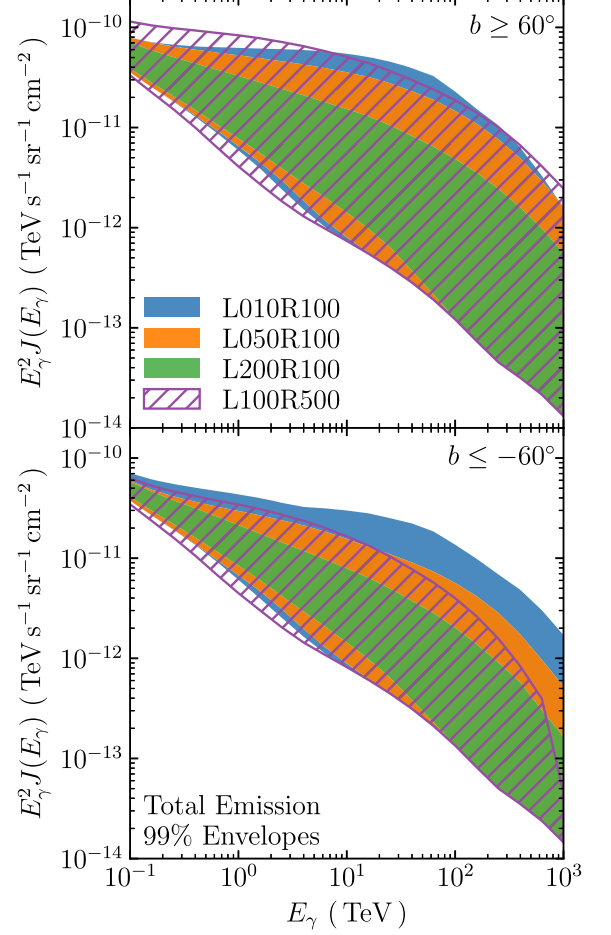


Figure 7. Differential γ -ray spectra for the polar regions for the final 5 Myr across all source parameter combinations. The 99% envelopes are shown for the total γ -ray emission for the following source parameter combinations: L010R100 (blue shaded band), L050R100 (orange shaded band), L200R100 (green shaded band), and L100R500 (purple diagonally hatched band). The northern pole ($b \geq 60^\circ$) is shown in the top panel and the southern pole ($b \leq -60^\circ$) is shown in the bottom panel.

the population of primary electrons. Since the IC component from primary electrons is dominant for all source parameter combinations for the majority of the simulated epochs, and because the IC emission at these energies probe beyond the local TeV-electron horizon, the polar regions present an opportunity to constrain the current CR electron densities around the Solar neighborhood. LHAASO, HAWC, and SWGO may be able to observe the polar γ -ray emission in the upcoming decade as their exposures increase (G. di Sciascio & LHAASO Collaboration 2016; A. U. Abeysekara et al. 2017b; A. Albert et al. 2019).

CTA is currently under construction and is likely to observe the diffuse emission around the Galactic center region. With its proposed order-of-magnitude improvement to sensitivity in the TeV regime, we must consider the time-dependent modeling uncertainty toward the GC. Figure 8 shows the S_{68} and S_{95} containment factor in the flux averaged over the HGPS analysis region (defined by $|l| \leq 40^\circ$ and $-1.5 \leq b \leq 1.0$). As energy

THE ASTROPHYSICAL JOURNAL, 981:93 (13pp), 2025 March 1

Marinos et al.

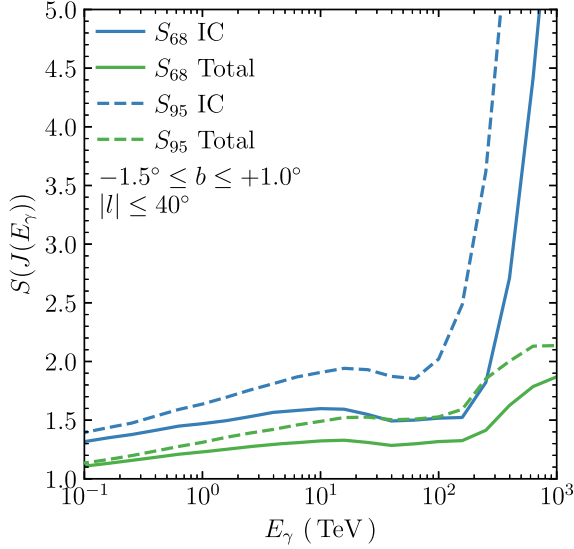


Figure 8. Containment factor in the γ -ray emission toward the GC region, defined by $|l| \leq 40^\circ$ and $-1.5^\circ \leq b \leq +1.0^\circ$, for the final 5 Myr across all six source parameter combinations. The S_{68} containment factor (solid lines) and the S_{95} (dashed lines) are shown for the IC γ -ray emission (blue) and the total γ -ray emission (green).

increases above 1 TeV the IC emission becomes increasingly dominant in the GC region and imparts its variability onto the total emission. The situation changes for γ -ray energies ≥ 200 TeV. The time-dependent IC component becomes softer and the π^0 -decay emission begins to contribute a larger fraction to the total emission. However, the time-independent total flux remains harder than that of the steady-state flux up to higher energies. Since the containment factor is calculated from the steady-state values, the variation grows more rapidly above 200 TeV.

We compare the GALPROP predictions to the HGPS using a sliding window analysis. The windows have a width of $\Delta w = 15^\circ$ and height of $\Delta h = 2.5^\circ$, centered at a latitude of $b_0 = -0.25$ and spaced $\Delta s = 1^\circ$ apart. We use the HGPS flux map with an integration radius of $R_c = 0.2$. We subtract both the cataloged and unresolved source components and consider the residual HGPS emission as an estimate of the diffuse γ -ray emission integrated above 1 TeV. For details on the sliding window analysis and the computation of the residual HGPS emission, see P. D. Marinos et al. (2023) and references therein. We note that the HGPS residual emission is below the survey's 5σ sensitivity, and is therefore not a detection of the diffuse emission at TeV energies.

Figure 9 shows a comparison between the HGPS longitudinal profile and the GALPROP envelopes after applying the averaging window. The purple and orange hatched bands are the 68% and 99% envelopes, respectively, for the total integrated γ -ray flux above 1 TeV across all six source parameter combinations. These bands represent the full range of time-dependent predictions. These predictions from GALPROP for all source parameter combinations that we tested agree with the diffuse γ -ray emission estimates we calculated from the HGPS. The temporal variability in the γ -ray emission integrated above 1 TeV averaged along the Galactic plane is given by the containment factor $S_{95} = 1.4$. The temporal

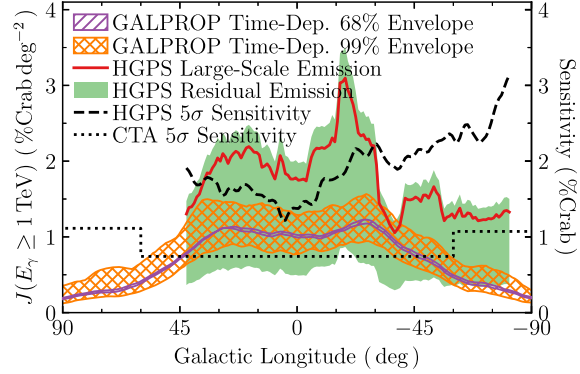


Figure 9. Longitudinal profiles integrated above 1 TeV in units of % Crab deg^{-2} for the 68% and 99% GALPROP envelopes over the final 5 Myr and all six source parameter combinations are shown by the purple and orange hatched bands, respectively. The HGPS profile is shown after cataloged sources are subtracted (solid red). Also shown are the results after accounting for the $\pm 30\%$ HGPS flux uncertainty and subtracting the contributions due to both the cataloged and unresolved sources (green). The 5σ sensitivity is shown in units of %Crab for the HGPS (dashed black) and CTA GPS (dotted black). Averaging windows were applied to all profiles (see text).

variability along the Galactic plane at 1 TeV is similar in magnitude to the modeling uncertainty over a range of ISM distributions under the steady-state approximation. Similarly as for Figures 6 and 7, the longitudinal profiles of the diffuse TeV γ -ray emission exhibit some degeneracy between the six source parameter combinations. Hence, observations of the diffuse TeV γ -ray emission along the Galactic plane do not currently offer any further constraints on the CR source lifetimes or creation rates.

5. Discussion

Our previous work (P. D. Marinos et al. 2023) was the first systematic study of the modeling the variation in the TeV γ -ray emission over a grid of steady-state models. We found that extending to higher energies required time-dependent modeling. The work presented here is the first systematic study of the time-dependent modeling variation that arises from placing CR sources stochastically throughout the MW.

It has been well known for decades that the CR electron spectrum measured at Earth (see Figure 1) is not representative of the Galactic spectrum (e.g., T. A. Porter & R. J. Protheroe 1997). If there are no electron accelerators within ~ 200 pc of the Earth, then a break in the local spectrum at TeV energies is expected (e.g., C. Evoli et al. 2021; T. Sudoh & J. F. Beacom 2023) independent of any cutoff in the injection spectrum. Further Monte Carlo results from P. Mertsch (2018) have shown that any potential break in the local CR electron spectrum can arise naturally from a population of discrete CR sources. For this reason, we used an electron injection spectrum that is fitted in the GeV energy range that reproduces the local CR observations only up to 1 TeV. We do not apply any spectral alterations (e.g., by introducing a cut off to the injection spectrum in the TeV regime) because many PWNe have recently shown some evidence of electron acceleration up to energies of 1–10 PeV (e.g., Z. Cao et al. 2021; LHAASO Collaboration 2021; D. A. Burgess et al. 2022; K. Yan et al. 2024) for at least the first 15 kyr of their lives (Y.-M. Liu et al. 2024). Our results are able to reproduce a TeV cutoff in the local electron

spectrum for timesteps with no nearby sources. From Figure 2, we found that the modeling uncertainty at the 68% level in the CR electron flux is larger than $\pm 50\%$ at 10 TeV. At the 95% level, the flux varies by over a factor of four. Since the electron flux above 1 TeV is so strongly coupled to the locations of nearby accelerators, CR propagation codes (such as GALPROP) must consider their placement of discrete sources in this energy regime. The spectral shape of the CR electron observations above 1 TeV should be reproduced by considering the placement of the CR sources. Including effects such as SDZs around sources may be required to improve the match between observations and the 68% envelope predictions. Other alterations to the models (e.g., altering the source injection spectrum) are not required to reproduce CR observations.

5.1. Resolved, Unresolved, and Diffuse Emission

We consider CRs to be local to their sites of acceleration, while their trajectories are governed by the dynamics of the source (e.g., magnetic fields, turbulence, etc.). Any γ rays emitted by these CRs are defined as “source” or “local” emission. For the γ -ray source to be resolved, it must be luminous enough to be detected confidently above the diffuse background emission. However, even if the source cannot be confidently detected, the γ -ray flux local to it will still contribute to the observations. We refer to these γ rays as unresolved source emission. Diffuse emission is then what remains— γ rays from CRs which are not governed by the dynamics of their acceleration site. The large-scale residual γ -ray emission, found after subtracting all resolved source emission and a relative contribution from unresolved sources, is assumed to be the diffuse emission. Due to the uncertain nature of unresolved emission, it is widely accepted that there will be some contamination in the observations.

For this paper, the hadronic component of the emission is diffuse by construction (see Appendix). Our modeled leptonic component the γ rays can be either diffuse or source emission. All IC emission from secondary leptons (i.e., leptons created via hadronic interactions) is diffuse by construction of our models. For the primary electrons (i.e., those injected by sources), only the IC emission from once they have diffused far from their sources is diffuse. There will be some threshold energy in the range of 1–100 TeV above which the primary electrons cool before they can escape the source environments. Most of the IC emission that remains in the residual emission above ~ 10 TeV is a spatially unresolved component.

LHAASO has detected the diffuse emission above 10 TeV (Z. Cao et al. 2023), with their estimates lying above the hadronic, diffuse component of our steady-state predictions (e.g., Figure 6). There are multiple potential explanations; for example, there could be an unknown additional diffuse hadronic component, new physics, or there could be some contamination from sources. We found that the LHAASO observations can be reproduced by current CR propagation models by considering a steady-state hadronic component with a time-dependent leptonic component. Hence, no additional hadronic components (or other alterations to the models) are required to reproduce the observations.⁹ Additional constraints on the hadronic emission can be obtained from the recent

IceCube observations (Icecube Collaboration et al. 2023). The neutrino predictions from GALPROP are in full agreement with the IceCube observations, and will be shown in a forthcoming paper. Therefore, the LHAASO excess can be explained by GALPROP under the chosen set of models without any additional hadronic components.

Our comparisons to LHAASO imply that γ -ray sources contribute approximately half of the measured diffuse emission in the “inner” region. This source component could be from unresolved sources, agreeing with the results from K. Yan et al. (2024), who found that unresolved PWNe are able to make a considerable contribution to the measured diffuse γ -ray emission observed by LHAASO. The source component could also have some contribution from possible residual emission from resolved sources that were not fully masked (E. Chen et al. 2024), though we are not able to comment on the fraction of contamination versus unresolved flux.

We should also note that for kinetic energies $\gg 1$ PeV, the CR transport starts to transition from the diffusive to the ballistic regime. As GALPROP reproduces the LHAASO emission, use of the diffusion approximation remains appropriate for calculations of the γ -ray emission up to 1 PeV. For higher energies, and as observations improve, the use of the diffusion approximation may need to be reevaluated.

5.2. Variability of the Interstellar Emissions

We quantified the temporal variability of the γ -ray flux by using the containment factors given in Equation (2). This quantification of the variability is shown across the whole sky in Figure 4 and for the GC region in Figure 8. The variability of the total γ -ray emission depends on both the energy of the γ rays and the amount of the ISM in the LOS integral, with denser areas of the ISM being less variable over time. For the chosen model components, the polar regions and the outer Galaxy are the most variable regions in the sky.

Since the CR source lifetimes and creation rates are not precisely known, we simulated over a range of reasonable parameter combinations (see Table 1). We find that if the number of sources per unit time increases, the temporal variability decreases. The diffuse γ -ray emission has a strong dependence on the CR source parameters. However, there is significant degeneracy between the predictions, with all of the tested combinations reproducing the diffuse emission observations. The properties of the CR sources play some factor in the spectrum and brightness of the diffuse emission but are not necessarily recoverable from either on- or off-plane observations. The source properties and placement impact the γ -ray morphology nearby to the sites of acceleration. However, the all-sky morphology over long periods of time is largely identical between the source parameters, with only the amplitude of the variability increasing for models with fewer CR sources (as seen in Figure 4). None of the source parameter combinations that we tested can be excluded by current measurements of the diffuse γ -ray sky.

For on-plane regions, the steady-state π^0 -decay is a significant component of the diffuse γ -ray emission. Additionally, since the CR electrons have a theoretical maximum energy on the order of a few PeV (e.g., LHAASO Collaboration 2021, and references therein), and as the IC scattering cross section becomes Klein–Nishina (KN) suppressed, the leptonic emission will rapidly become subdominant to the π^0 -decay above a few PeV. Therefore, considering a time-dependent solution to

⁹ The ARGO–YBJ TeV diffuse emission results (B. Bartoli et al. 2015) are also reproduced by GALPROP. We do not show comparisons as the ARGO–YBJ analyses use different regions to LHAASO.

the transport equation is a modeling consideration only for the γ -ray emission in the energy range of ~ 1 TeV to ~ 1 PeV.

Toward the GC, our estimates of the γ -ray variability (Figure 8) can only be considered as lower limits because we do not model the GC as a separate variable CR accelerator. Additionally, we do not model the CR sources with injection spectra that evolve over time (e.g., F. A. Aharonian & A. M. Atoyan 1996; S. Gabici & F. A. Aharonian 2007; S. Casanova et al. 2010) and we do not consider two-zone diffusion around sources (e.g., Y. Fujita et al. 2010; K. Fang et al. 2018; G. Jóhannesson et al. 2019). While GALPROP is currently able to model both of these effects, we do not use that functionality in this paper. We also do not model lower-energy CRs being trapped within the source volume for longer than the higher-energy particles (e.g., S. Gabici et al. 2009; A. M. W. Mitchell et al. 2021). Including these three effects increases the complexity of the simulations and is left for future studies. Trapping lower-energy CRs and utilizing injection spectra that evolve over time are expected to increase the variability in the γ -ray sky. Utilizing two-zone models will also introduce a spectral cutoff to the local CR electron spectrum (Figure 1) more often, reducing the predicted envelope across all models.

5.3. Dependence on the Source Distribution

Our previous results in P. D. Marinos et al. (2023) showed that the total TeV γ -ray emission did not strongly depend on the chosen ISRF. Additionally, the structure of the GMF was observable in the IC emission above 10 TeV but had a minor impact on the total emission. We found that the source distribution was the Galactic model parameter that had the largest impact on the total γ -ray emission. Toward the GC at 1 TeV, the source distribution impacted the total emission by $\sim 20\%$. We were unable to perform time-dependent simulations over the same five CR source distributions used in P. D. Marinos et al. (2023) (SA0, SA25, SA50, SA75, and SA100) in this work due to the required computational resources. Simulations were performed with the SA100 source distribution for a small-scale comparison to the SA50 model. The results are summarized here.

The source distributions are normalized such that the CR injection around the Solar neighborhood is consistent between them (T. A. Porter et al. 2017). For the time-dependent simulations, this normalization condition results in the probability of a CR source being placed within a few hundred parsecs of the Solar location being approximately equal across the source distributions. The 99% envelopes for the CR electron flux at the Solar location was found to be consistent between the SA50 and SA100 distributions.

The variability in the total γ -ray flux was also similar between the SA50 and SA100 source distributions. Below 1 TeV, the γ -ray flux and containment factors are broadly similar between SA50 and SA100, with differences being $\lesssim 5\%$ within the Galactic plane. The differences are larger along the spiral-arm tangents, with the upper bounds of the longitudinal profiles typically being 10% higher for the SA100 distribution at 1 TeV. However, the minimum bound of the total γ -ray flux along the spiral-arm tangents is approximately equal between the two source distributions. Hence, the SA100 distribution is $\sim 5\%$ more variable along the spiral-arm tangents.

Across the entire simulated energy range the impact of the source distribution is minor compared to the variability that is

introduced from the time-dependent solution. For example, at 1 TeV the difference between the source distributions along the spiral-arm tangents is $\sim 20\%$. Along the spiral-arm tangents the variability introduced by the time-dependent solution can be as large as $\sim 60\%$.

6. Summary

We have performed a systematic comparison between observations and the time-dependent CR and γ -ray fluxes predicted by GALPROP. The time-dependent models exhibit large fluctuations in both the CR electron and total γ -ray fluxes, with the magnitude of the variations depending on the underlying source parameters, such as their injection fluxes, lifetimes, and their creation rates. To quantify the full range of time-dependent uncertainties, we simulated over six source parameter combinations with lifetimes 10–100 kyr and creation intervals 50–500 yr (Table 1). As expected, the source parameter combinations with fewer sources and shorter-lived sources have the largest fluctuations for both the CR and γ -ray fluxes. While the source parameters influence the spectral shape and brightness of the diffuse emission, we found the resulting CR and γ -ray fluxes exhibit significant degeneracy with one another. On the basis of a single-class source distribution, the underlying source parameters are not recoverable from observations of either the local CR flux or diffuse γ -ray emission for any single snapshot in time. However, we have assumed that there is only one “average” source class. The source parameters may be more easily extracted if using multiple source classes (e.g., SNRs, PWNe, stellar clusters, etc.), with each distributed uniquely, and is left for future work.

The magnitude of the fluctuations in the local CR electron flux above 1 TeV can be as large a factor of 10 over a period of 5 Myr. The fluctuations in the leptonic γ -ray emission are typically as large as factors of 1.2–2 depending on the region, representing a significant modeling uncertainty for the total emission. At 1 TeV, the fluctuations in the γ -ray emission along the Galactic plane found by our time-dependent modeling is similar in magnitude to the variations over a grid of steady-state models found by P. D. Marinos et al. (2023). For the outer Galactic regions, the time-dependent fluctuations for the total emission can be as large as a factor of 10. For the Galactic polar regions, the total γ -ray emission can fluctuate by over a factor of 100 over a 5 Myr period. Additionally, because the γ -ray emission toward the Galactic poles in the TeV–PeV regime is purely Galactic in origin and dominated by the IC component, future observations will be able to constrain the 1–100 TeV CR electron flux outside of the Solar neighborhood.

Due to the KN suppression of the IC scattering cross section for the ISRF and CMB photon fields, the leptonic fraction of the simulated γ -ray emission begins to decrease above 100 TeV. Since the hadronic component is steady in the VHE regime, utilizing a time-dependent solution is only required for the computation of the leptonic component for γ -ray energies between ~ 1 TeV to ~ 1 PeV.

Our GALPROP predictions of the diffuse γ -ray emission for all timesteps agree with the lower limits inferred from the HGPS (H.E.S.S. Collaboration et al. 2018) after accounting for both the cataloged and unresolved source components. We also compared the time-dependent predictions to the diffuse emission observations by LHAASO up to 1 PeV (Z. Cao et al. 2023). After the same exclusion regions used in the LHAASO analysis were masked from our predictions, we

found that the models and observations are in agreement within their respective uncertainties. Hence, GALPROP has now been shown to successfully reproduce the Galactic diffuse γ -ray emission from energies below 100 GeV (e.g., F. Acero et al. 2016a, 2016b; M. Ajello et al. 2016) up to 1 PeV. As the LHAASO emission is reproduced, additional hadronic components, such as increasing the ISM gas density, are required. The most likely explanation for the excess γ -ray emission observed in the 10 TeV to 1 PeV energy range is then contamination from unresolved sources. We have found that the diffusion approximation is able to reproduce current observations for γ -ray energies up to 1 PeV.

Acknowledgments

This research was partly supported by an Australian Government Research Training Program Scholarship. GALPROP development is partially funded via NASA grants 80NSSC22K0477, 80NSSC22K0718, and 80NSSC23K0169. Some of the results in this paper have been derived using the HEALPix (K. M. Górski et al. 2005) and Astropy (Astropy Collaboration et al. 2013, 2018) packages. This work was supported with supercomputing resources provided by the Phoenix HPC service at the University of Adelaide, and we want to thank F. Voisin in particular.

Appendix Time-dependent Hadron Results

As discussed in Section 2.1, propagating hadrons is considerably more computationally expensive compared to leptons for time-dependent simulations. Both hydrogen and helium must be propagated for accurate computation of the γ -ray sky maps, and comparisons to the B/C ratio requires the inclusion of elements up to and including iron (though including up to silicon is typically sufficient). Additionally, while the CR electrons only require approximately 100 Myr to reach their steady-state fluxes, the hadronic species require 450 Myr of simulation time (T. A. Porter et al. 2019). These computations are unnecessary because the CR hadrons have long residence times (~ 1 Gyr) and multikiloparsec cooling distances. Hence, we can expect the hadronic species, and the related hadronic γ -ray emissions, to be steady over time.

Here, we use the same model setup as for the time-dependent leptonic runs discussed in Section 2.1, with the diffusion and spectral parameters given in the supplied data.tar.gz package. We propagate CRs with nuclear charges $Z \leq 14$ (i.e., up to and including silicon) with 10 bins per decade ranging from 1 GeV nuc^{-1} to 1 PeV nuc^{-1} , allowing accurate computation of the secondary boron fluxes up to $\sim 30 \text{ TeV nuc}^{-1}$. The source lifetime was set to 100 kyr and the source creation rate was set to one source per century, i.e., we use the L100R100 source parameter combination. The hadronic species were propagated for an initial 500 Myr to allow all CR species at all energies to reach their steady-state values. The CRs were then propagated for an additional 5 Myr with a timestep $\Delta t = 5 \text{ kyr}$ and an output frequency of once every 25 kyr. All analyses in this appendix are performed on the final 5 Myr.

As is done for the local electron and γ -ray fluxes, we use the containment factor (Equation (2)) to quantify the variations in the CR hadrons. Figure 10 shows the containment factors for the proton, helium, and B/C ratios up to 1 PeV. The variations in the three spectra are similar in magnitude to one another. The

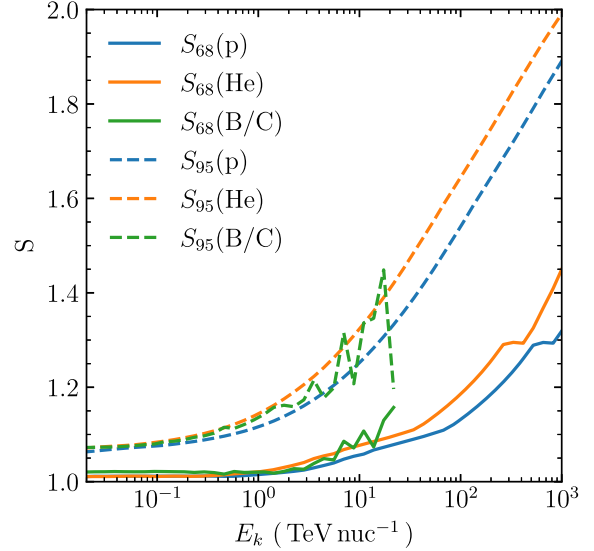


Figure 10. Variation factors for the hadronic spectra at the Solar location for the final 5 Myr for the L100R100 source parameter combination. The GALPROP containment factors are calculated over a 5 Myr period, and are shown by: S_{68} (solid lines), S_{95} (dashed lines), protons (blue), helium (orange), and the B/C ratio (green).

hadronic spectra are effectively constant below 1 TeV. Above 1 TeV, the CR fluxes are generally higher than the steady-state values. The containment factors reach up to $S_{68} = 1.05$ and $S_{95} = 1.20$ at 10 TeV. This stability is in contrast to the electron variation found in Figure 2, which shows that the local electron flux at 10 TeV varies by the containment factors of $S_{68} = 2.1$ and $S_{95} = 3$. Furthermore, the γ -ray flux is generally more stable than the CR flux due to the LOS integral averaging over small variations. Hence, any time-dependent variations in the total γ -ray emissions will be dominated by variations in the leptonic γ -ray fluxes. Using the steady-state assumption for the hadronic γ -ray flux is valid until observational uncertainties of the various γ -ray observations are reduced.

ORCID iDs

P. D. Marinos <https://orcid.org/0000-0003-1734-0215>
T. A. Porter <https://orcid.org/0000-0002-2621-4440>
G. P. Rowell <https://orcid.org/0000-0002-9516-1581>
G. Jóhannesson <https://orcid.org/0000-0003-1458-7036>
I. V. Moskalenko <https://orcid.org/0000-0001-6141-458X>

References

- Abdollahi, S., Ackermann, M., Ajello, M., et al. 2017, *PhRvD*, **95**, 082007
- Abeysekara, A. U., Albert, A., Alfaro, R., et al. 2017a, *Sci*, **358**, 911
- Abeysekara, A. U., Albert, A., Alfaro, R., et al. 2017b, *ApJ*, **843**, 39
- Abramowski, A., Aharonian, F., Ait Benkhali, F., et al. 2014, *PhRvD*, **90**, 122007
- Acero, F., Ackermann, M., Ajello, M., et al. 2016a, *ApJS*, **223**, 26
- Acero, F., Ackermann, M., Ajello, M., et al. 2016b, *ApJS*, **224**, 8
- Ackermann, M., Ajello, M., Atwood, W. B., et al. 2012, *ApJ*, **750**, 3
- Ackermann, M., Albert, A., Atwood, W. B., et al. 2014, *ApJ*, **793**, 64
- Ackermann, M., Ajello, M., Albert, A., et al. 2015, *ApJ*, **799**, 86
- Adriani, O., Akaïke, Y., Asano, K., et al. 2023, *PhRvL*, **131**, 191001
- Aguilar, M., Ali Cavazonza, L., Ambrosi, G., et al. 2021, *PhR*, **894**, 1
- Aharonian, F., Yang, R., & de Oña Wilhelmi, E. 2019, *NatAs*, **3**, 561
- Aharonian, F., Akhperjanian, A. G., Anton, G., et al. 2009, *A&A*, **508**, 561

- Aharonian, F., Benkhali, F. A., Aschersleben, J., et al. 2024, [PhRvL](#), **133**, 221001
- Aharonian, F. A., & Atayan, A. M. 1996, [A&A](#), **309**, 917
- Ajello, M., Albert, A., Atwood, W. B., et al. 2016, [ApJ](#), **819**, 44
- Albert, A., Alfaro, R., Ashkar, H., et al. 2019, arXiv:1902.08429
- Ambrosi, G., An, Q., Asfandiyarov, R., et al. 2017, [Natur](#), **552**, 63
- Astropy Collaboration, Price-Whelan, A. M., Sipőcz, B. M., et al. 2018, [AJ](#), **156**, 123
- Astropy Collaboration, Robitaille, T. P., Tollerud, E. J., et al. 2013, [A&A](#), **558**, A33
- Bartoli, B., Bernardini, P., Bi, X. J., et al. 2015, [ApJ](#), **806**, 20
- Berezinskii, V. S., Bulanov, S. V., Dogiel, V. A., & Ptuskin, V. S. 1990, *Astrophysics of Cosmic Rays* (Amsterdam: North-Holland)
- Blasi, P., & Amato, E. 2012, [JCAP](#), **2012**, 010
- Boschini, M. J., Della Torre, S., Gervasi, M., et al. 2020, [ApJS](#), **250**, 27
- Burgess, D. A., Mori, K., Gelfand, J. D., et al. 2022, [ApJ](#), **930**, 148
- Bykov, A. M. 2014, [A&ARv](#), **22**, 77
- Bykov, A. M., Ellison, D. C., Kalyashova, M. E., & Osipov, S. M. 2019, [RLSFN](#), **30**, 155
- Cao, Z., Aharonian, F. A., An, Q., et al. 2021, [Natur](#), **594**, 33
- Cao, Z., Aharonian, F., An, Q., et al. 2023, [PhRvL](#), **131**, 151001
- Casanova, S., Jones, D. I., Aharonian, F. A., et al. 2010, [PASJ](#), **62**, 1127
- Chen, E., Fang, K., & Bi, X. 2024, [ChPhC](#), **48**, 115105
- di Sciascio, G. & LHAASO Collaboration 2016, [NPPPP](#), **166**, 279
- Diehl, R., Haloin, H., Kretschmer, K., et al. 2006, [Natur](#), **439**, 45
- Evoli, C., Amato, E., Blasi, P., & Aloisio, R. 2021, [PhRvD](#), **104**, 123029
- Faherty, J., Walter, F. M., & Anderson, J. 2007, [Ap&SS](#), **308**, 225
- Fang, K., Bi, X.-J., Yin, P.-F., & Yuan, Q. 2018, [ApJ](#), **863**, 30
- Fang, K., & Murase, K. 2021, [ApJ](#), **919**, 93
- Fujita, Y., Ohira, Y., & Takahara, F. 2010, [ApJL](#), **712**, L153
- Gabici, S., & Aharonian, F. A. 2007, [ApJL](#), **665**, L131
- Gabici, S., Aharonian, F. A., & Casanova, S. 2009, [MNRAS](#), **396**, 1629
- Giacinti, G., Mitchell, A. M. W., López-Coto, R., et al. 2020, [A&A](#), **636**, A113
- Górski, K. M., Hivon, E., Banday, A. J., et al. 2005, [ApJ](#), **622**, 759
- H.E.S.S. Collaboration, Abdalla, H., Abramowski, A., et al. 2018, [A&A](#), **612**, A1
- Icecube Collaboration, Abbasi, R., Ackermann, M., et al. 2023, [Sci](#), **380**, 1338
- Jóhannesson, G., Porter, T. A., & Moskalenko, I. V. 2018, [ApJ](#), **856**, 45
- Jóhannesson, G., Porter, T. A., & Moskalenko, I. V. 2019, [ApJ](#), **879**, 91
- Kerszberg, D. 2017, PhD thesis, LPNHE
- LHAASO Collaboration 2024, arXiv:2411.16021
- LHAASO Collaboration, Cao, Z., Aharonian, F., et al. 2021, [Sci](#), **373**, 425
- Liu, Y.-M., Zeng, H.-D., Xin, Y.-L., Liu, S.-M., & Zhang, Y. 2024, [RAA](#), **24**, 075016
- Marinos, P. D., Rowell, G. P., Porter, T. A., & Jóhannesson, G. 2023, [MNRAS](#), **518**, 5036
- Mertsch, P. 2011, [JCAP](#), **2011**, 031
- Mertsch, P. 2018, [JCAP](#), **2018**, 045
- Mitchell, A. M. W., Rowell, G. P., Celli, S., & Einecke, S. 2021, [MNRAS](#), **503**, 3522
- Moskalenko, I. V., & Strong, A. W. 1998, [ApJ](#), **493**, 694
- Moskalenko, I. V., & Strong, A. W. 2000, [ApJ](#), **528**, 357
- Moskalenko, I. V., Strong, A. W., Ormes, J. F., & Potgieter, M. S. 2002, [ApJ](#), **565**, 280
- Porter, T. A., Jóhannesson, G., & Moskalenko, I. V. 2017, [ApJ](#), **846**, 67
- Porter, T. A., Jóhannesson, G., & Moskalenko, I. V. 2019, [ApJ](#), **887**, 250
- Porter, T. A., Jóhannesson, G., & Moskalenko, I. V. 2022, [ApJS](#), **262**, 30
- Porter, T. A., Moskalenko, I. V., Strong, A. W., Orlando, E., & Bouchet, L. 2008, [ApJ](#), **682**, 400
- Porter, T. A., & Protheroe, R. J. 1997, [JPhG](#), **23**, 1765
- Porter, T. A., Rowell, G. P., Jóhannesson, G., & Moskalenko, I. V. 2018, [PhRvD](#), **98**, 041302
- Pshirkov, M. S., Tinyakov, P. G., Kronberg, P. P., & Newton-McGee, K. J. 2011, [ApJ](#), **738**, 192
- Recchia, S., Gabici, S., Aharonian, F. A., & Vink, J. 2019, [PhRvD](#), **99**, 103022
- Robitaille, T. P., Churchwell, E., Benjamin, R. A., et al. 2012, [A&A](#), **545**, A39
- Rozwadowska, K., Vissani, F., & Cappellaro, E. 2021, [NewA](#), **83**, 101498
- Strong, A. W., & Moskalenko, I. V. 1998, [ApJ](#), **509**, 212
- Strong, A. W., Moskalenko, I. V., & Reimer, O. 2000, [ApJ](#), **537**, 763
- Strong, A. W., Moskalenko, I. V., & Reimer, O. 2004, [ApJ](#), **613**, 962
- Strong, A. W., Orlando, E., & Jaffe, T. R. 2011, [A&A](#), **534**, A54
- Sudoh, T., & Beacom, J. F. 2023, [PhRvD](#), **108**, 103015
- Yan, K., Liu, R.-Y., Zhang, R., et al. 2024, [NatAs](#), **8**, 628

Chapter 8

CTA, the Galactic Plane Survey, and the Diffuse Emission

The Cherenkov telescope array (CTA; [Acharya et al., 2018](#)) will be comprised of two imaging atmospheric Cherenkov telescope (IACT) arrays that are currently being constructed in both Paranal (Chile) and La Palma (Spain). Situating the observatory across two locations will provide CTA with access to both the southern and northern hemispheres. To cover a broad range of γ -ray energies the arrays will consist of three telescope sizes: large-sized telescopes (LSTs; approximately 2 GeV to 200 GeV), medium-sized telescopes (MSTs; approximately 100 GeV to 10 TeV), and small-sized telescopes (SSTs; approximately 1 TeV to 300 TeV).

The SSTs and MSTs will have a field-of-view (FoV) diameter of 8° (almost double the H.E.S.S. FoV) and the LSTs will have a FoV diameter of 5° . Additionally, CTA will have an angular resolution down to $\sim 1'$ (approximately five times better than H.E.S.S.) and will be approximately ten times more sensitive than H.E.S.S. ([Actis et al., 2011](#); [Acharya et al., 2018](#)). The sensitivity for both the southern and northern sites of CTA are shown in [Figure 3.6](#) with comparisons to various other γ -ray facilities. Much like H.E.S.S., one of the CTA consortium's key science goals is to perform a Galactic plane survey. CTA will be extremely sensitive to the details of the Galactic diffuse γ -ray emission ([Acero et al., 2013](#)), and the improved FoV compared to H.E.S.S. will enable more robust CR background subtraction methods. Additionally, the angular resolution and sensitivity improvements will aid in resolving fainter and smaller γ -ray sources that were not detected in the HGPS.

CTA's angular resolution of $\sim 1'$ will greatly improve studies of the γ -ray source morphology of the extended emission coming from the $\gtrsim 10$ –100 pc region surrounding CR accelerators, allowing more accurate estimates of the underlying source properties ([Acero et al., 2013](#); [Dubus et al., 2013](#); [Ambroggi et al., 2016](#)). CTA may be able to determine if the γ -ray sources with no association (discussed in [Section 3.3.2](#)) are part of the diffuse emission or are located near CR accelerators ([Martinez, 2013](#); [Mitchell et al., 2021](#)).

As CTA is expected to observe hundreds of new γ -ray sources in the Galactic plane the challenge of source confusion will need to be addressed ([Mestre et al., 2022](#)). Correctly resolving and identifying two or more individual low surface-brightness sources that are potentially overlapping one another necessitates an accurate and precise model of the diffuse background of γ -ray emission. The sliding window method employed in the HGPS (see [Section 3.4](#)) will be unable to prevent source confusion. Using a simulated diffuse model, such as GALPROP, will aid the morphological studies around γ -ray sources, especially if the sources are overlapping. Using GALPROP will also inform all spectral studies, especially below ~ 10 TeV where the diffuse emission can be a significant component for faint (i.e. $\lesssim 1\%$ Crab) γ -ray sources.

This chapter begins with a discussion of the Python package `gammapy` and the included

instrument response functions (IRFs) for CTA. A first look into the detectability of the diffuse γ -ray emission with CTA will be performed.

8.1 The ‘`gammapy`’ Python Package

The Python package named `gammapy` (Donath et al., 2015; Deil et al., 2017; Donath et al., 2023) was chosen as the “CTA science analysis tools” that will be used for the scientific analysis of all CTA data. The `gammapy` package is an open-source Python package that has been developed to analyse γ -ray data from IACTs such as H.E.S.S., MAGIC, VERITAS, and CTA. Recently, `gammapy` has been successfully used to analyse γ -ray data from the water-tank Cherenkov detector HAWC (Albert et al., 2022b), and the *Fermi*–LAT analysis tool `fermipy` (Wood et al., 2017) uses some elements of `gammapy`. This chapter makes use of `gammapy` version 1.1 for all calculations¹.

The `gammapy` package simplifies the computation of the so-called ‘data products’ from an observational event list. The data products include flux images, significance images, spectra, light curves, etc.. Additionally, the future performance of CTA can be estimated by using the IRFs and `gammapy` to predict the γ -ray flux that CTA would observe given some model γ -ray flux and assumed observational parameters.

8.1.1 Instrument Response Functions

IACTs observe airshowers and reconstruct the information on the particle or photon that initiated the airshower (such as the arrival direction, energy, etc; see Section 3.1). The performance of the IACTs is characterised by the IRFs. The CTA IRFs are calculated by performing Monte Carlo simulations of airshowers using CORSIKA (Heck et al., 1998), and then by modelling how the IACT array responds to CR and γ -ray airshowers for a range of observational parameters using `sim_telarray` (Bernlöhr, 2008). The IRFs that are commonly used for IACT observations are: the energy dispersion, the angular point spread function, the effective area, and the background rate.

- The true energy of a γ ray, E_{true} , is not directly observed and must be computed from the airshower parameters. The energy that is reconstructed, E_{reco} , is not necessarily equal to E_{true} . The energy dispersion IRF characterises this difference and is defined as the ratio of the reconstructed energy on the true energy ($E_{\text{reco}}/E_{\text{true}}$). For CTA, E_{reco} is typically within $\sim 8\%$ of E_{true} above 1 TeV.
- The arrival direction of the CR or γ ray that initiated the airshower must be reconstructed (e.g. see Figure 3.2). The point spread function (PSF) represents the angle between the true and reconstructed arrival positions within which 68% of γ rays of a given true energy will fall. The PSF of CTA will be $\sim 3'$ at 1 TeV and $\sim 1'$ at 100 TeV.

¹The most recent version can be found at <https://github.com/gammapy/gammapy>.

- The effective area (A_{eff}) is the collection area of the IACT during the observation. The effective area is a function of the CR or γ -ray energy and the zenith angle of the observation. As the sensitivity of the telescope decreases towards the edge of the FoV, the effective area is also a function of the offset angle (where the offset angle is defined as the angle between the centre of the FoV and the arrival position of the γ ray). The effective area for CTA is approximately 1 km^2 for energies above 1 TeV.
- The background rate is the number of non-signal events per unit of time, per reconstructed energy, per solid angle. The background events include CR airshowers that have been misidentified as γ rays and false triggers from the night-sky background. For observations the CR background is typically calculated via the standard ring background, reflected ring background, or the adaptive ring background (see Section 3.2.3). For this work the CR background (J_{CR}) is given as the number of events per square degree following the simulated curves from Bernlöhner et al. (2013), and is approximately a powerlaw in energy.

The IRFs used here are similar to those from Bernlöhner et al. (2013) but are calculated with a more recent version of CORSIKA, an updated detector model, and a more recent telescope layout. The IRFs are based on the ‘alpha-configuration’ of the CTA-South site, which has 14 MSTs and 37 SSTs, and have been optimised for a 20° zenith angle and a 50 hr livetime².

8.1.2 Reconstructing the GALPROP Diffuse Flux

For some input γ -ray flux (J_γ) taken from GALPROP, `gammapy` is used to calculate the number of γ -ray counts that CTA would be expected to observe (given by N_γ). The expected number of γ -ray counts are then be converted to a reconstructed γ -ray flux assuming the background CR flux is given by J_{CR} . The predicted number of γ -ray events is given by:

$$N_\gamma = N_{\text{on}} - \alpha N_{\text{off}} \quad (8.1)$$

$$N_{\text{on}} = J_\gamma(E_{\text{reco}}, t_{\text{on}}, \Omega_{\text{on}}) A_{\text{eff}}(E_{\text{reco}}) t_{\text{on}} \Omega_{\text{on}} \quad (8.2)$$

$$N_{\text{off}} = J_{\text{CR}}(E_{\text{reco}}, t_{\text{off}}, \Omega_{\text{off}}) A_{\text{eff}}(E_{\text{reco}}) t_{\text{off}} \Omega_{\text{off}} \quad (8.3)$$

$$\alpha = \frac{t_{\text{on}} \Omega_{\text{on}}}{t_{\text{off}} \Omega_{\text{off}}} \quad (8.4)$$

where E_{reco} is the reconstructed energy of the particle or photon that initiated the air shower, t_{on} and t_{off} are the livetimes for the *on* and *off* regions, respectively, Ω_{on} and Ω_{off} are the solid angles of the *on* and *off* regions, respectively, and α is the ratio of exposure between the *on* and *off* regions. The number of background counts (N_{off}) is sampled from the CR flux, J_{CR} , which is provided by the IRFs (Bernlöhner et al., 2013; Donath et al., 2023). The number of on-region counts (N_{on}) is sampled from the input γ -ray flux, J_γ . The reconstructed fluxes in this chapter utilise an offset angle of 0.5° , the *on* and *off* regions have solid angles defined by $\Omega_{\text{on}} = \Omega_{\text{off}} = 2\pi[1 - \cos(0.2^\circ)]$, and the livetimes are

²The alpha-configuration IRFs for both the southern and northern sites for various zenith angles, livetimes, and sub-arrays can be found at <https://zenodo.org/record/5499840#.YUYa5WYzbUI>.

assumed to be equal (i.e. $t_{\text{on}} = t_{\text{off}}$). Hence, the ratio of exposures simplifies to $a = 1$. As ‘on’ and ‘off’ are only symbolic terms in the current application of `gammapy`, these assumptions were found to have only a minor impact on the results.

Assuming N_{on} and N_{off} follow a Poisson distribution, the significance of the excess counts as a function of the reconstructed energy is given by $S(E_{\text{reco}})$. Taking the sum of the significances in quadrature gives the total significance of the reconstruction, S_{total} , across all energies. Therefore, the significances are given by:

$$S(E_{\text{reco}}) = \frac{N_{\gamma}(E_{\text{reco}})}{\sqrt{N_{\text{off}}(E_{\text{reco}})}} \quad (8.5)$$

$$S_{\text{total}} = \sqrt{\sum_{E_{\text{reco}}} [S(E_{\text{reco}})]^2} \quad (8.6)$$

where all parameters have been defined previously. The reconstructed flux points are shown as upper limits if $S(E_{\text{reco}}) < 2$.

8.2 Detectability of the Diffuse Gamma-Ray Emission with CTA

For spectral and morphological studies performed by CTA, the diffuse γ -ray emission will contaminate estimates of γ -ray sources. This contamination will be strongest in locations where the diffuse γ -ray emission is brightest – e.g. along the spiral-arm tangents ($20^\circ \leq |\ell| \leq 40^\circ$; see [Chapter 5](#)). Accounting for this contamination will be particularly important for the $\gtrsim 10$ –100 pc region around SNRs, as CRs that may have escaped the SNR will interact with the surrounding ISM and create γ -ray structures (e.g. [Aharonian and Atoyan, 1996](#); [Gabici et al., 2009](#); [Casanova et al., 2010](#); [Malkov et al., 2013](#); [Einecke et al., 2023](#); [Rowell et al., 2023](#)). Hence, the analyses presented here are restricted to regions around SNRs detected by H.E.S.S. towards Galactic longitudes $20^\circ \leq |\ell| \leq 40^\circ$. The two chosen source regions are HESS J1614–518 ([Aharonian et al., 2005a](#)) and RX J1713.7–3946 ([Pfeffermann and Aschenbach, 1996](#)).

In this section, the variations over all GALPROP predictions will be used. For the time-independent envelope, the variation is across the SA0, SA25, SA50, SA75, and SA100 source distributions (see [Section 2.3](#)), the F98 and R12 interstellar radiation field (ISRF) models (see [Section 2.5](#)), and the GASE and PBSS Galactic magnetic field (GMF) models (see [Section 2.6](#)). The time-independent variations are presented in [Chapter 5](#). For the time-dependent variations, the envelope is calculated over six combinations of source lifetimes and source creation rates (see [Section 6.2.2](#)). The source lifetimes range from 10 kyr to 200 kyr, and the source creation intervals range from one source every 50 yr to one source every 500 yr. The time-dependent variations are presented in [Chapter 7](#).

In this section the GALPROP diffuse γ -ray fluxes will be processed through the CTA-South IRFs using `gammapy` (i.e. J_{γ} used in [Equation 8.2](#) will be taken from GALPROP).

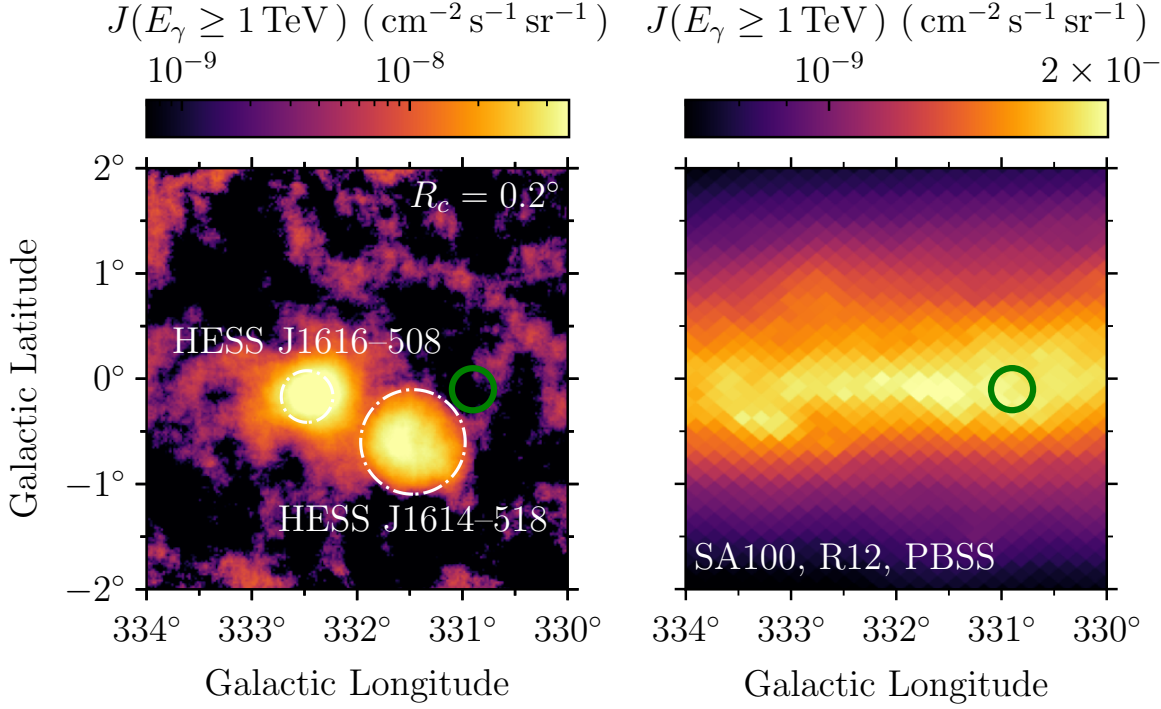


Figure 8.1: Integrated γ -ray flux above 1 TeV around HESS J1614–518 from the HGPS (left) and the steady-state SA100/R12/PBSS combination from GALPROP (right). The analysis region used for extracting the GALPROP emission is shown by the green circle. The HGPS sources HESS J1614–518 and HESS J1616–508 are shown by the white circles.

8.2.1 Diffuse Gamma-Ray Emission Near HESS J1614–518

HESS J1614–518 (Aharonian et al., 2005a) is an SNR (Lau et al., 2017; Abdalla et al., 2018a) located at $(\ell, b) = (331.47^\circ, -0.60^\circ)$ with a radius of 0.49° (Abdalla et al., 2018e). The γ -ray emission observed in the HGPS around HESS J1614–518 is shown in Figure 8.1 alongside the predicted diffuse emission from the steady-state SA100/R12/PBSS combination from GALPROP for the same region. Both the SNR HESS J1614–518 and the unidentified source HESS J1616–508 are shown by white circles.

The CTA reconstruction is computed from the midpoint of the GALPROP flux envelope, i.e. the average between the upper and lower bound. The envelope represents the variation over the grid of twenty steady-state models from Chapter 5 as well as the six time-dependent models from Chapter 7. The GALPROP envelope is extracted from the analysis region shown by the green circle placed at the coordinates $(\ell, b) = (330.9^\circ, -0.1^\circ)$ with a radius of 0.2° . The HGPS shows no significant emission in this region. However, as the chosen analysis region lies on the edge of the SNR shell it may contain some γ -ray emission from recently escaped CRs. Therefore, the GALPROP emission in the region represents a lower bound on the expected γ -ray flux.

Both the GALPROP envelope and the CTA reconstruction are shown in Figure 8.2. The computation was performed with three energy bins per decade. Additionally, the reconstruction uses a livetime of 50 hr, which is the minimum expected observation time along the Galactic plane in the first ten years of the CTA GPS (Acharya et al., 2018). The diffuse emission predicted by GALPROP below 1 TeV is on the lower edge of CTA’s sensitivity. The GALPROP flux is reconstructed for 0.2–1 TeV with the predicted flux

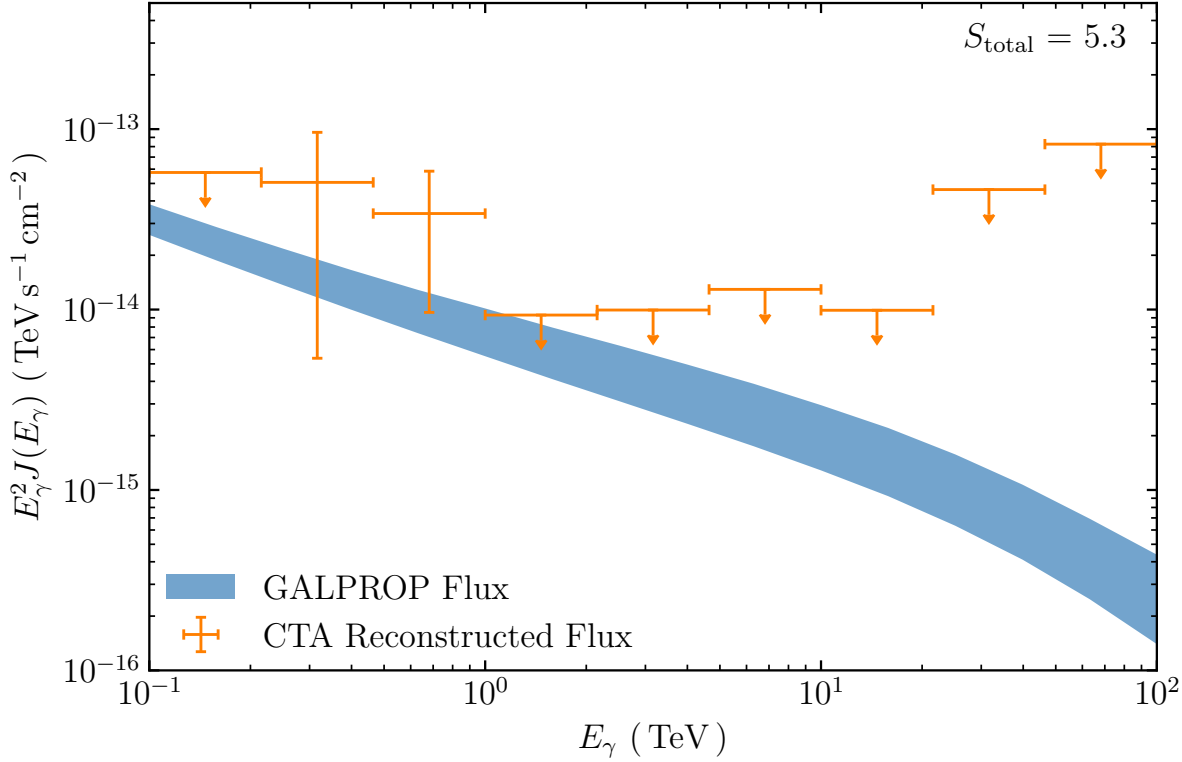


Figure 8.2: Differential photon flux envelope from GALPROP (blue shaded band) and the CTA reconstruction (orange points). Energy bins with $S < 2$ are shown as upper limits, with the total significance shown in the top right corner. The reconstruction is calculated with three bins per decade and a livetime of 50 hr.

envelope contained within the uncertainties. For energies above 1 TeV the reconstructed points are shown as upper bounds as $S(E_{\text{reco}}) < 2$. Hence, CTA is expected to observe the diffuse emission around HESS J1614–518 below 1 TeV given a 50 hr livetime. For γ -ray energies in the range 1–10 TeV CTA will need to utilise, for example, more complex background subtraction methods or longer livetimes, for any potential detections the diffuse emission.

8.2.2 Diffuse Gamma-Ray Emission Near RX J1713.7–3946

The SNR RX J1713.7–3946 (Pfeffermann and Aschenbach, 1996) is one of the brightest and most studied TeV γ -ray sources (e.g. Koyama et al., 1997; Aharonian et al., 2004; Moriguchi et al., 2005; Acero et al., 2009; Maxted et al., 2012; Tsuji et al., 2019; Leike et al., 2021). Previous studies have predicted regions around RX J1713.7–3946 to be emitting γ rays due to the escaping CRs colliding with the surrounding gas (e.g. Casanova et al., 2010; Rowell et al., 2023). Some of the emission predicted to be around RX J1713.7–3946 was later observed by H.E.S.S. (Abdalla et al., 2018d). CTA observations around RX J1713.7–3946 have the potential to confirm or deny the SNR as an accelerator of PeV hadrons – which is unconfirmed for SNRs in general (e.g. Lagage and Cesarsky, 1983; Bell, 2004).

RX J1713.7–3946 is located at $(\ell, b) = (347.31^\circ, -0.46^\circ)$ with a radius of 0.6° (Abdalla et al., 2018e). The γ -ray emission observed in the HGPS around the SNR is shown in

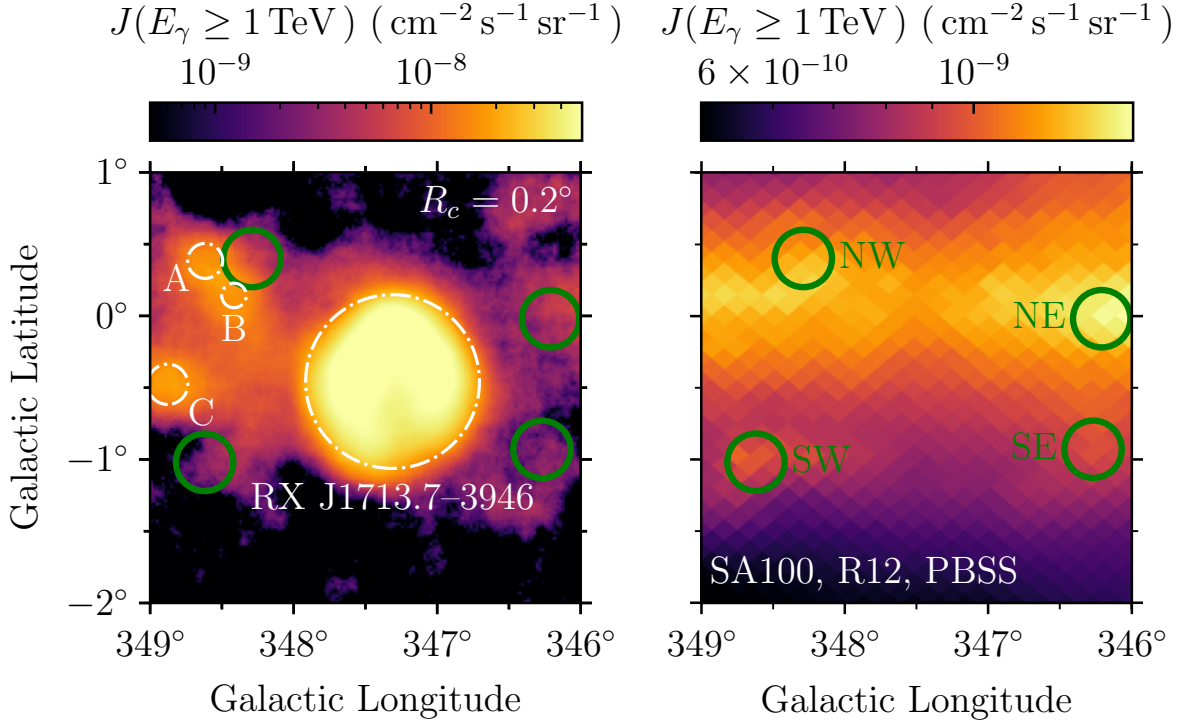


Figure 8.3: Integrated γ -ray flux above 1 TeV around RX J1713.7–3946 from the HGPS (left) and the steady-state SA100/R12/PBSS combination from GALPROP (right). The four analysis regions used for extracting the GALPROP emission are shown by green circles (labelled as NW, NE, SW, and SE). The HGPS sources RX J1713.7–3946, HESS J1713–381 (labelled A), HESS J1714–385 (labelled B), and HESS J1718–385 (labelled C) are shown by white circles.

Figure 8.3 alongside the predicted diffuse emission from the steady-state SA100/R12/PBSS combination from GALPROP for the same region. RX J1713.7–3946, along with the three nearby γ -ray sources HESS J1713–381, HESS J1714–385, and HESS J1718–385 (labelled A, B, and C, respectively) are shown by the white circles.

Similarly as to the calculation around HESS J1614–518, the CTA reconstruction is computed from the midpoint of the GALPROP flux envelope. The variation in the GALPROP flux over the grid of twenty steady-state models from Chapter 5 as well as the six time-dependent models from Chapter 7. The GALPROP envelope is extracted from the analysis regions shown by the green circles with radii of 0.2° located at: NW; $(\ell, b) = (348.29^\circ, 0.40^\circ)$, NE; $(346.21^\circ, -0.02^\circ)$, SW; $(346.27^\circ, -0.93^\circ)$, and SE; $(348.62^\circ, -1.02^\circ)$. These four regions contain ISM clouds that are located at approximately the same line-of-sight distance from Earth and are predicted to emit additional γ -ray emission above the diffuse background (Rowell et al., 2023).

The GALPROP envelopes and the CTA reconstructions are shown for the four regions in Figure 8.4. As additional observation time is planned for RX K1713.7-3946 (Acharya et al., 2018) the computation was performed with a livetime of 100 hr. Just as for the HESS J1614–518 reconstruction, the diffuse emission predicted by GALPROP is on the lower edge of the sensitivity of CTA. Below 1 TeV CTA should be able to observe the diffuse emission, while for γ -ray energies 1–10 TeV the reconstructed flux points are only presented as upper limits.

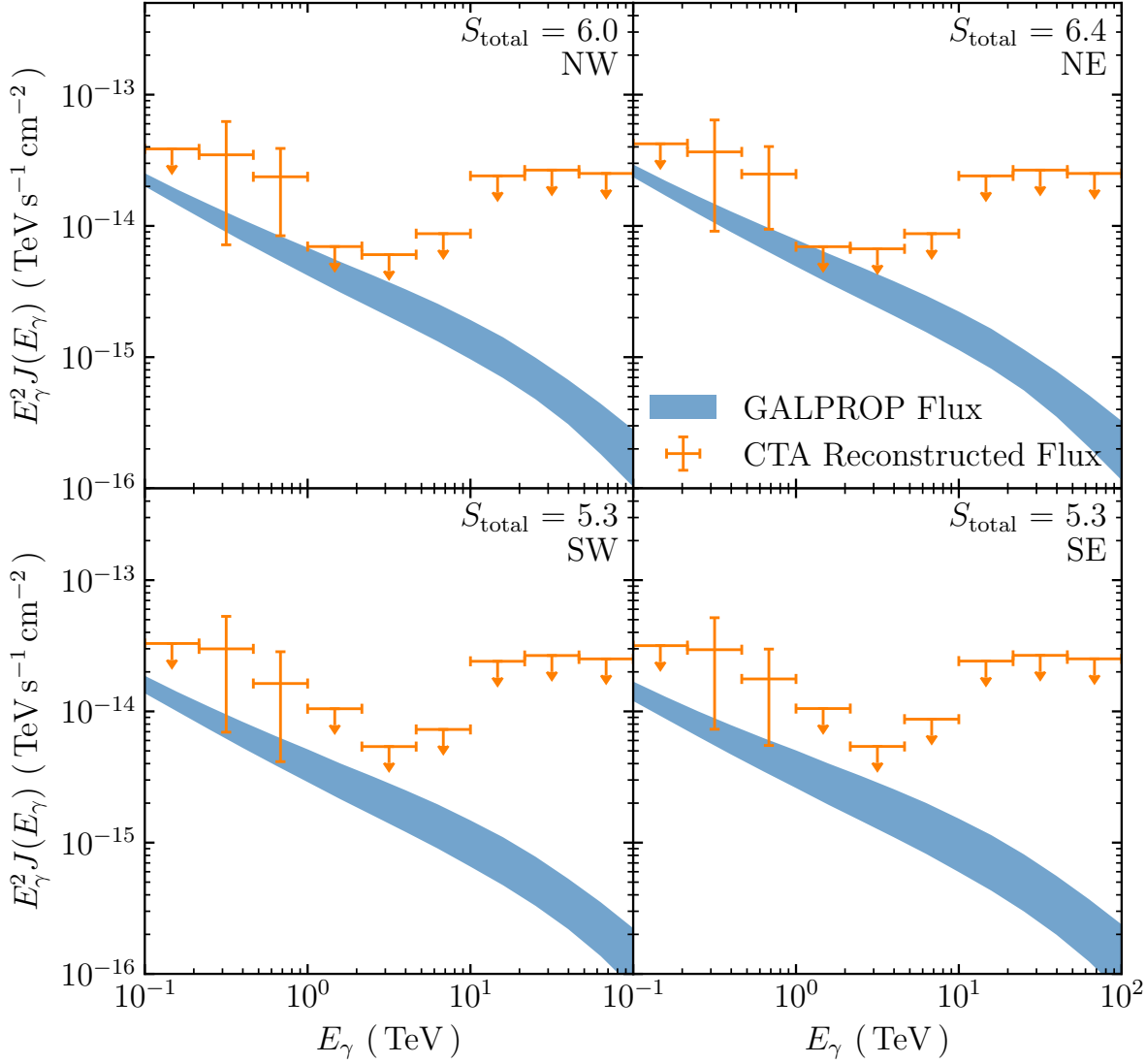


Figure 8.4: Differential photon flux envelopes from GALPROP (blue shaded band) and the CTA reconstructions (orange points). Energy bins with $S < 2$ are shown as upper limits, with the total significance shown in the top right corner of each panel. The reconstruction is calculated with five bins per decade and a livetime of 100 hr for the NW region (top left), NE (top left), SW (bottom left), and SE (bottom right).

The γ -ray brightening due to CRs escaping the SNR was modelled by [Rowell et al. \(2023\)](#) for the same analysis regions presented here. By comparing the models from [Rowell et al. \(2023\)](#) to the diffuse γ -ray predictions in [Figure 8.4](#), it can be seen that the diffuse γ -ray emission below 10 TeV could contribute up to half of the observed γ -ray flux. Hence, future observations by CTA for the regions around RX J1713.7–3946 must account for the diffuse γ -ray emission before performing spectral and morphological analyses.

The calculations presented here demonstrate that CTA should detect the diffuse γ -ray emission. However, it should be noted that the *on* and *off* regions are purely symbolic representations. A more accurate representation of the reconstructed fluxes would involve utilising the entire flux maps and computing the background counts from, e.g. the ring background method (see [Section 3.2.3](#)). Defining spatially separate *on* and *off* regions would allow more robust calculations of the significance, e.g. [Li and Ma \(1983\)](#) (see [Equation 3.15](#)). These calculations are left for future studies.

Chapter 9

Summary and Future Work

Galactic CR transport models, such as GALPROP, have previously reproduced the Galactic diffuse γ -ray emission successfully up to 100 GeV (Ackermann et al., 2012). However, the diffuse γ -ray emission predicted by GALPROP had never been compared in detail to γ -ray observations at TeV (or higher) energies. This thesis presents the first comparison between the simulated diffuse TeV γ -ray emission from GALPROP to the TeV γ -ray observations from H.E.S.S.. GALPROP was demonstrated to agree to the HGPS within modelling and experimental uncertainties. This thesis also presents the first demonstration that GALPROP agrees with the recent diffuse emission estimates from LHAASO up to 1 PeV (Cao et al., 2023). Hence, the work in this thesis extended the demonstrated energy range that GALPROP can reproduce the diffuse γ -ray emission by an additional four orders of magnitude beyond previous comparisons.

For the CR transport models there will be some variation in the TeV predictions due to degeneracies in the Galactic distributions, such as in the CR source distribution, the interstellar radiation field (ISRF), and Galactic magnetic field (GMF). Additionally, due to the short cooling times of the electrons above 10 TeV, it becomes important to consider the injection of the CRs by discrete sources. The placement of the sources leads to another component of the modelling variation above 1 TeV. This thesis presents the first quantification of all components of the modelling variation in the TeV γ -ray predictions.

The steady-state modelling variation was quantified by simulating the diffuse γ -ray emission over a grid of reasonable Galactic distributions (see Chapter 5). The choice of ISRF altered the simulated diffuse TeV emission by less than 5%, while the choice of source distribution and GMF altered the simulated diffuse TeV emission by $\sim 40\%$. The time-dependent variation was quantified by simulating over multiple possible CR source lifetimes and CR source creation rates (see Chapter 7). The time-dependent variation at 1 TeV was similar to the full variation over all steady-state models, i.e. $\sim 40\%$.

For the TeV observations from the H.E.S.S. Galactic plane survey (HGPS; Abdalla et al., 2018e), there are multiple components that need to be considered before finding an estimate of the diffuse TeV γ -ray emission. These components are the γ -ray emission from catalogued γ -ray sources, the emission from unresolved γ -ray sources, and the large-scale diffuse γ -ray emission. The residual emission after subtracting the two γ -ray source components is considered to be an estimate of the observed diffuse emission.

After accounting for all of the uncertainties in the HGPS diffuse γ -ray estimate and the simulated diffuse γ -ray emission from GALPROP, it was found that the predictions are in good agreement with the observations. However, the uncertainty band on the HGPS diffuse emission estimates found in this thesis can be as large as a factor of five. Firm conclusions on the diffuse γ -ray emission in the TeV energy regime will require the observations from the future TeV γ -ray observatory, the Cherenkov telescope array (CTA; Acharya et al., 2018).

At 1 TeV the diffuse γ -ray emission was found to have a significant leptonic component, especially above and below the Galactic plane. For Galactic longitudes $\ell \leq |90^\circ|$ the leptonic component of the diffuse emission is approximately equal to the hadronic component of the flux. For the steady-state models the leptonic contribution to the diffuse γ -ray emission increased with γ -ray energy, accounting for up to 90% of the total flux at 100 TeV for $\ell \leq |90^\circ|$. Extending to the time-dependent simulations, the increasing leptonic component of the diffuse emission can be seen as an increasing contribution due to unresolved leptonic CR sources. Additionally, it was found that the local observed CR electron spectrum is entirely consistent with no discrete CR electron sources being located within 200 pc of Earth, agreeing with various other types of models (e.g. [Porter and Protheroe, 1997](#); [Mertsch, 2018](#)). It was also found that the electron flux above 10 TeV can vary by over a factor of ten over a few million years. This result shows that the injected CR electron spectrum used by any CR transport simulation cannot be normalised to the local CR electron spectrum above ~ 1 TeV, as is commonly performed in the literature.

This thesis also provided an initial look into the detectability of the diffuse TeV γ -ray emission by CTA. The uncertainty band for both the HGPS diffuse γ -ray emission estimate and the variations in the GALPROP predictions are almost entirely above the proposed sensitivity for the CTA Galactic plane survey for Galactic longitudes $|\ell| \lesssim 45^\circ$. Therefore, CTA will detail the TeV diffuse emission, allowing the origin of the diffuse emission to be identified in the TeV regime and complementing the analysis of discrete γ -ray sources.

9.1 Future Work

The GALPROP modelling variation along the Galactic plane that was calculated in this thesis is an upper bound. For example, the GASE GMF ([Strong et al., 2000](#), see [Section 2.6](#)) was included in the estimate of the γ -ray modelling variation as it is commonly used throughout the literature. However, the GASE GMF is not a complete representation of the MW. The modelling variation can be reduced by using other GMF models that are consistent with observations of extra-Galactic rotation measures, such as [Jansson and Farrar \(2012\)](#). Similarly, the SA0 and SA100 source distributions do not necessarily reproduce the data well but were included in the estimate of the modelling variation as they are commonly used throughout the literature. For the time-dependent modelling variation the CR sources were approximated into a single average source class, with a wide range of values for the CR source lifetimes and CR source creation rates being taken. Adding more recent, physically motivated Galactic distributions, finding tighter constraints on the CR source parameters, and accounting for the different classes of sources (e.g. SNRs, PWNe, etc.), will allow a more representative estimate of the modelling variation to be calculated.

Currently, GALPROP uses the LAB HI-survey ([Kalberla et al., 2005](#)) and the CfA composite CO survey ([Dame et al., 2001](#)) in the construction of the interstellar medium (ISM) gas models (see [Section 2.4](#)). These gas models are used for both the CR transport calculations and the γ -ray emission calculations. The gas surveys used in the construction of the ISM models have angular resolutions of approximately 0.1° , limiting the maximum angular resolution for the γ -ray emission maps calculated by GALPROP to $6.9' = 0.1145^\circ$.

The maximum resolution of GALPROP is currently adequate for comparisons to H.E.S.S., which has a point spread function (PSF) full-width half-maximum (FWHM) reaching $4.8' = 0.08^\circ$. However, CTA will have a PSF FWHM reaching $1' \approx 0.017^\circ$. More recent, higher-resolution maps of the ISM gas would allow GALPROP to simulate the diffuse emission to a greater resolution and will be required before GALPROP can be used as a diffuse model by the CTA observatory. Potential higher-resolution surveys that could be integrated into GALPROP include: Mopra CO (Braiding et al., 2015; Braiding et al., 2018; Çubuk et al., 2023) and GASKAP HI/OH (Dickey et al., 2013) for the southern hemisphere, and Nobeyama 45m CO (Minamidani et al., 2015; Umemoto et al., 2017) and THOR HI/OH (Beuther et al., 2016; Wang et al., 2020) for the northern hemisphere.

9.1.1 Applications to TeV Gamma-Ray Observations

Currently H.E.S.S. uses an ad-hoc model of the large-scale emission that is calculated from the observations. With the large amount of significant emission that CTA is expected to observe along the Galactic plane a more robust method of subtracting the diffuse γ -ray background will be required. By integrating the GALPROP predictions with the Python package `gammapy` it will be possible to create a robust diffuse emission template that can be subtracted from analyses. This template could be applied retroactively to the HGPS, allowing for additional faint sources such as PWNe and transient sources to be discovered. Chapter 8 presented a first look at the detectability of the diffuse emission with GALPROP using `gammapy` and the provided IRFs. It was found that CTA should be able to directly measure the diffuse emission below 1 TeV. Above 1 TeV the diffuse emission will still be a significant component for faint (i.e. $<1\%$ Crab) sources and will need to be considered for spectral and morphological studies. Implementing a diffuse model will be integral for CTA as it is expected to detect hundreds of faint sources, making source confusion a future challenge for the observatory (Mestre et al., 2022).

CR air shower events typically outnumber γ -ray air showers by a factor of a thousand. Throughout the literature there are many techniques to subtract the CR background from γ -ray observations, such as: the on-off method (Weekes et al., 1989), the template method (Rowell, 2003), the standard ring and reflected ring methods (Berge et al., 2007), and the field-of-view method (Berge et al., 2007). The technique used in the HGPS was the adaptive ring background method (see Section 3.2.3). The adaptive ring background assumes that there is no γ -ray background contributing to the estimate of the CR flux. However, the diffuse γ -ray emission will contaminate estimates of the CR background for all regions along the Galactic plane. For the HGPS, the diffuse γ -ray emission and its morphology was not considered in the calculation of the CR background estimates. Hence, the CR background is overestimated in the HGPS. The degree to which the CR background is overestimated will depend on the Galactic coordinates of the observation, as well as the pre-defined exclusion regions (see Section 3.2.3). A diffuse emission model, such as GALPROP, could be used to estimate the γ -ray flux that would be contaminating the CR background estimate. This estimate could then be used to apply a correction, improving the significance of the observations. Integrating a diffuse γ -ray model into the CR background pipeline could also be applied to CTA, e.g. to aid in identifying two overlapping, low-surface-brightness γ -ray sources.

Appendix A

Running GALPROP

Producing physically meaningful and accurate results with GALPROP requires an appropriate setup, especially in regards to the size of the timestep (see [Section 2.7.2](#)) and the size of the of the propagation cells (see [Section 2.7.3](#)). Most of the GALPROP run parameters are defined within the GALDEF file, with some CR injection parameters defined in the SOURCECLASS file. Example GALDEF and SOURCECLASS files are included in the installation, with many more examples available on the GALPROP website¹. Details on the parameters within the GALDEF file can be found in either the GALPROP explanatory supplement² or the example files included in the GALPROP installation. The information in this appendix supplements the information given in the two aforementioned sources and is current as of GALPROP version 57. This appendix ends with visualisations of some GALPROP outputs.

A.1 Grid Coordinate Setup

GALPROP numerically solves the CR energy density flowing from one volume element, or cell, into adjacent cells. There are three propagation grids that GALPROP can use: ‘linear’ and ‘tan’, ‘step’. The latter is not discussed in this thesis, while the linear and tan grids and their functional definitions are discussed in [Section 2.7.3](#).

The grid function is defined in the GALDEF file, and each axis is specified independent of one another. The grid function is chosen via the parameters `x_grid`, `y_grid`, and `z_grid`, which can be set to `linear`, `tan`, or `step`. The parameters discussed in [Section 2.7.3](#) are shown alongside their GALDEF names in [Table A.1](#).

Appropriate values for the grid parameters need to be calculated before running GALPROP. To save computation time and RAM/storage requirements, the parameters should be adjusted for the goals of the given simulation. Calculating values for the grid size requires an analysis of the cooling distances of all CR species and energies that are being simulated. To accurately capture the CRs moving from one cell to an adjacent cell, the cell size along any given axis (ΔX , ΔY , ΔZ) should be smaller than the shortest cooling distance of any included CR. The cooling distances for the various energy-loss processes are given by Equations 2.44–2.47 and shown in [Figure 2.7](#). Note that if using the time-dependent solution, and depending on which solver is chosen, the grid size typically needs to be less than half of the shortest cooling distance (see [Porter et al., 2022](#), Appendix D).

¹<https://galprop.stanford.edu/>

²The latest version of the explanatory supplement as of the writing of this thesis is the development version from April 2013 ([Strong et al., 2013](#)). All versions of the explanatory supplement are available at <https://galprop.stanford.edu/code.php?option=manual>.

Table A.1: The GALPROP coordinate parameters discussed in [Section 2.7.3](#) with how they are referred to in the GALDEF file.

GALDEF Parameter	Symbolic Representation
<code>x_min</code>	X_{\min}
<code>x_max</code>	X_{\max}
<code>dx</code>	ΔX
<code>x_grid_pars</code>	$X_0, X_{\text{ref}}, \lambda_X$
<code>y_min</code>	Y_{\min}
<code>y_max</code>	Y_{\max}
<code>dy</code>	ΔY
<code>y_grid_pars</code>	$Y_0, Y_{\text{ref}}, \lambda_Y$
<code>z_min</code>	Z_{\min}
<code>z_max</code>	Z_{\max}
<code>dz</code>	ΔZ
<code>z_grid_pars</code>	$Z_0, Z_{\text{ref}}, \lambda_Z$

To further optimise computation time, memory, and storage, the tan grid ([Equation 2.90](#)) can be utilised. The tan grid function uses the scaling parameter, λ , to increase the cell size from ΔX at some ‘central’ point, X_0 , to the size $\lambda \Delta X$ at some reference point, X_{ref} . By making some further assumptions, the tan grid parameters can be optimised to provide accurate diffusion calculations in the most important regions while sacrificing accuracy from regions far away from the central point. Reasonable values will change depending on the specifics of each individual simulation. Ideally, the grid parameters should be chosen such that the particle transport will be accurately modelled at the Solar position. To accurately model the CR transport and γ -ray emission within and across the spiral arms in the MW, the region between $X \approx 4$ kpc and the Solar position ($X = S_{\odot}$) should also be similar to the shortest cooling time.

To capture CR transport accurately for the entire MW, all ISM structures must be included within the propagation grid. For the XY -plane the maximum extent must be set to at least ± 20 kpc to capture all of the ISM structures (e.g. ISM gas, GMF, etc.). Increasing the extent of the XY -plane beyond ± 20 kpc does not significantly alter the γ -ray results as there is no large-scale structure beyond these limits. For the Z -axis there is a large-scale structure named the *Fermi* bubbles ([Dobler et al., 2010](#); [Su et al., 2010](#)) which extends to heights of ± 15 kpc ([Ackermann et al., 2014](#)). However, the mechanisms behind the *Fermi* bubbles are still debated³, and GALPROP is not currently designed to reproduce them. Reproducing the local observations of radioactive secondary CR ratios requires that the Z -axis limits are set to at least ± 6 kpc ([Moskalenko et al., 2005](#); [Orlando and Strong, 2013](#); [Jóhannesson et al., 2016](#)), and increasing the Z -axis limit beyond ± 6 kpc does not significantly change the γ -ray results ([Jóhannesson et al., 2016](#)).

³See, e.g. [Ackermann et al. \(2014\)](#); [Crocker et al. \(2015\)](#); [Bland-Hawthorn et al. \(2019\)](#), and references therein, for discussions on possible mechanisms behind the *Fermi* bubbles.

Table A.2: The GALPROP time parameters discussed in [Section 2.7.2](#) and [Section 6.2.3](#) with how they are referred to in the GALDEF file.

GALDEF Parameter	Symbolic Representation	
	Time Independent	Time Dependent
<code>end_timestep</code>	Δt_{final}	Δt
<code>start_timestep</code>	$\Delta t_{\text{initial}}$	t_{initial}
<code>timestep_output</code>	–	t_{out}
<code>timestep_init</code>	–	t_{warm}
<code>timestep_factor</code>	ℓ	–
<code>timestep_repeat</code>	M	t_{final}

A.2 Time Coordinate Setup

GALPROP solves the transport equation ([Equation 2.14](#)) numerically with a variety of finite differencing solvers that can be chosen by the user. For the ‘Operator Splitting’ solver the solution method choices are: ‘Explicit’, ‘Implicit’, and ‘Crank-Nicholson’. In version 57 the ‘Eigen BiGCStab’ solver was added, with the solution method choices ‘Diagonal’ and ‘IncompleteLUT’. All available solution methods operate under the same principle – the CR density is calculated at some given time, and then the solution steps forward some length in time.

GALPROP can solve the transport equation using either a ‘time-independent’ (also known as ‘steady-state’) solution or a ‘time-dependent’ solution. The time-independent solution uses a variable timestep length and a static distribution of sources, and the time-dependent solution uses a constant timestep length and a probabilistic source distribution. The time-independent timestep is discussed in more depth in [Section 2.7.2](#) and the time-dependent timestep is discussed in more depth in [Section 6.2.3](#).

The time-independent and time-dependent solution methods are chosen in the GALDEF file, where `time_dependent_solution = 0` specifies the use of the time-independent solution and `time_dependent_solution = 1` specifies the use of the time-dependent solution. The time-independent grid is defined by the parameters discussed in [Section 2.7.2](#) and the time-dependent grid is defined by the parameters discussed in [Section 6.2.3](#). All the parameters for both the time-independent and time-dependent solutions are shown in [Table A.2](#) alongside their names in the GALDEF file.

Similar to the propagation grid, reasonable values for the time parameters need to be calculated before running GALPROP and will change depending on the specifics of each individual run. To accurately model the cooling of the CRs the timestep needs to be shorter than the most rapid cooling time of the CR species and energies included in the simulation and is critical for accurate modelling of the CR and γ -ray spectra. For time-independent solutions, the smallest timestep (Δt_{final}) needs to be smaller than the fastest cooling time. For time-dependent solutions, all timesteps (Δt) need to be smaller than the fastest cooling time. The timestep size is especially important for time-dependent simulations as the computation time can be on the order of weeks for timesteps $\Delta t < 10$ kyr.

Table A.3: The GALPROP parameters that control the number of sources in the MW and how they are referred to in the SOURCECLASS file.

SOURCECLASS Parameter	Symbolic Representation
epoch	t_{epoch}
number_of_sources	N_{source}
source_on_time	t_{life}
rng_seed	—

Time-dependent models have additional parameters to control the characteristics of the individual sources. These parameters are discussed in [Section 6.2.2](#) and are defined in the SOURCECLASS file. The number of sources created in the MW is given by N_{source} , and each source will inject CRs into the MW for the length of time given by t_{life} . The time t_{epoch} defines the length of time that GALPROP will create new CR accelerators. The seed for the random number generator (RNG) is also defined in the SOURCECLASS file. The RNG seed is the first number fed into the RNG algorithm. For ease of reproducibility the RNG seed is set to some known value such as zero. The source parameters defined in the SOURCECLASS file are shown alongside their symbolic representation in [Table A.3](#).

When using a time-dependent solution the required computation time for VHE CRs can be on the order of weeks. It can be useful to operate GALPROP in a ‘warm start’ mode, where the simulation can be paused and restarted. This is especially useful on a high-performance computing cluster, where the γ -ray skymap creation can be split over many nodes. The start mode is set in the GALDEF file with the parameter `warm_start`, where `warm_start = 0` specifies that the calculation will start at the time t_{initial} . For `warm_start = 1` and `warm_start = 2` the calculation will start at the warm-start initialisation time t_{warm} , with the latter only calculating the γ -ray skymaps. Note that to operate GALPROP in a warm-start mode, the runtime developer flag, `-c`, must be specified in the command line.

Note that in the time-dependent mode GALPROP uses the timestep number ($t_{\text{initial}}/\Delta t$) for reading and writing files. If performing a warm start with an altered timestep (e.g. to improve runtime efficiency, see [Section 6.2.3](#)), the nuclei files will need to be renamed.

A.3 GALPROP Output Examples

Results from GALPROP are output as either `.fits` or compressed `.fits` (i.e. `.fits.gz`) files. The CR nuclei outputs are stored as `.fits` tables in units of $\text{MeV cm}^{-2} \text{s}^{-1} \text{sr}^{-1}$ with array axes (CR, E_k , Z, Y, X), where E_k is the kinetic energy of the CR species. The γ -ray skymaps are stored as 3D HEALPix files in units of $\text{MeV}^{-1} \text{cm}^{-2} \text{s}^{-1} \text{sr}^{-1}$ with an axis for the γ -ray energy, E_γ . Each emission type is stored as a separate HEALPix file.

This section contains visualisations for the GALPROP outputs. The model used in the creation of the visualisations was the SA50 source distribution (see [Section 2.3](#)), the R12 ISRF (see [Section 2.5.2](#)), and the PBSS GMF (see [Section 2.6.2](#)).

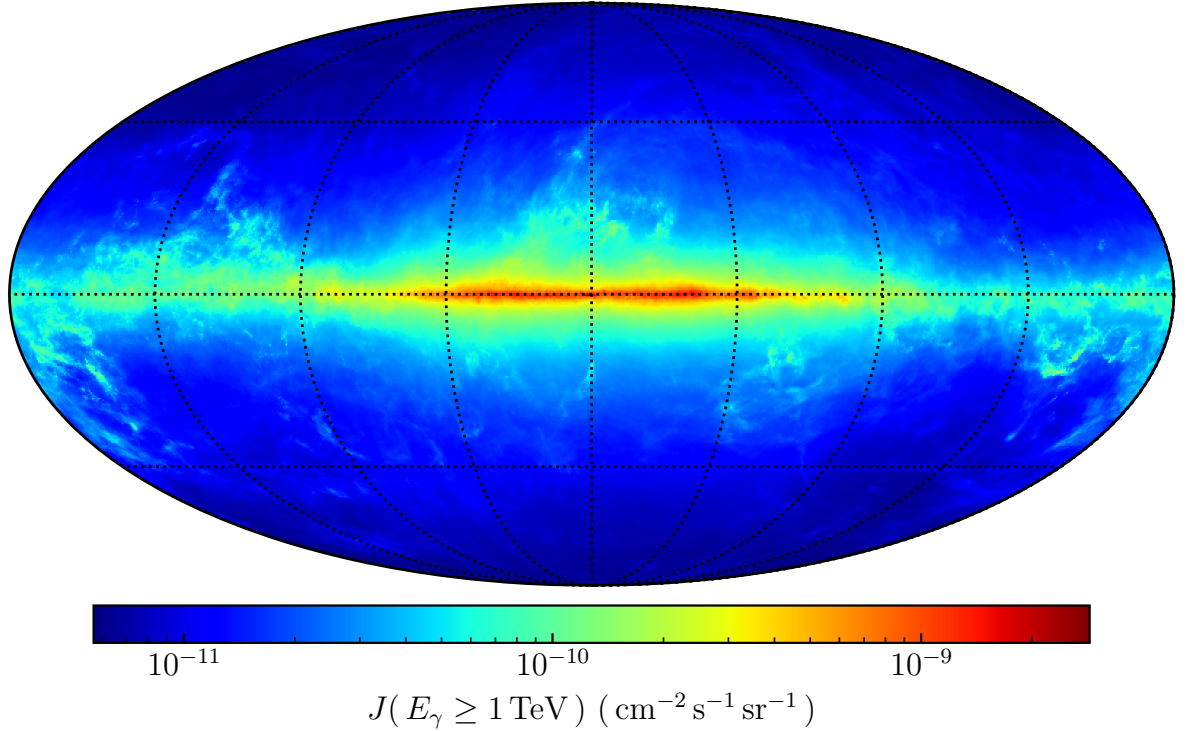


Figure A.1: The total, integrated, time-independent γ -ray emission skymap from GALPROP in units of $\text{cm}^{-2} \text{ s}^{-1} \text{ sr}^{-1}$. All components (pion-decay emission, bremsstrahlung, and IC emission) have been summed together, and the flux has been integrated above 1 TeV.

A.3.1 Time-Independent Output Examples

For time-independent solution methods, all outputs are written to files after the propagation calculations have finished. An example visualisation of the total (i.e. sum over all γ -ray components) γ -ray skymap integrated above 1 TeV is shown in [Figure A.1](#). Although it is not a direct output from GALPROP, the total, integrated skymap is used for the comparisons between GALPROP and H.E.S.S. throughout this thesis, and is included here for reference.

An example visualisation of the CR proton and CR electron energy densities for various kinetic energies can be found in [Figure A.2](#). The CR proton density has a near-constant morphology across all energies as they travel distances on the order of 1 kpc (i.e. they are diffuse). Conversely, as the CR electrons travel shorter distances with increasing energy, their morphology has a strong dependence on energy. The structure in the CR electron density is strongly correlated with the source distribution (SA50; [Figure 2.8](#)) and strongly anti-correlated with the GMF (PBSS; [Figure 2.12](#)), with both structures apparent at 100 TeV. The impact of the tan gridding function increasing the cell size on the other side of the MW can be seen in [Figure A.2](#) as a reduced resolution for negative X values.

An example visualisation of the pion-decay and IC γ -ray emission skymaps can be found in [Figure A.3](#) for various energies in the range 0.01–100 TeV. The pion-decay emission morphology is strongly correlated with the ISM gas density and independent of the γ -ray energy (see [Equation 2.40](#)), while the IC emission morphology is strongly anti-correlated with the GMF and depends on the γ -ray energy.

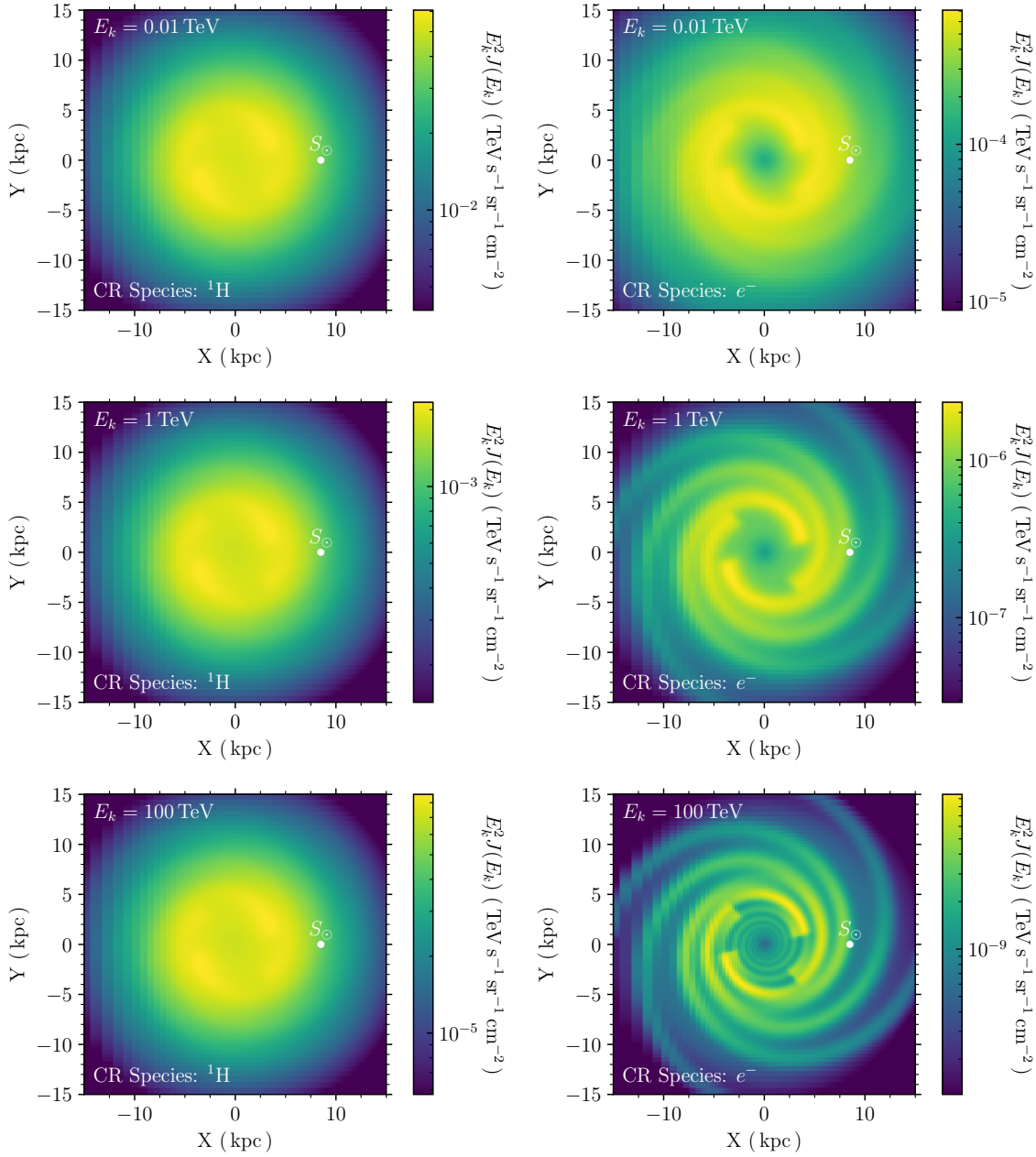


Figure A.2: The time-independent CR proton energy density (left) and time-independent CR electron energy density (right) for the kinetic energies 10 GeV (top), 1 TeV (centre), and 100 TeV (bottom), with the Solar position shown by S_{\odot} . The density has been summed over the Z -axis, and the colourbar represents the CR energy density in units of $\text{TeV cm}^{-2} \text{s}^{-1} \text{sr}^{-1}$.

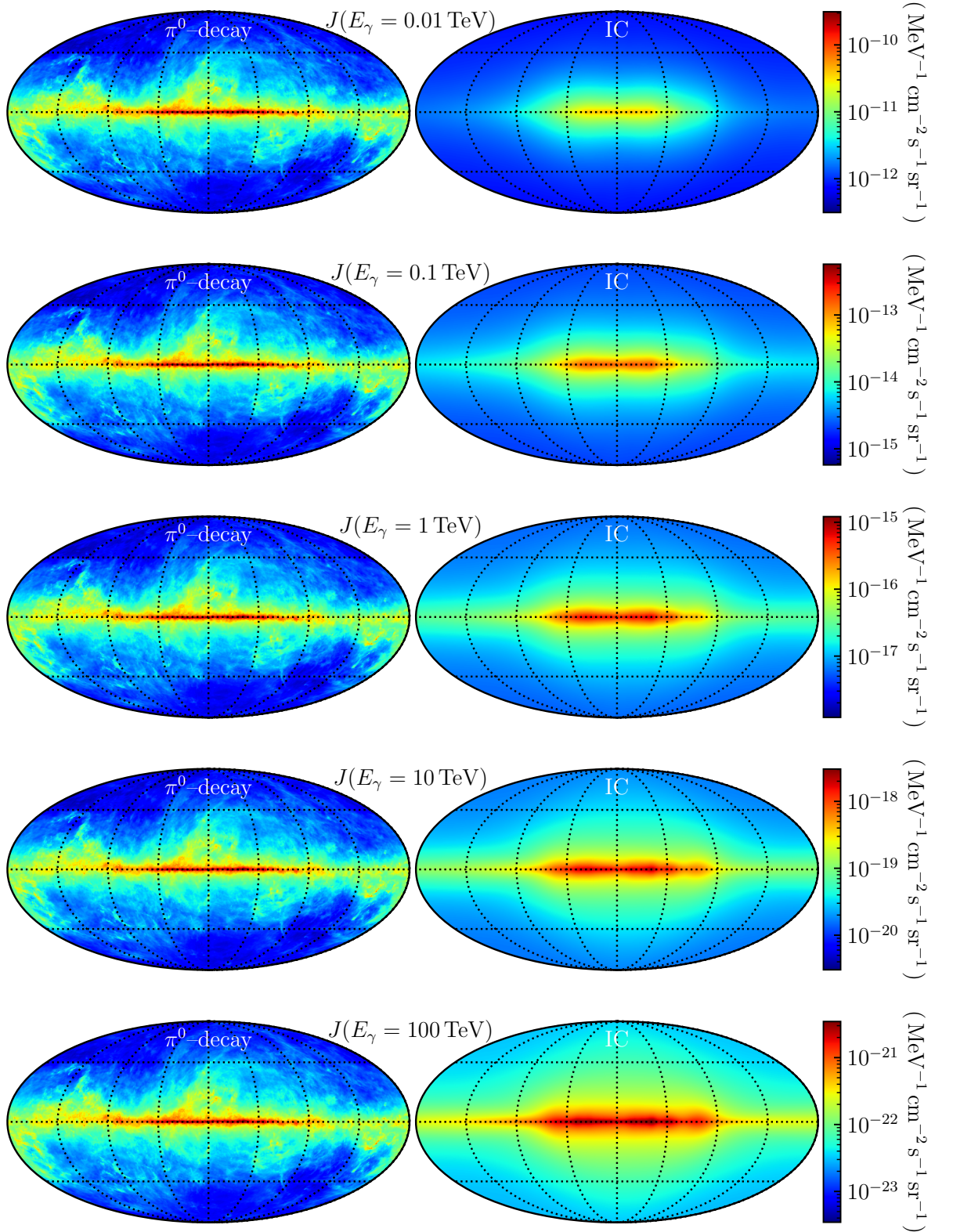


Figure A.3: The time-independent pion-decay emission (left) and time-independent IC emission (right) for various γ -ray energies between 10 GeV (top) and 100 TeV (bottom). The flux is shown in units of $\text{MeV}^{-1} \text{cm}^{-2} \text{s}^{-1} \text{sr}^{-1}$, with the scale applied to both emission types for a given energy.

A.3.2 Time-Dependent Output Examples

The time-dependent outputs are formatted in an identical manner as their time-independent counterparts. The nuclei files are written at each output timestep, t_{out} , with the timestep number appended to the end of the filename. After all nuclei files have been created, GALPROP normalises the CR energy densities to the measured values at the Solar location for all CR species using the method described in [Section 2.7.1](#). The normalisation constants are calculated for the final timestep and are then applied retroactively. After the nuclei have been normalised, GALPROP then begins creation of the γ -ray skymaps.

An example visualisation of the CR proton and CR electron energy densities at 1 TeV around the Solar neighbourhood for various timesteps are shown in [Figure A.4](#) and [Figure A.5](#), respectively. The CR proton density does not vary significantly with time as the CR protons are diffuse at 1 TeV; however, some CR sources are visible above the diffuse CR sea. For the 1 TeV CR electrons the individual sources are easily visible – they do not travel far enough from their injection sites to form a diffuse sea. A cloud of VHE electrons continues to exist for some time after the CR accelerator ceases injecting CRs into the ISM. The length of time that a CR source will inject CRs into the ISM for, and how often sources are placed, is discussed in more depth in [Section 6.2.1](#). The length of time that the VHE electrons remain after the sources disappear depends on the kinetic energy of the CRs.

An example visualisation of the total (i.e. sum over all γ -ray components) γ -ray skymap integrated above 1 TeV for various timesteps is shown in [Figure A.6](#). Similarly as for the CR electron density over time, the γ -ray emission shows bright spots caused by CR sources accelerating CRs into the ISM. As discussed in [Section 6.2.2](#), only a single, ‘average’ source type is defined. Hence, all CR sources in the time-dependent model injects both hadrons and leptons. Therefore, a diffuse sphere of IC emission can be observed around each of the CR sources. Additionally, increased pion-decay emission can be observed from the ISM gas nearby each CR source.

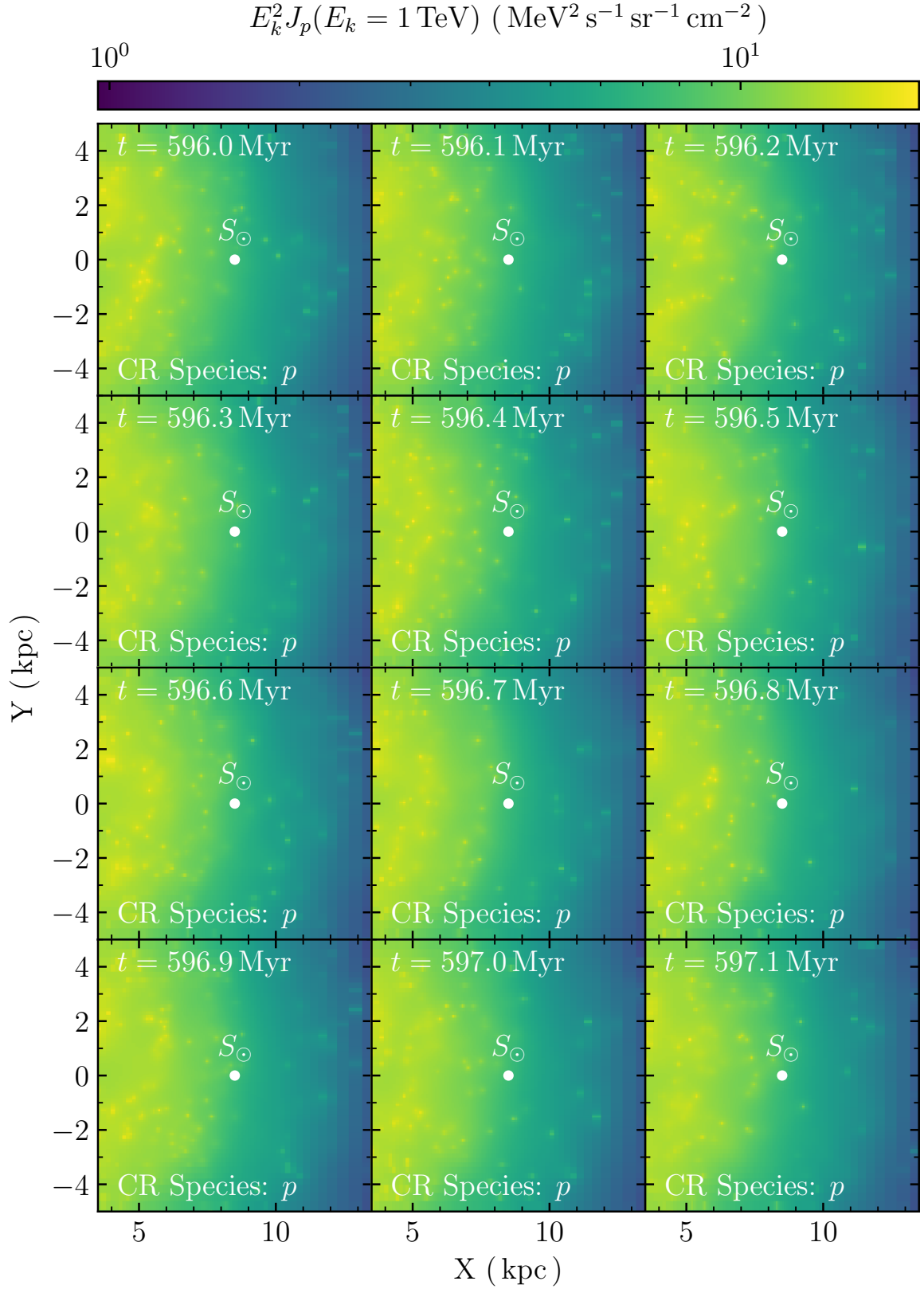


Figure A.4: The time-dependent CR proton energy density at 1 TeV, with the Solar position shown by S_{\odot} . The CR energy density is shown in units of $\text{MeV}^2 \text{cm}^{-2} \text{s}^{-1} \text{sr}^{-1}$. Each frame represents a 0.1 Myr step in time, which is approximately equal to the lifetime of the sources.

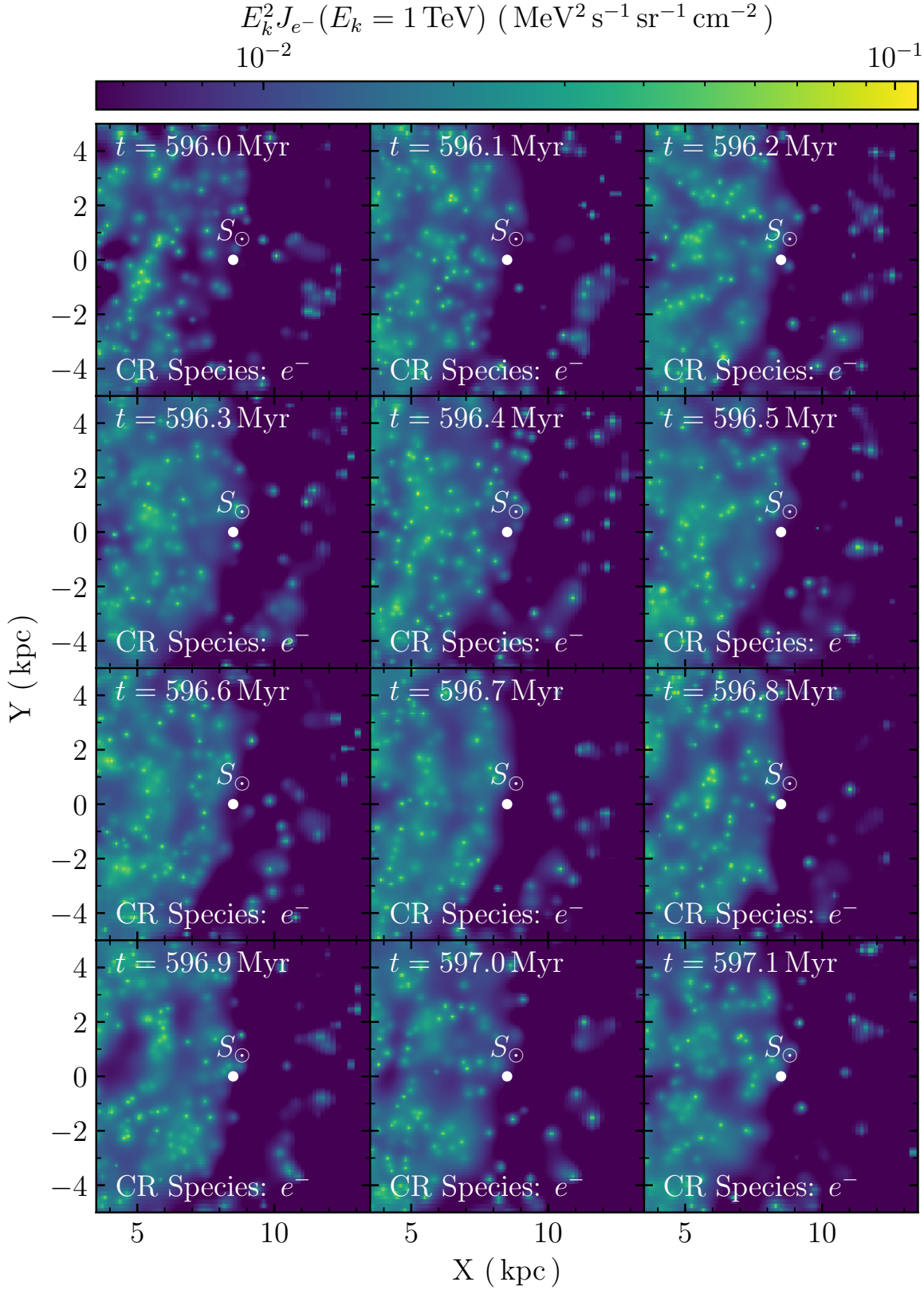


Figure A.5: The time-dependent CR electron energy density at 1 TeV, with the Solar position shown by S_{\odot} . The CR energy density is shown in units of $\text{MeV}^2 \text{ cm}^{-2} \text{ s}^{-1} \text{ sr}^{-1}$. Each frame represents a 0.1 Myr step in time, which is approximately equal to the lifetime of the sources.

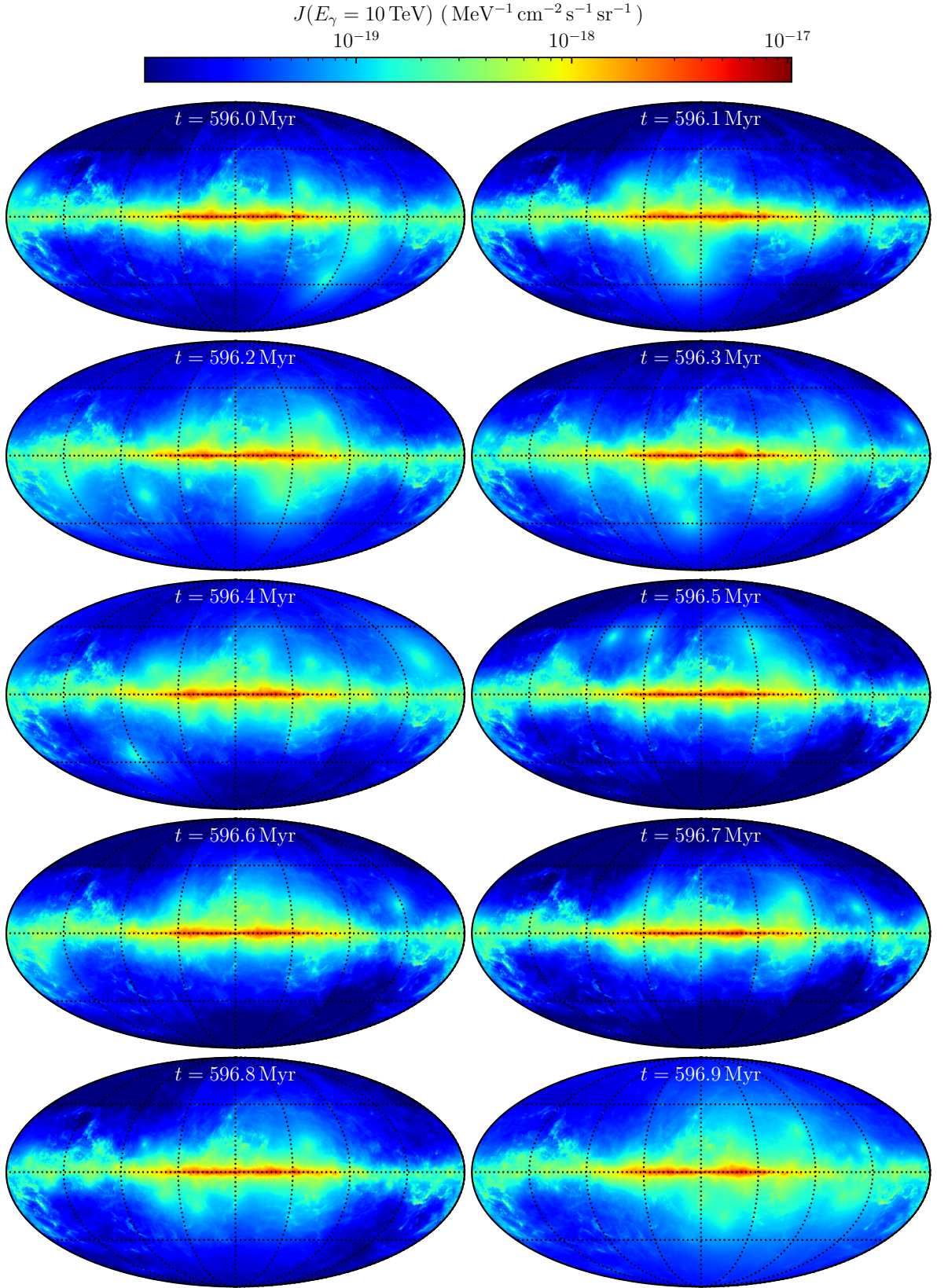


Figure A.6: The GALPROP skymaps of the time-dependent total γ -ray emission at $E_\gamma = 10 \text{ TeV}$ in units of $\text{MeV}^{-1} \text{ cm}^{-2} \text{ s}^{-1} \text{ sr}^{-1}$. All components (pion-decay, bremsstrahlung, and IC emissions) have been summed together. Each frame represents a 0.1 Myr step in time, which is approximately equal to the lifetime of the sources.

Appendix B

HGPS Source Parameters

The procedure to mask a source from the HGPS is detailed in [Section 4.3.1](#). In particular, the equations that model the γ -ray source emission are given by Equations [3.22](#) to [3.24](#). Modelling each source requires the position of the source (given in Galactic longitude and latitude), the radius of the source (given as a Gaussian standard deviation; σ_{source}), and the totally spatially integrated flux of the source (F_{source}). The source surface brightness is modelled as a function of the radial distance from the centre of the source ($S_{\text{source}}(r)$; [Equation 3.22](#)).

To calculate the source parameters the H.E.S.S. collaboration first subtracted their model of the large-scale emission ([Section 3.4](#)) from the HGPS flux map. The large-scale model implicitly includes the diffuse γ -ray emission as well as emission from unresolved γ -ray sources. The residual emission then represents only the γ -ray emission from catalogued sources. The source parameters were approximated from the residual emission, and the surface brightness for each source was calculated by using Equations [3.22](#) to [3.24](#). The modelled surface brightness of each of the source was then subtracted from the flux map, with the source parameters being adjusted iteratively until the residual emission was minimised. For more depth, see [Section 4.8](#) of [Abdalla et al. \(2018e\)](#).

All sources in the HGPS are listed in [Table B.1](#) along with their spatial model, association, and modelling parameters. The association of each identified source is discussed in [Section 3.3.2](#).

For the source-masking procedure in [Section 4.3.1](#), the sources with the ‘shell’ spatial model were excluded from the map such that they did not contribute to any estimate of the diffuse emission. The Galactic centre was excluded in a similar fashion, and is defined by the bounds: $-1.0^\circ \leq l \leq +1.5^\circ$ and $|b| \leq 0.4^\circ$ ([Abdalla et al., 2018e](#)).

Table B.1: A list of all 78 catalogued γ -ray sources in the HGPS, with the parameter values from [Abdalla et al. \(2018e\)](#) and the HGPS catalogue. Longitude and latitude are listed in Galactic coordinates. For the ‘shell’ spatial models, the value of σ_{source} is taken from the radius of the spectral analysis region used by the H.E.S.S. collaboration. For all other sources the value of σ_{source} is listed as the radius of the source.

Source Name	Spatial Model	Association	Longitude (deg)	Latitude (deg)	σ_{source} (deg)	F_{source} ($10^{-12} \text{ cm}^{-2} \text{ s}^{-1}$)
HESS J0835–455	3-Gaussian	PWN	263.96	−3.05	0.58 ± 0.05	15.36 ± 0.53
HESS J0852–463	Shell	SNR	266.29	−1.24	1.00	23.39 ± 2.35
HESS J1018–589 A	Gaussian	Binary	284.35	−1.67	0.00	0.30 ± 0.05
HESS J1018–589 B	Gaussian	Not Firmly Identified	284.22	−1.77	0.15 ± 0.03	0.83 ± 0.17
HESS J1023–575	Gaussian	Stellar Cluster	284.19	−0.40	0.17 ± 0.01	2.56 ± 0.17
HESS J1026–582	Gaussian	Not Firmly Identified	284.85	−0.52	0.13 ± 0.04	0.69 ± 0.19
HESS J1119–614	Gaussian	Composite	292.13	−0.53	0.10 ± 0.01	0.87 ± 0.13
HESS J1302–638	Gaussian	Binary	304.18	−1.00	0.01	0.40 ± 0.05
HESS J1303–631	2-Gaussian	PWN	304.24	−0.35	0.18 ± 0.01	5.26 ± 0.27
HESS J1356–645	Gaussian	PWN	309.79	−2.50	0.23 ± 0.02	5.53 ± 0.53
HESS J1418–609	Gaussian	PWN	313.24	0.14	0.11 ± 0.01	3.01 ± 0.31
HESS J1420–607	Gaussian	PWN	313.58	0.27	0.08 ± 0.01	3.28 ± 0.24
HESS J1427–608	Gaussian	Not Firmly Identified	314.42	−0.16	0.05	0.74 ± 0.10
HESS J1442–624	Shell	SNR	315.43	−2.29	0.30 ± 0.02	2.44 ± 0.67
HESS J1457–593	Gaussian	N/A	318.35	−0.42	0.33 ± 0.04	2.50 ± 0.40
HESS J1458–608	Gaussian	Not Firmly Identified	317.95	−1.70	0.37 ± 0.03	2.44 ± 0.30
HESS J1503–582	Gaussian	N/A	319.57	0.29	0.28 ± 0.03	1.89 ± 0.28
HESS J1507–622	Gaussian	Not Firmly Identified	317.97	−3.48	0.18 ± 0.02	2.99 ± 0.31
HESS J1514–591	3-Gaussian	PWN	320.32	−1.19	0.14 ± 0.03	6.43 ± 0.21
HESS J1534–571	Shell	SNR	323.70	−1.02	0.40 ± 0.04	1.98 ± 0.23
HESS J1554–550	Gaussian	PWN	327.16	−1.08	0.02	0.36 ± 0.06
HESS J1614–518	Shell	Not Firmly Identified	331.47	−0.60	0.42 ± 0.01	5.87 ± 0.42
HESS J1616–508	2-Gaussian	Not Firmly Identified	332.48	−0.17	0.23 ± 0.03	8.48 ± 0.44
HESS J1626–490	Gaussian	N/A	334.82	−0.12	0.20 ± 0.03	1.65 ± 0.33
HESS J1632–478	Gaussian	Not Firmly Identified	336.39	0.26	0.18 ± 0.02	2.93 ± 0.51
HESS J1634–472	Gaussian	Not Firmly Identified	337.12	0.26	0.17 ± 0.01	2.90 ± 0.37
HESS J1640–465	2-Gaussian	Composite	338.28	−0.04	0.11 ± 0.03	3.33 ± 0.19
HESS J1641–463	Gaussian	Not Firmly Identified	338.52	0.08	0.04	0.27 ± 0.06
HESS J1646–458	Gaussian	Stellar Cluster	339.33	−0.78	0.50 ± 0.03	5.48 ± 0.46
HESS J1702–420	Gaussian	N/A	344.23	−0.19	0.20 ± 0.02	3.91 ± 0.65
HESS J1708–410	Gaussian	N/A	345.67	−0.44	0.06 ± 0.01	0.88 ± 0.09
HESS J1708–443	Gaussian	Not Firmly Identified	343.07	−2.32	0.28 ± 0.03	2.28 ± 0.32
HESS J1713–381	Gaussian	Not Firmly Identified	348.62	0.38	0.09 ± 0.02	0.65 ± 0.13
HESS J1713–397	Shell	SNR	347.31	−0.46	0.50	16.88 ± 0.82
HESS J1714–385	Gaussian	Composite	348.42	0.14	0.03	0.25 ± 0.05
HESS J1718–374	Point-Like	SNR	349.72	0.17	0.00	0.12 ± 0.04
HESS J1718–385	Gaussian	Not Firmly Identified	348.88	−0.48	0.12 ± 0.01	0.80 ± 0.14
HESS J1729–345	Gaussian	N/A	353.39	−0.02	0.19 ± 0.03	0.86 ± 0.17
HESS J1731–347	Shell	SNR	353.54	−0.67	0.27 ± 0.02	2.01 ± 0.15
HESS J1741–302	Point-Like	N/A	358.28	0.05	0.00	0.16 ± 0.04
HESS J1745–290	Point-Like	Not Firmly Identified	359.94	−0.04	0.00	1.70 ± 0.08
HESS J1745–303	Gaussian	N/A	358.64	−0.56	0.18 ± 0.02	0.94 ± 0.21
HESS J1746–285	Point-Like	Not Firmly Identified	0.14	−0.11	0.00	0.15 ± 0.05
HESS J1746–308	Gaussian	Not Firmly Identified	358.45	−1.11	0.16 ± 0.04	0.68 ± 0.22
HESS J1747–248	Gaussian	Stellar Cluster	3.78	1.71	0.06 ± 0.01	0.29 ± 0.05
HESS J1747–281	Point-Like	PWN	0.87	0.08	0.00	0.60 ± 0.13
HESS J1800–240	Gaussian	Not Firmly Identified	5.96	−0.42	0.32 ± 0.04	2.44 ± 0.35
HESS J1801–233	Gaussian	SNR	6.66	−0.27	0.17 ± 0.03	0.45 ± 0.10
HESS J1804–216	2-Gaussian	Not Firmly Identified	8.38	−0.09	0.24 ± 0.03	5.88 ± 0.27
HESS J1808–204	Gaussian	Not Firmly Identified	10.01	−0.24	0.06	0.19 ± 0.04
HESS J1809–193	3-Gaussian	Not Firmly Identified	11.11	−0.02	0.40 ± 0.05	5.27 ± 0.29
HESS J1813–126	Gaussian	Not Firmly Identified	17.31	2.49	0.21 ± 0.03	1.08 ± 0.24

HESS J1813–178	Gaussian	Composite	12.82	–0.03	0.05 ± 0.00	1.98 ± 0.15
HESS J1818–154	Gaussian	PWN	15.41	0.16	0.00	0.17 ± 0.04
HESS J1825–137	3-Gaussian	PWN	17.53	–0.62	0.46 ± 0.03	18.41 ± 0.56
HESS J1826–130	Gaussian	Not Firmly Identified	18.48	–0.39	0.15 ± 0.02	0.86 ± 0.17
HESS J1826–148	Gaussian	Binary	16.88	–1.29	0.01	1.28 ± 0.04
HESS J1828–099	Gaussian	N/A	21.49	0.38	0.05	0.43 ± 0.07
HESS J1832–085	Gaussian	N/A	23.21	0.29	0.02	0.21 ± 0.05
HESS J1832–093	Gaussian	Not Firmly Identified	22.48	–0.16	0.00	0.17 ± 0.03
HESS J1833–105	Gaussian	Composite	21.50	–0.90	0.02	0.39 ± 0.07
HESS J1834–087	2-Gaussian	Composite	23.26	–0.33	0.21 ± 0.04	3.34 ± 0.24
HESS J1837–069	3-Gaussian	PWN	25.15	–0.09	0.36 ± 0.03	12.05 ± 0.45
HESS J1841–055	2-Gaussian	Not Firmly Identified	26.71	–0.23	0.41 ± 0.03	10.16 ± 0.42
HESS J1843–033	2-Gaussian	Not Firmly Identified	28.90	0.07	0.24 ± 0.06	2.88 ± 0.30
HESS J1844–030	Gaussian	Not Firmly Identified	29.41	0.09	0.02	0.26 ± 0.05
HESS J1846–029	Gaussian	Composite	29.71	–0.24	0.01	0.45 ± 0.05
HESS J1848–018	Gaussian	Stellar Cluster	30.92	–0.21	0.25 ± 0.03	1.74 ± 0.35
HESS J1849–000	Gaussian	PWN	32.61	0.53	0.09 ± 0.02	0.53 ± 0.09
HESS J1852–000	Gaussian	Not Firmly Identified	33.11	–0.13	0.28 ± 0.04	1.30 ± 0.25
HESS J1857+026	2-Gaussian	Not Firmly Identified	36.06	–0.06	0.26 ± 0.06	3.77 ± 0.40
HESS J1858+020	Gaussian	N/A	35.54	–0.58	0.08 ± 0.02	0.53 ± 0.11
HESS J1908+063	Gaussian	Not Firmly Identified	40.55	–0.84	0.49 ± 0.03	6.53 ± 0.50
HESS J1911+090	Point-Like	SNR	43.26	–0.19	0.00	0.15 ± 0.03
HESS J1912+101	Shell	Not Firmly Identified	44.46	–0.13	0.49 ± 0.04	2.49 ± 0.35
HESS J1923+141	Gaussian	Not Firmly Identified	49.08	–0.40	0.12 ± 0.02	0.78 ± 0.15
HESS J1930+188	Gaussian	Composite	54.06	0.27	0.02	0.29 ± 0.09
HESS J1943+213	Gaussian	Not Firmly Identified	57.78	–1.30	0.03	0.32 ± 0.10

Bibliography

- Abbasi, R., M. Ackermann, J. Adams, et al. (June 2023). “Observation of High-Energy Neutrinos from the Galactic Plane”. [Science](#) 380.6652, pp. 1338–1343.
- Abdalla, H., A. Abramowski, F. Aharonian, et al. (Apr. 2018a). “A Search for New Supernova Remnant Shells in the Galactic Plane with H.E.S.S.” [A&A](#) 612, A8.
- Abdalla, H., A. Abramowski, F. Aharonian, et al. (Apr. 2018b). “Characterising the VHE Diffuse Emission in the Central 200 Parsecs of our Galaxy with H.E.S.S.” [A&A](#) 612, A9.
- Abdalla, H., A. Abramowski, F. Aharonian, et al. (Apr. 2018c). “HESS J1741–302: a Hidden Accelerator in the Galactic Plane”. [A&A](#) 612, A13.
- Abdalla, H., A. Abramowski, F. Aharonian, et al. (Apr. 2018d). “H.E.S.S. Observations of RX J1713.7–3946 with Improved Angular and Spectral Resolution: Evidence for Gamma-Ray Emission Extending Beyond the X-Ray Emitting Shell”. [A&A](#) 612, A6.
- Abdalla, H., A. Abramowski, F. Aharonian, et al. (Apr. 2018e). “The H.E.S.S. Galactic Plane Survey”. [A&A](#) 612, A1.
- Abdalla, H., A. Abramowski, F. Aharonian, et al. (Apr. 2018f). “The Supernova Remnant W49B as Seen with H.E.S.S. and Fermi-LAT”. [A&A](#) 612, A5.
- Abdalla, H., F. Aharonian, F. Ait Benkhali, et al. (Aug. 2021). “TeV Emission of Galactic Plane Sources with HAWC and H.E.S.S.” [ApJ](#) 917.1, p. 6.
- Abdo, A. A., M. Ackermann, M. Ajello, et al. (June 2010). “Fermi Large Area Telescope First Source Catalog”. [ApJS](#) 188.2, pp. 405–436.
- Abdollahi, S., F. Acero, M. Ackermann, et al. (Mar. 2020). “Fermi Large Area Telescope Fourth Source Catalog”. [ApJS](#) 247.1, p. 33.
- Abdollahi, S., M. Ackermann, M. Ajello, et al. (Apr. 2017). “Cosmic-Ray Electron-Positron Spectrum from 7 GeV to 2 TeV with the Fermi Large Area Telescope”. [PhRvD](#) 95.8, p. 082007.
- Abe, S., A. Aguasca-Cabot, I. Agudo, et al. (May 2023). “Multiwavelength Study of the Galactic PeVatron Candidate LHAASO J2108+5157”. [A&A](#) 673, A75.
- Abeysekara, A. U., A. Albert, R. Alfaro, et al. (Nov. 2017a). “Extended Gamma-Ray Sources Around Pulsars Constrain the Origin of the Positron Flux at Earth”. [Science](#) 358, pp. 911–914.
- Abeysekara, A. U., A. Albert, R. Alfaro, et al. (July 2017b). “Observation of the Crab Nebula with the HAWC Gamma-Ray Observatory”. [ApJ](#) 843.1, p. 39.
- Abeysekara, A. U., A. Albert, R. Alfaro, et al. (Jan. 2020). “Multiple Galactic Sources with Emission Above 56 TeV Detected by HAWC”. [PhRvL](#) 124.2.
- Abramowski, A., F. Acero, F. Aharonian, et al. (July 2011a). “A New SNR with TeV Shell-Type Morphology: HESS J1731–347”. [A&A](#) 531, A81.
- Abramowski, A., F. Acero, F. Aharonian, et al. (Sept. 2011b). “Discovery of the Source HESS J1356–645 Associated with the Young and Energetic PSR J1357–6429”. [A&A](#) 533, A103.
- Abramowski, A., F. Acero, F. Aharonian, et al. (July 2011c). “Very-High-Energy Gamma-Ray Emission from the Direction of the Galactic Globular Cluster Terzan 5”. [A&A](#) 531, p. L18.
- Abramowski, A., F. Acero, F. Aharonian, et al. (Dec. 2012). “Probing the Extent of the Non-Thermal Emission from the Vela X Region at TeV Energies with H.E.S.S.” [A&A](#) 548, A38.

- Abramowski, A., F. Aharonian, F. Ait Benkhali, et al. (Dec. 2014a). “Diffuse Galactic Gamma-Ray Emission with H.E.S.S.” [PhRvD](#) 90.12 (12), p. 122007.
- Abramowski, A., F. Aharonian, F. Ait Benkhali, et al. (Feb. 2014b). “HESS J1818–154, a New Composite Supernova Remnant Discovered in TeV Gamma Rays and X-Rays”. [A&A](#) 562, A40.
- Abramowski, A., F. Aharonian, F. Ait Benkhali, et al. (May 2015a). “Discovery of Variable VHE γ -Ray Emission from the Binary System 1FGL J1018.6–5856”. [A&A](#) 577, A131.
- Abramowski, A., F. Aharonian, F. Ait Benkhali, et al. (May 2015b). “Discovery of Variable VHE γ -Ray Emission from the Binary System 1FGL J1018.6–5856”. [A&A](#) 577, A131.
- Abramowski, A., F. Aharonian, F. Ait Benkhali, et al. (Jan. 2015c). “H.E.S.S. Detection of TeV Emission from the Interaction Region Between the Supernova Remnant G349.7+0.2 and a Molecular Cloud”. [A&A](#) 574, A100.
- Abramowski, A., F. Aharonian, F. Ait Benkhali, et al. (Feb. 2015d). “Probing the Gamma-Ray Emission from HESS J1834–087 using H.E.S.S. and Fermi–LAT Observations”. [A&A](#) 574, A27.
- Abramowski, A., F. Aharonian, F. Ait Benkhali, et al. (Apr. 2018). “Detailed Spectral and Morphological Analysis of the Shell Type Supernova Remnant RCW 86”. [A&A](#) 612, A4.
- Abramowski, A., F. Aharonian, F. Ait Benkhali, et al. (Apr. 2014c). “HESS J1640–465 – an Exceptionally Luminous TeV γ -Ray Supernova Remnant”. [MNRAS](#) 439.3, pp. 2828–2836.
- Acciari, V. A., E. Aliu, T. Arlen, et al. (Aug. 2010). “Discovery of Very High Energy γ -Ray Emission from the SNR G54.1+0.3”. [ApJL](#) 719.1, pp. L69–L73.
- Acciari, V. A., S. Ansoldi, L. A. Antonelli, et al. (Sept. 2020). “Studying the Nature of the Unidentified Gamma-Ray Source HESS J1841–055 with the MAGIC Telescopes”. [MNRAS](#) 497.3, pp. 3734–3745.
- Acero, F., M. Ackermann, M. Ajello, et al. (Apr. 2016a). [ApJS](#) 223.2, p. 26.
- Acero, F., M. Ackermann, M. Ajello, et al. (May 2016b). “The First Fermi–LAT Supernova Remnant Catalog”. [ApJS](#) 224.1, p. 8.
- Acero, F., J. Ballet, A. Decourchelle, et al. (Oct. 2009). “A Joint Spectro-Imaging Analysis of the XMM-Newton and H.E.S.S. Observations of the Supernova Remnant RX J1713.7–3946”. [A&A](#) 505.1, pp. 157–167.
- Acero, F., A. Bamba, S. Casanova, et al. (Mar. 2013). “Gamma-Ray Signatures of Cosmic Ray Acceleration, Propagation, and Confinement in the Era of CTA”. [Astropart. Phys.](#) 43, pp. 276–286.
- Acharya, B. S., I. Agudo, I. Al Samarai, et al. (2018). *Science with the Cherenkov Telescope Array*. Singapore: World Scientific Publishing Company.
- Ackermann, M., M. Ajello, A. Albert, et al. (Jan. 2015). “The Spectrum of Isotropic Diffuse Gamma-Ray Emission between 100 MeV and 820 GeV”. [ApJ](#) 799, p. 86.
- Ackermann, M., M. Ajello, W. B. Atwood, et al. (Apr. 2012). “Fermi-LAT Observations of the Diffuse γ -Ray Emission: Implications for Cosmic Rays and the Interstellar Medium”. [ApJ](#) 750.1, p. 3.
- Ackermann, M., A. Albert, W. B. Atwood, et al. (Sept. 2014). “The Spectrum and Morphology of the Fermi Bubbles”. [ApJ](#) 793.1, p. 64.
- Actis, M., G. Agnetta, F. Aharonian, et al. (Dec. 2011). “Design Concepts for the Cherenkov Telescope Array CTA: an Advanced Facility for Ground-Based High-Energy Gamma-Ray Astronomy”. [Exp. Astron.](#) 32.3, pp. 193–316.
- Adriani, O., Y. Akaike, K. Asano, et al. (Nov. 2023). “Direct Measurement of the Spectral Structure of Cosmic-Ray Electrons+Positrons in the TeV Region with CALET on the International Space Station”. [PhRvL](#) 131.19, p. 191001.

- Aghanim, N., M. Ashdown, J. Aumont, et al. (Dec. 2016). “Planck Intermediate Results XLVIII: Disentangling Galactic Dust Emission and Cosmic Infrared Background Anisotropies”. *A&A* 596, A109.
- Aguilar, M., D. Aisa, B. Alpat, et al. (Nov. 2015a). “Precision Measurement of the Helium Flux in Primary Cosmic Rays of Rigidities 1.9 GV to 3 TV with the Alpha Magnetic Spectrometer on the International Space Station”. *PhRvL* 115.21, p. 211101.
- Aguilar, M., D. Aisa, B. Alpat, et al. (May 2015b). “Precision Measurement of the Proton Flux in Primary Cosmic Rays from Rigidity 1 GV to 1.8 TV with the Alpha Magnetic Spectrometer on the International Space Station”. *PhRvL* 114.17, p. 171103.
- Aguilar, M., D. Aisa, A. Alvino, et al. (Sept. 2014). “Electron and Positron Fluxes in Primary Cosmic Rays Measured with the Alpha Magnetic Spectrometer on the International Space Station”. *PhRvL* 113.12, p. 121102.
- Aguilar, M., L. Ali Cavazonza, B. Alpat, et al. (Dec. 2017). “Observation of the Identical Rigidity Dependence of He, C, and O Cosmic Rays at High Rigidities by the Alpha Magnetic Spectrometer on the International Space Station”. *PhRvL* 119.25, p. 251101.
- Aguilar, M., L. Ali Cavazonza, G. Ambrosi, et al. (Jan. 2018). “Observation of New Properties of Secondary Cosmic Rays Lithium, Beryllium, and Boron by the Alpha Magnetic Spectrometer on the International Space Station”. *PhRvL* 120.2, p. 021101.
- Aguilar, M., L. Ali Cavazonza, G. Ambrosi, et al. (Feb. 2021). “The Alpha Magnetic Spectrometer (AMS) on the International Space Station: Part II – Results From the First Seven Years”. *PhR* 894, pp. 1–116.
- Aharonian, F., F. Ait Benkhali, E. O. Angüner, et al. (Apr. 2022a). “Time-Resolved Hadronic Particle Acceleration in the Recurrent Nova RS Ophiuchi”. *Science* 376.6588, pp. 77–80.
- Aharonian, F., A. G. Akhperjanian, G. Anton, et al. (Dec. 2009). “Probing the ATIC Peak in the Cosmic-Ray Electron Spectrum with H.E.S.S.” *A&A* 508.2, pp. 561–564.
- Aharonian, F., A. G. Akhperjanian, K. M. Aye, et al. (Mar. 2005a). “A New Population of Very High Energy Gamma-Ray Sources in the Milky Way”. *Science* 307.5717, pp. 1938–1942.
- Aharonian, F., A. G. Akhperjanian, K. M. Aye, et al. (May 2005b). “Discovery of Extended VHE Gamma-Ray Emission from the Asymmetric Pulsar Wind Nebula in MSH 15–52 with H.E.S.S.” *A&A* 435.1, pp. L17–L20.
- Aharonian, F., A. G. Akhperjanian, K. M. Aye, et al. (Oct. 2005c). “Discovery of the Binary Pulsar PSR B1259–63 in Very-High-Energy Gamma Rays Around Periastron with H.E.S.S.” *A&A* 442.1, pp. 1–10.
- Aharonian, F., A. G. Akhperjanian, K. M. Aye, et al. (Mar. 2005d). “Very High Energy Gamma Rays from the Composite SNR G 0.9+0.1”. *A&A* 432.2, pp. L25–L29.
- Aharonian, F., A. G. Akhperjanian, U. Barres de Almeida, et al. (Nov. 2008a). “Discovery of a VHE Gamma-Ray Source Coincident with the Supernova Remnant CTB 37A”. *A&A* 490.2, pp. 685–693.
- Aharonian, F., A. G. Akhperjanian, A. R. Bazer-Bachi, et al. (July 2005e). “Detection of TeV γ -Ray Emission from the Shell-Type Supernova Remnant RX J0852.0–4622 with H.E.S.S.” *A&A* 437.1, pp. L7–L10.
- Aharonian, F., A. G. Akhperjanian, A. R. Bazer-Bachi, et al. (Dec. 2006a). “3.9 Day Orbital Modulation in the TeV γ -Ray Flux and Spectrum from the X-Ray Binary LS 5039”. *A&A* 460.3, pp. 743–749.
- Aharonian, F., A. G. Akhperjanian, A. R. Bazer-Bachi, et al. (Sept. 2006b). “Discovery of the Two “Wings” of the Kookaburra Complex in VHE γ -Rays with H.E.S.S.” *A&A* 456.1, pp. 245–251.

- Aharonian, F., A. G. Akhperjanian, A. R. Bazer-Bachi, et al. (Dec. 2006c). “Energy Dependent γ -Ray Morphology in the Pulsar Wind Nebula HESS J1825–137”. *A&A* 460.2, pp. 365–374.
- Aharonian, F., A. G. Akhperjanian, A. R. Bazer-Bachi, et al. (Mar. 2006d). “First Detection of a VHE Gamma-Ray Spectral Maximum from a Cosmic Source: H.E.S.S. Discovery of the Vela X Nebula”. *A&A* 448.2, pp. L43–L47.
- Aharonian, F., A. G. Akhperjanian, A. R. Bazer-Bachi, et al. (Oct. 2006e). “Observations of the Crab Nebula with H.E.S.S.” *A&A* 457.3, pp. 899–915.
- Aharonian, F., A. G. Akhperjanian, A. R. Bazer-Bachi, et al. (Jan. 2006f). “The H.E.S.S. Survey of the Inner Galaxy in Very High Energy Gamma Rays”. *ApJ* 636.2, pp. 777–797.
- Aharonian, F., A. G. Akhperjanian, A. R. Bazer-Bachi, et al. (Apr. 2008b). “Discovery of Very High Energy Gamma-Ray Emission Coincident with Molecular Clouds in the W 28 (G6.4–0.1) Field”. *A&A* 481.2, pp. 401–410.
- Aharonian, F., H. Ashkar, M. Backes, et al. (Oct. 2022b). “A Deep Spectromorphological Study of the γ -Ray Emission Surrounding the Young Massive Stellar Cluster Westerlund 1”. *A&A* 666, A124.
- Aharonian, F., F. Ait Benkhali, J. Aschersleben, et al. (Nov. 2024). “High-Statistics Measurement of the Cosmic-Ray Electron Spectrum with H.E.S.S.” *PhRvL* 133.22, p. 221001.
- Aharonian, F. A. (2004). *Very High Energy Cosmic Gamma Radiation*. World Scientific.
- Aharonian, F. A., A. G. Akhperjanian, K. M. Aye, et al. (Nov. 2004). “High-Energy Particle Acceleration in the Shell of a Supernova Remnant”. *Nature* 432.7013, pp. 75–77.
- Aharonian, F. A. and A. M. Atoyan (May 1996). “On the Emissivity of π^0 -Decay Gamma Radiation in the Vicinity of Accelerators of Galactic Cosmic Rays”. *A&A* 309, pp. 917–928.
- Aharonian, F. A., A. M. Atoyan, and T. Kifune (Oct. 1997). “Inverse Compton Gamma Radiation of Faint Synchrotron X-Ray Nebulae Around Pulsars”. *MNRAS* 291.1, pp. 162–176.
- Aharonian, Felix, Ruizhi Yang, and Emma de Oña Wilhelmi (Mar. 2019). “Massive Stars as Major Factories of Galactic Cosmic Rays”. *Nature Astro.* 3, pp. 561–567.
- Ajello, M., A. Albert, W. B. Atwood, et al. (Mar. 2016). “Fermi–LAT Observations of High-Energy Gamma-Ray Emission toward the Galactic Center”. *ApJ* 819.1, p. 44.
- Albert, A., R. Alfaro, C. Alvarez, et al. (Sept. 2022a). “Limits on the Diffuse Gamma-Ray Background Above 10 TeV with HAWC”. *arXiv e-prints*, [arXiv:2209.08106](https://arxiv.org/abs/2209.08106).
- Albert, A., R. Alfaro, J. C. Arteaga-Velázquez, et al. (Nov. 2022b). “Validation of Standardized Data Formats and Tools for Ground-Level Particle-Based Gamma-Ray Observatories”. *A&A* 667, A36.
- Albert, A., R. Alfaro, H. Ashkar, et al. (Feb. 2019). “Science Case for a Wide Field-of-View Very-High-Energy Gamma-Ray Observatory in the Southern Hemisphere”. *arXiv e-prints*, [arXiv:1902.08429](https://arxiv.org/abs/1902.08429).
- Aleksić, J., S. Ansoldi, L. A. Antonelli, et al. (Mar. 2015). “Measurement of the Crab Nebula Spectrum Over Three Decades in Energy with the MAGIC Telescopes”. *JHEAP* 5, pp. 30–38.
- Aleksić, J., S. Ansoldi, L. A. Antonelli, et al. (Jan. 2016). “The Major Upgrade of the MAGIC Telescopes, Part II: A Performance Study Using Observations of the Crab Nebula”. *Astropart. Phys.* 72, pp. 76–94.
- Ambrogio, L., E. De Oña Wilhelmi, and F. Aharonian (July 2016). “On the Potential of Atmospheric Cherenkov Telescope Arrays for Resolving TeV Gamma-Ray Sources in the Galactic Plane”. *Astropart. Phys.* 80, pp. 22–33.

- Ambrosi, G., Q. An, R. Asfandiyarov, et al. (Dec. 2017). “Direct Detection of a Break in the Teraelectronvolt Cosmic-Ray Spectrum of Electrons and Positrons”. [Nature](#) 552.7683, pp. 63–66.
- Amenomori, M., Y. W. Bao, X. J. Bi, et al. (Apr. 2021). “First Detection of sub-PeV Diffuse Gamma Rays from the Galactic Disk: Evidence for Ubiquitous Galactic Cosmic Rays Beyond PeV Energies”. [PhRvL](#) 126 (14), p. 141101.
- Anderson, C. D. and S. H. Neddermeyer (Aug. 1936). “Cloud Chamber Observations of Cosmic Rays at 4300 Meters Elevation and Near Sea-Level”. [Phys. Rev.](#) 50.4, pp. 263–271.
- Atwood, W. B., A. A. Abdo, M. Ackermann, et al. (June 2009). “The Large Area Telescope on the Fermi Gamma-Ray Space Telescope Mission”. [ApJ](#) 697.2, pp. 1071–1102.
- Auger, P., P. Ehrenfest, R. Maze, et al. (July 1939). “Extensive Cosmic-Ray Showers”. [Rev. Mod. Phys.](#) 11.3–4, pp. 288–291.
- Baixeras, C. (Jan. 2003). “The MAGIC Telescope”. [Nucl. Phys. B Proc. Supp.](#) 114, pp. 247–252.
- Barashenkov, V. S. and A. Polanski (1994). *Electronic Guide for Nuclear Cross-Sections: Version 1994*. Tech. rep. Dubna: Joint Inst. Nucl. Res.
- Bartoli, B., P. Bernardini, X. J. Bi, et al. (June 2015). “Study of the Diffuse Gamma-Ray Emission from the Galactic Plane with ARGO-YBJ”. [ApJ](#) 806.1, p. 20.
- Bayet, E., D. A. Williams, T. W. Hartquist, et al. (June 2011). “Chemistry in Cosmic Ray Dominated Regions”. [MNRAS](#) 414.2, pp. 1583–1591.
- Beck, R. (Oct. 2001). “Galactic and Extragalactic Magnetic Fields”. [Space Sci. Rev.](#) 99, pp. 243–260.
- Becker Tjus, Julia and Lukas Merten (Aug. 2020). “Closing in on the Origin of Galactic Cosmic Rays Using Multimessenger Information”. [PhR](#) 872, pp. 1–98.
- Bell, A. R. (Sept. 2004). “Turbulent Amplification of Magnetic Field and Diffusive Shock Acceleration of Cosmic Rays”. [MNRAS](#) 353.2, pp. 550–558.
- Ben Bekhti, N., L. Flöer, R. Keller, et al. (Oct. 2016). “HI4PI: A Full-Sky HI Survey Based on EBHIS and GASS”. [A&A](#) 594, A116.
- Berezinskii, V. S., S. V. Bulanov, V. A. Dogiel, et al. (1990). *Astrophysics of Cosmic Rays*. Amsterdam, The Netherlands: North-Holland.
- Berge, D., S. Funk, and J. Hinton (May 2007). “Background Modelling in Very-High-Energy γ -Ray Astronomy”. [A&A](#) 466.3, pp. 1219–1229.
- Bernlöhr, K., A. Barnacka, Y. Becherini, et al. (Mar. 2013). “Monte Carlo Design Studies for the Cherenkov Telescope Array”. [Astropart. Phys.](#) 43, pp. 171–188.
- Bernlöhr, Konrad (Oct. 2008). “Simulation of Imaging Atmospheric Cherenkov Telescopes with CORSIKA and sim_telarray”. [Astropart. Phys.](#) 30.3, pp. 149–158.
- Beuermann, K., G. Kanbach, and E. M. Berkhuijsen (Dec. 1985). “Radio Structure of the Galaxy – Thick Disk and Thin Disk at 408 MHz”. [A&A](#) 153, pp. 17–34.
- Beuther, H., S. Bühr, M. Rugel, et al. (Oct. 2016). “The HI/OH/Recombination Line Survey of the Inner Milky Way (THOR). Survey Overview and Data Release 1”. [A&A](#) 595, A32.
- Bignami, G. F. and W. Hermsen (Jan. 1983). “Galactic Gamma-Ray Sources”. [ARA&A](#) 21, pp. 67–108.
- Bignami, G. F. and G. Piccinotti (July 1977). “Inverse Compton Revisited: Galactic Far Infrared and Optical Photon Fields, High Energy Electrons and Medium Energy Gamma Rays”. [A&A](#) 59.2, pp. 233–238.
- Binney, James, Ortwin Gerhard, and David Spergel (June 1997). “The Photometric Structure of the Inner Galaxy”. [MNRAS](#) 288.2, pp. 365–374.

- Bland-Hawthorn, Joss, Philip R. Maloney, Ralph Sutherland, et al. (Nov. 2019). “The Large-Scale Ionization Cones in the Galaxy”. *ApJ* 886.1, p. 45.
- Blasi, Pasquale and Elena Amato (Jan. 2012). “Diffusive Propagation of Cosmic Rays from Supernova Remnants in the Galaxy. I: Spectrum and Chemical Composition”. *JCAP* 2012.1, p. 010.
- Blementhal, G. R. and R. J. Gould (Apr. 1970). “Bremsstrahlung, Synchrotron Radiation, and Compton Scattering of High-Energy Electrons Traversing Dilute Gases”. *Rev. Mod. Phys.* 42 (2), pp. 237–270.
- Bloom, Steven D. and Alan P. Marscher (Apr. 1996). “An Analysis of the Synchrotron Self-Compton Model for the Multi-Wave Band Spectra of Blazars”. *ApJ* 461, p. 657.
- Boschini, M. J., S. Della Torre, M. Gervasi, et al. (Oct. 2020). “Inference of the Local Interstellar Spectra of Cosmic-Ray Nuclei $Z \leq 28$ with the GALPROP-HELMOD Framework”. *ApJS* 250.2, p. 27.
- Braiding, Catherine, M. G. Burton, R. Blackwell, et al. (May 2015). “The Mopra Southern Galactic Plane CO Survey – Data Release 1”. *PASA* 32, e020.
- Braiding, Catherine, G. F. Wong, N. I. Maxted, et al. (Aug. 2018). “The Mopra Southern Galactic Plane CO Survey—Data Release 3”. *PASA* 35, e029.
- Burgess, Daniel A., Kaya Mori, Joseph D. Gelfand, et al. (May 2022). “The Eel Pulsar Wind Nebula: A PeVatron-Candidate Origin for HAWC J1826–128 and HESS J1826–130”. *ApJ* 930.2, p. 148.
- Bykov, A. M., D. C. Ellison, M. E. Kalyashova, et al. (Dec. 2019). “High-Energy Cosmic Rays from Supernovae in Young Clusters of Massive Stars”. *Rend. Lincei. Sci. Fis. Nat.* 30, pp. 155–158.
- Bykov, Andrei M. (Nov. 2014). “Nonthermal Particles and Photons in Starburst Regions and Superbubbles”. *A&ARv* 22, p. 77.
- Cao, Zhen, F. Aharonian, Q. An, et al. (Oct. 2023). “Measurement of Ultra-High-Energy Diffuse Gamma-Ray Emission of the Galactic Plane from 10 TeV to 1 PeV with LHAASO-KM2A”. *PhRvL* 131.15, p. 151001.
- Cao, Zhen, F. Aharonian, Axikegu, et al. (Feb. 2025). “Measurement of Very-High-Energy Diffuse Gamma-Ray Emissions from the Galactic Plane with LHAASO-WCDA”. *PhRvL* 134.8, p. 081002.
- Cao, Zhen, F. A. Aharonian, Q. An, et al. (July 2021a). “Peta-Electron Volt Gamma-Ray Emission from the Crab Nebula”. *Science* 373, pp. 425–430.
- Cao, Zhen, F. A. Aharonian, Q. An, et al. (June 2021b). “Ultra-High-Energy Photons up to 1.4 Petaelectronvolts from 12 γ -Ray Galactic Sources”. *Nature* 594.7861, pp. 33–36.
- Carey, S. J., A. Noriega-Crespo, D. R. Mizuno, et al. (Jan. 2009). “MIPSGAL: A Survey of the Inner Galactic Plane at 24 and 70 μm ”. *PASP* 121.875, p. 76.
- Casanova, Sabrina, David I. Jones, Felix A. Aharonian, et al. (Oct. 2010). “Modeling the Gamma-Ray Emission Produced by Runaway Cosmic Rays in the Environment of RX J1713.7–3946”. *Publ. Astron. Soc. Jpn.* 62.5, pp. 1127–1134.
- Cataldo, M., G. Pagliaroli, V. Vecchiotti, et al. (Dec. 2019). “Probing Galactic Cosmic Ray Distribution with TeV Gamma-Ray Sky”. *JCAP* 2019.12, p. 050.
- Cataldo, M., G. Pagliaroli, V. Vecchiotti, et al. (Nov. 2020). “The TeV Gamma-Ray Luminosity of the Milky Way and the Contribution of H.E.S.S. Unresolved Sources to Very High Energy Diffuse Emission”. *ApJ* 904.2, p. 85.
- Chandrasekhar, S. (Jan. 1943). “Stochastic Problems in Physics and Astronomy”. *Rev. Mod. Phys.* 15.1, pp. 1–89.
- Chen, En-Sheng, Kun Fang, and Xiao-Jun Bi (Nov. 2024). “A New Perspective on the Diffuse Gamma-Ray Emission Excess”. *Chinese Phys. C* 48.11, p. 115105.

- Cherenkov, P. A. (1937). “Visible Emission of Clean Liquids by Action of Gamma Radiation”. *Proc. USSR Acad. Sci.* 2, pp. 451–457.
- Choi, G., S. Aggarwal, Y. Amare, et al. (Mar. 2022). “Analysis Result of the High-Energy Cosmic-Ray Proton Spectrum from the ISS–CREAM Experiment”. *37th International Cosmic Ray Conference*, p. 94.
- Churchwell, Ed, Brian L. Babler, Marilyn R. Meade, et al. (Mar. 2009). “The Spitzer and GLIMPSE Surveys: A New View of the Milky Way”. *PASP* 121.877, p. 213.
- Clay, R. and B. Dawson (1997). *Cosmic Bullets: High Energy Particles in Astrophysics*. Frontiers of Science. St Leonards, N.S.W.: Allen & Unwin.
- Clemens, Dan P., David B. Sanders, and Nicholas Z. Scoville (Apr. 1988). “The Large-Scale Distribution of Molecular Gas in the First Galactic Quadrant”. *ApJ* 327, p. 139.
- Cohen, M. (May 1993). “A Model of the 2–35 micron Point Source Infrared Sky”. *AJ* 105, p. 1860.
- Cohen, M. (Feb. 1994). “Powerful Model for the Point Source Sky: Far-Ultraviolet and Enhanced Midinfrared Performance”. *AJ* 107, p. 582.
- Cohen, M. (May 1995). “The Displacement of the Sun from the Galactic Plane Using IRAS and FAUST Source Counts”. *ApJ* 444, p. 874.
- Collins, T., G. Rowell, A. M. W. Mitchell, et al. (June 2021). “Explaining the Extended GeV Gamma-Ray Emission Adjacent to HESS J1825–137”. *MNRAS* 504.2, pp. 1840–1853.
- Condon, J. J., W. D. Cotton, E. W. Greisen, et al. (May 1998). “The NRAO VLA Sky Survey”. *AJ* 115.5, pp. 1693–1716.
- Conrad, J. and O. Reimer (Mar. 2017). “Indirect Dark Matter Searches in Gamma and Cosmic Rays”. *Nature Phys.* 13.3, pp. 224–231.
- Cordes, J. M. (Dec. 2004). “NE2001: A New Model for the Galactic Electron Density and its Fluctuations”. *Milky Way Surveys: The Structure and Evolution of our Galaxy*. Ed. by Dan Clemens, Ronak Shah, and Teresa Brainerd. Vol. 317. Astronomical Society of the Pacific Conference Series, p. 211.
- Cordes, J. M. and T. J. W. Lazio (July 2002). “NE2001.I. A New Model for the Galactic Distribution of Free Electrons and its Fluctuations”. [arXiv e-prints](#), [astro-ph/0207156](#).
- Cordes, J. M. and T. J. W. Lazio (Jan. 2003). “NE2001. II. Using Radio Propagation Data to Construct a Model for the Galactic Distribution of Free Electrons”. [arXiv e-prints](#), [astro-ph/0301598](#).
- Cowsik, R. and W. Voges (Nov. 1974). “Inverse Compton Gamma Rays from the Galactic Disc”. *The Context and Status of Gamma-Ray Astronomy*, pp. 229–239.
- Crocker, Roland M., Geoffrey V. Bicknell, Andrew M. Taylor, et al. (Aug. 2015). “A Unified Model of the Fermi Bubbles, Microwave Haze, and Polarized Radio Lobes: Reverse Shocks in the Galactic Center’s Giant Outflows”. *ApJ* 808.2, p. 107.
- Çubuk, K. O., M. G. Burton, C. Braiding, et al. (Sept. 2023). “The Mopra Southern Galactic Plane CO Survey – Data Release 4 – Complete Survey”. *PASA* 40, e047.
- Cummings, A. C., E. C. Stone, B. C. Heikkilä, et al. (Nov. 2016). “Galactic Cosmic Rays in the Local Interstellar Medium: Voyager 1 Observations and Model Results”. *ApJ* 831.1, p. 18.
- Dame, T. M., D. Hartmann, and P. Thaddeus (Feb. 2001). “The Milky Way in Molecular Clouds: A New Complete CO Survey”. *ApJ* 547.2, pp. 792–813.
- Deil, C., R. Zanin, J. Lefaucheur, et al. (Jan. 2017). “Gammapy – A Prototype for the CTA Science Tools”. *35th International Cosmic Ray Conference (ICRC2017)*. Vol. 301. International Cosmic Ray Conference, p. 766.
- Dermer, C. D. (Aug. 1986a). “Binary Collision Rates of Relativistic Thermal Plasmas. II. Spectra”. *ApJ* 307, p. 47.

- Dermer, C. D. (Mar. 1986b). “Secondary Production of Neutral pi-Mesons and the Diffuse Galactic Gamma Radiation”. *A&A* 157.2, pp. 223–229.
- Di Sciascio, G (Oct. 2016). “The LHAASO experiment: From Gamma-Ray Astronomy to Cosmic Rays”. *Nucl. Part. Phys. Proc.* 279–281, pp. 166–173.
- Dickey, John M., Naomi McClure-Griffiths, Steven J. Gibson, et al. (Jan. 2013). “GASKAP—The Galactic ASKAP Survey”. *PASA* 30, e003.
- Diehl, Roland, Hubert Halloin, Karsten Kretschmer, et al. (Jan. 2006). “Radioactive ^{26}Al from Massive Stars in the Galaxy”. *Nature* 439.7072, pp. 45–47.
- Dobbs, C. L. and A. Burkert (Apr. 2012). “The Myth of the Molecular Ring”. *MNRAS* 421.4, pp. 2940–2946.
- Dobler, Gregory, Douglas P. Finkbeiner, Ilias Cholis, et al. (July 2010). “The Fermi Haze: A Gamma-Ray Counterpart to the Microwave Haze”. *ApJ* 717.2, pp. 825–842.
- Donath, A., C. Deil, M. Paz Arribas, et al. (July 2015). “Gammapy: An Open-Source Python Package for Gamma-Ray Astronomy”. *34th International Cosmic Ray Conference (ICRC2015)*. Vol. 34. International Cosmic Ray Conference, p. 789.
- Donath, Axel, Régis Terrier, Quentin Remy, et al. (Oct. 2023). “Gammapy: A Python Package for Gamma-Ray Astronomy”. *A&A* 678, A157.
- Draine, B. T. and A. Li (Mar. 2007). “Infrared Emission from Interstellar Dust. IV. The Silicate-Graphite-PAH Model in the Post-Spitzer Era”. *ApJ* 657.2, pp. 810–837.
- Dubus, G. (Sept. 2006). “Gamma-Ray Binaries: Pulsars in Disguise?” *A&A* 456.3, pp. 801–817.
- Dubus, G., J. L. Contreras, S. Funk, et al. (Mar. 2013). “Surveys with the Cherenkov Telescope Array”. *Astropart. Phys.* 43, pp. 317–330.
- Dzhatdov, Timur (Apr. 2021). “Implications of the Detection of sub-PeV Diffuse γ Rays from the Galactic Disk Apart from Discrete Sources”. *arXiv e-prints*, [arXiv:2104.02838](https://arxiv.org/abs/2104.02838).
- Einecke, S., G. P. Rowell, J. Pilosof, et al. (June 2023). “Modelling the Gamma-Ray Morphology of the Supernova Remnant W28”. *38th International Cosmic Ray Conference*, p. 923.
- Engel, R., D. Heck, and T. Pierog (Nov. 2011). “Extensive Air Showers and Hadronic Interactions at High Energy”. *Annu. Rev. Nucl. Part. Sci.* 61.1, pp. 467–489.
- Evoli, C., D. Gaggero, A. Vittino, et al. (Feb. 2017). “Cosmic-Ray Propagation with DRAGON2: I. Numerical Solver and Astrophysical Ingredients”. *JCAP* 2017.2, p. 15.
- Evoli, Carmelo, Elena Amato, Pasquale Blasi, et al. (Dec. 2021). “Stochastic Nature of Galactic Cosmic-Ray Sources”. *PhRvD* 104.12, p. 123029.
- Evoli, Carmelo, Daniele Gaggero, Dario Grasso, et al. (Oct. 2008). “Cosmic Ray Nuclei, Antiprotons and Gamma Rays in the Galaxy: A New Diffusion Model”. *JCAP* 2008.10, p. 018.
- Faherty, Jacqueline, Frederick M. Walter, and Jay Anderson (Apr. 2007). “The Trigonometric Parallax of the Neutron Star Geminga”. *Ap&SS* 308.1–4, pp. 225–230.
- Fang, Ke and Kohta Murase (Oct. 2021). “Multimessenger Implications of Sub-PeV Diffuse Galactic Gamma-Ray Emission”. *ApJ* 919.2, p. 93.
- Fang, Kun, Xiao-Jun Bi, Peng-Fei Yin, et al. (Aug. 2018). “Two-zone Diffusion of Electrons and Positrons from Geminga Explains the Positron Anomaly”. *ApJ* 863.1, p. 30.
- Faraday, Michael (Jan. 1832). *Experimental Researches in Electricity*. Vol. 122. Philosophical Transactions of the Royal Society of London, pp. 125–162.
- Feijen, K., G. Rowell, S. Einecke, et al. (Dec. 2020). “Arcminute-Scale Studies of the Interstellar Gas Towards HESS J1804–216: Still an Unidentified TeV Gamma-Ray Source”. *PASA* 37.
- Fermi, E. (Apr. 1949). “On the Origin of the Cosmic Radiation”. *Phys. Rev.* 75 (8), pp. 1169–1174.

- Ferrando, P., W. R. Webber, P. Goret, et al. (Apr. 1988). “Measurement of ^{12}C , ^{16}O , and ^{56}Fe Charge Changing Cross Sections in Helium at High Energy, Comparison with Cross Sections in Hydrogen, and Application to Cosmic-Ray Propagation”. [PhRvC](#) 37.4, pp. 1490–1501.
- Ferrière, K. M. (Oct. 2001). “The Interstellar Environment of Our Galaxy”. [Rev. Mod. Phys.](#) 73, pp. 1031–1066.
- Fixsen, D. J. (Dec. 2009). “The Temperature of the Cosmic Microwave Background”. [ApJ](#) 707.2, pp. 916–920.
- Freudenreich, H. T. (Sept. 1996). “The Shape and Color of the Galactic Disk”. [ApJ](#) 468, p. 663.
- Freudenreich, H. T. (Jan. 1998). “A COBE Model of the Galactic Bar and Disk”. [ApJ](#) 492, pp. 495–510.
- Fujita, Yutaka, Yutaka Ohira, and Fumio Takahara (Apr. 2010). “Slow Diffusion of Cosmic Rays Around a Supernova Remnant”. [ApJL](#) 712.2, pp. L153–L156.
- Funk, S., J. A. Hinton, Y. Moriguchi, et al. (July 2007). “XMM-Newton Observations of HESS J1813–178 Reveal a Composite Supernova Remnant”. [A&A](#) 470.1, pp. 249–257.
- Gabici, S., F. A. Aharonian, and S. Casanova (July 2009). “Broad-Band Non-Thermal Emission from Molecular Clouds Illuminated by Cosmic Rays from Nearby Supernova Remnants”. [MNRAS](#) 396.3, pp. 1629–1639.
- Gabici, Stefano and Felix A. Aharonian (Aug. 2007). “Searching for Galactic Cosmic-Ray Pevatrons with Multi-TeV Gamma Rays and Neutrinos”. [ApJL](#) 665.2, pp. L131–L134.
- Gabici, Stefano, Felix A. Aharonian, and Pasquale Blasi (June 2007). “Gamma Rays from Molecular Clouds”. [Ap&SS](#) 309.1–4, pp. 365–371.
- Gaensler, B. M. and S. Johnston (Dec. 1995). “The Pulsar/Supernova Remnant Connection”. [MNRAS](#) 277, pp. 1243–1253.
- Gaensler, B. M., G. J. Madsen, S. Chatterjee, et al. (Nov. 2008). “The Vertical Structure of Warm Ionised Gas in the Milky Way”. [PASA](#) 25.4, pp. 184–200.
- Gaensler, Bryan M. and Patrick O. Slane (Sept. 2006). “The Evolution and Structure of Pulsar Wind Nebulae”. [ARA&A](#) 44.1, pp. 17–47.
- Gaisser, T. K. (1990). *Cosmic Rays and Particle Physics*. Cambridge, England: Cambridge University Press.
- Ghisellini, Gabriele, Paul W. Guilbert, and Roland Svensson (Nov. 1988). “The Synchrotron Boiler”. [ApJL](#) 334, p. L5.
- Giacinti, G., A. M. W. Mitchell, R. López-Coto, et al. (Apr. 2020). “Halo Fraction in TeV-Bright Pulsar Wind Nebulae”. [A&A](#) 636, A113.
- Ginzburg, V. L. and S. I. Syrovatskii (1964). *The Origin of Cosmic Rays*. Oxford: Pergamon Press.
- Górski, K. M., E. Hivon, A. J. Banday, et al. (Apr. 2005). “HEALPix: A Framework for High-Resolution Discretization and Fast Analysis of Data Distributed on the Sphere”. [ApJ](#) 622, pp. 759–771.
- Gotthelf, E. V. and J. P. Halpern (Aug. 2009). “Discovery of a Highly Energetic X-Ray Pulsar Powering HESS J1813–178 in the Young Supernova Remnant G12.82–0.02”. [ApJL](#) 700.2, pp. L158–L161.
- Gotthelf, E. V., J. A. Tomsick, J. P. Halpern, et al. (June 2014). “NuSTAR Discovery of a Young, Energetic Pulsar Associated with the Luminous Gamma-Ray Source HESS J1640–465”. [ApJ](#) 788.2, p. 155.
- Grenier, Isabelle A., Jean-Marc Casandjian, and Régis Terrier (Feb. 2005). “Unveiling Extensive Clouds of Dark Gas in the Solar Neighborhood”. [Science](#) 307.5713, pp. 1292–1295.

- Grieder, P. K. F. (2010). *Extensive Air Showers: High Energy Phenomena and Astrophysical Aspects, a Tutorial Reference Manual and Data Book*. Springer.
- Guo, Xiao-Lei, Yu-Liang Xin, Neng-Hui Liao, et al. (Jan. 2017). “HESS J1427–608: An Unusual Hard, Unbroken Gamma-Ray Spectrum in a Very Wide Energy Range”. *ApJ* 835.1, p. 42.
- Harris, Charles R., K. Jarrod Millman, Stéfan J. van der Walt, et al. (Sept. 2020). “Array Programming with NumPy”. *Nature* 585.7825, pp. 357–362.
- Hartman, R. C., D. L. Bertsch, S. D. Bloom, et al. (July 1999). “The Third EGRET Catalog of High-Energy Gamma-Ray Sources”. *ApJS* 123.1, pp. 79–202.
- Haverkorn, M., J. C. Brown, B. M. Gaensler, et al. (June 2008). “The Outer Scale of Turbulence in the Magnetoionized Galactic Interstellar Medium”. *ApJ* 680, pp. 362–370.
- Heck, D., J. Knapp, J. N. Capdevielle, et al. (Feb. 1998). *CORSIKA: A Monte Carlo Code to Simulate Extensive Air Showers*.
- Heitler, W. (1954). *The Quantum Theory of Radiation*. 3rd ed. International series on monographs on physics. Oxford: Clarendon Press.
- Hess, V. (1912). “Observations in Low Level Radiation During Seven Free Balloon Flights”. *Phys. Ziet.* 13.
- Hill, John M. (June 2010). “The Large Binocular Telescope”. *Appl. Opt.* 49.16, pp. D115–D122.
- Hillas, A. M. (Aug. 1985). “Cerenkov Light Images of EAS Produced by Primary Gamma Rays and by Nuclei”. *19th International Cosmic Ray Conference (ICRC19), Volume 3*. Vol. 3. International Cosmic Ray Conference, p. 445.
- Hillas, A. M. (Apr. 2005). “Can Diffusive Shock Acceleration in Supernova Remnants Account for High-Energy Galactic Cosmic Rays?” *J. Phys. G* 31.5, R95–R131.
- Hinton, J. A. and W. Hofmann (Sept. 2009). “Teraelectronvolt Astronomy”. *ARA&A* 47.1, pp. 523–565.
- Holler, M., D. Berge, C. van Eldik, et al. (Sept. 2015). “Observations of the Crab Nebula with H.E.S.S. Phase II”. *arXiv e-prints*, [arXiv:1509.02902](https://arxiv.org/abs/1509.02902).
- Horan, D., R. W. Atkins, H. M. Badran, et al. (Jan. 2007). “Very High Energy Observations of Gamma-Ray Burst Locations with the Whipple Telescope”. *ApJ* 655.1, pp. 396–405.
- Hunter, J. D. (May 2007). “Matplotlib: A 2D Graphics Environment”. *Comput. Sci. Eng.* 9.3, pp. 90–95.
- Hunter, S. D., D. L. Bertsch, J. R. Catelli, et al. (May 1997). “EGRET Observations of the Diffuse Gamma-Ray Emission from the Galactic Plane”. *ApJ* 481.1, pp. 205–240.
- Iroshnikov, P. S. (Feb. 1964). “Turbulence of a Conducting Fluid in a Strong Magnetic Field”. *Soviet Astron.* 7, p. 566.
- Jaffe, T. R., J. P. Leahy, A. J. Banday, et al. (Jan. 2010). “Modelling the Galactic Magnetic Field on the Plane in Two Dimensions”. *MNRAS* 401, pp. 1013–1028.
- Jansson, R. and G. R. Farrar (Aug. 2012). “A New Model of the Galactic Magnetic Field”. *ApJ* 757.1, p. 14.
- Jauch, J. M. and F. Rohrlich (1976). *The Theory of Photons and Electrons The Relativistic Quantum Field Theory of Charged Particles with Spin One-Half*. 2nd ed. 1976. Theoretical and Mathematical Physics. Berlin, Heidelberg: Springer Berlin Heidelberg.
- Jóhannesson, G., R. Ruiz de Austri, A. C. Vincent, et al. (June 2016). “Bayesian Analysis of Cosmic Ray Propagation: Evidence against Homogeneous Diffusion”. *ApJ* 824, p. 16.
- Jóhannesson, Guðlaugur, T. A. Porter, and I. V. Moskalenko (Mar. 2018). “The Three-Dimensional Spatial Distribution of Interstellar Gas in the Milky Way: Implications for Cosmic Rays and High-Energy Gamma-Ray Emissions”. *ApJ* 856.1, p. 45.
- Jóhannesson, Guðlaugur, Troy A. Porter, and Igor V. Moskalenko (July 2019). “Cosmic-Ray Propagation in Light of the Recent Observation of Geminga”. *ApJ* 879.2, p. 91.

- Jones, T. W., S. L. O'Dell, and W. A. Stein (Mar. 1974). "Physics of Compact Nonthermal Sources. I. Theory of Radiation Processes". *ApJ* 188, pp. 353–368.
- Kachelrieß, M., I. V. Moskalenko, and S. Ostapchenko (Dec. 2019). "AAfrag: Interpolation Routines for Monte Carlo Results on Secondary Production in Proton-Proton, Proton-Nucleus and Nucleus-Nucleus Interactions". *Comput. Phys. Commun.* 245, p. 106846.
- Kachelrieß, M. and S. Ostapchenko (Aug. 2012). "Deriving the Cosmic-Ray Spectrum from Gamma-Ray Observations". *PhRvD* 86.4, p. 043004.
- Kachelrieß, Michael, Igor V. Moskalenko, and Sergey S. Ostapchenko (July 2014). "Nuclear Enhancement of the Photon Yield in Cosmic Ray Interactions". *ApJ* 789.2, p. 136.
- Kachelrieß, Michael, Igor V. Moskalenko, and Sergey S. Ostapchenko (Apr. 2015). "New Calculation of Antiproton Production by Cosmic Ray Protons and Nuclei". *ApJ* 803.2, p. 54.
- Kalberla, P. M. W., W. B. Burton, L. Hartmann, et al. (Sept. 2005). "The Leiden/Argentine/Bonn (LAB) Survey of Galactic HI: Final Data Release of the Combined LDS and IAR Surveys with Improved Stray-Radiation Corrections". *A&A* 440.2, pp. 775–782.
- Kamae, Tuneyoshi, Niklas Karlsson, Tsunefumi Mizuno, et al. (Aug. 2006). "Parameterization of γ , $e^{+/-}$, and Neutrino Spectra Produced by p-p Interaction in Astronomical Environments". *ApJ* 647.1, pp. 692–708.
- Kanbach, G., D. L. Bertsch, C. E. Fichtel, et al. (Jan. 1989). "The Project EGRET (Energetic Gamma-Ray Experiment Telescope) on NASA's Gamma-Ray Observatory GRO". *Space Sci. Rev.* 49.1–2, pp. 69–84.
- Kaplan, D. L., S. Chatterjee, B. M. Gaensler, et al. (Apr. 2008). "A Precise Proper Motion for the Crab Pulsar, and the Difficulty of Testing Spin-Kick Alignment for Young Neutron Stars". *ApJ* 677.2, pp. 1201–1215.
- Kaufmann, S. and O. Tibolla (Apr. 2018). "Ancient Pulsar Wind Nebulae as a Natural Explanation for Unidentified Gamma-Ray Sources". *Nucl. Part. Phys. Proc.* 297–299, pp. 91–95.
- Keane, E. F. and M. Kramer (Dec. 2008). "On the Birthrates of Galactic Neutron Stars". *MNRAS* 391.4, pp. 2009–2016.
- Kelner, S. R., F. A. Aharonian, and V. V. Bugayov (Aug. 2006). "Energy Spectra of Gamma Rays, Electrons, and Neutrinos Produced at Proton-Proton Interactions in the Very High Energy Regime". *PhRvD* 74.3, p. 034018.
- Kerr, F. J. and D. Lynden-Bell (Aug. 1986). "Review of Galactic Constants". *MNRAS* 221, pp. 1023–1038.
- Kerszberg, Daniel (2017). "Étude du Fond Diffus Galactique des Électrons et Positrons et Étude des Performances de la Seconde Phase de l'Expérience H.E.S.S." PhD thesis. LPNHE.
- Kissmann, R. (Mar. 2014). "PICARD: A Novel Code for the Galactic Cosmic Ray Propagation Problem". *Astropart. Phys.* 55, pp. 37–50.
- Kissmann, R., M. Werner, O. Reimer, et al. (Oct. 2015). "Propagation in 3D Spiral-Arm Cosmic-Ray Source Distribution Models and Secondary Particle Production Using PICARD". *Astropart. Phys.* 70, pp. 39–53.
- Kobayashi, T., Y. Komori, K. Yoshida, et al. (Jan. 2004). "The Most Likely Sources of High-Energy Cosmic-Ray Electrons in Supernova Remnants". *ApJ* 601.1, pp. 340–351.
- Koch, H. W. and J. W. Motz (Oct. 1959). "Bremsstrahlung Cross-Section Formulas and Related Data". *Rev. Mod. Phys.* 31.4, pp. 920–955.
- Kolmogorov, A. (Jan. 1941). "The Local Structure of Turbulence in Incompressible Viscous Fluid for Very Large Reynolds' Numbers". *Proc. USSR Acad. Sci.* 30, pp. 301–305.

- Korsmeier, Michael and Alessandro Cuoco (May 2022). “Testing the Universality of Cosmic-Ray Nuclei from Protons to Oxygen with AMS-02”. [PhRvD](#) 105.10, p. 103033.
- Koyama, Katsuji, Kenzo Kinugasa, Keiichi Matsuzaki, et al. (June 1997). “Discovery of Non-Thermal X-Rays from the Northwest Shell of the New SNR RX J1713.7–3946: The Second SN 1006?”. [Publ. Astron. Soc. Jpn.](#) 49, pp. L7–L11.
- Kraichnan, Robert H. (July 1965). “Inertial-Range Spectrum of Hydromagnetic Turbulence”. [PhF](#) 8.7, pp. 1385–1387.
- Kraushaar, W. L., G. W. Clark, G. P. Garmire, et al. (Nov. 1972). “High-Energy Cosmic Gamma-Ray Observations from the OSO-3 Satellite”. [ApJ](#) 177, p. 341.
- Kronberg, P. P. and K. J. Newton-McGee (June 2011). “Remarkable Symmetries in the Milky Way Disc’s Magnetic Field”. [PASA](#) 28.2, pp. 171–176.
- Lagage, P. O. and C. J. Cesarsky (Sept. 1983). “The Maximum Energy of Cosmic Rays Accelerated by Supernova Shocks”. [A&A](#) 125, pp. 249–257.
- Lattes, C. M. G., H. Muirhead, G. P. S. Occhialini, et al. (May 1947). “Processes Involving Charged Mesons”. [Nature](#) 159.4047, pp. 694–697.
- Lau, J. C., G. Rowell, F. Voisin, et al. (Dec. 2017). “A Study of the Interstellar Medium Towards the Unidentified Dark TeV γ -Ray Sources HESS J1614–518 and HESS J1616–508”. [PASA](#) 34, e064.
- Lee, M. A. (Apr. 1979). “A Statistical Theory of Cosmic-Ray Propagation from Discrete Galactic Sources”. [ApJ](#) 229, pp. 424–431.
- Leike, R., S. Celli, A. Krone-Martins, et al. (May 2021). “Optical Reconstruction of Dust in the Region of Supernova Remnant RX J1713.7–3946 from Astrometric Data”. [Nature Astro.](#) 5, pp. 832–838.
- Lemaître, G. and M. S. Vallarta (Jan. 1933). “On Compton’s Latitude Effect of Cosmic Radiation”. [Phys. Rev.](#) 43.2, pp. 87–91.
- Li, T. and Y. Ma (Sept. 1983). “Analysis Methods for Results in Gamma-Ray Astronomy”. [ApJ](#) 272, pp. 317–324.
- Lingenfelter, R. E. and J. C. Higdon (Jan. 1973). “Cosmic Ray Prehistory and Propagation”. *International Cosmic Ray Conference*. Vol. 1. International Cosmic Ray Conference, p. 621.
- Lingenfelter, R. E. and R. Ramaty (Jan. 1971). “Cosmic Ray Propagation and Source Distribution”. *12th International Cosmic Ray Conference (ICRC12), Volume 1*. Vol. 1. International Cosmic Ray Conference, p. 377.
- Lingenfelter, Richard E. (Dec. 1969). “Pulsars and Local Cosmic Ray Prehistory”. [Nature](#) 224.5225, pp. 1182–1186.
- Lipari, Paolo and Silvia Vernetto (Aug. 2018). “Diffuse Galactic Gamma-Ray Flux at Very High Energy”. [PhRvD](#) 98.4, p. 043003.
- Liu, Wei, Pierre Salati, and Xuelei Chen (Jan. 2015). “TeV Cosmic-Ray Proton and Helium Spectra in the Myriad Model II”. [RAA](#) 15.1, pp. 15–27.
- Liu, Yi-Ming, Hou-Dun Zeng, Yu-Liang Xin, et al. (July 2024). “Evolution of High-energy Electron Distribution in Pulsar Wind Nebulae”. [RAA](#) 24.7, p. 075016.
- Macias, Oscar (Nov. 2017). Private communications.
- Macias, Oscar, Shunsaku Horiuchi, Manoj Kaplinghat, et al. (Sept. 2019). “Strong Evidence that the Galactic Bulge is Shining in Gamma Rays”. [JCAP](#) 2019.9, p. 042.
- Malkov, M. A., P. H. Diamond, R. Z. Sagdeev, et al. (May 2013). “Analytic Solution for Self-regulated Collective Escape of Cosmic Rays from Their Acceleration Sites”. [ApJ](#) 768.1, p. 73.
- Marandon, V., A. Djannati-Atai, R. Terrier, et al. (Dec. 2008). “A Closer Look at HESS J1837–069 Following the Pulsar Discovery”. *American Institute of Physics*

- Conference Series*. Ed. by Felix A. Aharonian, Werner Hofmann, and Frank Rieger. Vol. 1085. American Institute of Physics Conference Series, pp. 320–323.
- Marinos, P. D., G. P. Rowell, T. A. Porter, et al. (Feb. 2023). “The Steady-State Multi-TeV Diffuse Gamma-Ray Emission Predicted with GALPROP and Prospects for the Cherenkov Telescope Array”. *MNRAS* 518.4, pp. 5036–5048.
- Marinos, P. D., G. P. Rowell, T. A. Porter, et al. (Mar. 2025). “On the Temporal Variability of the Galactic Multi-TeV Interstellar Emissions”. *ApJ* 981.1, p. 93.
- Martin, Pierrick, Luigi Tibaldo, Alexandre Marcowith, et al. (Oct. 2022). “Population Synthesis of Pulsar Wind Nebulae and Pulsar Halos in the Milky Way – Predicted Contributions to the Very-High-Energy Sky”. *A&A* 666, A7.
- Martinez, M. (Mar. 2013). “Introducing the CTA Concept”. *Astropart. Phys.* 43.C, pp. 3–18.
- Mathis, J. S., P. G. Mezger, and N. Panagia (Nov. 1983). “Interstellar Radiation Field and Dust Temperatures in the Diffuse Interstellar Medium and in Giant Molecular Clouds”. *A&A* 128, pp. 212–229.
- Maxted, Nigel I., Gavin P. Rowell, Bruce R. Dawson, et al. (May 2012). “3 to 12 Millimetre Studies of Dense Gas Towards the Western Rim of Supernova Remnant RX J1713.7–3946”. *MNRAS* 422.3, pp. 2230–2245.
- Mertsch, P. (Feb. 2011). “Cosmic-Ray Electrons and Positrons from Discrete Stochastic Sources”. *JCAP* 2011.2, p. 031.
- Mertsch, Philipp (Nov. 2018). “Stochastic Cosmic-Ray Sources and the TeV Break in the All-Electron Spectrum”. *JCAP* 2018.11, p. 045.
- Mestre, Enrique, Emma de Oña Wilhelmi, Diego F. Torres, et al. (Aug. 2021). “Probing the Hadronic Nature of the Gamma-Ray Emission Associated with Westerlund 2”. *MNRAS* 505.2, pp. 2731–2740.
- Mestre, Enrique, Diego F. Torres, Emma de Oña Wilhelmi, et al. (Dec. 2022). “Testing Source Confusion and Identification Capability in Cherenkov Telescope Array Data”. *MNRAS* 517.3, pp. 3550–3567.
- Mewaldt, R. A. (Oct. 1994). “Galactic Cosmic Ray Composition and Energy Spectra”. *Adv. Space Res.* 14.10, pp. 737–747.
- Millikan, R. A. and G. H. Cameron (Oct. 1928). “The Origin of the Cosmic Rays”. *Phys. Rev.* 32.4, pp. 533–557.
- Minamidani, T., T. Umemoto, A. Nishimura, et al. (May 2015). “Nobeyama CO Galactic Plane Survey: New Chapter of the Nobeyama 45 m Telescope”. *EAS Publications Series*. Vol. 75–76. EAS Publications Series, pp. 193–194.
- Mirabel, I. F. (June 2006). “Very Energetic Gamma-Rays from Microquasars and Binary Pulsars”. *Science* 312, p. 1759.
- Mitchell, A. M. W., G. P. Rowell, S. Celli, et al. (May 2021). “Using Interstellar Clouds to Search for Galactic PeVatrons: Gamma-Ray Signatures from Supernova Remnants”. *MNRAS* 503.3, pp. 3522–3539.
- Miville-Deschênes, Marc-Antoine and Guilaine Lagache (Apr. 2005). “IRIS: A New Generation of IRAS Maps”. *ApJS* 157.2, pp. 302–323.
- Miyake, S., H. Muraishi, and S. Yanagita (Jan. 2015). “A Stochastic Simulation of the Propagation of Galactic Cosmic Rays Reflecting the Discreteness of Cosmic-Ray Sources: Age and Path Length Distribution”. *A&A* 573, A134.
- Moderski, R., M. Sikora, P. S. Coppi, et al. (Nov. 2005). “Klein-Nishina Effects in the Spectra of Non-Thermal Sources Immersed in External Radiation Fields”. *MNRAS* 363.3, pp. 954–966.

- Moriguchi, Y., K. Tamura, Y. Tawara, et al. (Oct. 2005). “A Detailed Study of Molecular Clouds Toward the TeV Gamma-Ray Supernova Remnant G347.3–0.5”. *ApJ* 631.2, pp. 947–963.
- Moskalenko, I. V., T. A. Porter, and A. W. Strong (Apr. 2006). “Attenuation of Very High Energy Gamma Rays by the Milky Way Interstellar Radiation Field”. *ApJL* 640, pp. L155–L158.
- Moskalenko, I. V. and A. W. Strong (Jan. 1998). “Production and Propagation of Cosmic-Ray Positrons and Electrons”. *ApJ* 493.2, pp. 694–707.
- Moskalenko, I. V. and A. W. Strong (Jan. 2000). “Anisotropic Inverse Compton Scattering in the Galaxy”. *ApJ* 528, pp. 357–367.
- Moskalenko, Igor V., Andrew W. Strong, and Stepan G. Mashnik (May 2005). “Propagation of Cosmic Rays: Nuclear Physics in Cosmic-Ray Studies”. *International Conference on Nuclear Data for Science and Technology*. Ed. by Robert C. Haight, Mark B. Chadwick, Toshihiko Kawano, et al. Vol. 769. American Institute of Physics Conference Series, pp. 1612–1617.
- Moskalenko, Igor V., Andrew W. Strong, Stepan G. Mashnik, et al. (Apr. 2003). “Challenging Cosmic-Ray Propagation with Antiprotons: Evidence for a “Fresh” Nuclei Component?” *ApJ* 586.2, pp. 1050–1066.
- Moskalenko, Igor V., Andrew W. Strong, Jonathan F. Ormes, et al. (Jan. 2002). “Secondary Antiprotons and Propagation of Cosmic Rays in the Galaxy and Heliosphere”. *ApJ* 565.1, pp. 280–296.
- Neronov, A. and D. Semikoz (Jan. 2020). “Galactic Diffuse Gamma-Ray Emission at TeV Energy”. *A&A* 633, A94.
- Nicolet, M. (Apr. 1975). “On the Production of Nitric Oxide by Cosmic Rays in the Mesosphere and Stratosphere”. *Planet. Space Sci.* 23.4, pp. 637–649.
- Ohm, S., C. van Eldik, and K. Egberts (June 2009). “ γ /Hadron Separation in Very-High-Energy γ -Ray Astronomy Using a Multivariate Analysis Method”. *Astropart. Phys.* 31.5, pp. 383–391.
- Orlando, Elena and Andrew Strong (Dec. 2013). “Galactic Synchrotron Emission with Cosmic Ray Propagation Models”. *MNRAS* 436.3, pp. 2127–2142.
- Paredes, Josep M., Josep Martí, Marc Ribó, et al. (June 2000). “Discovery of a High-Energy Gamma-Ray-Emitting Persistent Microquasar”. *Science* 288.5475, pp. 2340–2342.
- Park, Jaeyeun, Chanhoo Kim, Jooyun Woo, et al. (Mar. 2023a). “A Broadband X-Ray Study of the Rabbit Pulsar Wind Nebula Powered by PSR J1418–6058”. *ApJ* 945.1, p. 66.
- Park, Jaeyeun, Chanhoo Kim, Jooyun Woo, et al. (Mar. 2023b). “X-Ray Studies of the Pulsar PSR J1420–6048 and its TeV Pulsar Wind Nebula in the Kookaburra Region”. *ApJ* 945.1, p. 33.
- Pfeffermann, E. and B. Aschenbach (Feb. 1996). “ROSAT Observation of a New Supernova Remnant in the Constellation Scorpius”. *Roentgenstrahlung from the Universe*. Ed. by H. U. Zimmermann, J. Trümper, and H. Yorke, pp. 267–268.
- Popescu, C. C., R. Yang, R. J. Tuffs, et al. (Sept. 2017). “A Radiation Transfer Model for the Milky Way: I. Radiation Fields and Application to High-Energy Astrophysics”. *MNRAS* 470.3, pp. 2539–2558.
- Porter, T. A., G. Jóhannesson, and I. V. Moskalenko (Sept. 2017). “High-Energy Gamma Rays from the Milky Way: Three-Dimensional Spatial Models for the Cosmic-Ray and Radiation Field Densities in the Interstellar Medium”. *ApJ* 846.1, p. 67.
- Porter, T. A., G. Jóhannesson, and I. V. Moskalenko (Dec. 2019). “Deciphering Residual Emissions: Time-Dependent Models for the Nonthermal Interstellar Radiation from the Milky Way”. *ApJ* 887.2, p. 250.

- Porter, T. A., G. Jóhannesson, and I. V. Moskalenko (Sept. 2022). “The GALPROP Cosmic-Ray Propagation and Nonthermal Emissions Framework: Release v57”. [ApJS](#) 262.1, p. 30.
- Porter, T. A. and R. J. Protheroe (Nov. 1997). “Cosmic-Ray Electrons and the Diffuse Gamma-Ray Spectrum”. [J. Phys. G](#) 23.11, pp. 1765–1784.
- Porter, T. A., G. P. Rowell, G. Jóhannesson, et al. (Aug. 2018). “Galactic PeVatrons and Helping to Find Them: Effects of Galactic Absorption on the Observed Spectra of Very High Energy Gamma-Ray Sources”. [PhRvD](#) 98 (4), p. 041302.
- Porter, T. A. and A. W. Strong (Jan. 2005). “A New Estimate of the Galactic Interstellar Radiation Field Between $0.1\mu\text{m}$ and $1000\mu\text{m}$ ”. *29th International Cosmic Ray Conference (ICRC29), Volume 4*. Vol. 4. International Cosmic Ray Conference, p. 77.
- Porter, Troy A., Igor V. Moskalenko, Andrew W. Strong, et al. (July 2008). “Inverse Compton Origin of the Hard X-Ray and Soft Gamma-Ray Emission from the Galactic Ridge”. [ApJ](#) 682.1, pp. 400–407.
- Press, William H., Saul A. Teukolsky, William T. Vetterling, et al. (1992). *Numerical Recipes in FORTRAN: The Art of Scientific Computing*. 2nd ed. Cambridge, England: Cambridge University Press.
- Price-Whelan, A. M., B. M. Sipőcz, H. M. Günther, et al. (Sept. 2018). “The Astropy Project: Building an Open-Science Project and Status of the v2.0 Core Package”. [AJ](#) 156.3, p. 123.
- Pshirkov, M. S., P. G. Tinyakov, P. P. Kronberg, et al. (Aug. 2011). “Deriving the Global Structure of the Galactic Magnetic Field From Faraday Rotation Measures of Extragalactic Sources”. [ApJ](#) 738.2, p. 192.
- Ptuskin, V. S., F. C. Jones, E. S. Seo, et al. (Jan. 2006). “Effect of Random Nature of Cosmic-Ray Sources Supernova Remnants on Cosmic Ray Intensity Fluctuations, Anisotropy, and Electron Energy Spectrum”. [Adv. Space Res.](#) 37.10, pp. 1909–1912.
- Qiao, Bing-Qiang, Wei Liu, Meng-Jie Zhao, et al. (Aug. 2022). “Galactic Cosmic Ray Propagation: sub-PeV Diffuse Gamma-Ray and Neutrino Emission”. [Front. Phys.](#) 17.4, p. 44501.
- Ramaty, R., D. V. Reames, and R. E. Lingenfelter (Apr. 1970). “Statistical Discrete-Source Model of Local Cosmic Rays”. [PhRvL](#) 24.16, pp. 913–916.
- Recchia, S., S. Gabici, F. A. Aharonian, et al. (May 2019). “Local Fading Accelerator and the Origin of TeV Cosmic-Ray Electrons”. [PhRvD](#) 99.10, p. 103022.
- Robitaille, T. P., E. Churchwell, R. A. Benjamin, et al. (Sept. 2012). “A Self-Consistent Model of Galactic Stellar and Dust Infrared Emission and the Abundance of Polycyclic Aromatic Hydrocarbons”. [A&A](#) 545, A39.
- Robitaille, T. P., E. J. Tollerud, P. Greenfield, et al. (Oct. 2013). “Astropy: A Community Python Package for Astronomy”. [A&A](#) 558, A33.
- Rowell, G. P. (Oct. 2003). “A New Template Background Estimate for Source Searching in TeV Gamma-Ray Astronomy”. [A&A](#) 410, pp. 389–396.
- Rowell, G. P., S. Einecke, R. König, et al. (June 2023). “Modelling Cosmic Rays Escaping From RX J1713.7–3946 – is it Really a PeVatron?” *38th International Cosmic Ray Conference*, p. 676.
- Rozwadowska, Karolina, Francesco Vissani, and Enrico Cappellaro (Feb. 2021). “On the Rate of Core Collapse Supernovae in the Milky Way”. [N. Astron.](#) 83, p. 101498.
- Rybicki, George B. and Alan P. Lightman (1985). *Radiative Processes in Astrophysics*. John Wiley & Sons, Ltd.
- Sako, T. K., K. Kawata, M. Ohnishi, et al. (Oct. 2009). “Exploration of a 100 TeV Gamma-Ray Northern Sky Using the Tibet Air-Shower Array Combined with an Underground Water-Cherenkov Muon-Detector Array”. [Astropart. Phys.](#) 32.3, pp. 177–184.

- Semenov, V. A., A. V. Kravtsov, and D. Caprioli (Apr. 2021). “Cosmic-Ray Diffusion Suppression in Star-Forming Regions Inhibits Clump Formation in Gas-Rich Galaxies”. [ApJ](#) 910.2, p. 126.
- Seo, E. S. and V. S. Ptuskin (Aug. 1994). “Stochastic Reacceleration of Cosmic Rays in the Interstellar Medium”. [ApJ](#) 431, p. 705.
- Shen, C. S. (Dec. 1970). “Pulsars and Very High-Energy Cosmic-Ray Electrons”. [ApJL](#) 162, p. L181.
- Shen, C. S. and C. Y. Mao (Aug. 1971). “Anisotropy of High Energy Cosmic-Ray Electrons in the Discrete Source Model”. [ApL](#) 9, p. 169.
- Steppa, C. and K. Egberts (Nov. 2020). “Modelling the Galactic Very-High-Energy Gamma-Ray Source Population”. [A&A](#) 643, A137.
- Street, J. C. and E. C. Stevenson (Nov. 1937). “New Evidence for the Existence of a Particle of Mass Intermediate Between the Proton and Electron”. [Phys. Rev.](#) 52.9, pp. 1003–1004.
- Strong, A. W. (May 1996). “Diffuse Galactic Gamma-Ray Continuum Emission”. [Space Sci. Rev.](#) 76.3–4, pp. 205–230.
- Strong, A. W. and J. R. Mattox (Apr. 1996). “Gradient Model Analysis of EGRET Diffuse Galactic γ -Ray Emission”. [A&A](#) 308, pp. L21–L24.
- Strong, A. W. and I. V. Moskalenko (Aug. 2001a). “A 3D Time-Dependent Model for Galactic Cosmic Rays and Gamma Rays”. *International Cosmic Ray Conference*. Vol. 5. International Cosmic Ray Conference, pp. 1964–1967.
- Strong, A. W. and I. V. Moskalenko (Oct. 2001b). “SNR and Fluctuations in the Diffuse Galactic γ -Ray Continuum”. *Gamma 2001: Gamma-Ray Astrophysics*. Ed. by Steven Ritz, Neil Gehrels, and Chris R. Shrader. Vol. 587. American Institute of Physics Conference Series, pp. 533–537.
- Strong, A. W., I. V. Moskalenko, T. A. Porter, et al. (July 2009). “The GALPROP Cosmic-Ray Propagation Code”. [arXiv e-prints](#), [arXiv:0907.0559](#).
- Strong, A. W., I. V. Moskalenko, T. A. Porter, et al. (2013). *GALPROP Explanatory Supplement*.
- Strong, A. W., E. Orlando, and T. R. Jaffe (Oct. 2011). “The Interstellar Cosmic-Ray Electron Spectrum from Synchrotron Radiation and Direct Measurements”. [A&A](#) 534, A54.
- Strong, A. W. and G. Youssefi (Jan. 1993). “Spectrum of Electrons with Inhomogeneous Energy Losses”. *23rd International Cosmic Ray Conference (ICRC23), Volume 2*. Vol. 2. International Cosmic Ray Conference, p. 124.
- Strong, A. W. and G. Youssefi (Jan. 1995). “Propagation Models for CR Nucleons and Electrons and Predictions of the Galactic Gamma-Ray Spectrum”. *International Cosmic Ray Conference*. Vol. 3. International Cosmic Ray Conference, p. 48.
- Strong, Andrew W. and Igor V. Moskalenko (Dec. 1998). “Propagation of Cosmic-Ray Nucleons in the Galaxy”. [ApJ](#) 509.1, pp. 212–228.
- Strong, Andrew W., Igor V. Moskalenko, and Vladimir S. Ptuskin (Nov. 2007). “Cosmic-Ray Propagation and Interactions in the Galaxy”. [Annu. Rev. Nucl. Part. Sci.](#) 57.1, pp. 285–327.
- Strong, Andrew W., Igor V. Moskalenko, and Olaf Reimer (July 2000). “Diffuse Continuum Gamma Rays from the Galaxy”. [ApJ](#) 537.2, pp. 763–784.
- Strong, Andrew W., Igor V. Moskalenko, and Olaf Reimer (Oct. 2004). “Diffuse Galactic Continuum Gamma Rays: A Model Compatible with EGRET Data and Cosmic-Ray Measurements”. [ApJ](#) 613.2, pp. 962–976.

- Su, Meng, Tracy R. Slatyer, and Douglas P. Finkbeiner (Dec. 2010). “Giant Gamma-Ray Bubbles from Fermi-LAT: Active Galactic Nucleus Activity or Bipolar Galactic Wind?” [ApJ](#) 724.2, pp. 1044–1082.
- Sudoh, Takahiro and John F. Beacom (Nov. 2023). “Where is the End of the Cosmic-Ray Electron Spectrum?” [PhRvD](#) 108.10, p. 103015.
- Sun, X. H., W. Reich, A. Waelkens, et al. (Jan. 2008). “Radio Observational Constraints on Galactic 3D-Emission Models”. [Astropart. Phys.](#) 477.2, pp. 573–592.
- Sun, Xiao-Hui and Wolfgang Reich (Dec. 2010). “The Galactic Halo Magnetic Field Revisited”. [RAA](#) 10.12, pp. 1287–1297.
- Swordy, Simon P. (July 2003). “Stochastic Effects on the Electron Spectrum Above TeV Energies”. *International Cosmic Ray Conference*. Vol. 4. International Cosmic Ray Conference, p. 1989.
- Tan, L. C. and L. K. Ng (Feb. 1983). “Calculation of the Equilibrium Antiproton Spectrum”. [J. Phys. G](#) 9.2, pp. 227–242.
- Thomson, J. J. and G. P. Thomson (1933). *Conduction of Electricity Through Gases*. 3rd Edition. Vol. II. Cambridge, England: Cambridge University Press.
- Tripathi, R. K., Francis A. Cucinotta, and John W. Wilson (Oct. 1996). “Accurate Universal Parameterization of Absorption Cross Sections”. [Nucl. Instrum. Methods Phys. Res. B](#) 117.4, pp. 347–349.
- Tsuji, Naomi, Yasunobu Uchiyama, Felix Aharonian, et al. (June 2019). “NuSTAR Observations of the Supernova Remnant RX J1713.7–3946”. [ApJ](#) 877.2, p. 96.
- Umemoto, Tomofumi, Tetsuhiro Minamidani, Nario Kuno, et al. (Oct. 2017). “FOREST Unbiased Galactic Plane Imaging Survey with the Nobeyama 45 m Telescope (FUGIN). I. Project Overview and Initial Results”. [Publ. Astron. Soc. Jpn.](#) 69.5, p. 78.
- Vallée, Jacques P. (June 2020). “A New Multitracer Approach to Defining the Spiral Arm Width in the Milky Way”. [ApJ](#) 896.1, p. 19.
- Vecchiotti, V., F. L. Villante, and G. Pagliaroli (Sept. 2023). “Setting an Upper Limit for the Total TeV Neutrino Flux from the Disk of Our Galaxy”. [JCAP](#) 2023.9, p. 027.
- Vecchiotti, V., F. Zuccarini, F. L. Villante, et al. (Mar. 2022). “Unresolved Sources Naturally Contribute to PeV Gamma-Ray Diffuse Emission Observed by Tibet AS γ ”. [ApJ](#) 928.1, p. 19.
- Virtanen, Pauli, Ralf Gommers, Travis E. Oliphant, et al. (Feb. 2020). “SciPy 1.0: Fundamental Algorithms for Scientific Computing in Python”. [Nat. Methods](#) 17, pp. 261–272.
- Waelkens, A., T. Jaffe, M. Reinecke, et al. (Feb. 2009). “Simulating Polarized Galactic Synchrotron Emission at all Frequencies. The Hammurabi Code”. [A&A](#) 495.2, pp. 697–706.
- Wainscoat, R. J., M. Cohen, K. Volk, et al. (Nov. 1992). “A Model of the 8–25 micron Point Source Infrared Sky”. [ApJS](#) 83, p. 111.
- Wang, Y., H. Beuther, M. R. Rugel, et al. (Feb. 2020). “The HI/OH/Recombination Line Survey of the Inner Milky Way (THOR): Data Release 2 and HI Overview”. [A&A](#) 634, A83.
- Webber, W. R. (Oct. 1998). “A New Estimate of the Local Interstellar Energy Density and Ionization Rate of Galactic Cosmic Rays”. [ApJ](#) 506.1, pp. 329–334.
- Weekes, T. C., H. Badran, S. D. Biller, et al. (May 2002). “VERITAS: The Very Energetic Radiation Imaging Telescope Array System”. [Astropart. Phys.](#) 17.2, pp. 221–243.
- Weekes, T. C., M. F. Cawley, D. J. Fegan, et al. (July 1989). “Observation of TeV Gamma Rays from the Crab Nebula Using the Atmospheric Cerenkov Imaging Technique”. [ApJ](#) 342, p. 379.

- Weingartner, J. C. and B. T. Draine (Dec. 2001). “Electron-Ion Recombination on Grains and Polycyclic Aromatic Hydrocarbons”. [ApJ](#) 563.2, pp. 842–852.
- Wellisch, H. P. and D. Axen (Sept. 1996). “Total Reaction Cross Section Calculations in Proton-Nucleus Scattering”. [PhRvC](#) 54.3, pp. 1329–1332.
- Werner, M., R. Kissmann, A. W. Strong, et al. (Apr. 2015). “Spiral Arms as Cosmic Ray Source Distributions”. [Astropart. Phys.](#) 64, pp. 18–33.
- Woo, Jooyun, Hongjun An, Joseph D. Gelfand, et al. (Sept. 2023). “Hard X-Ray Observation and Multiwavelength Study of the PeVatron Candidate Pulsar Wind Nebula “Dragonfly””. [ApJ](#) 954.1, p. 9.
- Wood, M., R. Caputo, E. Charles, et al. (July 2017). “Fermipy: An Open-Source Python Package for Analysis of Fermi-LAT Data”. *35th International Cosmic Ray Conference (ICRC2017)*. Vol. 301. International Cosmic Ray Conference, p. 824.
- Yan, Kai, Ruo-Yu Liu, Rui Zhang, et al. (May 2024). “Insights from LHAASO and IceCube into the Origin of the Galactic Diffuse Teraelectronvolt-Petaelectronvolt Emission”. [Nature Astro.](#) 8, pp. 628–636.
- Yusifov, I. and I. Küçük (Aug. 2004). “Revisiting the Radial Distribution of Pulsars in the Galaxy”. [A&A](#) 422, pp. 545–553.
- Zhao, S., R. Zhang, Y. Zhang, et al. (Mar. 2022). “Measurement of the Diffuse Gamma-Ray Emission from Galactic Plane with LHAASO-KM2A”. *37th International Cosmic Ray Conference*, p. 859.
- Zyla, P. A., R. M. Barnett, J. Beringer, et al. (Aug. 2020). “Review of Particle Physics”. [Prog. Theor. Exp. Phys.](#) 2020.8, p. 083C01.